Optimizing Pillar Design for Improved Stability and Enhanced Production in Underground Stone Mines

Aman Soni

Dissertation submitted to the faculty of the
Virginia Polytechnic Institute and State University
in partial fulfillment of the requirements for the degree of

Doctor of Philosophy
in
Mining Engineering

Nino S. Ripepi, Chair
Erik C. Westman
Mario G. Karfakis
Jim Hazzard

May 5, 2022
Blacksburg, VA

Keywords: underground mining, karst, hard rock, stone, pillar design, local stability, global stability, discrete element modeling, finite volume modeling, enhanced recovery

Optimizing Pillar Design for Improved Stability and Enhanced Production in Underground Stone Mines

Aman Soni

(ABSTRACT)

"*Safety is a value, not just a Priority*"

Geomechanically stable underground excavations require continuous assessment of rock mass behavior for maximizing safety. Optimizing pillar design is essential for preventing hazardous incidents and improving production in room-and-pillar mines. Maintaining regional and global stability is complicated for underground carbonate or stone deposits, where extensive fracture networks and groundwater flow become leading factors for generating unsteady ground conditions including karsts. A sudden encounter with karst cavities during mine advance may lead to safety issues, including ground collapse and outflow of unconsolidated sediments and groundwater. The presence of these eroded zones in pillars may cause their failure and poses a risk to the lives of miners apart from disrupting the pre-planned mining operations.

A pervasive presence of joints and fractures plays a primary role in promoting structurally controlled failures in stone mines, which accelerates upon interaction with the karst cavities. The prevalent empirical and analytical approaches for pillar design ignore the geotechnical complexities such as the spatial density of discontinuities, karst voids, and deviation from the design during short-range mine planning. With the increasing market demand for limestone products, mining organizations, as well as enforcement agencies, are investing in research for increasing the efficiency of extracting valuable resources. While economical productivity is essential, preventing risks and ensuring the safety of miners remains the

cardinal objective of mining operations. According to the Mine Safety and Health Administration (MSHA), since 2000, about 31% of occupational fatalities at all underground mines in the United States are caused due to ground collapse, which rises to 39% for underground stone mines.

The objective of this study is to provide a reliable and methodological approach for pillar design in underground room-and-pillar hard rock mines for safe and efficient ore recovery. The numerical modeling techniques, implemented for a case study stone mine, could provide a pragmatic framework to assess the effect of karsts on rock mass behavior, and design future pillars detected with voids. The research uses data acquired from using remote sensing techniques, such as LiDAR and Ground-penetrating Radar surveys, to map the excavation characteristics. Discontinuum modeling was valuable for analyzing the pillar strength in the presence of discontinuities and cavities, as well as estimating a safe design standard. Discrete Fracture Networks, created using statistical information from discontinuity mapping, were employed to simulate the joints pervading the rock mass. This proposed research includes the calibration of rock mass properties to translate the effect of discontinuities to continuum models. Continuum modeling proved effective in analyzing regional stability along with characterizing the redistributed stress regime by imitating the excavation sequence. The results from pillar-scale and local-scale analyses are converged to optimize pillar design on a global scale and estimate the feasibility of secondary recovery in stone mines with a dominating discontinuity network and karst terrane. Stochastic analysis using finite volume modeling helped evaluate the performance of modified pillars to assist production while maintaining safety standards. The proposed research is valuable for improving future design parameters, excavation practices, and maintaining a balance between an approach towards increased safety while enhancing production.

Optimizing Pillar Design for Improved Stability and Enhanced Production in Underground Stone Mines

Aman Soni

(GENERAL AUDIENCE ABSTRACT)

"The most valuable resource to come back out of a mine is a miner" – Anonymous

The United States accounted for 27% of the global limestone market share which was valued at US$58.5 billion in 2020 [148]. It is projected to reach a target of US$65.3 billion in 2027, growing even in midst of the COVID-19. As surface reserves deplete, much of the mineral demand gap is supplemented by mining underground deposits. Underground mines extract minerals from deep within the earth compared to surface mines. As a result, the miners experience a greater number of accidents in a constricted environment because of roof/tunnel collapse, fewer escape routes, ventilation, explosions, or inundation. According to the Mine Safety & Health Administration (MSHA), about 15% of all underground mine injuries in the US were caused by rockfalls since 1983.

The majority of underground stone deposits are mined using the room-and-pillar mining method, which resembles a chessboard design where the light squares are mined, and the dark squares are left as rock pillars to support the tunnels. Limestone, a carbonate rock, contains a lot of fractures and joints (discontinuities). Erosion of rocks due to continuous water flow through the fractures leads to the formation of cavities known as karsts. Interaction of karsts with the prevalent fracture network increases rockfall risk during mining. The collapse of voids along with an inrush of filled rock-clay-water sludge can harm miners' lives, damage machinery, and stop further operations. Literature is scarce on topics that quantify the risk and disruption posed by these cavities in underground mines. Most

rock classification systems cannot classify their effect because of the unpredictability and extensive analysis required. The objective of this research is to provide a reliable and methodological approach for designing pillars in underground hard rock mines for ensuring a safe working environment and efficient mineral recovery.

This research starts with analyzing the strength of pillars, in which karst cavities were discovered while mining. The safety concerns often lead the miners to not excavate around the cavities and leave valuable resources unmined. Data from ground-penetrating radar and laser scanning surveys were used to characterize the voids and map the discontinuities. Discrete-element numerical modeling was used to simulate the pillars as an assembly of blocks jointed by the discontinuities. The simulation results help us understand the instability issues in the karst-ridden pillars and ways to improve upon the existing design. The findings were used to modulate the parameters for regional-scale models using finite volume modeling for less computationally intensive analyses and simulating rock as a continuum. The continuum models were highly effective in analyzing the instability issues due to the prevalent karstic network. This helps understand any alternative scenario that could have been implemented to optimize ore recovery while preventing risks. The results from the single pillar and regional analyses are combined to optimize pillar design on a global mine scale. This dissertation focuses on improving hazard mitigation in mines with unpredicted anomalies like karsts. Although this research is based on a specific mine site, it empowers the operators to explore the presented techniques to increase safety in all underground mines. The suggested methodology will help devise better strategies for handling instability issues without jeopardizing the mine operations. The primary motivation is to keep the underground miners safe from hazardous situations while fulfilling the secondary objective of maximizing mineral production.

Dedication

To my love,

Anuradha

Acknowledgments

I am fortunate to have been a part of the Ground Control research group during my time at Virginia Tech. No words will be able to express my gratitude to Dr. Nino Ripepi for his constant support and guidance. Nino is a great mentor and has always entrusted me with the freedom to explore my ideas during this research project.

I am grateful to Dr. Erik Westman & Dr. Mario Karfakis for steering me through my Ph.D. I could always count on their insightful advice and found encouragement in their support.

I feel honored to be Itasca's IEP scholar and feel grateful to have Dr. Jim Hazzard as my mentor. Jim's invaluable support and wonderful teaching pushed my thinking to a higher level, and I would not have been able to complete my research without him.

I acknowledge the generous financial support from the National Institute of Occupational Safety and Health for this research project. I thoroughly enjoyed the research discussions with Dr. Brent Slaker and Dr. Michael Murphy and appreciate their valuable feedback. I would also like to thank SME and WAAIME group for providing academic scholarships.

I would like to thank Mark Luxbacher, Nathan Bench, and the Lhoist Group for organizing field surveys, and providing the necessary resources and support during this project.

I am deeply grateful to my colleagues and friends, Juan Monsalve, Richard Bishop, and Jon Baggett for their consistent support in setting the foundation for my research. I would also like to appreciate the wonderful Mining Engineering faculty and staff at VT including, Dr. Kray Luxbacher, Warren Lucero, Michelle Crotto, Dr. Cigdem Keles, Angelo Biviano, Laurinda Gartner, and Lori Andrews for making my time at Virginia Tech feel like a breeze.

I feel blessed to have worked with Dr. Sripad Naik, who has been a source of inspiration and perseverance since I began my career in mining. I have been fortunate to have some amazing friends, Digvijay, Poorvesh, Marina, Ellie, Setareh, Nestor, Joe, Manuel, Lizeth, August, Festus, and Sharon. Their company has brought a sense of great joy to my life.

Finally, my family deserves my endless gratitude for their unfailing support. We have experienced some ups and downs in the past years, but I am forever indebted to my parents for their love (could not have done it without your genetics).

Notations

ρ	Density
ϕ	Angle of Friction
τ	Tensile Strength
σ	Normal Stress
ν	Poisson's Ratio
ψ	Angle of Dilation
g	Acceleration due to gravity
C, c	Cohesion
E	Young's Modulus
K	Bulk Modulus
G	Shear Modulus
S	Stress
W_{eff}	Effective Pillar Width
W	Width of a Square Pillar
H	Height of a Pillar
Pa	Pascals
MPa	Megapascals
GPa	Gigapascals
ft	feet
m/s	meter per second
μm/s	micrometer per second
m^3	Cubic meter
kg/m^3	Kilogram per cubic meter
N	Newton
MHz	Megahertz
[°]	degree

Contents

List of Figures

List of Tables

Preface

This dissertation is compiled using a manuscript-based format and is composed of seven chapters. The objective of the dissertation is to cohesively bring together the conducted doctoral research at different scales of ground control and safety for an underground mine environment. The research initiates by examining a single pillar in the mine and analyzing a local region to finally visualize optimization on a global scale. This document identifies the site-specific ground control challenges and proposes a comprehensive methodology for optimization of local and global stability for improving the safety of miners and mitigating exposure to rockfall-related hazards. The techniques discussed here would enable the incorporation of geotechnical mapping and monitoring data for enhancing ore recovery and improving safety in underground stone and large-opening mines. The principles identified through this research can be adapted to develop ground control management plans and estimate the feasibility of secondary extraction for underground metal and other hard rock deposits. Figure 7.1 shows the proposed framework, methodology, and techniques presented in this dissertation.

Chapter 1 introduces a detailed review of the literature related to the ground control challenges observed in stone mines, mainly pillar or roof collapse caused by the presence of karst voids. The chapter discusses the failure mechanisms of hard rock pillars and their behavior when subjected to different stress states. This part of the dissertation covers the relevant approaches to explain failure mechanics, including case-histories-based empirical methods, mathematically composed analytical methods, and the evolution of numerical modeling techniques for analyzing and predicting the complex geomechanical behavior of rock masses.

Chapter 2 discusses the ground control problems during mining operations caused by the interaction of karst voids with a prevalent discontinuity network. This chapter presents a numerical estimation of the effect of karst voids on the strength of pillars in an underground room-and-pillar limestone case study mine. It is shown that these cavities may contribute to a considerable decrease in pillar strength. Mining advances into such karstic formations may lead to a sudden in-rush of groundwater or unconsolidated sediments. The research develops on previous studies performed at the case study mine which used ground-penetrating radar (GPR) to map the karst boundaries inside the pillar and LiDAR scans to map the discontinuity network. Distinct-element modeling (DEM) is used to simulate the presence of voids and discontinuities in the form of Discrete Fracture Networks (DFN). An effort is made to understand the importance of pillar design and dimensions in an underground limestone mine with karst voids to prevent local instability related to pillar failures.

Chapter 3 presents the continued research from the previous study and provides a safe and reliable alternative design for safe and efficient ore recovery from a pillar. It was assessed from the calculated pillar strength and the estimated redistributed stresses that the pillar is capable of countering more stress than is currently imparted on it. Numerical modeling studies combining in situ stress determination and excavation sequencing were used to estimate the existing stresses on the pillar. Different possibilities of modification to existing pillar design were simulated using Distinct-element modeling (DEM) to determine better designs. An effort was made to understand the variation of pillar strength with height for karst-affected pillars using two different constitutive models. This chapter serves as a preliminary investigation in terms of improving the future design of pillars and recovering pillars from legacy workings.

Chapter 4 focuses on a simple yet novel concept of assessing pillar strength and optimizing pillar design. This study evaluates the stability and design of karst-prone and tall stone pillars in the case study mine by compartmentalizing them into separate zones. The pillars, left after stope extraction, may indicate visible deterioration at one place and still not show signs of yield or complete failure. Hence, along with evaluating the overall pillar's strength, stability analysis is carried out individually for compartmentalized zones of the pillars, especially those affected by karsts. This study demonstrates the benefit of conducting drone and terrestrial LiDAR surveys in underground environments. These surveys proved advantageous for mapping the discontinuity network around the pillars, both in terms of safety and convenience. Distinct-Element Modeling using 3DEC and Discrete Fracture Networks is used to replicate the stochastic nature of discontinuities interspersed in the rock mass.

Chapter 5 summarizes the shortcomings of prevalent empirical and analytical approaches which ignore the governing discontinuity network for an underground stone deposit. This chapter demonstrates a parametric study to discuss the effect of fracture density of discontinuity networks on pillar strength. P_{32}, a measure of the spatial frequency of discontinuities in a joint set, was varied to study the resultant effect on stone pillar strength. The effect of discontinuities is translated to continuum modeling based on their association with shear strength properties and elastic moduli of the intact rock. A sensitivity analysis is also done to assess the modulation of different properties required for calibrating the continuum model. Finally, a local model is simulated to analyze the existing instabilities in the area due to the presence of karsts. The results were useful for evaluating the behavior of excavations in a larger, local area mine model by taking the advantage of less computationally intensive continuum modeling.

Chapter 6 brings together the various single pillar and local-scale studies from previous chapters and applies them on a global mining scale. This chapter discusses the importance of improving pillar design while maintaining stability for a karst-prone and karst-free stone deposit. Comparisons are made between the existing layout and the improvised layout for a multi-level underground case study mine. Stochastic analysis is conducted using explicit finite volume modeling to evaluate the performance of the suggested design to improve recovery while maintaining stability. Based on field studies and geological surveys, unstable zones representing karst voids are embedded in the mine model using a pseudo-random number generator function. Multiple simulations from karst-embedded models provide sufficient data to analyze the shift in the factor of safety of pillar zones with a variation in redistributed stresses. Efforts are made to display the advantages of continuum models over analytical methods which often overestimate the strength of pillars and stability of surroundings. The results are interpreted to understand the need for the optimizing design and dimensions of pillars with varying depths for a hard rock mine to improve profitable ore production while maintaining safe working conditions.

Finally, Chapter 7 presents the conclusions of the doctoral research for improving safety while optimizing pillar design for ground control management in underground stone and other hard rock mines. The scope of the dissertation lays out the future possibilities for further developing research related to geomechanical advances for risk management using novel numerical modeling techniques for underground excavations.

Chapter 1

Literature Review

This chapter presents an overview of karst detection in limestone deposits, failure modes of stone pillars, and pillar design using different techniques. The review includes a comprehensive description of both experimental and theoretical investigations. The detailed review in this chapter is devoted to understanding the factors that impact pillar design in underground stone and other hard rock mines affected by karst voids.

1.1 Characterizing karst in limestone deposits

The prediction of karst cavities in underground stone mines has an important impact on safety and risk management. The occurrence of these ground collapses due to advancing into karst cavities may be controlled and managed by establishing a void detection system and planning mine design and excavation. In the past 40 years, about 12% of the reported injuries in the stone mining industry have been caused as a direct or indirect result of roof or pillar collapse [108]. The karstic features act as catalysts to ground failures during mining operations.

The presence of karst sinkholes in the metal and coal mines in China has been documented by Gongyu & Wanfang [49]. The association of sinkholes leading to a major inrush of water during mining poses a risk to mine safety. The authors further discussed taking some ground

control measures such as controlling mine drainage to prevent water flow and grouting karst conduits for managing cavity collapses.

Numerous pieces of literature have been published in recent years to address the issues posed by karsts to the mining industry. Beck addressed issues related to karst in general, as well as their engineering and environmental impacts [11]. There are a few individual pieces of literature that address the disruption caused by karst during mining activities. An active sinkhole collapse occurred while dewatering a zinc mine near Friedensville, Pennsylvania in 1953. More than 150 sinkholes were reportedly discovered until 1971 [103].

One of the most important methods of preventing ground failures due to karsts is by focusing on detecting the cavities beforehand using Ground-penetrating radar (GPR). The process uses the transmission of radio waves and differences in conductivity of the material to delineate open cavities. Baggett [7] demonstrated the use of GPR in the case study mine to detect the voids ahead of mining operations. The work shed light on the use of 2D and 3D surveys to map voids within a pillar in an underground stone mine. Sun et al. [134] performed Electrical Resistivity Imaging (ERI) around a mining area in the Chinese province of Guangxi. The purpose of the survey was to evaluate the high degree of karstification, and the presence of fracture networks formed due to a prolonged period of groundwater erosion of limestone deposits. The study was used to determine the geometry of voids at a certain depth and was verified using drilling experiments. While several techniques have been utilized throughout various industries for karst detection and mapping, there is a lack of literature on the applicability of GPR in underground mining scenarios.

While an earlier detection of karsts is an effective way to identify the instability phenomena and perform monitoring, stability assessment of pillars and subsequent mine design plays a

vital role in maintaining a stable and risk-free environment through future operations. This includes analyzing areas during the excavation for stability issues including pillars, roof, and sidewalls. Kortnik [78] discussed the importance of planning, monitoring, and optimization of stone pillars during underground excavation. The study mentions the extraction of natural stone blocks from an underground room-and-pillar mine in Slovenia. Due to mining at a shallow depth, insufficient confinement posed a risk of wedge-shaped rock blocks falling from the roof and pillars.

1.2 Failure Mechanisms of Hard Rock Pillars

Until a few years back, failure modes of stone or hard rock pillars did not receive the generous research attention as coal pillars. As a considerable number of stone mines are moving underground and the potential for stone pillars increases, research on them has also increased. Among the numerous factors deciding the failure criterion in hard rock pillars, the most important ones include in situ stresses, physico-mechanical properties of rock, local and regional geology, and hydrological conditions [19]. These are natural factors that cannot be controlled. Pillar design or slenderness, on the other hand, is an artificial factor and is considered paramount in deciding the failure mode.

The types of failure modes for stone pillar failure can however be categorized as Stress-controlled and Structure-controlled. The former type occurs at greater depths, where the in situ stresses are high and tensile fractures parallel to maximum principal stress lead to failure [58]. Whereas the latter causes failure due to low confinement conditions leading the rock to fail along the discontinuities as shown in Figure 1.1.

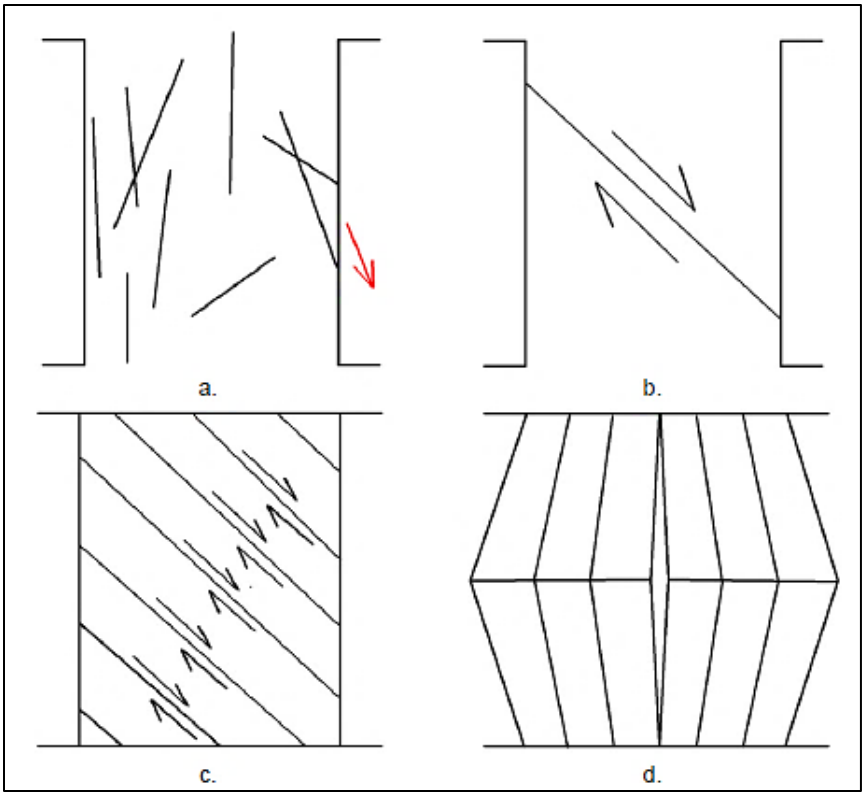

Figure 1.1 Structure controlled failures a) rock block sliding b) through going shear failure c) transgressive shear failure and d) buckling failure [19]

Lunder [89] classified the pillars into five categories based on the fractures observed on them from the underground mines of Westmin Resources. The five categories are described as Class I: when a pillar shows no signs of stress-induced fracturing on the outer skin; Class II: when the corners of the pillars start developing fractures; Class III: when the length of fractures on the outer skin of the pillar is less than or equal to half the pillar height and the fracture aperture is less than 5 mm; Class IV: when the fractures merge and the length of the fractures is greater than half the pillar height with apertures greater than 5 mm, and Class V: when the pillars disintegrate with blocks falling apart, the fractures pass through the pillar core with apertures greater than 10 mm.

Figure 1.2 depicts the classification of Denison mine pillars as described by Pritchard and Hedley [118]. The authors introduce five categories to illustrate the progressive failure mechanism of large pillars using stress-induced mechanics. The stages could be stated as:

- Stage I- Minor spalling in the pillar sidewalls
- Stage II- Low confining stresses cause major spalling and high tangential stresses lead to crack formation and slabbing in the direction of major principal stresses
- Stage III- Transfer of stresses to inner intact rock after the loss of pillar skin
- Stage IV- Damage to the inner core after the progressive loss of confinement
- Stage V- Total pillar failure

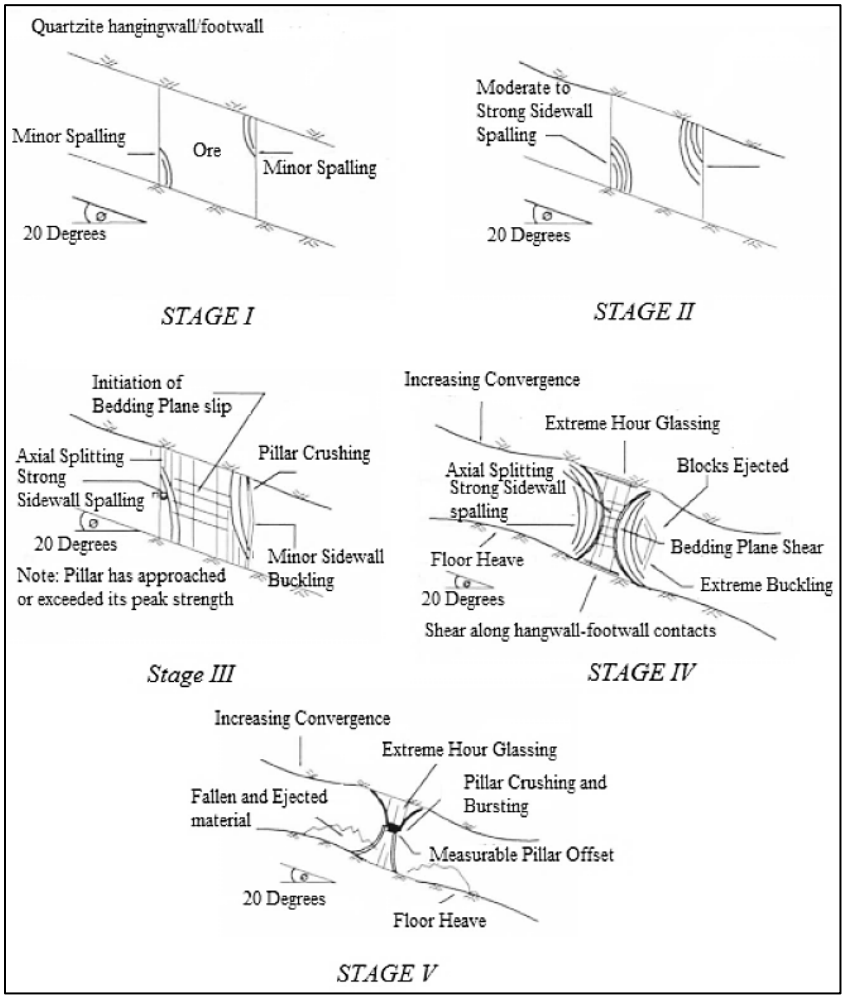

Figure 1.2 Pillar failure classification stages by Pritchard and Hedley [118].

Fang and Harrison [44] simulated failures for hard rock pillars by developing a local degradation model. It consisted of a degradation index that classified the rock fractures at a microscopic level into two components specifically, brittle and ductile. The brittle component is responsible for a reduction in local material elasticity and strength, whilst the ductile component leads to plastic deformation. The failure process was simulated for pillars with a width-to-height ratio of 2.0. The failure stages of the pillar are shown in Figure 1.3.

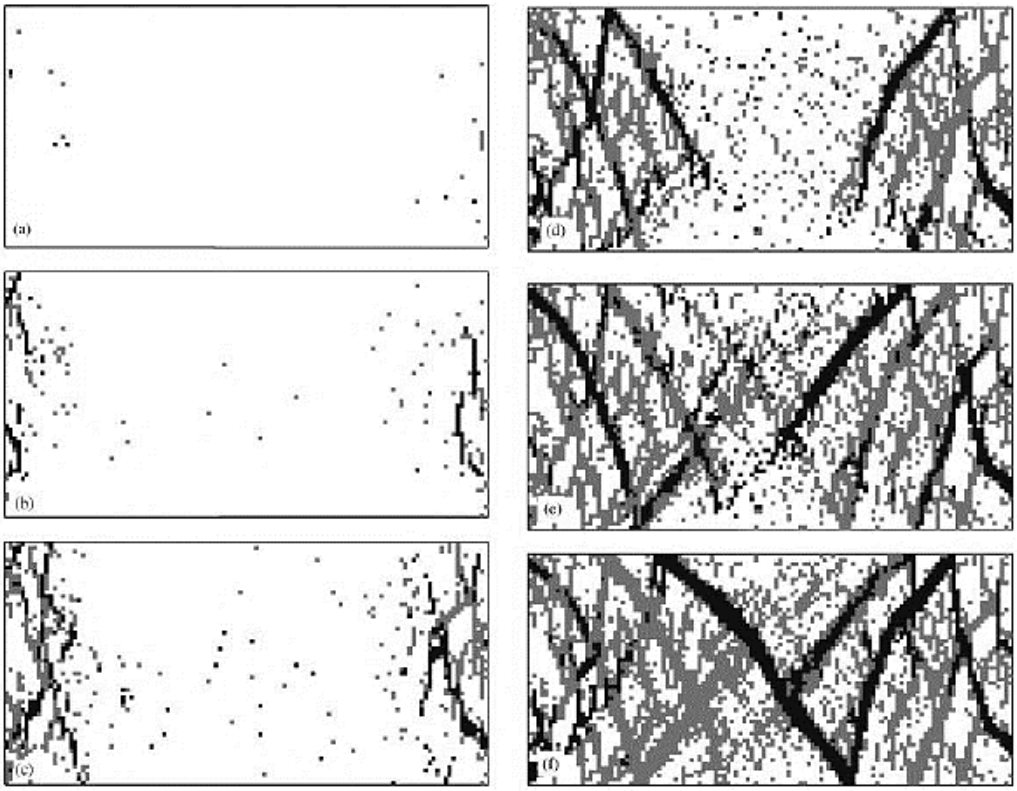

Figure 1.3 Pillar failure stages for a W/H ratio of 2.0 with local degradation model by Fang and Harrison [44].

In the figure above, Stage (a) shows the initiation of fractures followed by spalling caused by the merging of the fractures in Stage (b). In Stage (c), shear fractures initiate from one end of the pillar and emanate towards the other end in an inclined manner to the center of the pillar in stage (d). Fang and Harrison [44] also determined the development of shear to

the center of the pillar from both sides as the peak strength in Stage (e), and Stage (f) was caused by the extension of the shear fractures. Although the modeling was performed for the hard rock pillars, the model was calibrated to a coal pillar.

Esterhuizen et al. [42] conducted a series of pillar studies for the limestone mines in the United States. The author developed a pillar stress rating system similar to that proposed by Lunder [89], and a geological rating system that takes into account the effect of the geological discontinuities on pillar strength by visual inspection. The pillars' rating could be classified as none, minor, moderate, severe, and very severe according to the failing rock blocks as shown in Figure 1.4.

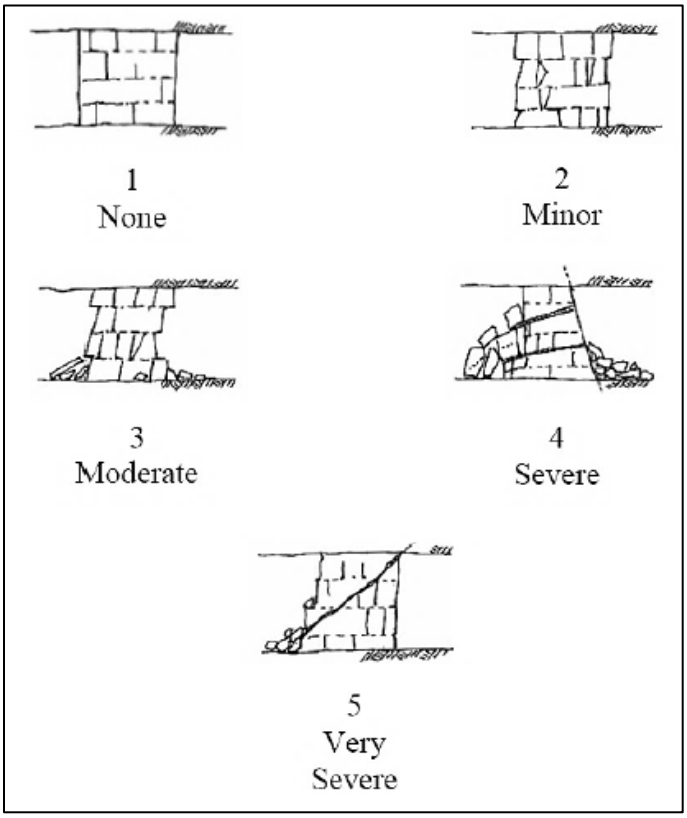

Figure 1.4 Geological rating system of pillar failure after Esterhuizen et al. [42].

'None' represents a joint block fallout with less than 0.3m, and that between 0.3-1 m was classified as 'Minor'. 'Moderate' represents a pillar affected with block fallout of about 1-3 m, and those higher than 3 m were recognized as 'Severe'. When a pillar was bisected with a through-going structural discontinuity with a dip angle of more than 35°, and the pillar strength depends on the discontinuity strength, it was classified as 'Very severe'.

Another progressive stress-induced pillar failure rating system was introduced by Roberts et al. [120]. This was a 6-stage rating system starting from an intact pillar at Stage 1 to failed pillar at Stage 6 as shown in Figure 1.5. In the first stage, the intact pillar shows no indication of stress-induced fracturing. The second stage defines minor spalling on the pillar face where the fractures are relatively small compared to the pillar height. A substantial spalling with feathery slabs on the pillar face denotes the third stage and the fractures can be estimated up to half the pillar height.

The fourth stage marks the onset of the hourglass formation with a large slab formation on the pillar face with fractures greater than half of the pillar height. The fifth stage comprises of well-developed hourglass formation with large open fractures piercing through the core along with massive spalling on the pillar face. Ultimately, a failed pillar in the sixth stage is classified with extreme hourglass formation or falls out of major blocks from the pillar after which it carries minimal residual load-carrying capacity. These stages were used as the primary reference for the numerical models.

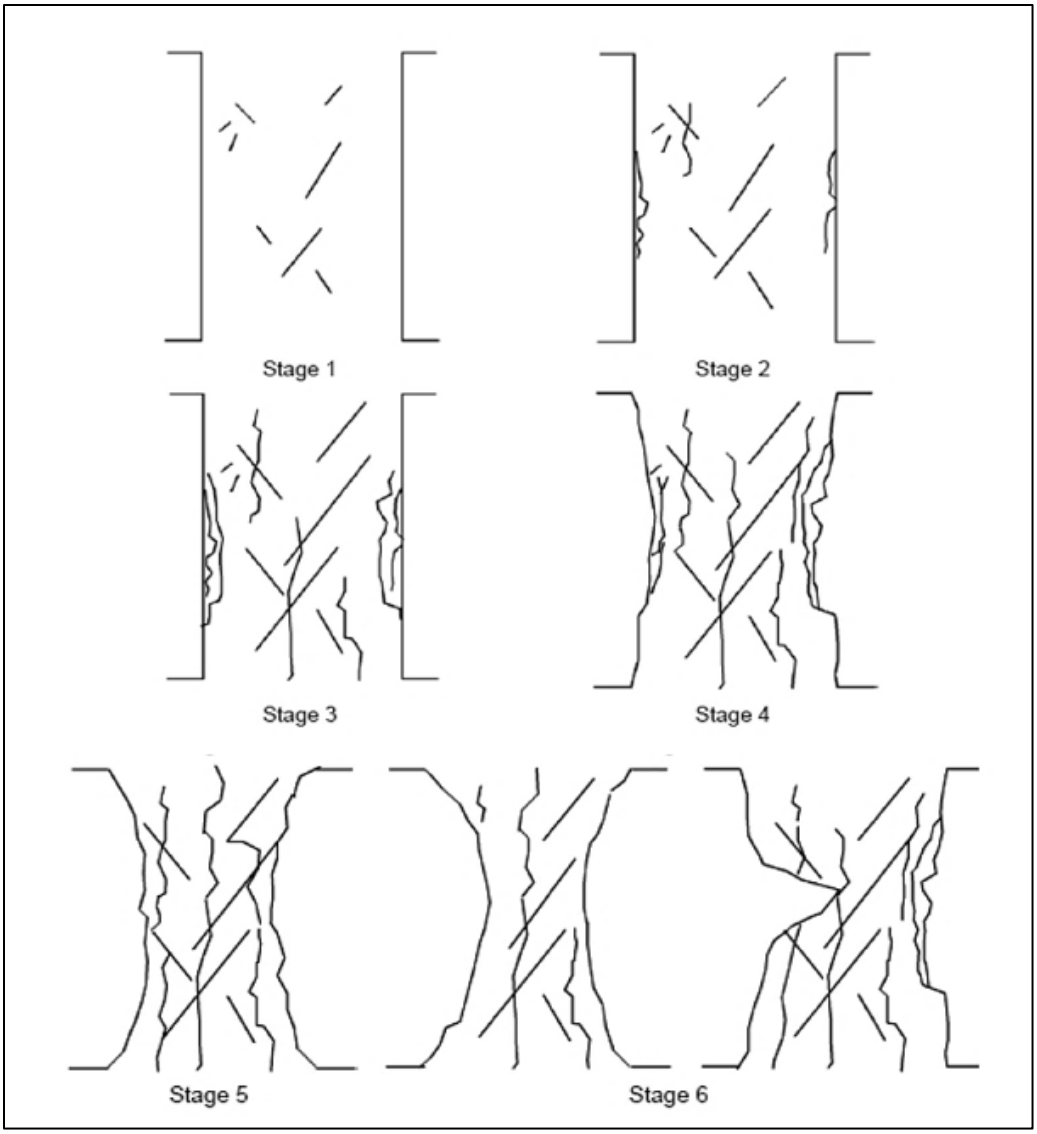

Figure 1.5 Pillar failure rating system; Stage 1: Intact pillar; Stage 2: Minor spalling; Stage 3: Substantial spalling; Stage 4: Formation of hourglass shape; Stage 5: Well-developed hourglass shape; Stage 6: Failed pillar - Two different ways by Roberts [120].

1.3 Pillar Design using Empirical Approaches

Several methods have been tried to assess and predict the response of pillars in underground mines over the last century. Most of these methods are based on coal mining environments and include back analysis from comparing stable and failed pillars in an area in a mine and

deriving empirical equations using a sufficient amount of data. Bunting [21] was one of the earliest researchers to suggest an empirically based pillar strength equation. A factor of safety value of 2.5 was considered to evaluate the behavior of eight pillars including one failed pillar. The pillar strength laboratory study was conducted by testing anthracite prisms with specimen sizes ranging between 5 cm and 10 cm. It was demonstrated that pillar strength is related to its dimensions and can be expressed as:

$$\sigma_{\mathrm{p}} = 700 + 300\frac{\mathrm{b}}{\mathrm{h}} \tag{1}$$

where σ_p is the crushing strength per unit area in psi, b is the least lateral dimension in inches, and h is the height in inches.

Obert and Duvall [114] derived a relationship between the strength and the W/H ratio of a pillar based on the experimental studies carried out on different rock types with W/H ratios varying from 0.5 to 3. The equation is as follows:

Martin and Maybee [100] compiled most of the common and widely used empirical approaches which have been used over the years to estimate the strength of pillars for different rock types. Most of these empirical approaches were derived by studying data and back analysis of pillar states in underground coal mines. These empirical equations are described in Table 1.1.

Table 1.1 Empirical approaches for estimating pillar strength

Empirical Pillar Strength (MPa)	**UCS (MPa)**	**Rock Type**	**Total Pillar Dataset Number**	**Primary Authors**
$K\left(\frac{W^{0.44}}{H^{0.66}}\right)$	-	Coal	125	Salaman and Munro [124]
$133\left(\frac{W^{0.44}}{H^{0.66}}\right)$	230	Quartzites	28	Hedley and Grant [55]
$65\left(\frac{W^{0.46}}{H^{0.66}}\right)$	94	Metasediments	57	Kimmelmann et al. [76]
$35.4\left(0.778+0.222\frac{W}{H}\right)$	100	Limestone	14	Krauland and Soder [82]
$0.42\ {}_c\frac{W}{H}$	-	Canadian Shield	23	Potvin et al. [117]
$74\left(0.778+0.222\frac{W}{H}\right)$	240	Limestone	9	Sjoberg [125]
$0.42\ {}_c(0.68+0.52K)$	-	Hard Rocks	178	Lunder and Pakalnis [88]
$k\left(\frac{\sqrt{W}}{H}\right)$	-	Coal	-	Holland & Gaddy [59]
$6.2\left(0.64+0.36\frac{W}{H}\right)$	-	Coal	66	Bieniawski et al. [15]
$6.2\left(0.64+0.36\frac{W}{H}-0.18\frac{W^2}{LH}\right)$		Coal		Mark et al. [97]

Lunder [89] documented 178 hard rock pillar case histories in Canadian mines and proposed an empirical approach to studying the effect of confinement for the rib and sill pillars over the W/H ratio of 1. Three classifications were proposed for pillar stability using the factor of safety (FOS). The pillars with FOS less than 1 were classified as failed, the pillars between FOS of 1 and 1.4 were labeled as unstable, whereas those with FOS greater than 1.4 were considered stable pillars. The empirical approach can be stated as:

$$_{\mathrm{p}} = \mathrm{K}^{*}\mathrm{UCS}^{*}\ (\mathrm{C}_1 + \mathrm{C}_2{}^{*}\ ) \tag{4}$$

where σ_p is the ultimate pillar strength (MPa), K is the pillar size factor, UCS is the uniaxial compressive strength of the intact rock (MPa), C_1 and C_2 are the empirical rock mass constants and κ is the friction term which can be calculated as:

$$= \tan\left(\cos^{-1}\left[\frac{1\text{-}\mathrm{C}_{\mathrm{pav}}}{1+\mathrm{C}_{\mathrm{pav}}}\right]\right) \tag{5}$$

$$\mathrm{C}_{\mathrm{pav}} = \mathrm{C}_{\mathrm{p}}\left\{\log\left(\frac{\mathrm{W}}{\mathrm{H}}+0.75\right)\right\}^{1.4\frac{\mathrm{W}}{\mathrm{H}}} \tag{6}$$

where C_{pav} is the average pillar confinement and C_p is the coefficient of pillar confinement. The pillar database was analyzed, and the predicted strengths were compared to the already existing pillar strength methods at the time [15], [55], [57], [114], [124].

Studies were conducted on limestone pillars by Iannacchione [62] where it was concluded that small pillars with W/H ratios of less than 1.2 exhibit low strength and are primarily affected by the discontinuity network present in the deposit. It was also concluded that pillars with a W/H ratio of 1.5 or greater could be considered high-strength pillars. The major discontinuity factor which affects pillar strength was determined to be the friction

angle ( ) of discontinuities. It was found that any discontinuity with an orientation of (45 + /2)° majorly affected the pillar strength.

Esterhuizen et al. [38] used numerical modeling to develop an empirical approach while addressing the discontinuities in the pillar. A fudge factor of value 0.65 was included in the equation to customize the uniaxial compressive strength (UCS) of the pillars indicating that the approach is restricted to use in limestone mines. The authors proposed that the pillar strength can be calculated as:

$$\mathrm{S} = 0.65{*}\mathrm{UCS}{*}\mathrm{LDF}{*}\left(\frac{\mathrm{W}^{0.30}}{\mathrm{H}^{0.59}}\right) \tag{7}$$

where S is the pillar strength, UCS is the Uniaxial Compressive Strength of the intact rock (MPa), W and H are the width and height of the pillar, respectively, and LDF is the Large Discontinuity Factor which may, in turn, can be expressed as:

$$\mathrm{LDF} = 1 - \mathrm{DDF}{*}\mathrm{FF} \tag{8}$$

where DDF is the Discontinuity Dip Factor and FF is the Frequency Factor. This empirical approach aims at providing the effect of large discontinuities on the strength of a pillar.

Elmo and Stead [32] proposed a graphical approach to explain the relationship between pillar strength and fracture intensity. The approach encapsulated the anisotropic and heterogeneous effects of joints instead of relying on the continuum or discontinuum representation of rock mass. The study concluded that axial pillar strength is inversely proportional to the fracture intensity. Relationships were established between the fracture intensity, fracture toughness, W/H ratio of pillars, jointing conditions, and occurrence of intact rock bridges. It was suggested that the intact rock behavior, joint conditions, fracture

intensity, joint shape and size, and loading conditions can be combined as a single entity to represent rock mass strength.

Ayres Da Silva [6] conducted laboratory testing on prismatic and cylindrical specimens to define a relationship between pillar strength and W/H ratio. Different relationships were determined for the three rock types tested which included manganese, basalt, and limestone. The size factor of the pillar was integrated with the shape effect and was implemented to improve pillar design in an underground manganese mine.

1.4 Pillar Design using Analytical Approaches

A good alternative to using an empirical approach for predicting rock mass behavior is to use analytical investigations which employ the principles of statistical methods, probability, and during recent years, artificial intelligence or a combination of a few or all methods. The use of analytical studies has become common to perform risk analysis and compute the failure probability of pillars. However, these methods do not consider the failure mechanism of the pillars and the variation in geotechnical conditions across different deposits or in a mine.

Esterhuizen [33] conducted a statistical investigation to estimate the strength of pillars in hard rock mines. It was concluded that both the rock mass properties and other mining operational factors can affect pillar strength. Griffiths et al. [52] researched underground pillar stability using Monte-Carlo simulations which is a type of probabilistic method. The authors were able to establish a direct relationship and predict the probability of failure using the factor of safety. Cauvin et al. [25] conducted studies to determine the uncertainties of the input parameters on the strength of pillars in the abandoned room-and-pillar mines.

Statistical distribution and probabilistic functions were utilized to predict the shortcomings of empirical approaches that use shape determination and back analysis for predicting the strength of the pillar.

Zhou et al. [145] implemented the Support Vector Machine (SVM) method and Fisher discriminant analysis technique to predict pillar stability by using the W/H ratio of the pillar, width, height, uniaxial compressive strength (UCS) of the intact rock, and stress on the pillar. It was concluded that the UCS and the height of a pillar are the most important parameters for defining stability, followed closely by the stress regime and W/H ratio. A comparison was also done between the SVM method and the Fisher discriminant analysis technique for determining pillar stability. It was predicted that the former is better than the latter in understanding pillar behavior in underground mines.

Regressive models have proven to be useful in predicting pillar stability. Wattimena [141] and Tomory et al. [135] applied log-linear regression based on categorized empirical data for underground hard rock mines. Artificial Neural Network technique was used by Idris et al. [63] to analyze pillar stability using stochastic methods. It was concluded that due to the uncertainties in the accurate prediction of the rock mass properties, the factor of safety cannot predict the stability of the pillars adequately. The probability of failure and the reliability assessment were determined to be the better parameters for estimating pillar stability.

Zhou et al. [146] compared six analytical approaches to assess the stability of hard rock pillars. The methods were: SVM, linear discriminant analysis, multilayer perceptron neural networks, multinomial logistic regression, gradient boosting machine, and random forest (RF). These methods were used to assess a database of 251 pillar case studies across different

mines. It was concluded that the SVM and RF methods were more realistic in representing the pillar stability for the complete database.

1.5 Pillar Design using Numerical Approaches

The numerical approaches for a stone pillar design can be subdivided into three categories, namely continuum, discrete, and hybrid models. The methods utilized by continuum models include the Boundary Element Method (BEM), the Finite Element Method (FEM), and the Finite Volume Method (FVM). Discontinuum methods mostly use the Discrete Element Method (DEM) along with Discrete Fracture Networks (DFN), whereas the hybrid models are a combination of continuum and discrete methods. The utilization of these methods depends on the presence and magnitude of discontinuities and the rock type. Continuum modeling is the preferred method of choice for massive or highly deteriorated rock mass. It may also be used for the rocks having fewer discontinuities with no significant effects on fracture opening and block separation. DEM is effective for modeling the abundance of complex discontinuities and large-scale displacement of the block movement [71].

1.5.1 Discrete Element Modeling (DEM)

This method calculates the contact forces for an assembly of the rigid or deformable blocks/particles by continuously updating the entire deformation process to represent a constitutive model. It is primarily based on equations of motion of rigid or deformable bodies using implicit and explicit formulations [71]. The computer codes used in DEM are UDEC

and 3DEC, which are two-dimensional and three-dimensional models, respectively, while PFC simulates granular particle modeling [64]–[66].

Esterhuizen et al. [43] performed pillar studies with UDEC for limestone mines with discontinuities dipping at different angles. It was concluded that slender pillars are most affected by the discontinuities whereas squat pillars are least affected. An equation was derived to estimate the strength of the pillars in the presence of discontinuities. It was observed that the pillar strength was affected severely in the presence of weak infilling like clay or soft bedding bands.

Zhang [144] utilized a Synthetic Rock Mass (SRM) approach to characterize the strength of jointed rock pillars and assess their failure mechanisms as shown in Figure 1.6. It was concluded that amongst many factors, fracture length, fracture intensity, and fracture orientation are the three important parameters affecting pillar strength. It was also concluded that the fracture length is inversely related to pillar strength at constant fracture intensity. At constant fracture intensity, the fracture initiation stress remained the same with different fracture orientations. This showed that fracture initiation stress can be used to measure the degraded uniaxial compressive strength for the empirical approaches.

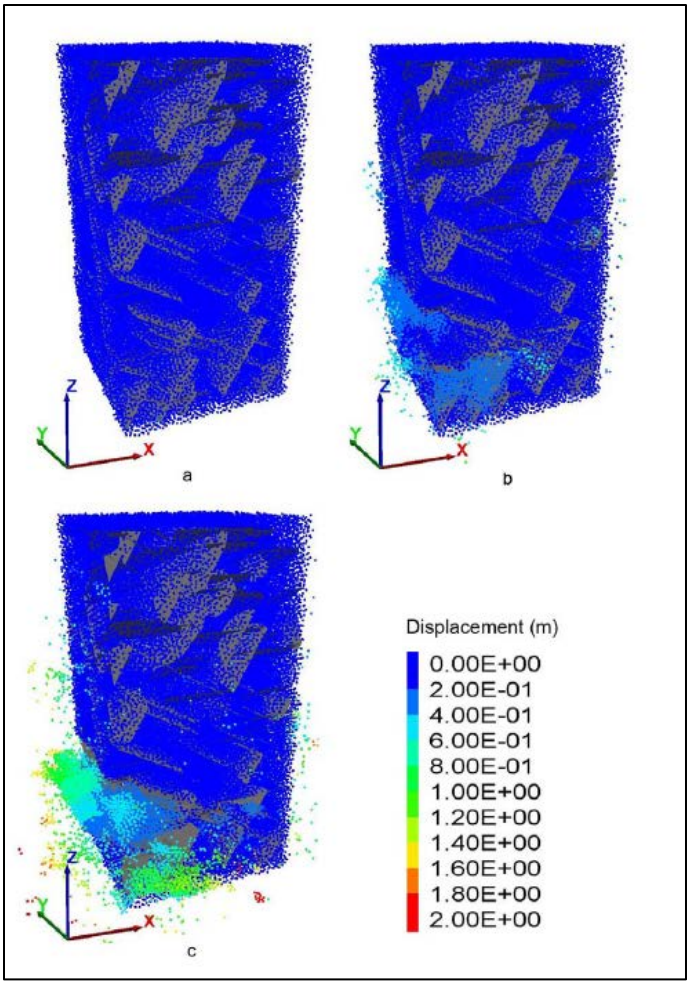

Figure 1.6 PFC model showing joints and progressive failure in pillars [144].

Muaka et al. [109] assessed the pillar failure mechanisms in presence of clay structures in the ore body, roof, and floor. The joints in the rock mass were modeled using discrete fracture networks in UDEC. It was concluded that the strain-softening region is dependent on tessellation size, damping magnitude, and loading velocity, making the modeling less intensive. It was found that calibration and validation play key roles along with the modeling method. In this study, the pillar failure mechanisms were found to be acceptable when compared to the empirical underground pillar failure mechanism.

1.5.2 Finite Volume Modeling (FVM)

This type of modeling technique can be carried out using three methods: explicit, implicit, or central difference. This modeling technique uses partial differential equations to convert volume integrals to surface integrals using divergence theory. Mostly used in continuum modeling software like FLAC3D, and can capture complex geotechnical behavior of models and simulate non-linear material behavior [67].

Esterhuizen & Ellenberger [41] simulated pillar models with the finite difference program FLAC2D to understand the response with different width-to-height (W/H) ratios and physical properties of the stone pillars. The study also discussed the reduction in the load-bearing capacity of the pillars by the presence of these weak bands. They reported failure modes like those observed in the field. It was concluded that bands were the cause of tensile stress development which leads the limestone pillars to fail at a lower stress than expected. The prime factors responsible for the degree of strength reduction were found to be dependent on the compressive strength, frictional resistance, and thickness of these bands. Figure 1.7 shows the model results show pillar failure modes with and without the presence of weak bands.

Dolinar & Esterhuizen [31] used FLAC3D to simulate the rectangular pillar models to study the effect of pillar length on their strength. The authors presented the effect of increasing pillar length for relatively low and high in situ stresses. The study explained the use of a finite difference program to simulate failure due to geologic structure at lower depths as well as failure due to vertical stresses overcoming pillar strength. It was observed that for slender pillars, length had very little effect on strength, while for the squatter pillars, the strength varies proportionately with length. It was also noticed that the discontinuity

normal to the longest axis of the pillar displayed higher strength compared to the one normal to the shortest axis of the pillar.

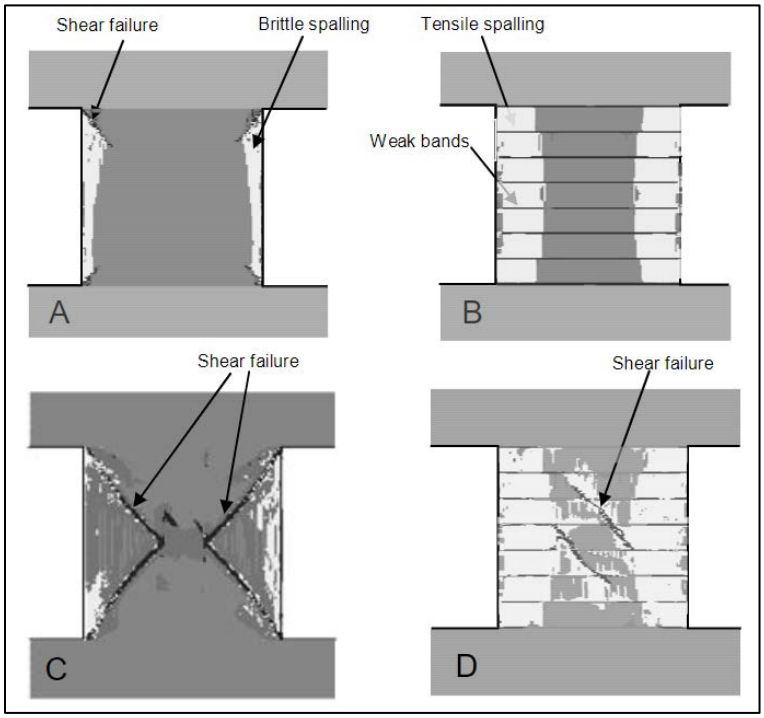

Figure 1.7 FLAC2D model results show pillar failure modes with and without the presence of weak bands [41].

Napa-García & Navarro Torres [110] performed numerical modeling research on pillars using FLAC-3D. They implemented Hoek and Brown constitutive model and studied the models by varying Geological Strength Index (GSI), uniaxial compressive strength (UCS), and W/H ratios. By using the Direct Strain evaluation method, the authors were able to establish a relationship between the ratio of failure strain to critical strain and the W/H ratio.

Vakili [136] proposed an improved unified constitutive model for numerical modeling of rock material in FLAC3D to accurately predict the stress-strain relationship of rock modeled as a continuum media. The author suggested using cohesion-friction softening at low

confinements and cohesion-softening and friction-hardening at high confinements. The concept of this constitutive model is similar to the research by Beck [11] and Dolinar et al. [30] to simulate the pillars using a ubiquitous strain softening/hardening model. However, the constitutive model presented limitations by not being able to simulate anisotropy and the effect of discontinuities.

Jessu and Spearing [70] performed numerical studies with finite-difference codes in FLAC-3D to evaluate the strength and failure mechanisms of inclined pillars. It was concluded that with an increase in inclination, the pillars with higher W/H ratios have low strength when compared to pillars with no inclination. The research also described that inclined pillars are prone to brittle failure where failure propagates from one corner of the pillar to the opposite corner of the pillar.

Chapter 2

Effect of Karst Voids on Pillar Strength in an Underground Limestone Mine[1]

2.1 Introduction

Over the past decade, underground mining operations in limestone deposits have become more common in the eastern United States. Compared to slope stability efforts in surface operations, ground control operations in underground mining are more complicated and require more engineering and training. Currently, there are 109 underground stone mines in the U.S., the majority of which employ room-and-pillar mining methods to extract limestone for crushed stone products [111]. Despite employing fewer miners than coal mines, stone mines experience a large number of reportable injuries. Since 1983, about 12% of all the reported injuries in the stone mining industry are because of rock falls from the roof or pillar ribs [108].

---

[1]

a.) A part of this chapter has been published by the Mining, Metallurgy & Exploration journal, titled as "*Effect of Karst Voids on Pillar Strength in an Underground Limestone Mine*". See Appendix B

b.) A part of the chapter has been accepted for publication by the American Rock Mechanics Association for the 56th US Rock Mechanics/Geomechanics Symposium, titled as "*Analysis of Pillar Strength and Design in a Karst-affected Underground Stone Mine".* See Appendix C

Of the 109 mines, the majority of them have the potential or have already encountered karst voids at some point during their excavation operations. This is due to the prevalent karstic network developed in the limestone rock masses [84]. These cavities are formed over a long time by the dissolution of carbonate rocks and can be unforeseen until encountered due to mining activities. The hindrance of mining operations due to karsts has been well documented by Gongyu et al. [49]. The disruption of mining operations while encountering karst cavities often requires potential ground control measures beyond the typical scope of a ground control management plan (GCMP) constituted for the mine. Even the rock mass classification schemes, such as the Rock Mass Rating (RMR) from Bieniawski and the Q-system from Barton, do not classify the karst-affected carbonate rock mass, and therefore the analysis of such cases requires geological analysis of the underground conditions [2].

This research evaluates the stability of a pillar (designated Pillar-X) with the presence of a karst void in an underground limestone mine. The case study mine is a multi-level room-and-pillar underground limestone mine. The pillar in question, i.e., Pillar-X, lies at a depth of about 180 m from the surface. The study discusses the methods which were utilized in determining the karst boundaries inside the suggested Pillar-X, using ground-penetrating radar (GPR). The size of Pillar-X was left to be bigger than the intended pillar dimensions of 24.5 m x 24.5 m x 30.5 m to counter any local instability issue which may have been suspected by the mine management. The mine has experienced ground control issues such as roof and rib failures in the past. The karst cavities, filled with unconsolidated clayey-rock material, may interact with the immediate roof or ribs in the mine drives, or even around a pillar. The interaction is also dominated by the discontinuity network, which is a typical feature of a naturally fractured limestone deposit. To study the stability of Pillar-X, a 3-dimensional numerical modeling tool 3DEC was used. This software utilizes a finite-difference distinct element method (DEM) to simulate the condition of an underground

excavation. The DEM is useful in characterizing the presence of discontinuous media in the rock mass. The pillar model is framed using the rock material and joint properties that were measured by the mine management and confirmed using laboratory testing. LiDAR scans of the pillar were used for discontinuity mapping of the pillar and assessing the different joint sets using Maptek's PointStudio point-cloud processing software [94]. Since all the joints' characteristics cannot be measured inside Pillar-X, a discrete fracture network (DFN) was employed to create a virtual network system which is the closest possible representation to a real-world joint system. Different scenarios were created to account for the irregularities found in the GPR surveys. For each scenario, the pillar model was analyzed for its strength based on a constant compressive velocity applied to it. The analysis characterizes the significant reduction in the pillar strength in the different scenarios, each with increased karst void volume. The research also discusses the importance of pillar design in the presence of karst cavities to maximize ore extraction as well as maintain local and global stability in a stone mine.

2.2 Background

2.2.1 Case Study Mine

The case-study mine is situated in a region with synclinal Ordovician limestone. The limestone deposit hosts an extensive network of interconnected karst cavities. These cavities are formed over several years due to the dissolution of limestone rock by the flow of groundwater or weak carbonic acid through the vast fracture network of a limestone deposit. The orebody is 30 m thick and dips at approximately 30° towards the southeast as visible from the outcrop. The levels of the mine are connected by a corkscrew ramp. Each level has

an east and west section branching from the corkscrew ramp; at present, each branch contains a footwall and hanging wall tunnel separated by 24.5 m x 24.5 m x 30.5 m rectangular pillars left after complete extraction from the eventual stoping, and tunnels are approximately 8 m tall and 12.8 m wide.

2.2.2 Pillar Location & Geometry

The pillar being analyzed in this chapter, named Pillar-X for this study, is shown in Figures 2.1 and 2.2. After the discovery of karst voids in Pillar-X, the stopes around it were not completely excavated leaving the pillar height to be 9.5 m as opposed to the intended pillar height of 30.5 m after the complete extraction of stope from the adjacent levels. During the initial preparation of the stope around the pillar, the mine employees faced a safety incident of ground collapse from the sidewall which opened to the karst cavity.

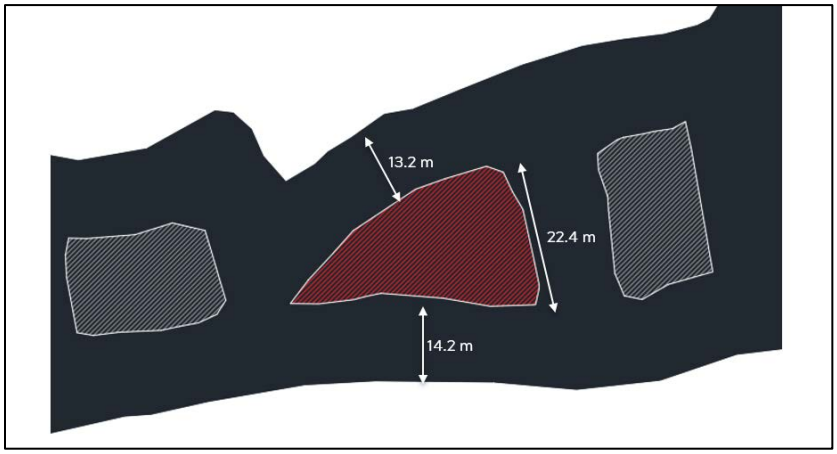

Figure 2.1 Plan view of Pillar-X in the underground mine.

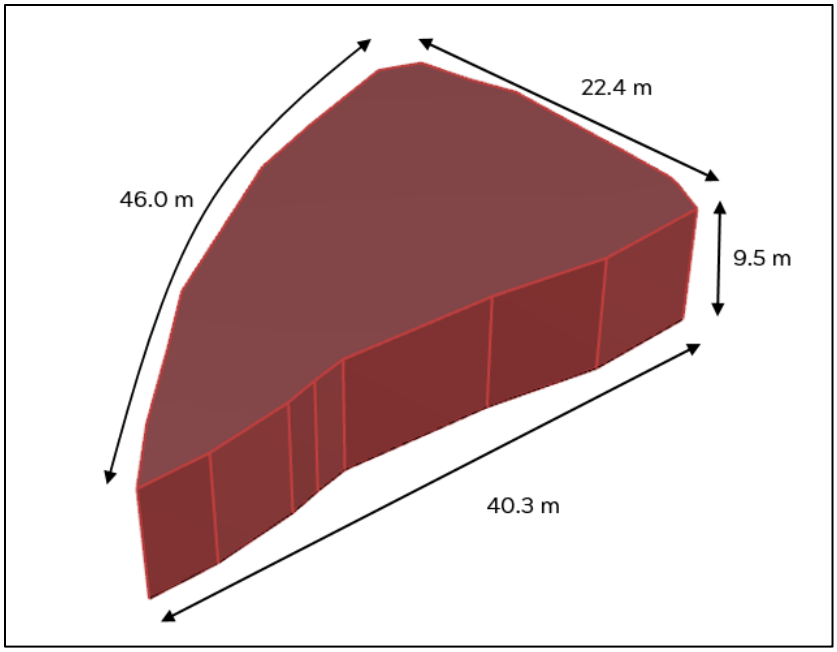

Figure 2.2 Perspective view of Pillar-X in the underground mine.

The spillage of wet clay along with the rock boulders did not result in any injuries but it hampered the operations in that region and required additional mucking and rehabilitation of ground support. Figure 2.3 shows the material collapse in the mine due to the opening of the karst cavity.

Figure 2.3 Material collapse from karst void in the case study mine [18].

The mine management employed temporary ground support measures such as plastic mesh pinned up with steel straps to prevent heading damage due to clayey-rock material and groundwater seepage. Further, grouting was done as a permanent ground control measure to prevent any suspected local instability issues. Figure 2.4 shows the temporary ground controls measure taken around the pillar.

Figure 2.4 Ground support around Pillar-X [18].

2.2.3 GPR Investigative Study

Ground-penetrating radar (GPR) surveys could be effective in detecting dielectric boundaries within a solid structure, such as rock mass or concrete pillars [7]. GPR's advantage to map bedrock depth and soil stratigraphy [4] and mapping fractures in gneissic rocks [51] among other works has been well renowned. In the case study mine, investigative work was conducted to detect the shape of any karst void(s) in the Pillar-X via a dense grid of 3-dimensional GPR survey [7].

Figure 2.5 3D GPR survey conducted along the Pillar-X.

The authors used a 3 sq. m tarp marked with gridded survey lines and shot locations. Figure 2.5 shows the authors surveying the underground case study mine. The survey was conducted on a total of 8 tarp positions along the ~46 m length along one side of Pillar-X. The survey was not extended along the 40.3 m length because of the mesh installed on the collapsed pillar rib to block any inflow of consolidated segments. This prevented any additional data collection for delineating the karst cavity boundaries, considering how groundwater and clayey material attenuate the signals. A 250 MHz antenna was selected by the authors as this frequency showed a penetration depth of greater than 20 meters and resolution was favorable to obtain surface reflections. To extract reflection events and ultimately convert these to either points or iso-surfaces, GPR Slice software was used by the authors [50]. The iso-surfaces from all tarp survey grids identified the commonalities and surface trends, as seen in Figure 2.6.

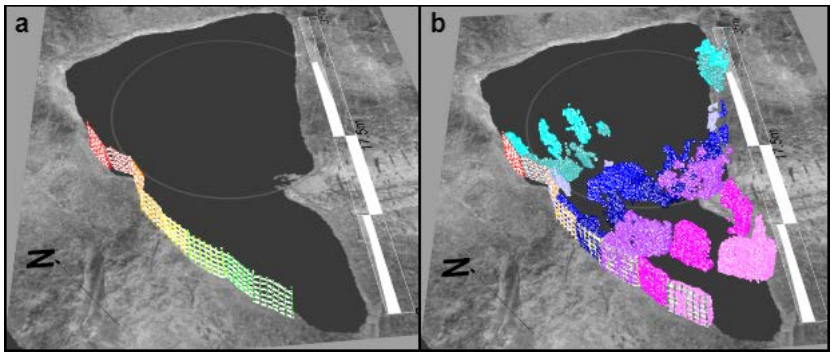

Figure 2.6 Reflection points obtained from the GPR survey along one side of the pillar [7].

The clusters of these iso-surfaces or points were connected to form meshes to produce representative surfaces of the karst void boundary. The plan view of the iso-surface mesh reflection boundary of the karst void inside the pillar is shown in Figure 2.7.

Figure 2.7 Iso-surface meshes created from the reflection points.

Conductive mediums, such as wet clays and water which fill the karst void, highly attenuate the GPR wave energy. Limestone rock is dry, homogenous and a resistive medium for GPR waves, and is ideal for strongly transmitted and reflected signals [4]. Since the conductive medium inside the void produced reflections, the authors could not propose a closed void

volume, which in terms of delineating void boundaries, would be an ideal case. Figure 2.8 shows a plan view of the approximated karst volume to area projection by the authors.

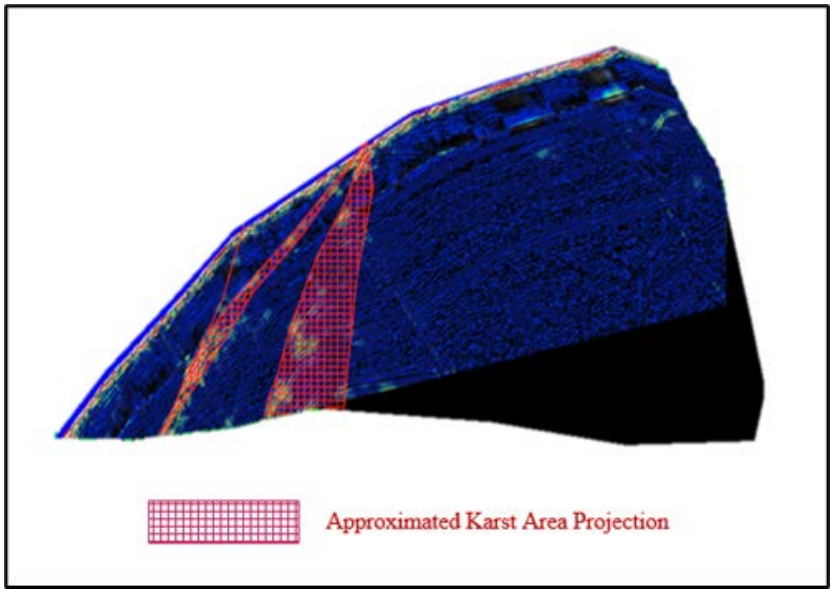

Figure 2.8 Plan view of an approximate karst area projected from the iso-surface meshes [7].

However, the GPR results from this study investigated the surfaces along the pillar sidewalls only. Therefore, there is no information regarding the continuation of discovered cavities above or below the survey window along the pillar. However, accounts from the mining personnel who performed the ground control measures at the site suggested the continuation of the voids in the immediate roof of the pillar. Also, the physical testing of the void fill material, as indicated by the observed characteristics of reflected radar signals, was not performed. To compensate for the missing information, the karst cavity was assumed to be continuous across the height of the pillar. This will always underestimate the pillar's strength as it will possess a larger void volume filled with weak material. Also, different scenarios were considered to include all possibilities for cavity shapes that may affect the pillar strength. These scenarios involved varying the size of karst volume ranging from the approximated volume to a worst-case scenario, where the outer boundaries of the iso-surface

reflections were considered with no limestone rock mass in between. These cases are explained further in the sections.

2.3 Distinct Element Modeling in 3DEC

3DEC is a three-dimensional numerical modeling code developed by Itasca Consulting Ltd. [64]. This software is based on the distinct element method (DEM) for simulating the response of the discontinuum network in rock masses such as joints and fractures. The software represents discontinuous media as an assembly of discrete blocks and the discontinuities between them as boundary conditions. For this study, individual blocks are set as deformable material and are meshed as finite different zones. The displacements along the joints and rotation of blocks facilitate us to observe the behavior of the pillar under increasing load.

Pillar strength in stone mines has been studied by many researchers. Esterhuizen et al. [34] suggested methods of estimating the pillar strength and supplemented them with numerical models. Iannacchione [62] addressed the pillar design issues that are typically faced in underground mines. DEM has frequently been used as a tool to analyze rock mass behavior, however, there is a lack of published research on analyzing pillar strength with karst voids detected using underground mining GPR applications.

2.4 Pillar Model Generation

2.4.1 Pillar-X Model Scenarios

For this study, three different scenarios were considered in which the pillar geometry was kept constant. However, the karst void volume was varied to simulate the effect of increasing void volume on pillar strength. The karst voids in the cases were assumed to be empty to underestimate any insignificant support provided by the clayey-rock material present inside the void. The constructed Pillar-X model dimensions were estimated by the LiDAR scans obtained around the pillar. The three scenarios are described in detail below:

(i) Scenario 1- In this case, the Pillar-X was assumed to be a solid limestone pillar without any karst voids. To assess the effect of karst voids on pillar strength, it is important to model a benchmark pillar strength value. In this case, it was done by simulating the case in which a solid pillar is subjected to increasing compressive stresses until failure is achieved. Figure 2.9 shows the geometry of the solid pillar. The volume of the original pillar is ~5580 m^3.

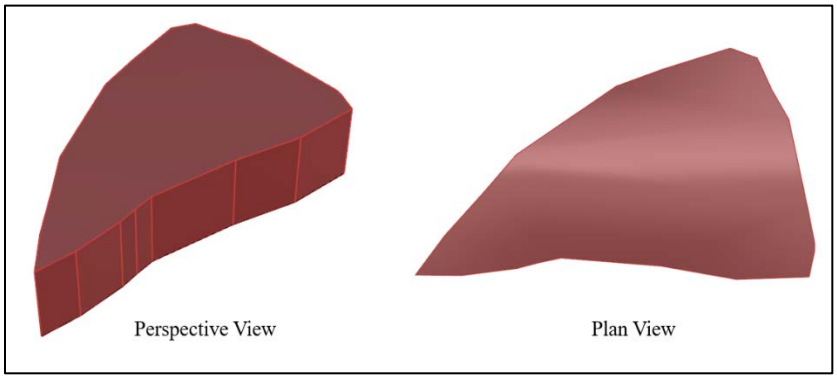

Figure 2.9 Simulated Pillar-X model in Scenario 1.

(ii) Scenario 2- In this scenario, the karst voids were created analogous to the iso-surface boundaries as suggested by the GPR study as shown in Figure 2.8. The karst voids

were assumed to run throughout the height of the pillar. This scenario simulates a most likely case which is suggested in this chapter and the authors that conducted the GPR study. Figure 2.10 shows the geometry of the pillar and karst void. The volume of the empty karst void simulated in Scenario 2 is roughly 482 m^3. constituting roughly 9% of the total volume.

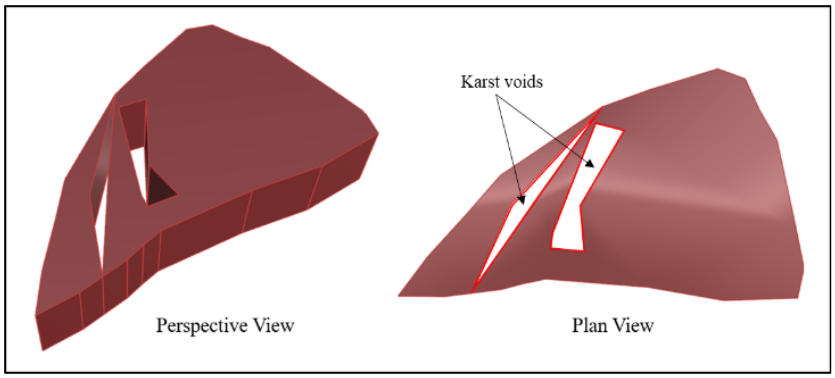

Figure 2.10 Simulated Pillar-X model in Scenario 2.

(iii) Scenario 3- In this case, Pillar-X is simulated with the karst voids having the largest volume. It is assumed that the outer boundaries of the GPR iso-surfaces form the shape of the void and there is no hard-rock wedge dividing the void as present in Scenario 2. The simulated pillar model of this case is shown in Figure 2.11. The karst void in Scenario 3 has the largest void volume of about 1009 m^3. constituting roughly 18% of the total volume.

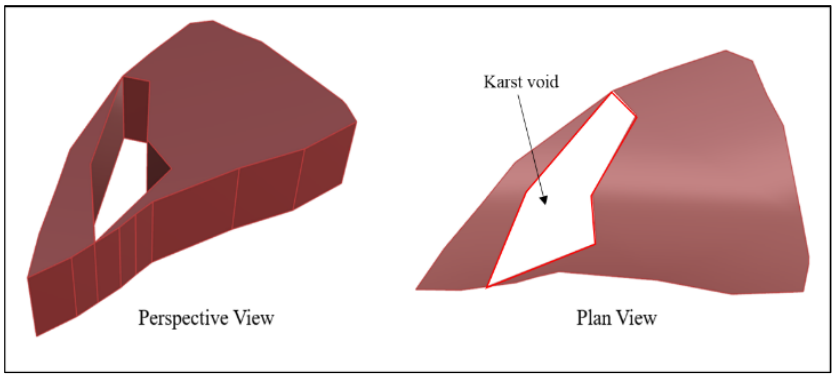

Figure 2.11 Simulated Pillar-X model in Scenario 3.

2.4.2 Physico-mechanical Properties

The physico-mechanical and geotechnical properties for the rock mass and joints used in the numerical model were measured by the mine management using geotechnical borehole measurements and laboratory testing mentioned in [105]. The calculated values for joint shear stiffness and joint normal stiffness are based on the work performed by Bandis, Lumsden, & Barton [8]. The properties are listed in Table 2.1. The lithology of the synclinal Ordovician limestone deposit in the ore body was characterized as Five Oaks limestone [101]. The Elastic-Isotropic constitutive model is used to represent rock behavior in the numerical model. This constitutive model characterizes the pillar to reflect reversible deformations upon unloading i.e., the stress-strain laws are linear and path-independent. The Coulomb-slip joint constitutive model is assigned to represent the physical response of rock joints. The model simulates the displacement of the discontinuities by weakening cohesive and tensile strength when shear or tensile failure begins [64].

Table 2.1 Physico-mechanical properties for intact rock and joints.

Intact Rock Properties	
Density, ρ	2690 kg/m^3
Bulk Modulus, K	37.86 GPa
Shear Modulus, G	20.57 GPa
Poisson's Ratio, ν	0.27
Joint Properties	
Joint Normal Stiffness	300 GPa/m
Joint Shear Stiffness	30 GPa/m
Joint Friction Angle	30^o
Joint Cohesion	0.0

2.4.3 Boundary Conditions

For assessing the pillar strength, compressive stresses were applied axially along the z-axis to the pillar. Since the pillar is not supported by any material on the sides, no boundary conditions were applied to the sidewall. Boundaries in the x- and y-direction were fixed at the top and bottom face of the pillar to prevent any lateral movement and ensure constant stress application with time steps. The load was applied to the pillar model in each scenario using an axial velocity on the top and bottom. The magnitude of the velocity applied was about 0.5 mm per timestep. It is assumed that only the vertical stress is being imparted along the axis of the pillar, thus compressing the pillar. Horizontal shear movements are not allowed on the top and bottom boundaries of the pillar model. Each scenario was cycled until failure of the pillar model in each scenario was observed.

2.4.4 Discontinuity Mapping

An important aspect of the numerical modeling of Pillar-X was to account for the discontinuity network affecting it. Joints play a major role in deciding the strength of a rock mass and detailed knowledge of them would help to simulate accurate conditions. A preliminary investigation was conducted at the case study mine which describes obtaining the LiDAR scans and virtually mapping the discontinuity network around the area from the scans [106]. Maptek I-Site, a point cloud processing, and modeling software were used to extract the discontinuities and different parameters such as joint orientation, fracture density, and size of joints in different joint sets. Figure 2.12 shows the plan view of the structural mapping performed around Pillar-X. Four discontinuity sets were defined from the mapped discontinuities. Figure 2.13 shows the process of structural discontinuity mapping in the I-Site.

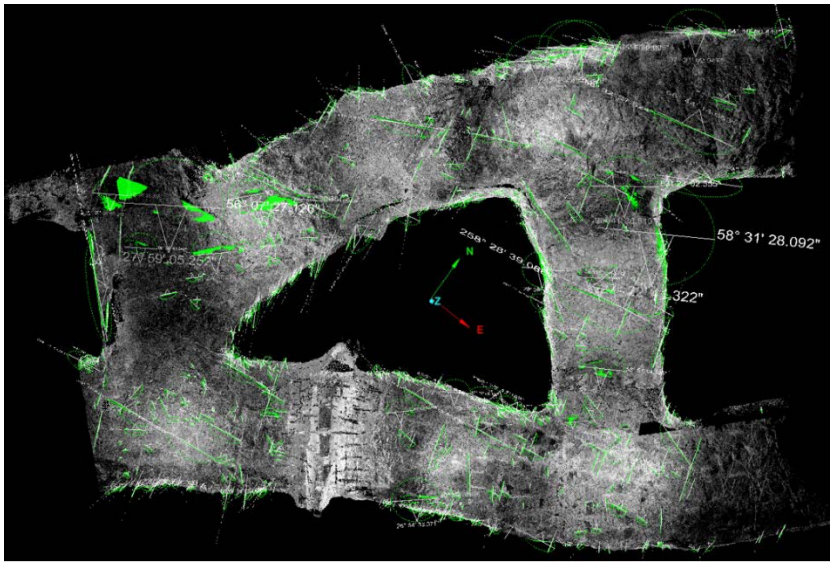

Figure 2.12 Virtual discontinuity mapping from LiDAR scans around the Pillar-X [106].

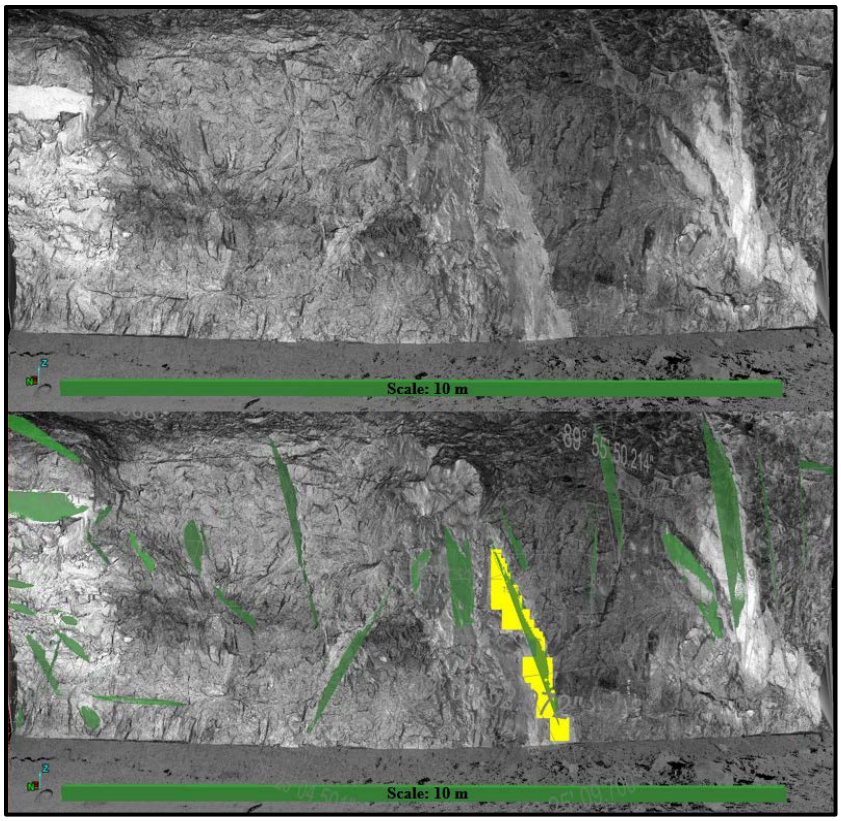

Figure 2.13 Discontinuity mapping from LiDAR scans in Maptek I-Site [106].

2.5 Discrete Fracture Network (DFN)

After sufficient information on the structural features was collected from the LiDAR scans, the data were classified into four joint sets. Extracted data included size information (trace length and area) and orientation information (dip, dip direction, and strike). All this information is used by 3DEC to generate DFNs which simulate a close representation of the geological structures in a rock mass. This fracture network is a set of discrete, planar, finite-size fracture disks, which intersect the model to generate a set of blocks that constitute a simulated jointed rock mass. These disks are created based on statistical data of the joint characteristics, such as orientation, size, and density, measured in the field [116], or in this

case, measured virtually from LiDAR point clouds. Table 2.2 summarizes the statistical data of the joint properties for each joint set used in the modeling study.

Table 2.2 Statistical data for each joint set used to generate discrete fracture networks.

	JOINT SETS		S1	S2	S3	S4 (Bedding)
PARAMETERS	Orientation	Dip [°]	88	68	75	29
		Dip Direction [°]	255	348	21	144
		K (Fisher Distribution)	103.9	102.4	69.5	197.3
	Size	Distribution	Log-normal	Log-normal	Log-normal	Log-normal
		Mean	0.353	0.318	0.018	0.778
		Standard deviation	0.659	0.772	0.749	0.934
	Density	P_{32} (Joint area/Volume)	0.045	0.095	0.181	0.227

One of the important parameters for generating DFNs is fracture density, which is a measure of the spatial frequency of discontinuities in a joint set. This parameter serves as a threshold condition while generating DFNs in 3DEC [22]. For this study, fracture density was defined as the area of fractures per unit volume of the rock mass or P_{32}. The DFN model is calibrated using the P_{32} values of the four joint sets measured in the DFNs for the model. Since the fractures per unit volume in the pillar cannot be measured practically through field mapping, P_{10}, also known as linear fracture intensity values, are measured. P_{10} is defined as the number of fractures measured along scanlines [104]. The P_{32} value is set in the numerical model such that the fractures generated in the model yield the P_{10} value equivalent to the one mapped in the field using virtual discontinuity mapping from LiDAR scans. Figure 2.14 shows the DFNs of different joint sets merged to form a combination of simulated fracture networks which was used to cut the Pillar-X model in all scenarios.

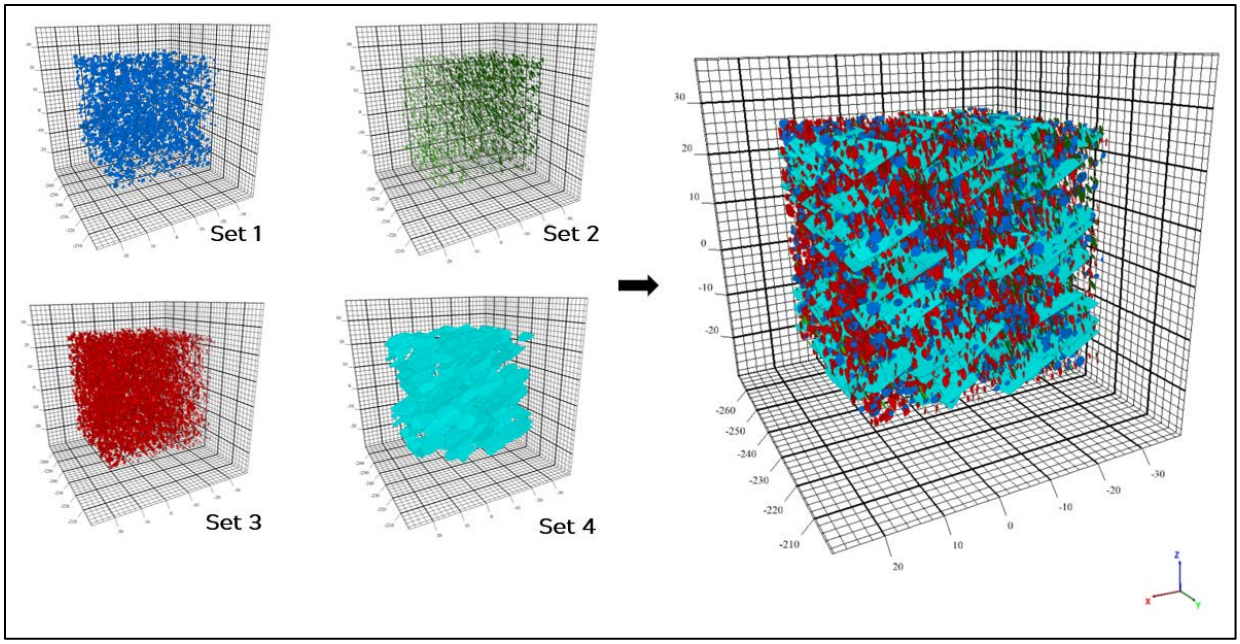

Figure 2.14 DFNs of different joint sets merged to form a combination fracture network in 3DEC.

2.6 Results and Analysis

The numerical modeling analysis for the three scenarios was performed to observe the deterioration of the pillar with increasing stress levels. It should be noted that the stress levels are plotted versus the axial strain along the pillar. Since a constant velocity boundary was applied to the top and bottom surface planes of the pillar model, visualizing stress with axial strain would also indicate the modulus of the rock mass with discontinuities. The analyses are explained below:

(i) Scenario 1- In scenario 1, numerical modeling was performed on the original pillar model without the presence of karst voids in it. The pillar model was cut from the discrete fracture network as explained in the previous section. The model was then subjected to increasing stress levels until yielding occurs and ultimately failure is achieved. Figure 2.15 shows the deterioration of the pillar with increasing stress

levels. It is observed that as the compressive stress increases, an increase in rock boulder failure and spalling from the sidewall occurs. The observed spalling is due to the increase in tensile stresses along the sidewall of the pillar. Also, major weakening occurs due to the simulated increase in compressive stresses. It is inferred that a combination of these stresses leads to the ultimate failure of the pillar rock mass yielding at its ultimate strength Simulating a solid pillar model without karsts allows us to make a comparison as to what is the effect of the introduction of cavities in the pillar has on its strength. It is visible that the pillar fails when the applied stress magnitude reaches ~54 MPa. Even before the stress value reaches failure level, at around ~43 MPa, the sidewall of the pillar looks to have significantly deteriorated.

(ii) Scenario 2- Figure 2.16 shows the condition of Pillar-X in Scenario 2 with the increase in stresses. It shows the simulation of the pillar with the suggested karst voids. It is observed that the ground failure from the sidewall has increased in this scenario for the same stresses in Scenario 1. Pillar-X yields and ultimately failure occurs at around 43 MPa. This shows that the strength of the pillar has reduced although not too much, but still proves that the presence of karst cavities reduces the pillar strength. The spike observed in the stress-strain curve is attributed to a simulation error that may have been generated due to a massive rock block separating from the pillar.

(iii) Scenario 3- Simulation of Pillar-X with the worst-case of assuming the biggest karst void is performed in Scenario 3. Figure 2.17 shows that the breakage of material and spalling has increased significantly compared to other scenarios. With increasing stress levels, the pillar yields and fails at a highly reduced value of ~28 MPa. This

suggests that with increasing karst void volume, the deterioration increases as the strength of the pillar decreases significantly.

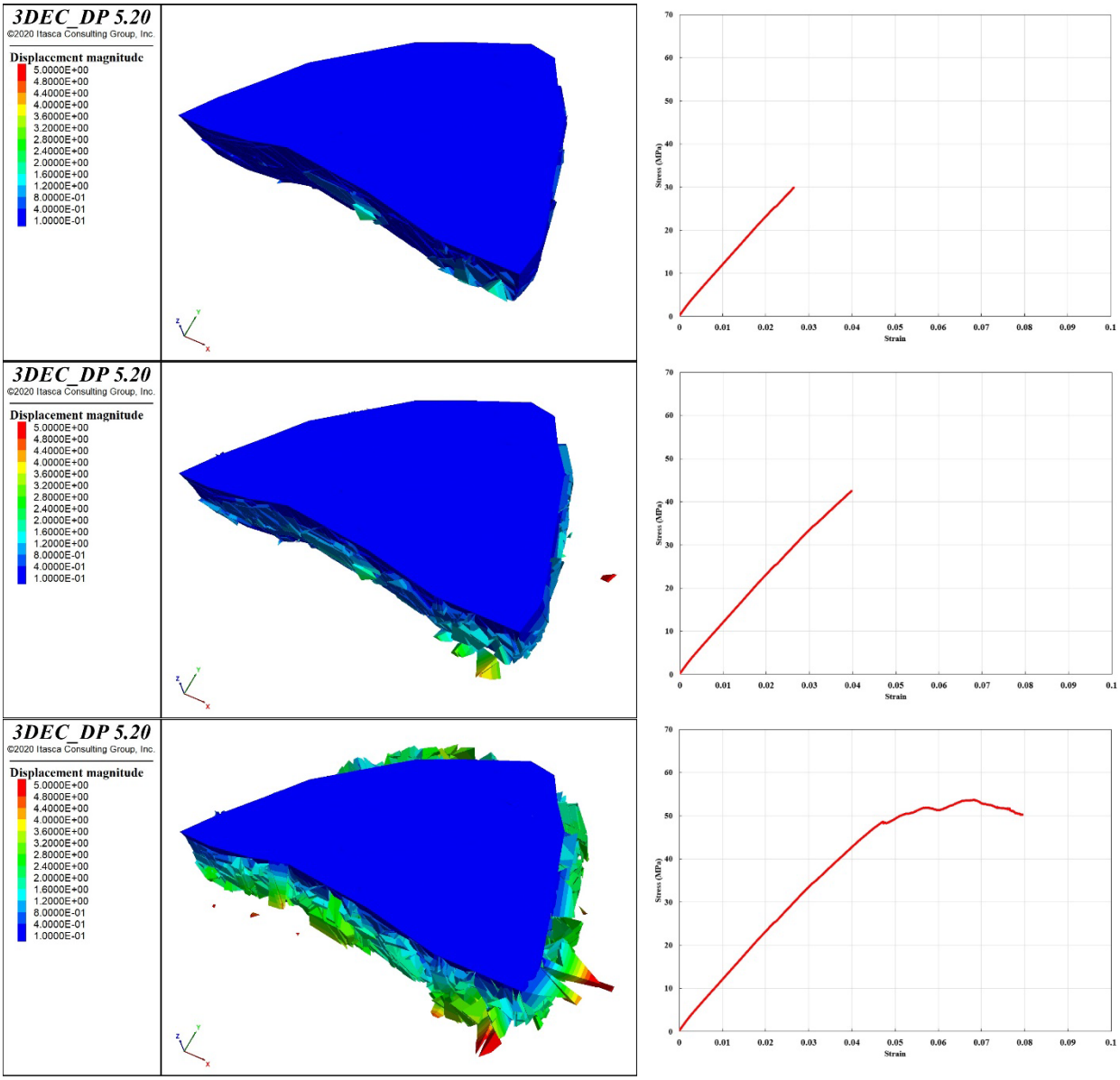

Figure 2.15 Deterioration phases of Pillar-X with increasing axial stress levels in Scenario 1.

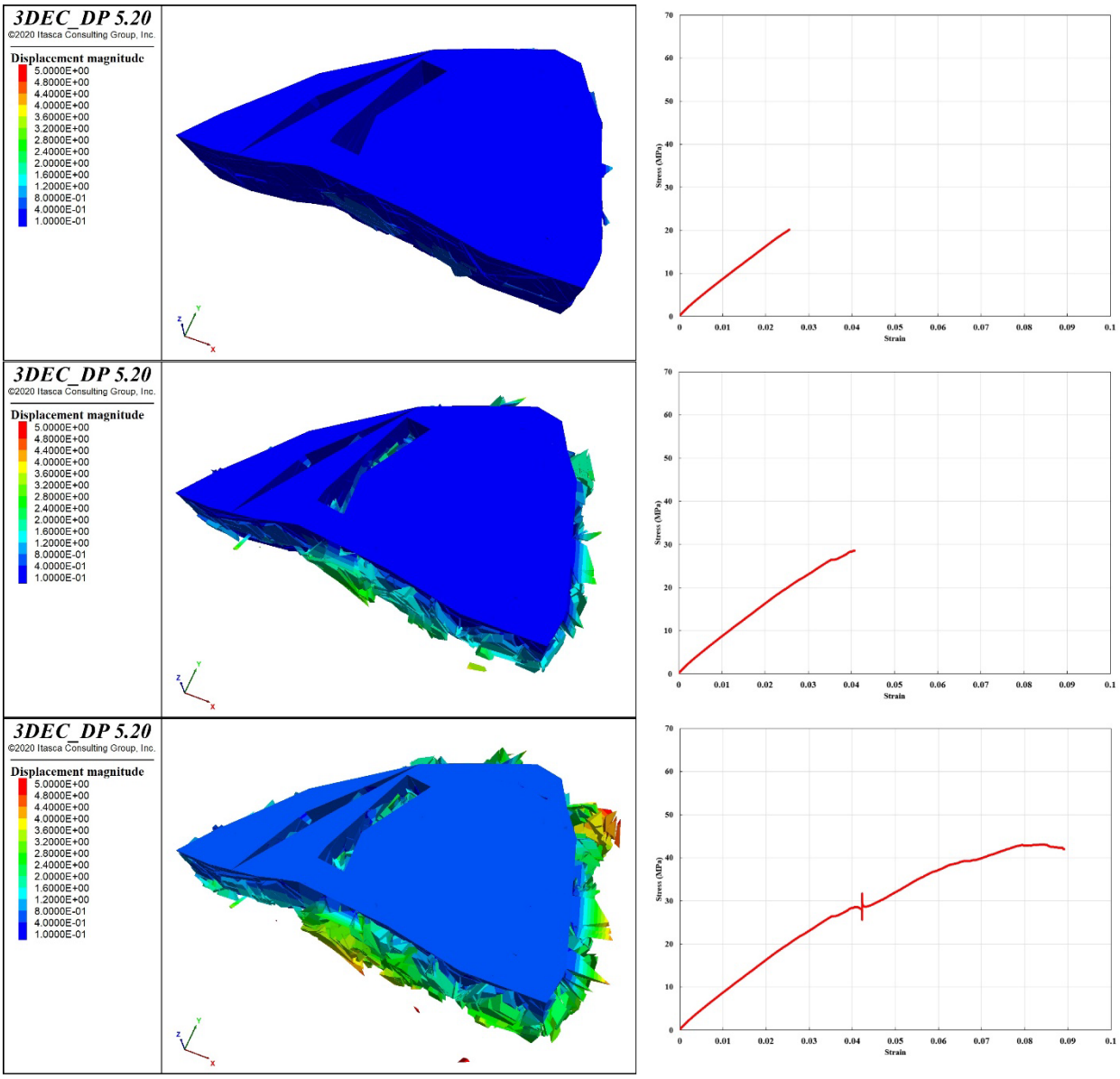

Figure 2.16 Deterioration phases of Pillar-X with increasing axial stress levels in Scenario 2.

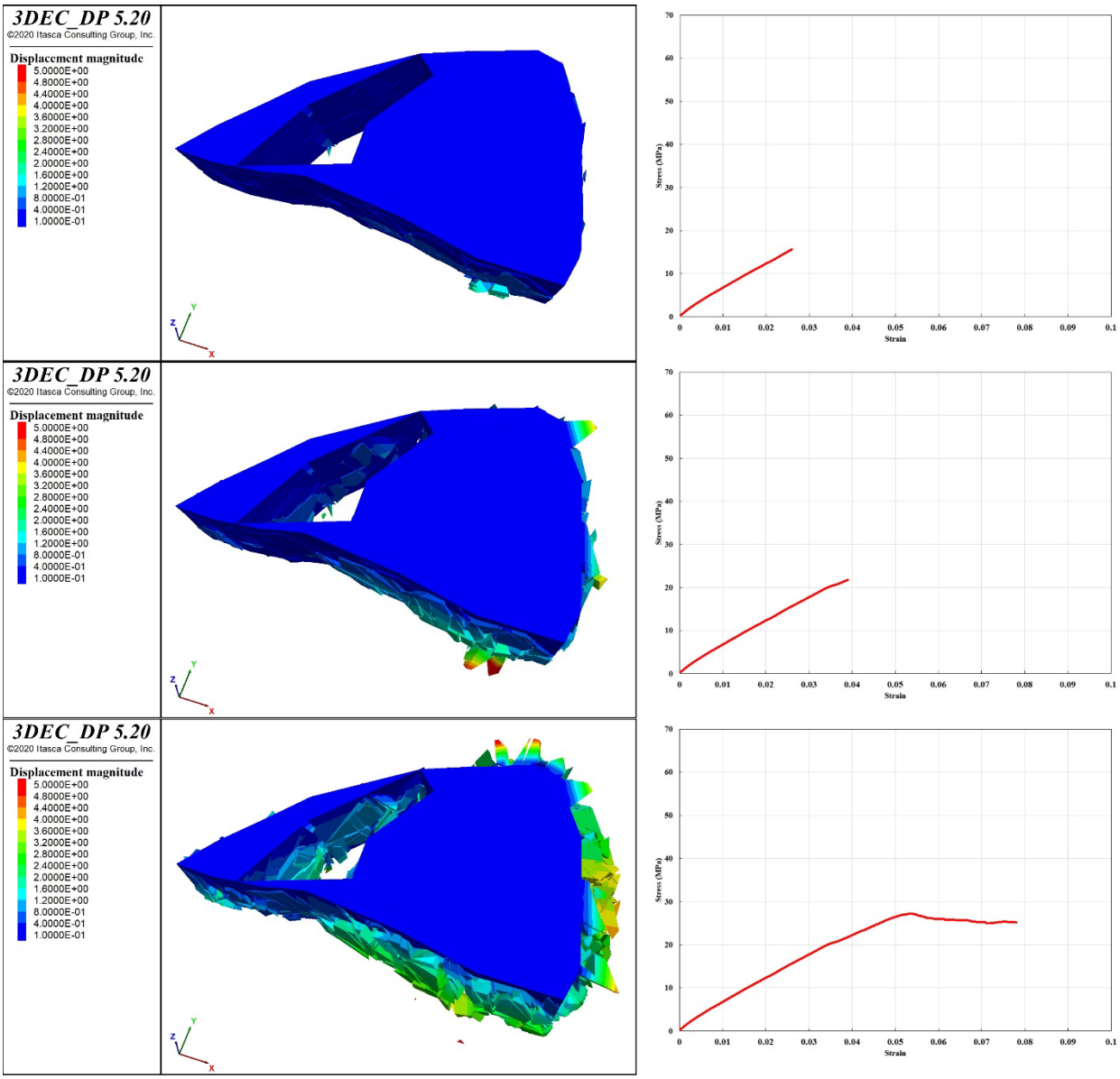

Figure 2.17 Deterioration phases of Pillar-X with increasing axial stress levels in Scenario 3.

2.7 Conclusions

This study simulates the presence of karst voids in a pillar in an underground limestone mine. Different results are achieved when testing the strength of Pillar-X in three different scenarios of varying karst cavity volume. The miners in the case study mine have had many encounters with karst-related safety incidents during excavation operations. This study is important to design the pillar and headings for future mining operations and the use of numerical modeling to assess local stability in the presence of karsts. The following conclusions can be drawn from this study:

(i) Karst-related safety incidents are quite common in stone mining operations. The karst voids, filled with rocky-clayey material, may interact with the immediate roof and fracture network resulting in ground collapse. This may endanger the safety of the mine workers and mine machinery.

(ii) To assess the strength of Pillar-X, different scenarios were simulated. The solid pillar with no karst voids failed at ~54 MPa showing the highest strength of all three scenarios. Stress was applied to the top and bottom face of the pillar in the form of constant velocity in 3DEC. Deterioration of the pillar was observed with increasing compressive stresses plotted against the axial strain.

(iii) The pillar with the suggested karst voids in Scenario 2 yielded and ultimately failed at ~43 MPa. It showed a reduced strength as compared to the original pillar in Scenario 1 indicating a reduction in strength due to the presence of karst inside.

(iv) The worst-case scenario with the biggest karst void showed the least strength of all the models. With a failure stress level of ~28 MPa, the pillar deteriorated too much as compared to the previous scenarios.

(v) The numerical modeling study suggested that as the void volume inside the pillar increases, the ability of the pillar to withstand higher stresses decreases. Figure 2.18 shows a comparison of all the scenario models with increasing stress with time steps.

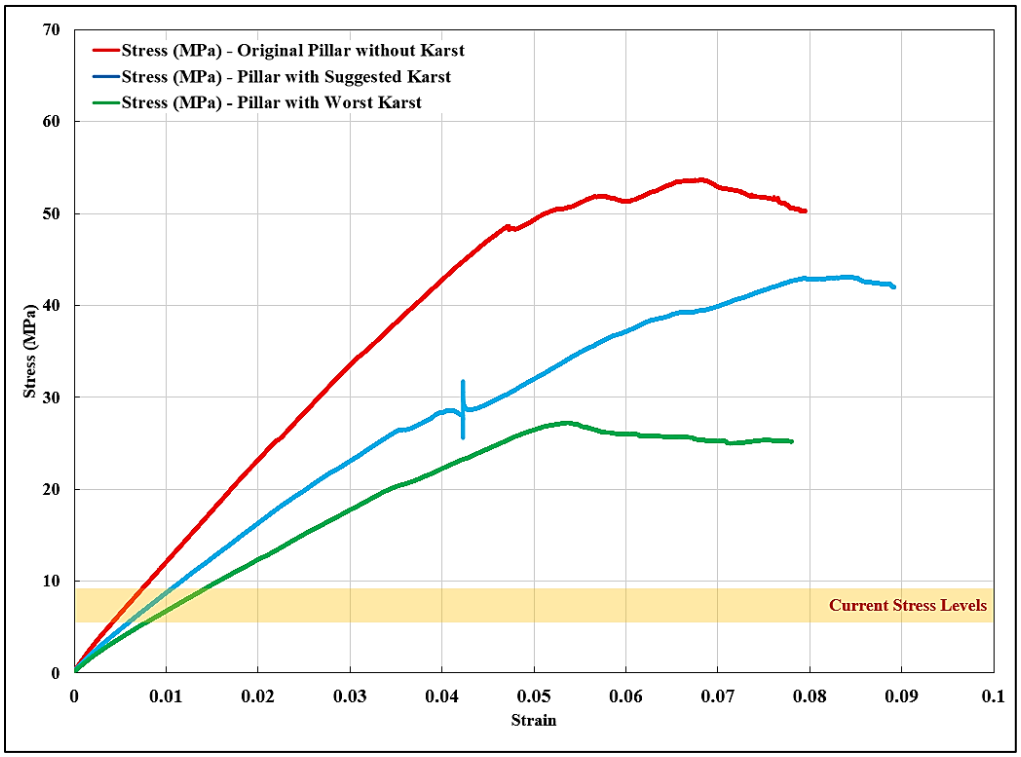

Figure 2.18 Axial stress with strain for all scenarios along with estimated stress levels in the pillar.

Concluding numerical modeling research to this study, which is published as a separate article, has been conducted at the case study mine. The study estimates the redistributed compressive stresses in and around the pillar to be in the range of 5-8 MPa. Looking at the strength of the pillar scenarios, it may be inferred that despite the presence of karsts, the pillar can withhold higher stresses than the current stress condition. Although the mine management would not like to design the pillar within their desired Factor of Safety limit so that the stresses would not reach anywhere near the yielding point where substantial deterioration may occur. In this case, the numerical modeling allows picturizing the ground

condition at the stress level at which the maximum limestone could be mined around the pillar without compromising the safety of the miners or machinery.

2.8 Scope of the Study

This chapter summarizes the numerical modeling analyses performed on the Pillar-X in a multi-level room-and-pillar underground limestone mine. Insufficient research exists to understand the impacts on pillar stability caused by the presence of karst voids. This study quantifies this effect in different scenarios, each with increasing the cavity volume to better understand the reduction in strength of a pillar with increasing compressive stresses. For this study, it is assumed that the compressive stress or vertical stress is imparted along the axis of the pillar, thus compressing the pillar. Even with the presence of the karst voids, the pillar could face higher stresses than the suggested current stress level of 5-8 MPa existing in and around the pillar. Hence, it may be inferred that there is room for improvement regarding the pillar design. It could be concluded that more ore could have been taken out of the pillar without compromising its safety.

However, the response of the pillar obtained using numerical modeling should be calibrated against field instrumentation data using extensometers or stress cells. This would enable the estimation of accurate pillar behavior with any stress variation caused by the modification of pillars in the mine. The picturization of pillar deterioration with the increase in stresses allows deciding the pillar strength at which the mine management would be comfortable with the pillar condition. And further improvements in design could be made until satisfaction is achieved with the pre-decided factor of safety of the pillar. The author will discuss working towards simulating models using different constitutive models to have

a comprehensive idea about the plastic behavior of the rock mass. This would allow us to further refine the pillar design and compare the results of this study to another one where the plastic behavior of the rock mass dominates. Since the pillars and headings around Pillar-X were designed based on its width dimensions, optimizing material extraction could only be done while modifying the pillar along its axis. The authors suggest extracting the stopes on the subsequent levels, which were not excavated thus leaving the pillar with its shortened height. A separate study is underway to suggest appropriate modifications to the pillar given its strength and existing stress levels.

At higher depths, the redistributed stress acting on the pillars is highly likely to increase. In this case, the numerical model would be an effective tool to reconsider the current rectangular design of the pillars in the case study mine. Also, if any karst cavities are encountered, the pillar or heading design could be varied and analyzed using 3DEC as a distinct element modeling tool to enclose the voids in the pillar while maintaining its stability. This study could also be important in helping with the secondary recovery from the remnant pillars in the mine to maximize ore extraction from the mine. Finally, when combined with karst-detection technologies such as probing or geophysical methods, numerical DEM could be effective to suggest any design changes while stoping and/or advancing while maintaining local as well as global mine stability.

Chapter 3

Modified Design of Pillar based on Estimated Stresses and Strength in an Underground Limestone Mine[2]

3.1 Introduction

Underground operations for mining limestone deposits experience a greater number of reported incidents compared to surface operations. To manage ground control issues during complex underground operations, special attention must be given to mine design for long-term planning. As a part of short-term planning, while undergoing development or stope extraction, operators must adjust pillar design to counter local stability issues as well as for efficient ore recovery. At present, 109 underground stone mines are operating in the United States, the majority of which are room-and-pillar mines [111]. Compared to flat deposits, ground stability management gets more complex in a dipping room-and-pillar mine.

The majority of underground limestone deposits have extensive fracture networks. Over a while, erosion of carbonate deposits due to groundwater flow through the fracture networks leads to the formation of cavities called karsts [47]. The karstic features including clay-filled

[2] This chapter has been accepted for publication to the Mining, Metallurgy & Exploration journal, titled as "*Modified Design of Pillar based on Estimated Stresses and Strength in an Underground Limestone Mine*" and is currently under review.

voids, dolines, and conduits, are usually connected with an aquifer and tend to increase groundwater flow into the mine [112]. The disruption of mining operations caused by karsts and the potential ground control measures have been documented by many researchers [26], [45], [115]. Non-destructive geophysical surveys, including Ground-penetrating Radar (GPR) surveys, are often conducted to detect these cavities as a suitable approach for detecting these geological anomalies in advance of excavation development [24].

Preventing pillar failure and maintaining local and global stability are the two cardinal factors in deciding on pillar design. Some major mine disasters, including the Crandall Canyon mine disaster in 2007, are proof enough that when going for economic recovery, global and local stability should be a primary concern for operators [98]. Geomechanical models, along with field instrumentation data analysis, play an important role in the evaluation of the structural behavior of pillars and the effect of stresses. This becomes particularly important in limestone deposits embedded with karsts, due to the variability of fractured rock mass and their pattern and orientation to in situ stresses [3].

This chapter evaluates the various modifications to the design of a pillar (designated Pillar-X) with the presence of a karst void in it. A previous study was conducted [129], which determined the effect of karst void on the strength of Pillar-X. Using the estimated pillar strength and the redistributed stresses, it was inferred that the pillar is capable of bearing more load than it is currently exposed to. Previously, at the case study mine, investigative work was conducted to detect the shape and volume of karst void(s) in the Pillar-X with the help of a 3-dimensional GPR survey [7]. The case study mine has frequently experienced ground control issues such as roof and rib failures because of karstic features in the past. The size of Pillar-X was left wider at the base and shorter in height than the usual pillar dimensions of 24.5 m x 24.5 m x 30.5 m to counter any potential instability issue because

of karst in it. The chapter also discusses the background of the research from the previous study showing the potential of modifying the height of Pillar-X. For this purpose, a rough schematic of the ideal mine layout along with the original excavation sequence is numerically simulated using FLAC3D to estimate the existential stress distribution on and around the pillar [67]. Because of the presence of a complex discontinuity network in the mine, Discrete Element Modeling (DEM) was used to simulate the rock mass as a discontinuous media for measuring pillar strength. For this purpose, the 3-dimensional numerical modeling software 3DEC was used along with Discrete Fracture Networks (DFN) to replicate the presence of complex discontinuities [64]. Since any discontinuities cannot be mapped within Pillar-X, DFNs become the closest possible representation to simulate the virtual network system compared to a real-world joint network. The physico-mechanical properties used were measured by the mining company and verified using laboratory testing. The joint properties were obtained based on the work performed by Monsalve [106] for the same case study mine. Pillar-X's strength was tested by modifying the height of the pillar model in a stepwise manner by increasing 10 ft or 3.05 m at a time. Since ground control measures were employed after the detection of karst in the pillar, changing the base dimensions of the pillar would present a difficult excavation scenario. Models with a subsequent increase in height were tested until the Factor of Safety for the pillar was above or equal to a value of 1.5 [43]. For each scenario, the pillar model was analyzed for its strength based on a constant axial compressive velocity applied to it. The analysis also characterizes the significant reduction in the pillar strength in the different scenarios, each with increased height. The research also discusses the best possible height scenario for the original square-base model of the pillar with the same improved height. This would compare to the situation where the decision to change the design of the pillar by the mine operator was better than the original design. The research discusses the importance of short-term planning in underground stone

mines for pillar design in the presence of karsts for efficient recovery as well as maintaining pillar stability.

3.2 Background

3.2.1 Original Pillar Design

The case-study mine is in a limestone deposit that hosts an extensive network of interconnected karst voids. The room-and-pillar mining method is employed to mine a 30 m thick orebody that dips at approximately 30° from the horizontal. The footwall and hanging wall tunnels which are approximately 8 m tall and 12 m wide are separated by 24.5 m x 24.5 m x 30.5 m rectangular pillars left after complete extraction from the stoping.

The pillar for which iterative simulations are conducted, named Pillar-X for this study, is shown in Figure 3.1. Figure 3.2 shows the positioning of karst cavities inside the pillar as determined using the GPR survey [7]. The excavation around Pillar-X was discontinued as a result of the opening up of the karst void with unconsolidated clayey material spilling out of the cavity. When the voids were discovered, the mine management decided to leave the pillar with bigger dimensions to counter local instability issues. Also, stope in the subsequent level was not excavated to provide extra stability to Pillar-X.

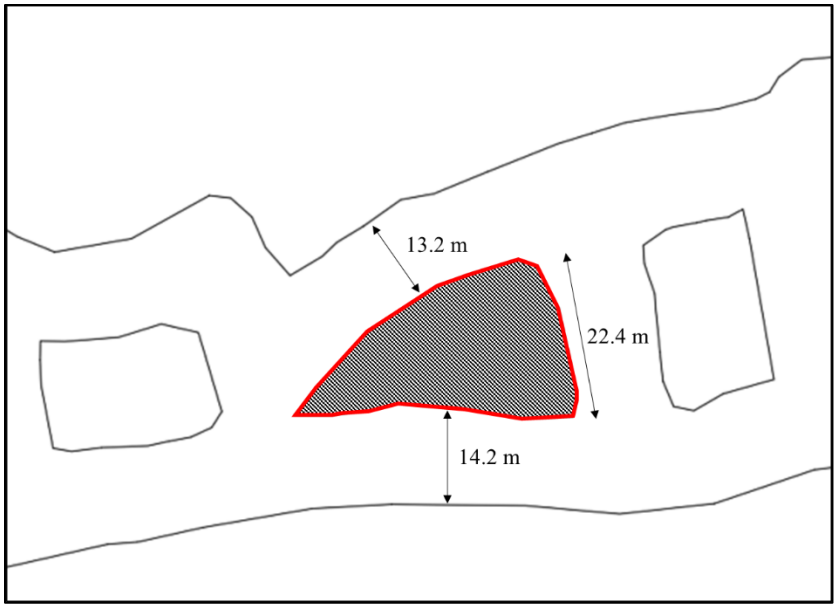

Figure 3.1 Schematic view of Pillar-X next to original design pillars.

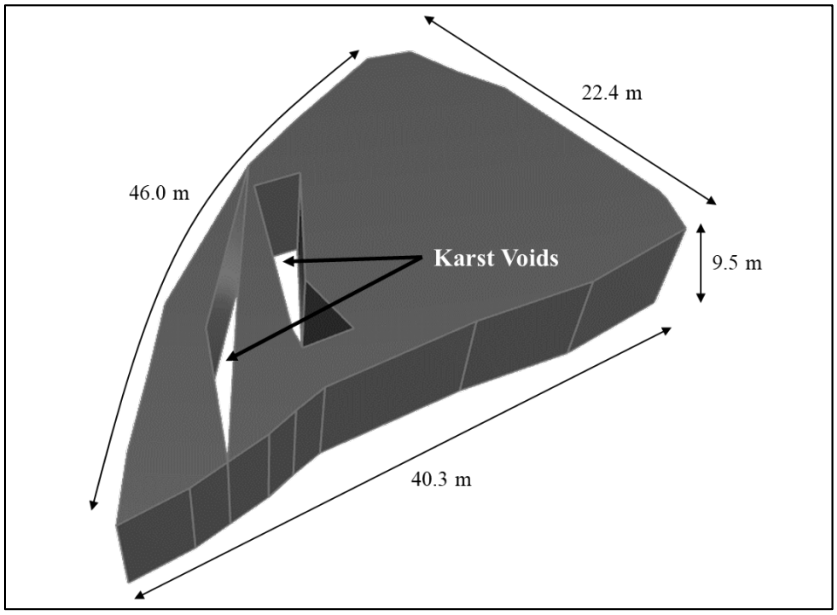

Figure 3.2 Modified dimensions of Pillar-X along with karst voids located in it.

The spillage of clayey-rocky material from the pillar required the mine management to employ ground support measures such as mesh pinned up with a steel strap. Further,

grouting was done as a ground control measure to prevent a further outflow of clayey sludge. Figure 2.4 shows the ground control measures taken around Pillar-X.

3.2.2 Pillar Strength Determination

Chapter 2 mentions the research study which simulates the presence of karst voids in Pillar-X and estimates its strength for various scenarios [129]. Different results were obtained when the strength of Pillar-X is tested for three scenarios of varying karst cavity volume in increasing order. The study was important preliminary research to understand the behavior of the original pillar design and local stability for future pillar design operations. It was also important to research the aspect of using numerical modeling to assess local stability using DFNs with the presence of karsts. The following conclusions were drawn from this study:

- The karst voids, filled with rocky-clayey material, interact with the immediate roof and fracture network resulting in a reduction of pillar strength
- Stress was applied to the top and bottom face of the pillar in the form of constant velocity in 3DEC. Deterioration of the pillar models was observed with increasing compressive stresses
- The solid pillar model with no voids failed at ~54 MPa showing the highest strength amongst all the three scenarios
- For scenario 2, the pillar model with the suggested karst voids yielded and failed at ~43 MPa. This indicated a significant reduction in strength due to the presence of a karst cavity inside. Figures 3.3(a) and 3.3(b) show the stress vs strain plot for a deteriorating elastic model with increasing compressive stress

- In scenario 3, the pillar model was simulated with the biggest karst void. It showed the least strength of all the models with a failure stress level of ~28 MPa. Also, the pillar model showed extensive deterioration compared to the previous scenarios Figures 3.4(a) and 3.4(b) show the stress vs strain plot for a deteriorating Mohr-Coulomb model with increasing compressive stress

- The research suggested that with increasing void volume inside the pillar, the ability of the pillar to withstand higher stresses decreases

- Based on the ground observations and the simulation results, it was concluded that Scenario 2 resembled the current ground conditions and how the karst cavity opened when the surrounding area was mined out. Figure 3.5 shows a comparison of pillar strength for simulating elastic and Mohr-Coulomb rock mass state

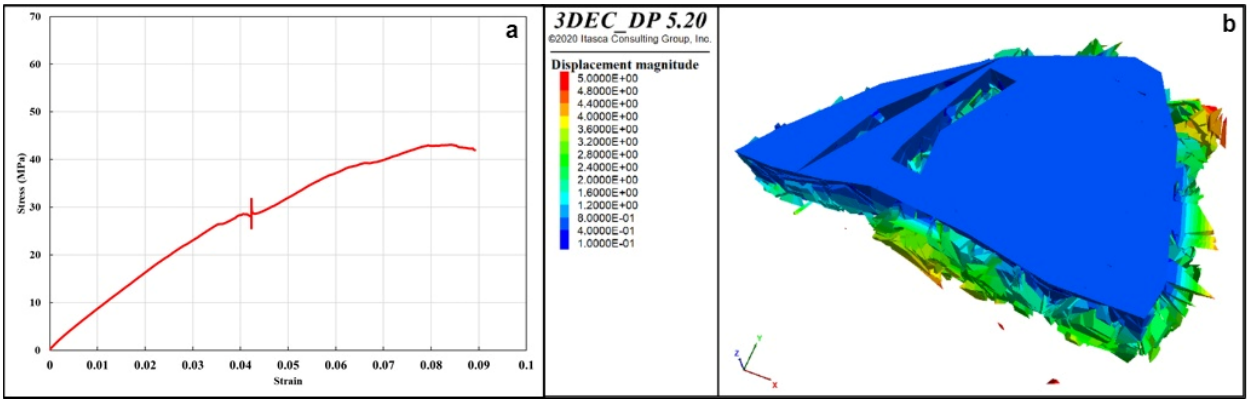

Figure 3.3 (a) Axial stress vs strain plot for Elastic pillar model; (b) Displacement magnitude and deterioration of the Elastic pillar model at its strength

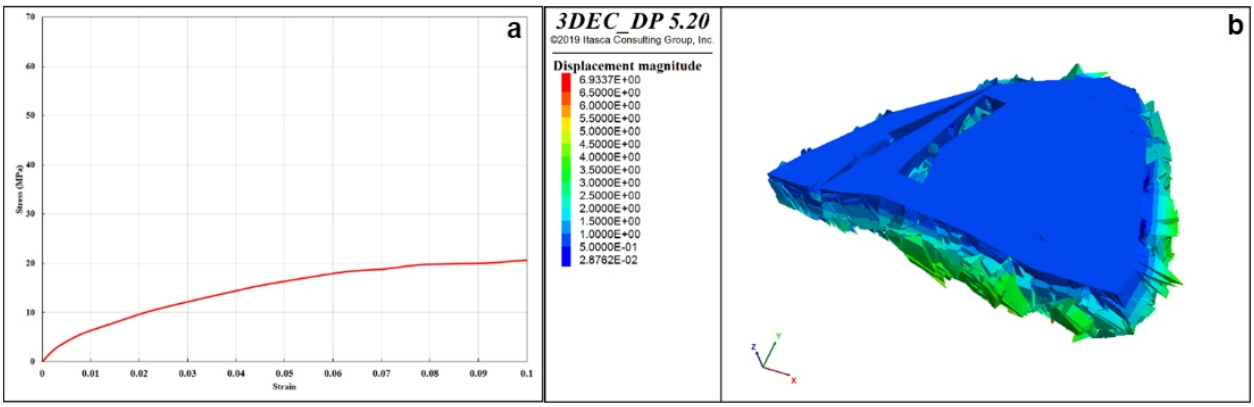

Figure 3.4 (a) Axial stress vs strain plot for Mohr-Coulomb pillar model; (b) Displacement magnitude and deterioration of the Mohr-Coulomb pillar model at its strength

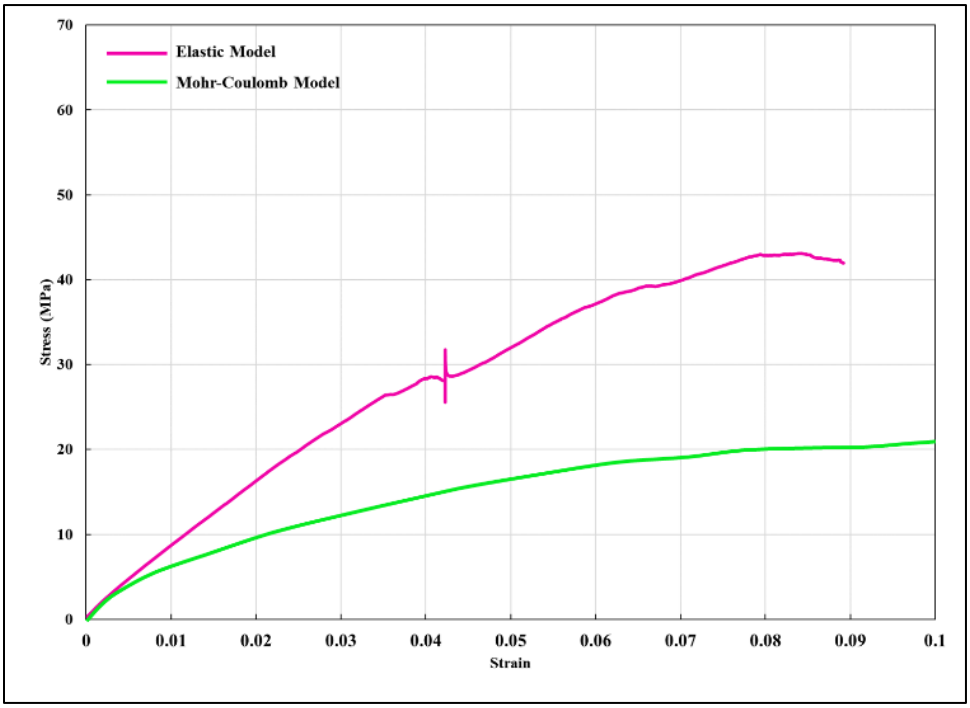

Figure 3.5 Axial stress vs strain plot for Pillar-X for Elastic vs Mohr-Coulomb constitutive model.

3.3 Estimating Stress Regime in FLAC3D

The estimation of prevailing stresses in the pillars of an underground mine is a complex task. This research required estimating pillar stresses to understand if any modifications could be made to the pillar design, having already determined the pillar strength. The development of an appropriate numerical rock model is very important for simulating the excavation sequence and redistributed stresses in the mine pillars. Also, the numerical model needs to be first calibrated using field instrumentation data for correctly estimating the response of pillars to redistributed loading. This involves using suitable physico-mechanical rock properties. FLAC3D was used for this sub-task involving numerical modeling and calibration of the mine model. To study the response of pillars to the redistributed stresses, a layout of the mine was modeled, and an excavation sequence was replicated to arrive at the current pillar layout. In this study, the rock mass properties are calibrated, and the redistributed stresses were determined using a suitable material model in FLAC3D.

3.3.1 Model Generation and Boundary Conditions

The case-study mine is situated in a region with middle- to lower-Ordovician-age, high-calcium limestone. The thickness of the orebody is about 30 m and dips at approximately 30° southeast as visible from the outcrop. Each level has an east and west section branching off the corkscrew ramp; at present, each branch contains a footwall and hanging wall tunnel separated by 24.5 m x 24.5 m x 30.5 m rectangular pillars left after complete extraction from the eventual stoping, and drives are approximately 8 m tall and 12.8 m wide. Figure 3.6 shows schematic views of the FLAC3D model with pillars and headings designed for the study. A simpler model was preferred for this sub-task to estimate the stress values using

numerical modeling. Although the layout designed for this study was based on the ideal mine plan, it will provide an approximation of the redistributed stresses post-mining.

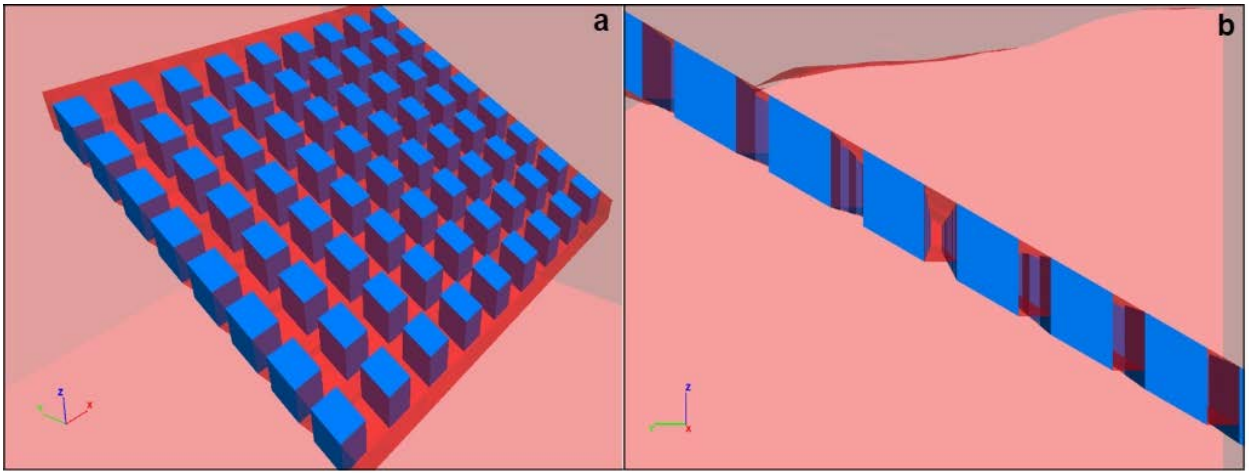

Figure 3.6 Perspective and cross-section schematic of the ideal layout of the case study mine.

The model size was limited by artificial boundaries wide enough to prevent any influence of bounding sides on the mine excavations. The top face was kept free, and the bottom and four side faces were bound as shown in Figure 3.7. The vertical and horizontal stress gradients were applied to the model as determined by the in situ stress measurements by the mine operator. These measurements were done using the United States Bureau of Mines (USBM) Borehole Deformation Gage (BDG) borehole measurements.

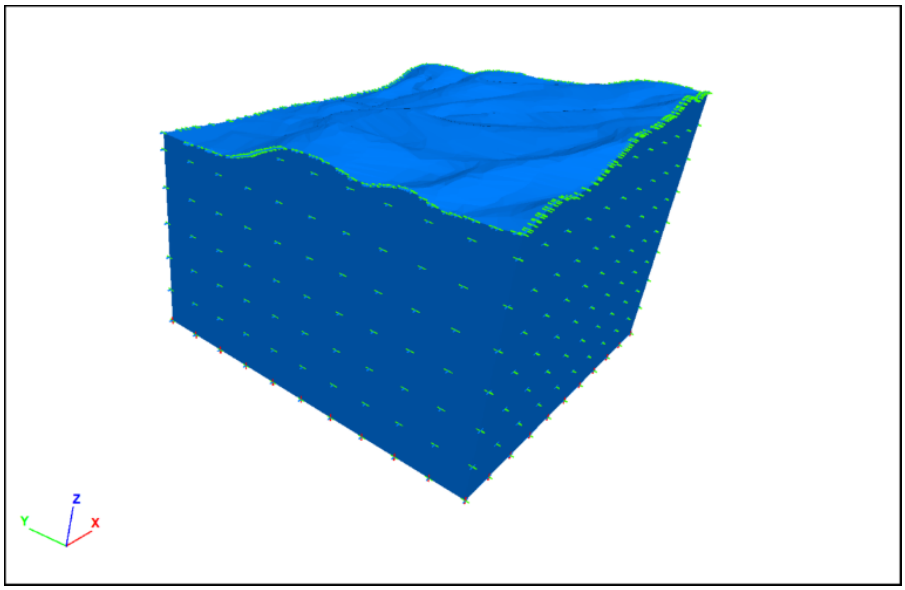

Figure 3.7 FLAC3D model extent with fixed boundaries marked by crosshairs and free topographic surface.

3.3.2 Assigning Rock Properties and Constitutive Models in FLAC3D

The physico-mechanical properties of the intact rock were measured by the mine management using laboratory testing of intact rock cores. Both the orebody and host rock are modeled as Mohr-Coulomb materials. A summary of all the intact rock parameters, namely density, shear modulus, bulk modulus, Poisson's ratio, cohesion, friction angle, and dilation angle is provided in Table 3.1.

Although the properties reflect the strength of the intact rock, simulating the model would not consider the presence of discontinuities inherent in the rock mass. The mapped joint network causes a reduction in the strength of the intact rock. To factor in this reduction, the material properties being used for FLAC3D must be calibrated so that they mimic the

rock mass behavior. The calibration of the FLAC3D model is explained in detail in the next section.

Table 3.1 Summary of intact rock input parameters for stress estimation.

Intact Rock Properties	Orebody	Hanging wall	Foot wall
Density, ρ	2690 kg/m^3	2691 kg/m^3	2722 kg/m^3
Bulk Modulus, K	37.86 GPa	32.81 GPa	37.69 MPa
Shear Modulus, G	20.57 GPa	25.64 GPa	25.18 MPa
Poisson's Ratio, μ	0.27	0.19	0.21
Cohesion, c	12.53 MPa	6.50 MPa	17.34 MPa
Friction Angle, ϕ	36.73	52.13	37.69
Dilation Angle, ψ	24.50	34.40	24.88
Tensile Strength, τ	2.69 MPa	2.77 MPa	3.30 MPa

3.3.3 Calibration of FLAC3D Model

The calibration of a numerical model is very important for replicating the evaluation of stresses and understanding the response of excavations to redistributed stress. Ideally, the numerical model needs to be calibrated using the field data of stress changes around the pillars of interest. Since the locations desired for taking the instrumentation data were not available due to the fieldwork time frame, the material properties of the rock mass used in FLAC3D were calibrated using the numerically simulated full-size pillar in 3DEC. Since it is cardinal to assess the stresses in the pillars after the mining, a 24.5 m x 24.5 m x 30.5 m rectangular pillar model was simulated in 3DEC. The 3DEC model simulates the real-life joints as a Discrete Fracture Network (DFN), along with the measured intact rock properties. The properties of the joints used in the 3DEC model are provided in Table 3.3.

Details about the DFNs are explained in Section 3.4.4. Figures 3.8(a) and 3.8(b) display the behavior of the pillar in 3DEC and FLAC3D, respectively.

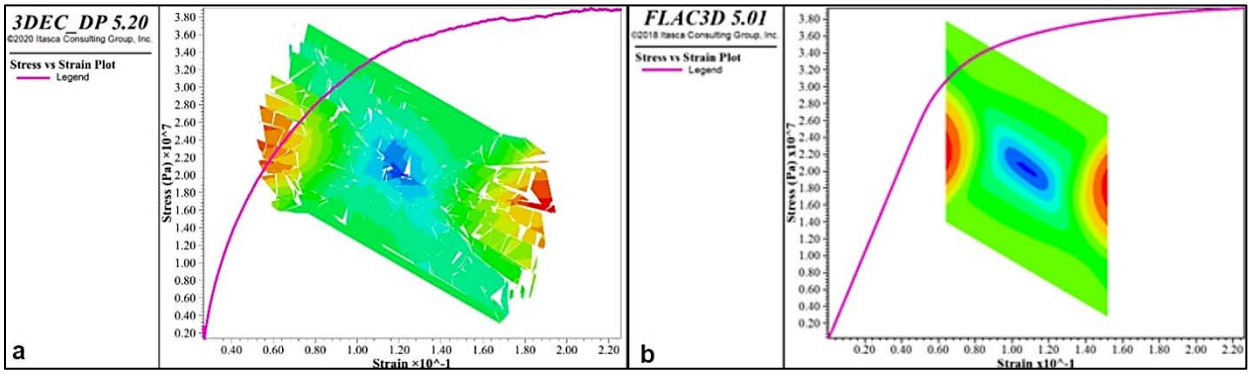

Figure 3.8 Displacement contour and axial stress-strain plot for **(a)** 3DEC model and **(b)** FLAC3D model.

The pillar model was simulated in both software to their peak strength. The rock mass properties for the FLAC3D model were modified to mimic the 3DEC pillar model filled with discontinuities as displayed in Figure 3.8. From the figures shown, it may be observed that both the pillar models yield at the same strength and follow nearly the same stress-strain plot. Since 3DEC simulates blocks as discrete and deformable elements displacing along the discontinuities, the pillar model shows rock deterioration when tested for strength. Whereas FLAC3D treats the rock mass as a continuum without any joints, hence, no deterioration is observed. Also, the graph for the FLAC3D model displays elastic behavior at low strains because all the pillar zones demonstrate the same strength with the application of load, but they follow the Mohr-Coulomb behavior near the pre-peak and the post-peak strains. Whereas for 3DEC, the presence of joints starts affecting the model from the very beginning and the pillar zones display the Mohr-Coulomb behavior from the start. Similar to orebody intact rock, a similar calibration was achieved for the hanging wall and footwall rock types. Table 3.2 shows the calibrated rock mass properties that were finally used for simulating the FLAC3D model for estimating the stresses in the pillars.

Table 3.2 Summary of rock mass parameters for stress estimation in FLAC3D.

Rock Mass Properties	Orebody	Hanging wall	Foot wall
Density, ρ	2690 kg/m^3	2691 kg/m^3	2722 kg/m^3
Bulk Modulus, K	378.6 MPa	328.1 MPa	376.9 MPa
Shear Modulus, G	205.7 MPa	256.4 MPa	251.8 MPa
Poisson's Ratio, μ	0.27	0.19	0.21
Cohesion, c	8.08 MPa	4.19 MPa	11.19 MPa
Friction Angle, ϕ	35.93	51.01	36.87
Dilation Angle, ψ	24.50	34.40	24.88
Tensile Strength, τ	2.69 MPa	2.77 MPa	3.30 MPa

3.3.4 Stress Estimation Results

Figures 3.9(a) and 3.9(b) show the contour of vertical stresses over the FLAC3D model before and after mining, respectively. In reality, the mine layout has not been followed perfectly. Often changes were made due to short-term mine planning for countering ground control issues while encountering karst voids and other occasional instability due to wedge formations in the immediate roof. Despite following the ideal case scenario, the extraction ratio in the model is approximately close to the real-life scenario. Figures 3.10(a) and 3.10(b) show the vertical stresses in the mine level where Pillar-X is located before excavation, whereas Figures 3.11(a) and 3.11(b) show the vertical stresses after mining, respectively. The relative location of Pillar-X is the same as the virtual pillar marked in Figure 3.11(b), and it is assumed that it is exposed to the same stresses as determined using the numerical model. From the figure, it can be observed that the stresses in the pillar vary between 5 MPa around the periphery of the pillar to 8 MPa at the core of the pillar.

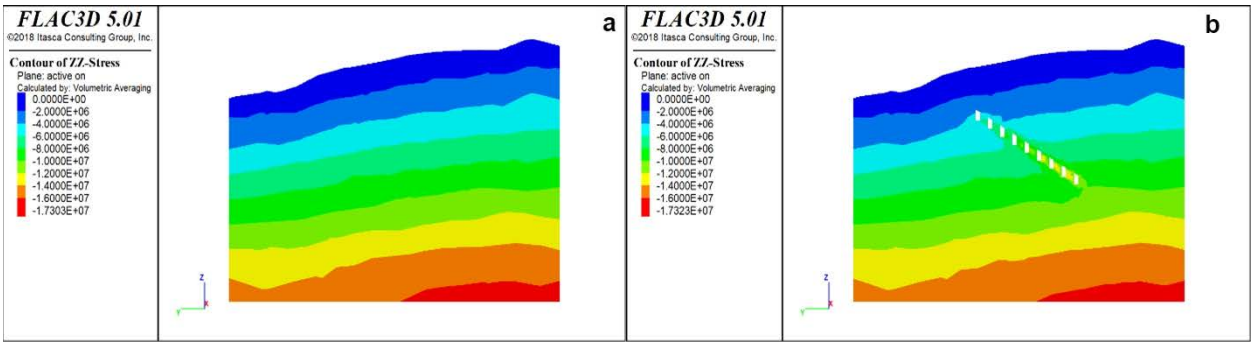

Figure 3.9 (a) Contour of pre-mining ZZ-stress; (b) Contour of post-mining ZZ-stress.

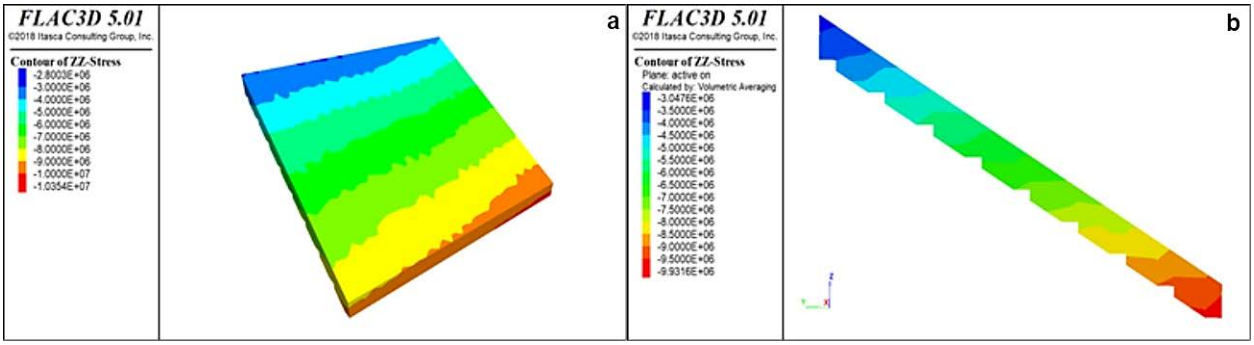

Figure 3.10 Perspective and cross-section view of the mine layout before excavation.

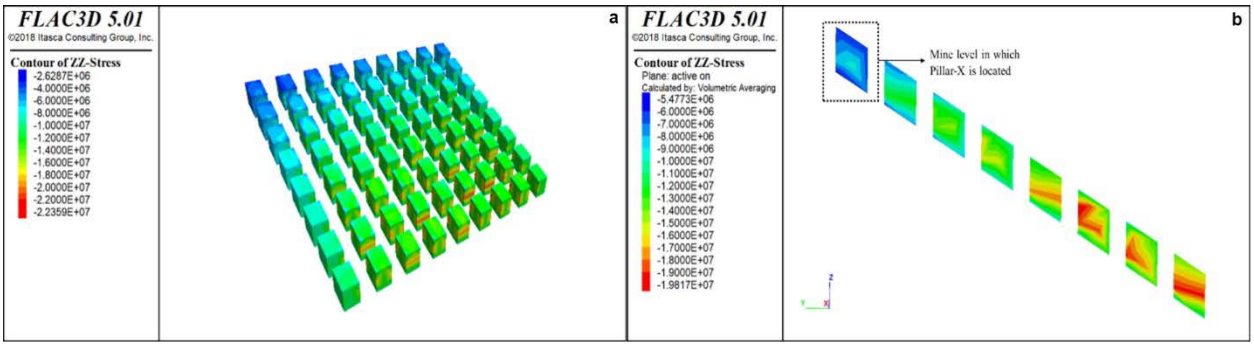

Figure 3.11 Perspective and cross-section view of the mine layout after mining.

3.4 Numerical Modeling of Modified Pillar Designs

After estimating the stress affecting Pillar-X, the numerical modeling tool 3DEC is utilized to determine the optimum height to which it could be excavated or may have been designed. The software uses the distinct element method (DEM) for simulating the rock as a discontinuum media comprised of discrete blocks formed with joints and fractures. Similar to the previous study, this research sets individual blocks as deformable materials which are meshed as finite different zones. The pillar strength is tested under increasing axial stress which leads to a movement along the joints and rotation of blocks.

3.4.1 Pillar-X Model Designs

For this study, the objective was to keep the pillar geometry constant in the lateral directions but increase the height of the pillar for subsequent model design testing. It should be noted that the current height of the pillar is 9.5 m or 30 ft and was kept as a precautionary measure for the karst void discovered while the mine advances. However, no further study or ground control analysis was done by the mine planning team to estimate the optimum design of the pillar without compromising the local stability. In this study, pillar height was increased in the intervals of 10 ft (3.05 m) starting from the initial height of 50 ft (15.24 m). Three scenarios were tested for pillar models of height 50 ft (15.24 m), 60 ft (18.3 m), and 70 ft (21.34 m). Numerical modeling for pillar models for heights above 70 ft was not carried out because the 70 ft tall pillar model did not meet the factor of safety criteria of 1.5 [43]. This is further discussed in detail in the results and analysis section. Figure 3.12 shows the pillar models with varying heights that were tested for pillar strength.

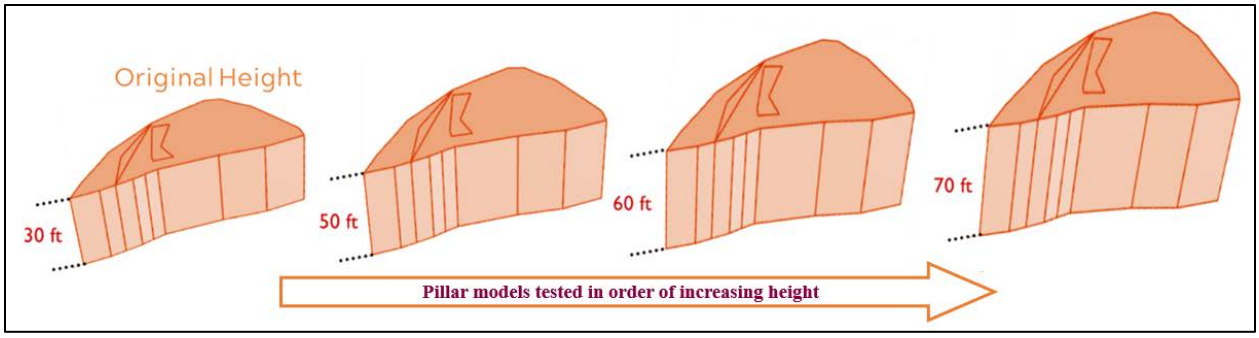

Figure 3.12 Pillar-X model designs tested with varying heights and constant lateral dimensions.

3.4.2 Physico-mechanical Properties

The physico-mechanical and geotechnical properties of the rock mass and joints used in the numerical model are tabulated in Table 3.3. As mentioned earlier, these properties are measured by the mine management using geotechnical borehole measurements and laboratory testing. The calculated values for joint shear stiffness and joint normal stiffness are based on the work performed by [8]. Both the Elastic-Isotropic and the Mohr-Coulomb constitutive models were used to simulate rock behavior in the numerical model. It is believed that the Mohr-Coulomb model could be the ideal model to study the response of the rock mass, but the Elastic-Isotropic model state closely follows the karst cavity failure observed in the mine. For this reason, the study covers evaluating the pillar behavior concerning both the constitutive models. The discontinuities, however, are modeled using the Coulomb slip constitutive model to represent the physical response of rock joints.

Table 3.3 Physico-mechanical properties for intact rock and joints.

Intact Rock Properties	
Density, ρ	2690 kg/m^3
Bulk Modulus, K	37.86 GPa
Shear Modulus, G	20.57 GPa
Poisson's Ratio, ν	0.27
Cohesion, c	12.53 MPa
Friction Angle, ϕ	36.73
Dilation Angle, ψ	24.50
Joint Properties	
Joint Normal Stiffness	300 GPa/m
Joint Shear Stiffness	30 GPa/m
Joint Friction Angle	30^o
Joint Cohesion	0.0

3.4.3 Boundary Conditions

Compressive stresses were applied axially along the vertical axis of the pillar models. Since the pillar is not bounded on the sides, boundary conditions were kept free on the sidewalls. Constant load application was initiated at the top and bottom of the pillar model using an applied velocity of about 0.5 μm per timestep [20]. It is assumed that no horizontal movement is present at the top and bottom faces of the pillar. To ensure this, boundaries were fixed in the lateral directions at the top and bottom faces of the models. Each numerical model was simulated until pillar model failure was observed for each height modification.

3.4.4 Discrete Fracture Network (DFN)

The use of a discrete fracture network in this study plays an important role in deciding the strength of the pillar models. Different parameters of the discontinuity network such as size information (trace length and area) and orientation information (dip, dip direction, and strike) were utilized in generating DFN using 3DEC. The details about the structural mapping in the case study mine and generating DFN using the statistical information provided in the previous study [129]. Figure 3.13 shows the pillar comprising multiple blocks formed after being cut by the DFN to simulate a close representation of the geological structures in a rock mass.

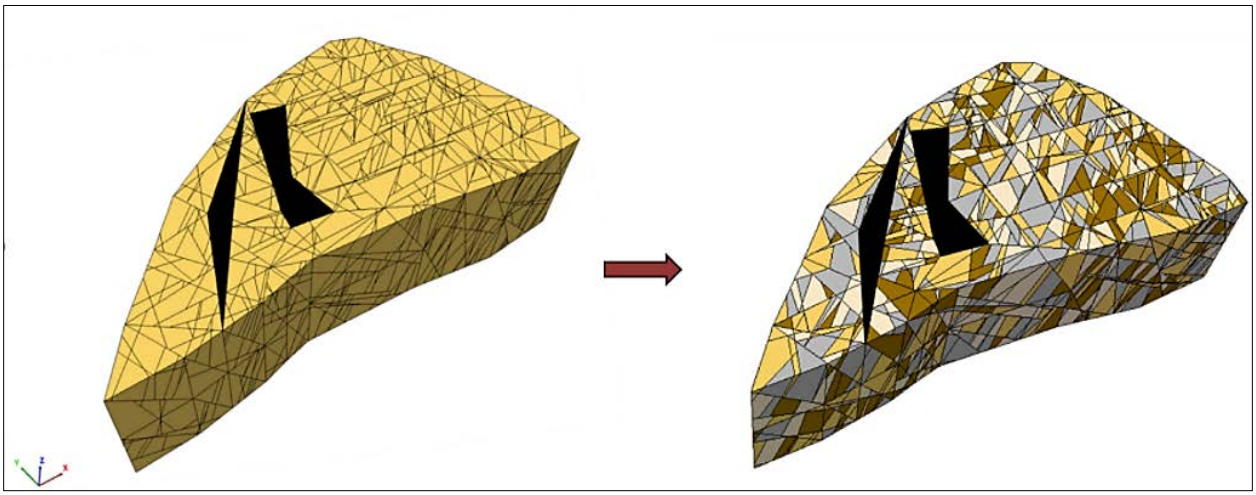

Figure 3.13 Pillar-X with karsts represented using jointed blocks in the presence of a discrete fracture network.

3.5 Results and Analysis

The numerical modeling analysis for the two constitutive models (Elastic & Mohr-Coulomb) was performed to evaluate the performance of the pillar models with increasing load. The stress levels are plotted versus axial strain along the pillar to study the behavior of rock

mass with increasing strain. The models were subjected to increasing axial stresses until yielding and ultimately failure is achieved. The criterion of failure is easy to identify in Elastic rock mass by observing for a sudden drop in the stress values and looking at the deterioration levels of the pillar models. For Mohr-Coulomb models, however, the simulation is stopped until the stress vs strain plot line attenuates and no substantial increase in stress is observed with strain. Figures 3.14, 3.15, and 3.16 show the different plots for pillar models of height 50 ft, 60 ft, and 70 ft for Elastic and Mohr-Coulomb model simulations. For all the simulated pillar models, it is observed that with an increase in compressive stress, tensile failures increase along the sidewall of the pillar leading to spalling. The pillar models fail upon reaching their ultimate strength with a subsequent increase in the compressive stresses. The karst void in every pillar model follows the same geometry. It is assumed that the karst volume extends in the roof and has the same height as a pillar model for equivalent comparison. From the study in FLAC3D for estimating stresses in the mine and Pillar-X, it can be inferred that the stresses inside the pillar exist in the range of 5-8 MPa.

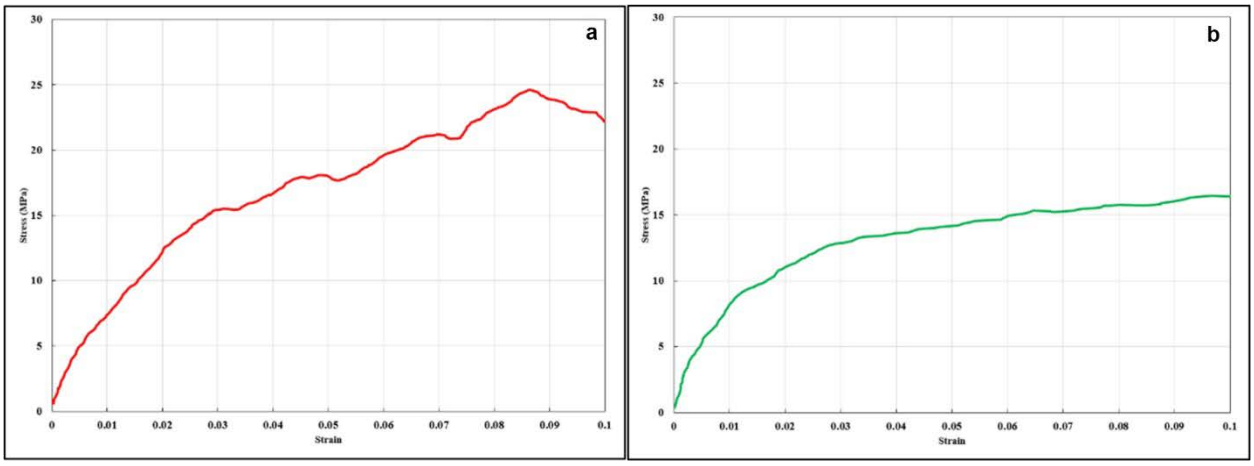

Figure 3.14 Axial stress vs strain plot for a 50 ft- (a) Elastic model; (b) Mohr-Coulomb model.

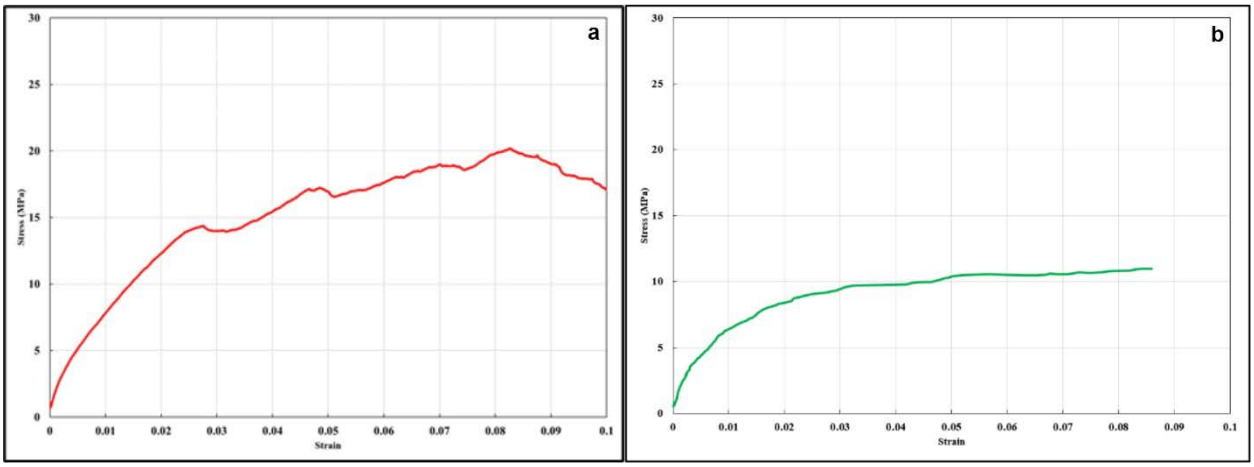

Figure 3.15 Axial stress vs strain plot for a 60 ft- (a) Elastic model; (b) Mohr-Coulomb model.

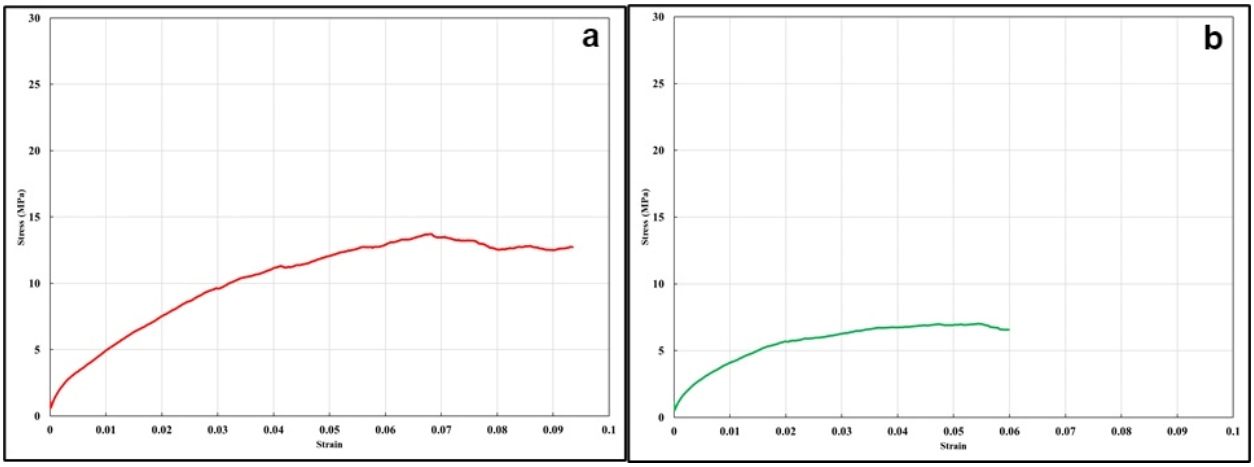

Figure 3.16 Axial stress vs strain plot for a 70 ft- (a) Elastic model; (b) Mohr-Coulomb model.

For further analysis, the highest value of 8 MPa is assumed to be the value of stress in Pillar-X. To maintain a Factor of Safety of 1.5 or higher, the pillar strength cannot fall below 12 MPa. The pillar models with larger heights will have a lower strength value compared to a model with a smaller height. Hence, pillar models with a subsequent increase in height of 10 ft were tested until the desired strength value is reached. The observations and their analyses are as follows:

- *Elastic Constitutive Criterion-* For the models simulating Elastic rock mass with Coulomb-slip discontinuities, it is observed that all three models meet the Factor of Safety criteria. The strength of the Pillar-X model when extended to a height of 50 ft was found to be 25 MPa, and that of a height of 60 ft was 20 MPa. When the height of the pillar model was extended to 70 ft, it yielded at 12.5 MPa, just over the Factor of Safety value by a small margin. It was concluded that any further increase in height would lead to a pillar strength of less than 12 MPa, hence, no further simulations were carried out. An interesting observation was that the 50 ft and 60 ft height pillar models followed the same path on the Stress vs Strain plot when subjected up to a stress of 15 MPa or a strain value of 0.03. However, the same was not true for a pillar model with a height of 70 ft. It is inferred that with increasing pillar height, the number of discontinuities also increases by virtue of increased pillar volume. Hence, after a certain point, the constitutive properties of the joint network dominate the mechanical behavior of the overall intact rock.

- *Mohr-Coulomb Constitutive Criterion-* For the models simulating Mohr-Coulomb rock mass behavior, it is observed that only the 50 ft high model of Pillar-X meets the Factor of Safety criteria. The model yielded at a stress level of 16.5 MPa. The 60 ft tall pillar model shows a strength of about 11.5 MPa, just falling short of meeting the Factor of Safety criteria, whereas the 70 ft pillar model does not meet the criteria and fails at 7 MPa. It can be observed that the Mohr-Coulomb pillar models show a considerable reduction in strength compared to the Elastic models. The pillar models tested in this scenario are simulating a perfectly plastic behavior of the rock mass. This has been done by implementing the dilation angle parameter in the inbuilt Mohr-Coulomb constitutive model in 3DEC. Furthermore, any intermediate heights for Pillar-X between 60 ft and 70 ft were not tested for this

scenario as the 60 ft tall pillar was almost on the boundary for meeting the Factor of Safety criteria and an increase in height was predicted not to meet the threshold value of 12 MPa.

- *Variation in Pillar Strength with Height*- The pillar strengths determined for various modified models for this study, plus the strength of the original pillar from the previous study were plotted against their height. The plot was constructed for both the Elastic and the Mohr-Coulomb failure criteria models. It may be observed that with an increase in height, the pillar strengths for both constitutive models approach each other. The data is not enough for predicting the approach of strengths towards a common point. However, at this stage, it may be predicted that as the height of the pillar model increases, the number of joints and fractures also increase manifold. Since the joint behavior is simulated using the Coulomb-slip model, the only difference in the two scenarios is the constitutive model for the intact rock. This may lead to a conclusion that the discontinuity features dominate the response of rock mass to stresses after a certain increase in the size of the pillar model. The strength/UCS of the intact rock in the case study mine is high (160 MPa). No instances of rock bursts or pillar failures have been observed at any point of time during the life of the mine. The only issues observed have been related to the collapse of ground affected by karst voids. In the absence of any such incident, it is difficult to assess the shift from stress to a structurally controlled failure mechanism. Figure 3.17 shows the variation in pillar strength for different heights for the Elastic and Mohr-Coulomb pillar models.

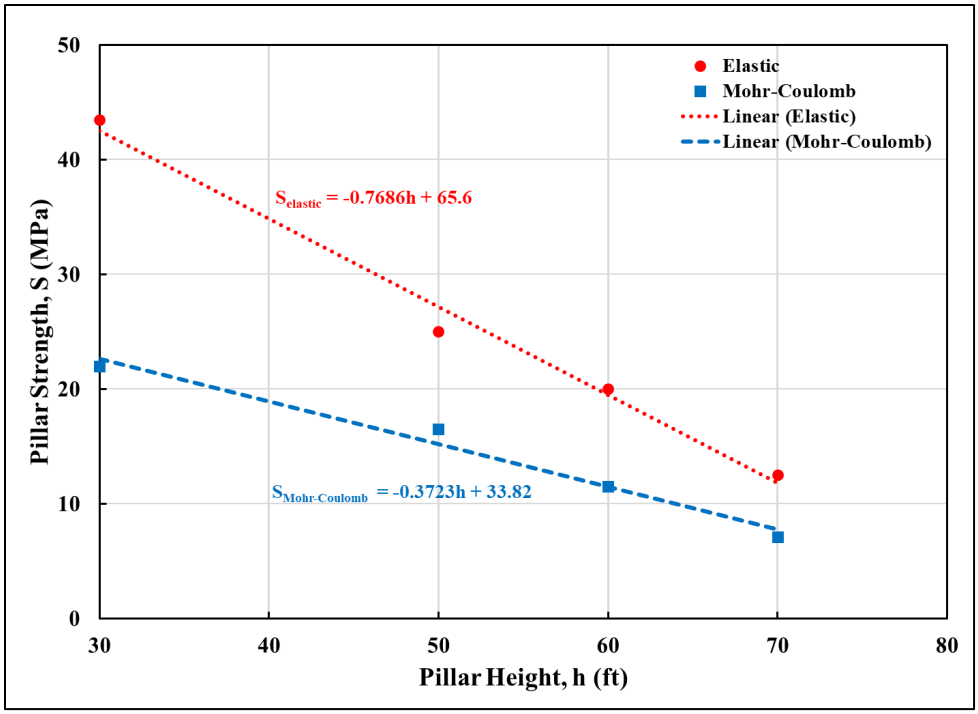

Figure 3.17 Pillar strength vs pillar height for Elastic & Mohr-Coulomb constitutive models.

3.6 Conclusions

This chapter studies the modification to the design of an underground stone pillar affected by the karst cavity. The modification is essential to understand the improvisation necessary to maintain stable design without compromising ore production. The primary aim is to tackle the instability issue in karst-ridden pillars and utilize numerical modeling to improve upon existing pillar design. Varying results are achieved when testing the strength of the Pillar-X model with a subsequent increase in height for each simulation. To understand the existing stress state of the pillar, numerical modeling was performed by utilizing in situ stresses and excavation planned throughout the mine. This study serves as a secondary and concluding research for the preliminary study aimed at estimating the effect of karsts on Pillar-X strength [129]. The research is important for understanding the current stress

regime and the response of pillars and excavated areas to any change in it, especially in a karst-affected area. This would help devise a good strategy for planning a secondary recovery from the pillars without jeopardizing local or global stability. Some important conclusions that can be drawn from this study are:

- In the case study mine, ground control issues were encountered when mining advanced into a karst-affected pillar, also known as Pillar-X. To counter this problem, the mine management decided to alter the design and increase the size of the pillar as a means of the ground control measure.

- A preliminary study estimated that despite hosting the cavity, the pillar can support higher stresses without causing local instability. This could be implemented by modifying the pillar design in terms of increasing its height and stoping it at the lower level.

- To understand a justifiable pillar design, existing stresses around and on the pillar were estimated by using modeling in FLAC3D. Calibration of the in situ model was carried out and excavation sequencing was implemented to arrive at the current redistributed stress regime. It was estimated that the current stress state in the range of 5-8 MPa could be acting on Pillar-X. Assuming a Factor of Safety value of 1.5, this would put a feasible pillar strength to be 12 MPa or above with a design modification.

- To assess the viable height increase, different models with the same pillar geometry but varying heights were numerically simulated. The height was increased in intervals of 10 ft until the pillar model tested for a strength of 12 MPa or less. Axial stress was applied to the pillar models for numerically testing their strength in 3DEC.

A discrete fracture network was also used to replicate the behavior close to real-world discontinuities.

- For pillar models with Elastic rock mass with Coulomb-slip joints, it was determined that the height of Pillar-X could be increased to 70 ft (21.34 m) while meeting the Factor of Safety criteria. The strength of the 70 ft pillar model was found to be 12.5 MPa based on the Stress vs Strain plot. An interesting observation was that, unlike the 70 ft pillar, the 50 ft and 60 ft pillar models followed the same curve on the Stress vs Strain plot up to a stress of 15 MPa or a strain value of 0.03.

- For pillar models with Mohr-Coulomb rock mass with Coulomb-slip joints, only the 50 ft pillar model meets the Factor of Safety criteria yielding at a strength of 16.5 MPa. In this case, the 60 ft model just fell short of meeting the criteria by testing at a strength of 11.5 MPa. The behavior of rock mass in the underground stone mine skews towards the Elastic rock mass criteria, but it is recommended to consider the Mohr-Coulomb constitutive model for numerical simulation after factoring in a conservative approach for a karst-affected mine.

From the plot of pillar strength vs height for both the constitutive models (Elastic and Mohr-Coulomb), it may be observed that with an increase in height, the pillar strengths tend to approach the same magnitude. The data is considerably less for this prediction and more simulations are desirable. But, at this point, it may be inferred that with an increase in height, the number of discontinuities increases manifold, and their response takes over the behavior of intact rock mass to stresses. The author also believes that experimenting with the strain-softening constitutive model could provide an accurate rock mass response with stress variation. This model could be utilized in this study due to the absence of appropriate properties which may be measured using rock laboratory testing.

Chapter 4

Strength Evaluation of Compartmentalized Pillar Zones using Drone & Terrestrial LiDAR Mapping in an Underground Stone Mine[3]

4.1 Background

The production of crushed stone and related aggregate products has been rising each year to meet the ever-growing demand. In 2021, over 1500 million metric tons of crushed stone were produced in the United States alone [132]. Underground stone mining operations help surface mines and quarries bridge the demand gap with supplemented ore production. As underground operations continue to grow, it also leads to an increase in incidents and risks for miners. Since October 2020, four incidents of massive pillar collapses at different mine sites have occurred in the US. Fortuitously, these collapses did not cause any injuries or fatalities [108].

The underground mines require additional ground control efforts for maintaining a safe work environment and preventing hazards. Placing special emphasis on supporting weaker

[3] The prepared manuscript for this chapter will be submitted for journal publication to the International Journal of Mining Sciences & Technology upon review by all the co-authors.

roof and sidewall structure is paramount especially when they are interacting with karst voids and channels promoting water inflow. Kortnik [78] discussed the importance of planning, monitoring, and optimization of stone pillars during underground excavation. Excavating into a karst-ridden heading may lead to sudden ground accidents and disrupt mining operations. Beck [11] addressed issues related to karst in general, as well as explained the engineering impacts of the disruption caused by karst during mining activities.

Limestone deposits have a prominent presence of discontinuities, faults, and bedding planes. It is important to monitor these discontinuities because their interaction with the voids may lead to the weakening of pillars and cause ground control issues. These discontinuities are also responsible for allowing the groundwater to move through limestone formations and ultimately form karst voids, which are common in limestone mines [75]. Monitoring a limestone pillar for improving its design may provide beneficial information related to its structural stability and the local ground movement. Traditional monitoring techniques and observations may prove hazardous to safety in unstable mining areas, especially in underground limestone mines with large mining heights. Also, geotechnical monitoring of discontinuities and pillow geometries is difficult for tall pillars even when using elevated work platforms or lifts.

Most of the observational techniques used for monitoring ground behavior require measurements at single or distinct points. Distinct point measuring devices have been used by the mining industry in the US for many years, including the Roof Monitoring Safety System (RMSS) [99]. Jones and Beck [73] describe the shortcomings of current methods on a qualitative interpretation of monitoring across the entire excavation. They also describe the advantages of using LiDAR technology for routine geotechnical measurements and mines facing ground control issues. Slaker et al. [127] used LiDAR to effectively track ground

deformations and cutter roof formation at the Pleasant Gap limestone mine. Sturzenegger [133] has documented the ability of laser scanners to rapidly capture geotechnical data such as discontinuities in highly inaccessible mine areas. Soni et al. [129] showed the advantage of Ground-penetrating Radar (GPR) and laser scanning for mapping discontinuities and estimating the strength of pillars with karst voids in a stone mine. Many researchers have shown the advantages of using remote sensing technologies such as LiDAR for rock mass characterization and accessing the hazardous areas in underground mining and tunneling [17], [46], [105], [126].

4.2 Objective

The research presented in this chapter analyzes the behavior of two pillars in the case study mine. The case study mine employs a multi-level room-and-pillar method to extract a dipping limestone deposit. The deposit has a prevalent karstic network that has been responsible for multiple ground control issues over the years. Figure 4.1 shows a picture of karst voids encountered in the case study mine.

Each sublevel contains hanging wall and footwall tunnels separated by rectangular pillars. The inclined, rectangular pillars are designed to be 24.5 m x 24.5 x 30.5 m, or 100 ft tall with 80 ft x 80 ft base dimensions. Figure 4.2 shows the layout of the case study mine. After the eventual benching of the stopes, the total height of the pillars comes out to be 100 ft tall which is a massive height for supporting the roof of the excavation. Figure 4.3 shows the enormous scale of a pillar in the mine compared to the author.

Figure 4.1 Karst voids in the underground case study mine [18].

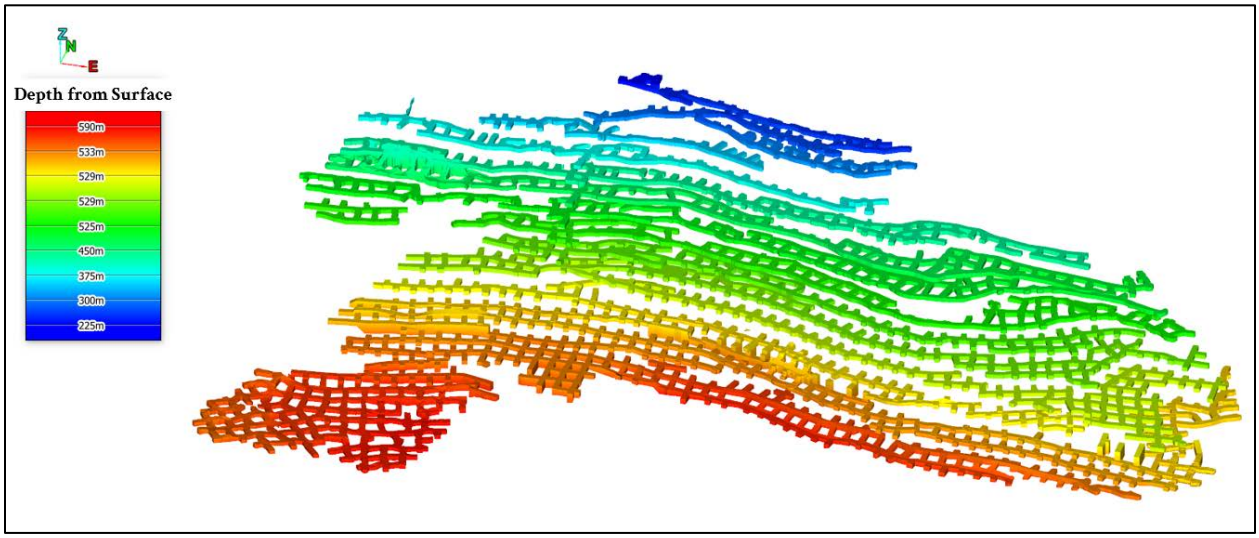

Figure 4.2 Layout by height gradient for the multi-level case study mine.

Figure 4.3 Massive 100 ft tall pillar in the underground limestone mine.

When these pillars interact with the redistributed stresses, their behavior is governed by how the joints and developed fractures constituting the rock mass interact with those stresses. The study hypothesizes that different regions of a pillar may behave uniquely to the stresses based on the setting of the discontinuity network. The motivation behind this study comes from the pilot studies as described in future sections. The details and specifics of the model creation, modeling procedure, inclusion of the discontinuity network, and geotechnical parameters are not explained in these pilot studies. Currently, emphasis is

placed on interpreting the results and building upon them to arrive at the aim of this research. The pilot studies are as follows:

4.2.1 Pilot Study 1

The first pilot study helps understand the behavior of a redesigned 50 ft (15 m) tall, inclined pillar with karst voids enclosed in it. Section 3.4 mentions the details of the numerical modeling process used to simulate the pillar model including the boundary conditions, physico-mechanical properties, and the discrete fracture network (DFN). Figure 4.4 shows the model of the hypothetical pillar in the 3DEC software. The simulation was designed to test the ultimate strength of the pillar model. The model behavior was observed with a gradual increase in the imparted stresses with the time step.

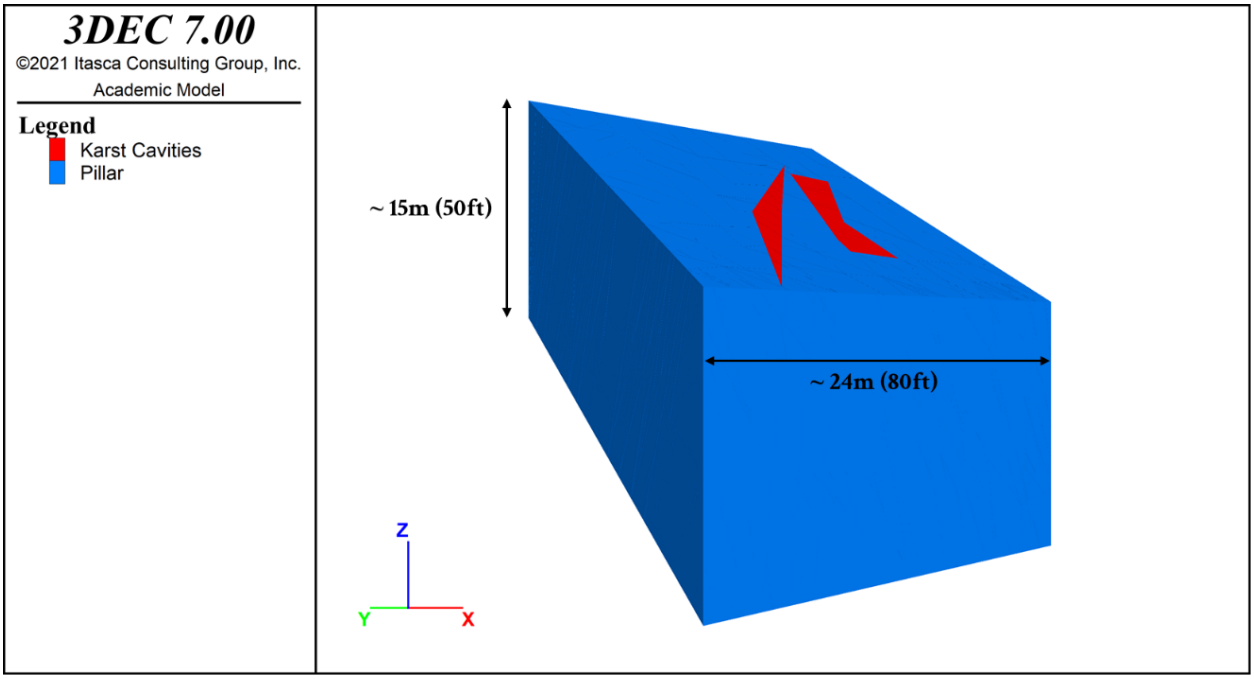

Figure 4.4 50 ft tall, inclined pillar model with karst cavities.

Distinct-element modeling (DEM) was used to simulate the response of the discontinuous rock mass with defined physico-mechanical properties and the Mohr-Coulomb constitutive model. Stresses were imparted on the top and bottom face of the model to replicate compressive action and estimate the ultimate yield strength of the pillar. All parts of Figure 4.5 show the deterioration in different stages of the model simulation along with the stress-strain plot. Figure 4.5(a) shows the initiation of displacement of blocks as the stresses are increased. Since DEM was used, the pillar behavior translates to the movement of discrete blocks along the joints. As the compressive load is built up, an increase in deterioration and excessive spalling are observed.

The pillar yields at about 22 MPa and the stress drops to 18 MPa, but the rock mass shows strain-hardening for a few more timesteps and ultimately fails at about 23 MPa. Figure 4.5(c) shows the state of the pillar and the stress-strain plot at 11 MPa. Interestingly, even when the stress is almost half of the yielding stress, substantial deterioration is observed on the sidewall and rear side of the pillar. The size of the block failing is almost the height of the pillar. The deterioration is occurring even when the pillar is showing no signs of distress or yielding on the whole. If this was a real scenario, no mine operator would want a pillar in such a state as observed in this pilot study. At this point, it would become necessary to take ground control measures to secure the stability of this pillar or redesign the heading so that the pillar is not extended to this height.

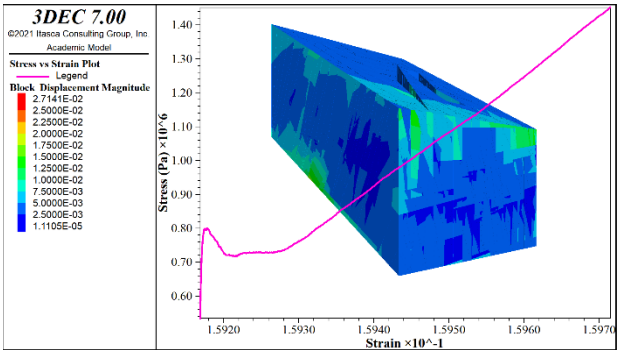

(a). State at 1.4 MPa

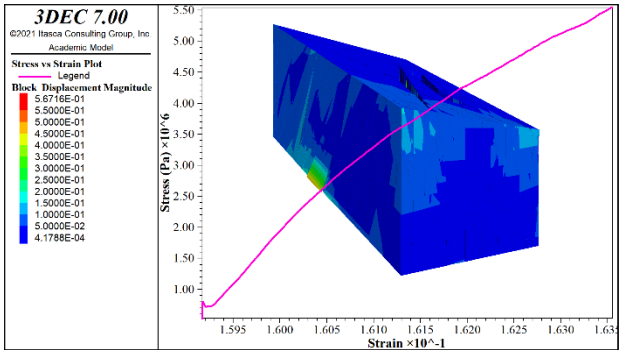

(b). State at 5.5 MPa

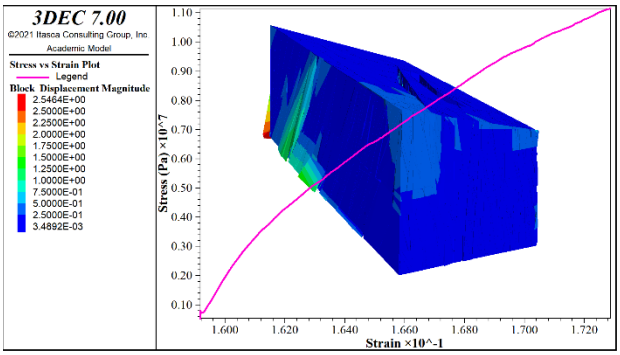

(c). State at 11 MPa

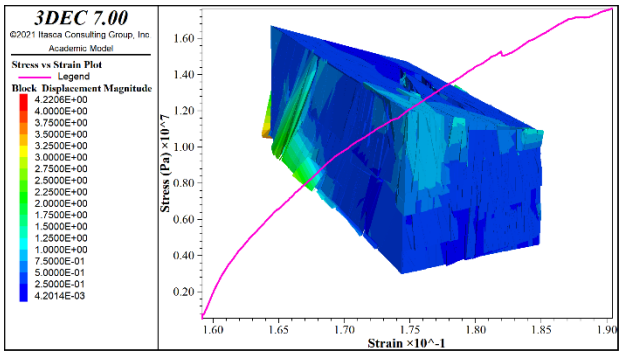

(d). State at 17 MPa

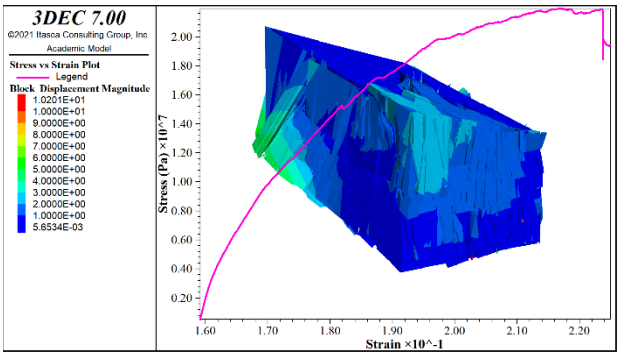

(e). State at 22 MPa

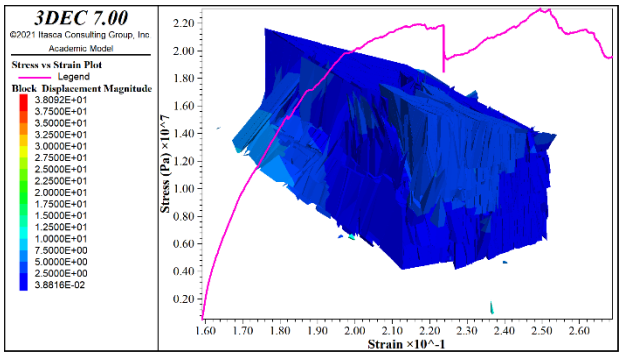

(f). State at 23 MPa

Figure 4.5 Displacement magnitude and axial stress-strain plot at different stages for strength estimation of the 50 ft tall, inclined pillar with karst voids.

4.2.2 Pilot Study 2

This pilot study is a follow-up to confirm and verify the previous pilot study. From the pillar failure study of the 50 ft tall, inclined pillar, it was needed to know how much activity is happening in one region compared to the other parts of a pillar. The idea here is to divide the pillar into different zones and analyze each zone while assessing the strength of the overall pillar. Figure 4.6 shows us the schematic of the rectangular rock sample used for this study.

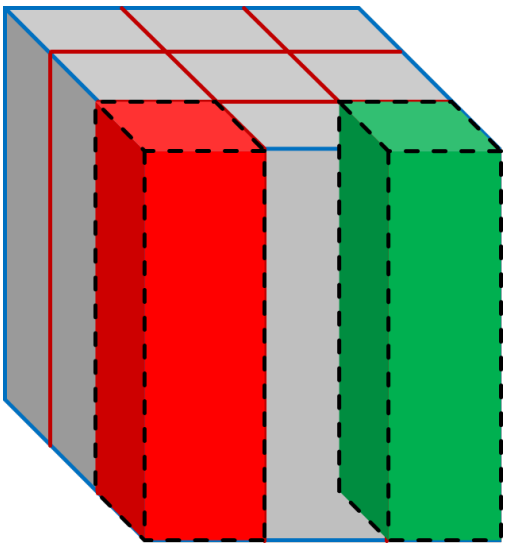

Figure 4.6 Schematic of the rock sample model showing different zones analyzed separately.

A rectangular limestone block model of dimensions 4 m x 4 m x 5 m was used for pilot study 2. A small-scale block model was created to shorten the processing time as well as verify pilot study 1. The model is allocated the same geotechnical properties and simulation conditions that were used in pilot study 1. The model was divided into 9 zones, which being parts of the same model, were analyzed separately for monitoring stress behavior. The overall pillar behavior was analyzed separately in these nine zones. Figure 4.7 shows the displacement magnitude contour and the stress profiles for each zone labeled separately

with different colors. To avoid any confusion between visualizing multiple stress profiles, the stress profile of the complete pillar is plotted on the positive Y-axis, and those of the compartmentalized zones or plotted on the negative Y-axis. When the different stress profiles are observed, it becomes clear that separate zones behave differently when compared to the overall pillar.

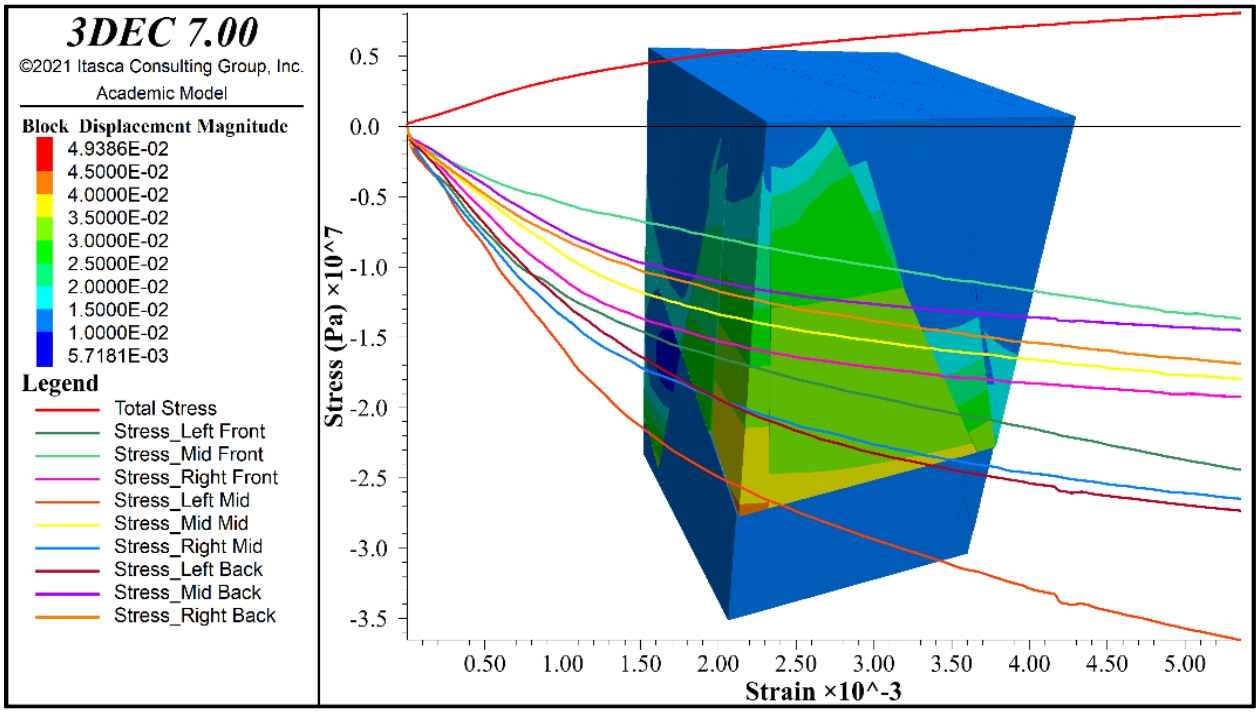

Figure 4.7 Displacement magnitude and axial stress-strain plots for nine separate zones and complete pillar.

4.2.3 Pilot Study Conclusions

From the pilot studies demonstrated above, it may be concluded that pillars react differently under varying stress conditions. Their behavior also depends on how the discontinuity network, or any cavities, interacts with stresses. For this reason, it becomes crucial to detect the effect of increasing stresses in the different zones of a pillar. This would not only help

to assess the pillar design during the advance period but also make decisions for redesigning pillars in case any secondary recovery is planned in the future. An important aspect of this study is to map the discontinuities in the pillar rock mass. The use of traditional geological mapping techniques and visual observation was not feasible around tall pillars in the case study mine. Also, from a safety point of view, it might be unsafe to do manual mapping around tall pillars, especially those prone to karst-based failures. For this purpose, an advantage of drone and terrestrial LiDAR surveys was taken for different settings, not only to map the pillow geometries but also to capture the joint network, on and around the pillars.

4.3 Drone & Terrestrial LiDAR Surveys

Two pillars were considered for this study, a regular conventional sized pillar, and an unusually shaped pillar with karst volumes. It was important to consider these pillars to compare the effect of karst on pillar design and understand pillar zoning considerations. Figure 4.8 shows the locations of the pillar in the mine layout. The pillars are located on the same mining level in the limestone mine. The pillar with karst cavities is named Pillar-A, and the regular full-sized pillar will be addressed as Pillar-B throughout this chapter.

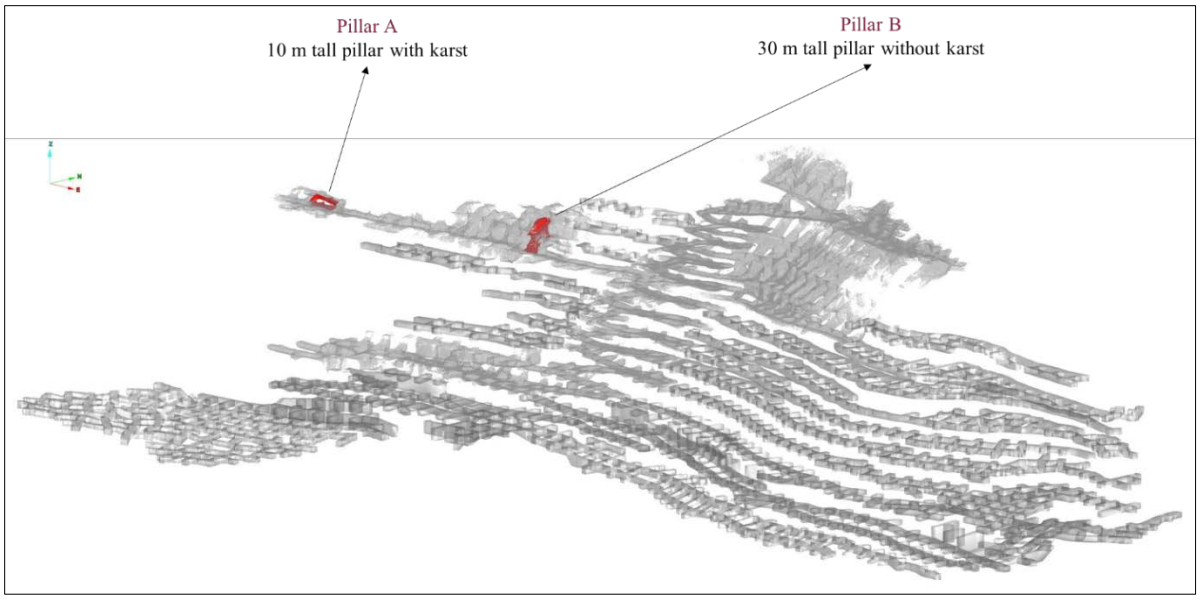

Figure 4.8 Relative location of the pillars in the same mine level chosen for this study [16].

For terrestrial laser surveys, a tripod-mounted FARO Focus 3D laser scanner was used. A custom-built DJI-M210 drone equipped with a compact Velodyne's Puck LiDAR scanner was used for the drone LiDAR surveys. Separate photogrammetry surveys were also conducted for both pillars. Photogrammetric surveys have helped gather useful information in terms of better visualization and help distinguish the karst cavities from regular deterioration in the pillars. The surveys for this study were conducted by a team of engineers from Exyn Technologies and Virginia Tech students including Richard Bishop and Alex Scheck [16].

Figures 4.9 and 4.10 show the project team conducting surveys around Pillar-A and Pillar-B, respectively. The photogrammetric surveys required special provisions for mounting LED lights to illuminate the survey sections. The flights were fully autonomous with a pre-defined surveillance region around the pillars.

Figure 4.9 Photogrammetric survey around Pillar A [16].

Figure 4.10 LiDAR and Photogrammetric surveys around Pillar B. The picture on the left shows the drone able to map inaccessible heights around the pillar [16].

4.3.1 Pillar-A

Pillar-A was mapped using terrestrial LiDAR surveys. Like most of the pillars in the case study mine, Pillar-A has karst voids pervading the rock mass. The pillar is 10 m (33 ft) in height and roughly 56 m (184 ft) along its length or longest dimension. The pillar has a variable width ranging from 13 m (43 ft) to 22 m (72 ft) at its widest dimension. Figure 4.11 shows the photogrammetry model of the pillar with the three prominent karst cavities.

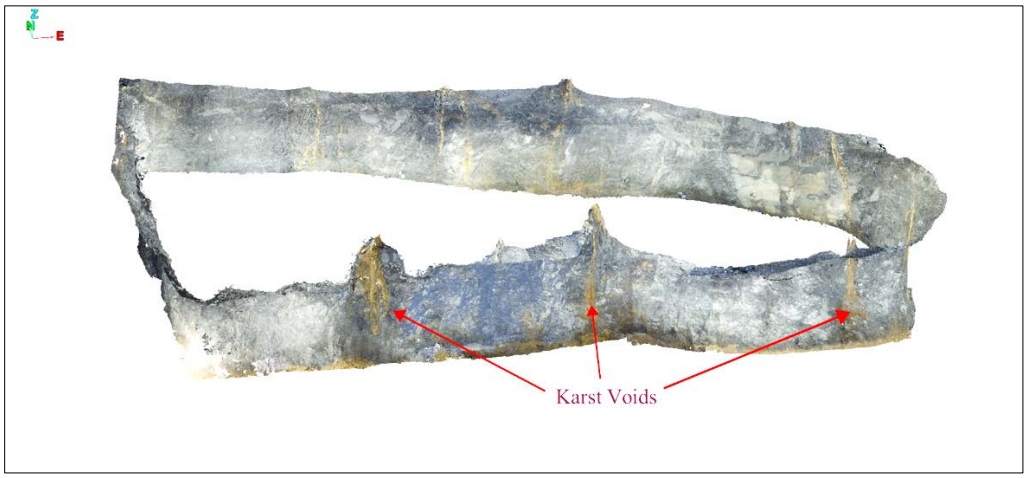

Figure 4.11 Photogrammetric model of Pillar-A with karst voids (Modified after [16]).

The smaller height of the pillar compared to the planned height of 30.5 m, was kept due to the presence of cavities. The mine management suspected instigation of ground failure issues, similar to the earlier pillars they have experienced in the past [129]. Figure 4.12 shows that the three karst cavities run across the pillar almost dividing it into four sections.

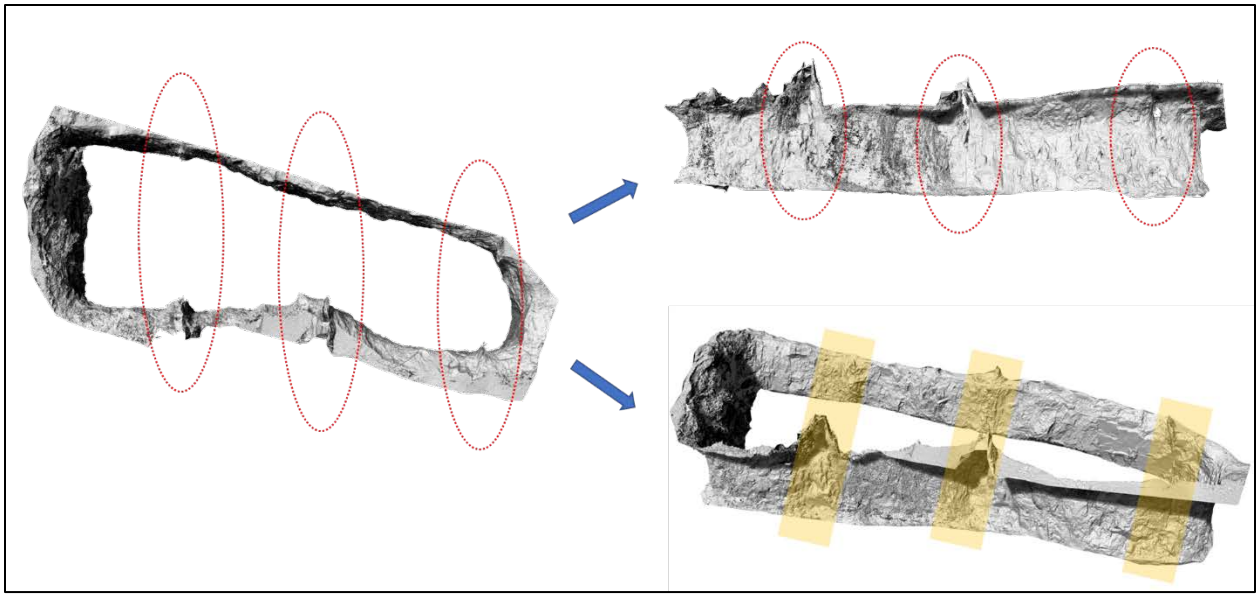

Figure 4.12 Positions of karsts inside Pillar-A.

4.3.2 Pillar-B

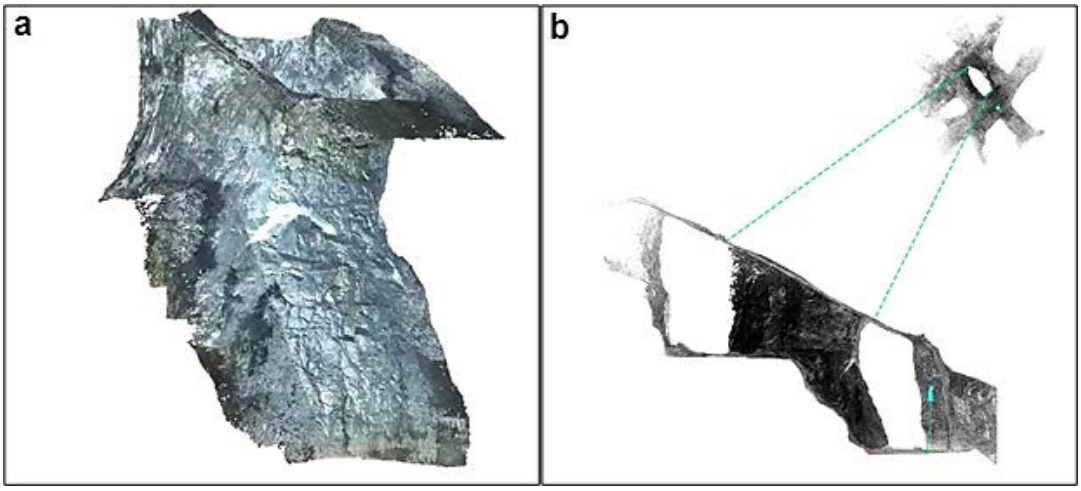

Figure 4.13 (a) Photogrammetric model of Pillar-B; (b) Area of survey around Pillar-B [16].

Pillar-B is a regulation-size pillar in the case study mine and was mapped using drone-based LiDAR surveys. The pillar is 30 m (100 ft) high and has a length of 32 m (106 ft) and a width of about 15 m (50 ft). The excavations in a typical mine are never perfect due to

the variability of rock, and similarly, this pillar does not have perfect planned dimensions. Also, pillar scaling was done to remove unstable rock blocks.

4.3.3 Manual-Virtual Discontinuity Mapping

One of the most important aspects of this study is to extract the discontinuity distribution data from the obtained laser scans of the pillars. Figures 4.14 and 4.15 show the LiDAR point clouds for Pillar-A and Pillar-B, respectively. Maptek PointStudio was used to process the point clouds and filter any irregularities in the data [94]. It should be noted that laser scan data from the terrestrial LiDAR scans were used to supplement the point cloud data of Pillar-B. This was done to utilize extra point cloud data for minimizing any general error caused by occlusion and enhance the coverage data for mapping.

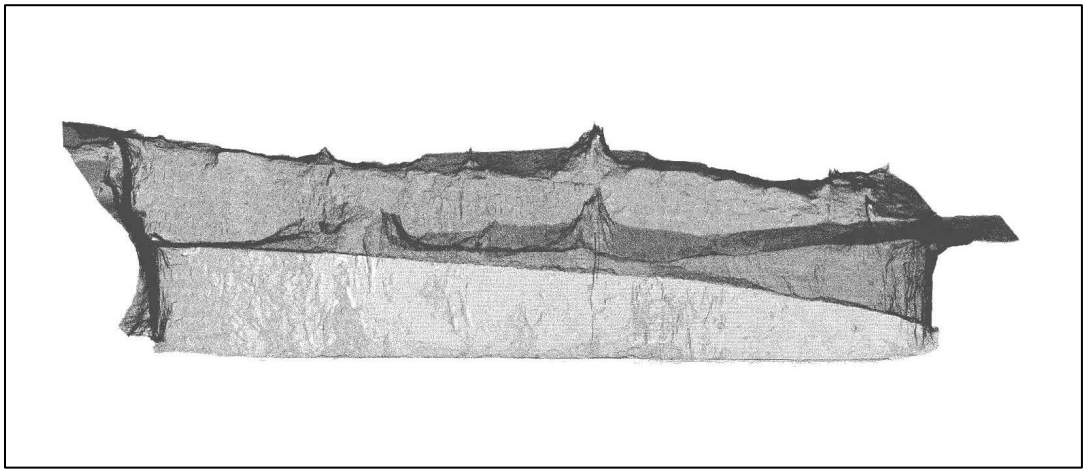

Figure 4.14 LiDAR point cloud of Pillar-A [16].

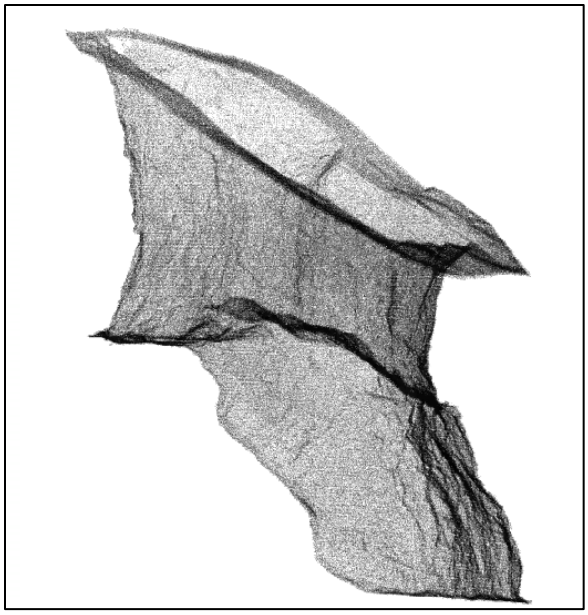

Figure 4.15 LiDAR point cloud of Pillar-B [16].

Discontinuities such as joints, fractures, and bedding planes play a vital role in determining the strength and behavior of the rock mass. It is important to identify the different joint sets and their orientation, fracture density, and size distribution to predict the placement of joints inside the pillar's rock mass. For this purpose, manual-virtual discontinuity mapping was performed for the obtained point clouds. The process involves the manual selection of joint planes using virtual scans rather than using traditional techniques of mapping them in the field. This mapping technique, completed in Maptek PointStudio, allows the users to filter out any irregularities and accurately estimate the joint plane orientation and size. Commercial software such as Maptek PointStudio and Discontinuity Set Extractor (DSE) allow users to choose an automated function for extracting all the joints, but the automated mapping software includes excessive amounts of smaller fractures and creates confusion for determining trace length and spacing of the joints [107]. Figures 4.16 and 4.17 show the structural mapping performed for Pillar-A and Pillar-B, respectively.

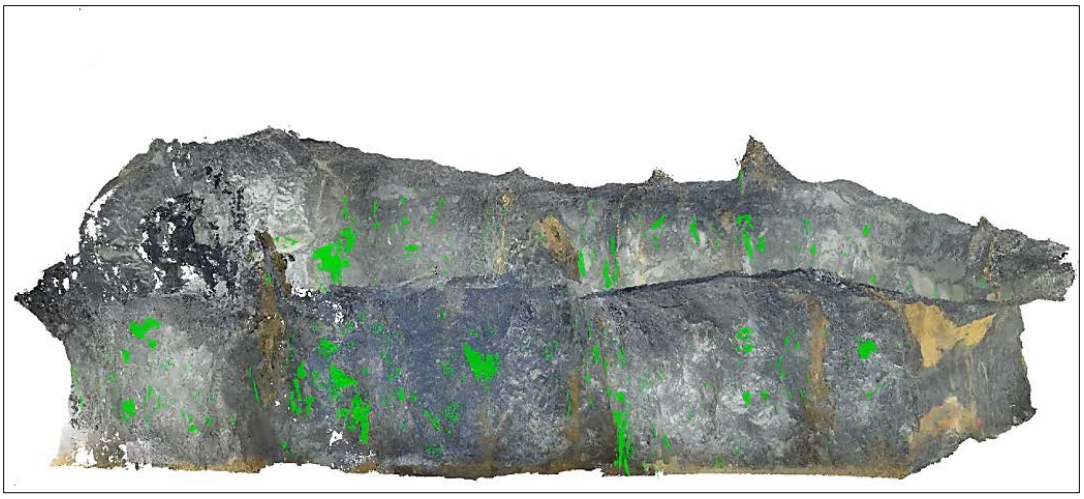

Figure 4.16 Mapped discontinuities for Pillar-A.

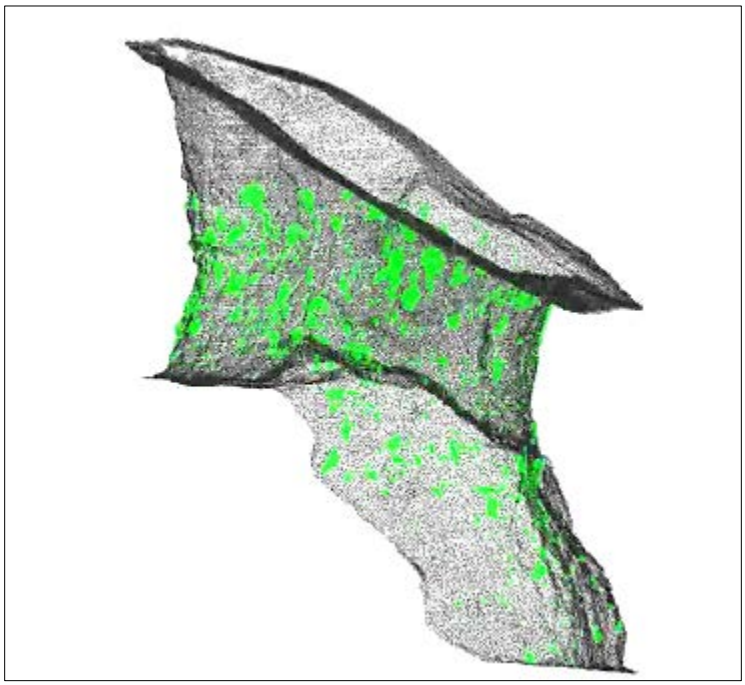

Figure 4.17 Mapped discontinuities for Pillar-B.

A total of four joint sets were estimated for both pillars. The dip and dip direction information were exported to Rocscience Dips software, and the stereonets were plotted for all the poles [122]. Zone clusters were defined for the poles to estimate the average dip and

dip direction for all the joint sets. Figures 4.18 and 4.19 show the stereonets for the mapped discontinuities around Pillar-A and Pillar-B, respectively.

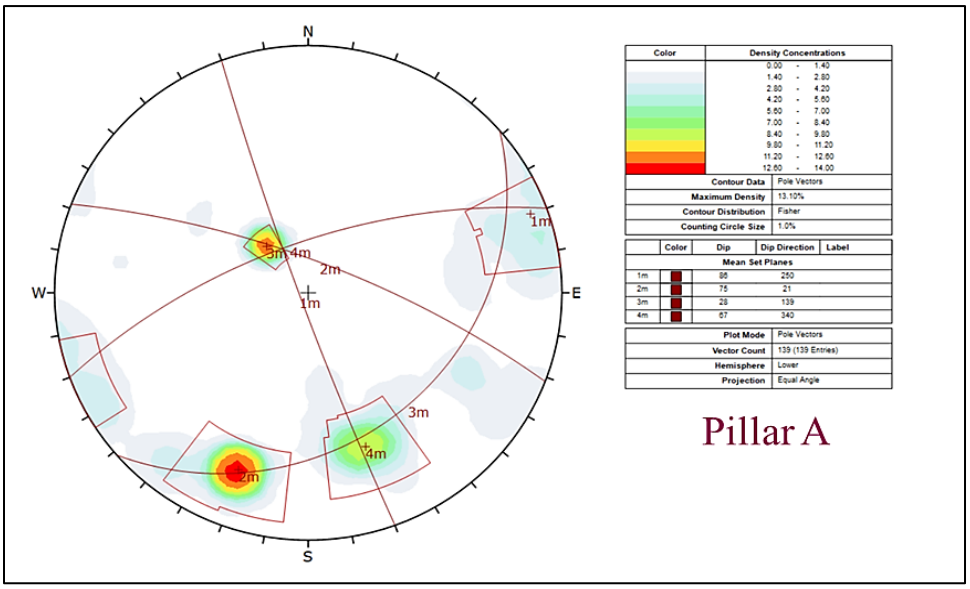

Figure 4.18 Stereonet for the mapped discontinuities (n=139) around Pillar-A.

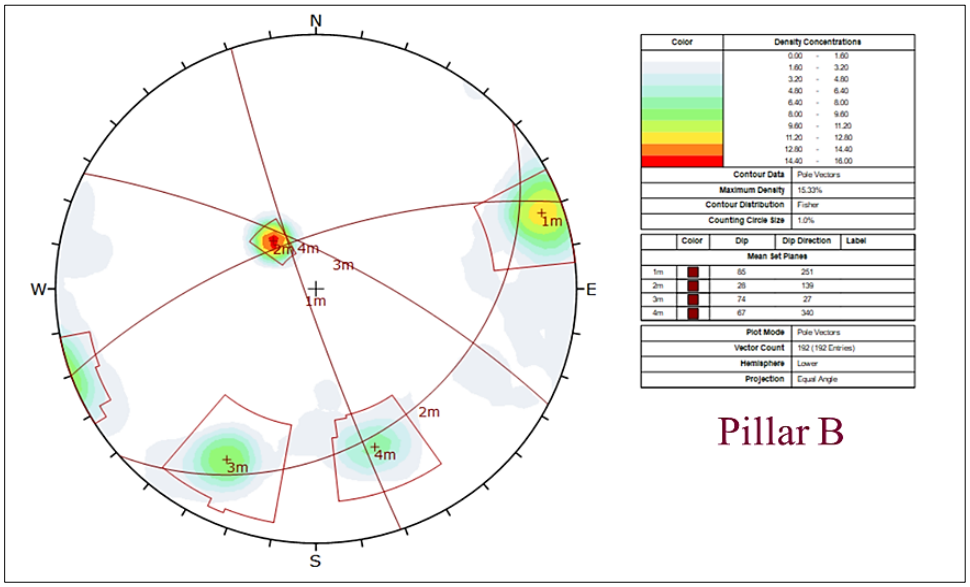

Figure 4.19 Stereonet for the mapped discontinuities (n=192) around Pillar-B.

It can be observed from the above figures that both the stereonets display similar joint sets. This was expected since both the pillars are located at the same mining level and any drastic changes in rock or joint properties are unlikely. Table 4.1 provides the statistical information for the joint orientation size and fracture density for all the joint sets for this study. This information will be later used to create a discrete fracture network (DFN) which simulates a stochastic representation of the joint distribution inside the pillar based on the mapped discontinuities. More details about implementing DFNs our explained later in the chapter.

Table 4.1 Statistical information for the mapped joint sets for Pillar-A and Pillar-B.

	JOINT SETS		**Set 1**	**Set 2**	**Set 3**	**Set 4**
Pillar A	Orientation	Dip [°]	86	67	75	28
		Dip Direction [°]	250	340	28	139
		K (Fisher Distribution)	57.5	220.8	105.9	107.6
	Size	Distribution	Log-normal	Log-normal	Log-normal	Log-normal
		Mean	1.251	1.019	1.410	1.306
		Standard deviation	0.664	0.599	0.470	0.981
	Density	P_{32} (Joint area/volume)	0.039	0.088	0.171	0.200
Pillar B	Orientation	Dip [°]	85	67	74	28
		Dip Direction [°]	251	340	27	139
		K (Fisher Distribution)	121.3	108.9	140.6	111.9
	Size	Distribution	Log-normal	Log-normal	Log-normal	Log-normal
		Mean	0.951	0.994	1.674	1.117
		Standard deviation	0.821	0.692	0.563	0.791
	Density	P_{32} (Joint area/volume)	0.041	0.101	0.211	0.251

4.4 Model Generation in 3DEC

3DEC software by Itasca Consulting Group allows observing the nonlinear response of rock application of load in different scenarios [64]. the software allows for the limestone to be represented as the structure of blocky rock mass joined by various discontinuities. Mohr-Coulomb Constitutive model was used to replicate the behavior of the rock mass. Also, the Coulomb-slip joint constitutive model was used to simulate the DFN.

4.4.1 Model Geometry

Using the surveys in the underground mine, the model geometry was recreated for the pillars using Rhinoceros-3D software [119]. These models, which were supposed to be numerically simulated, were simplified to remove sharp undulations from the surface. This process does not affect the results and also removes any computational complications during numerical modeling. Figures 4.20 and 4.21 show the final pillar models that were imported in 3DEC for numerical simulations. For Pillar-A, the size of the karst cavities is overestimated and assumed to be extended throughout the pillar at their widest dimensions. Any pinching or expansion inside the pillar volume is not considered. This results in a worst-case scenario for the pillar concerning the karsts.

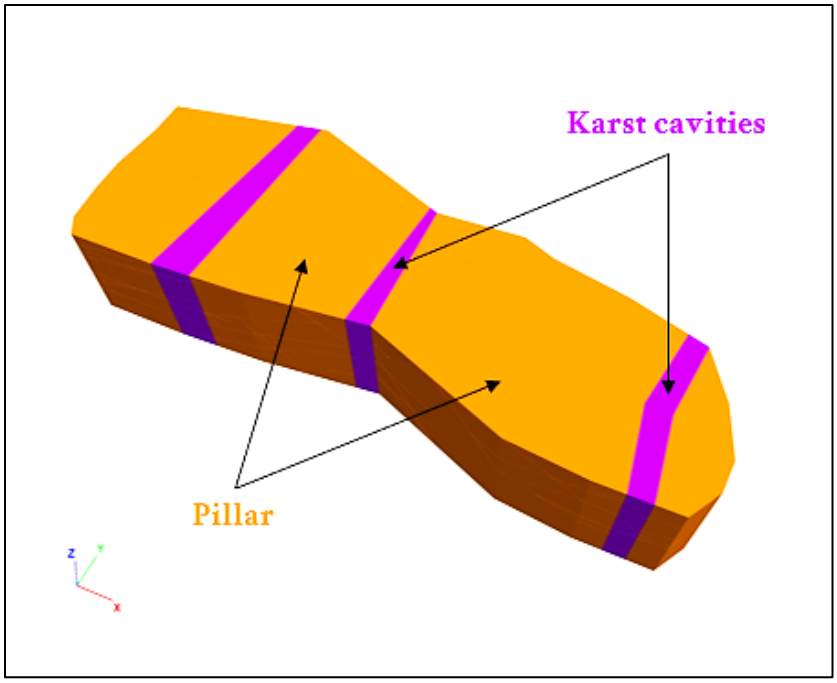

Figure 4.20 3DEC pillar model of Pillar-A with karst cavities.

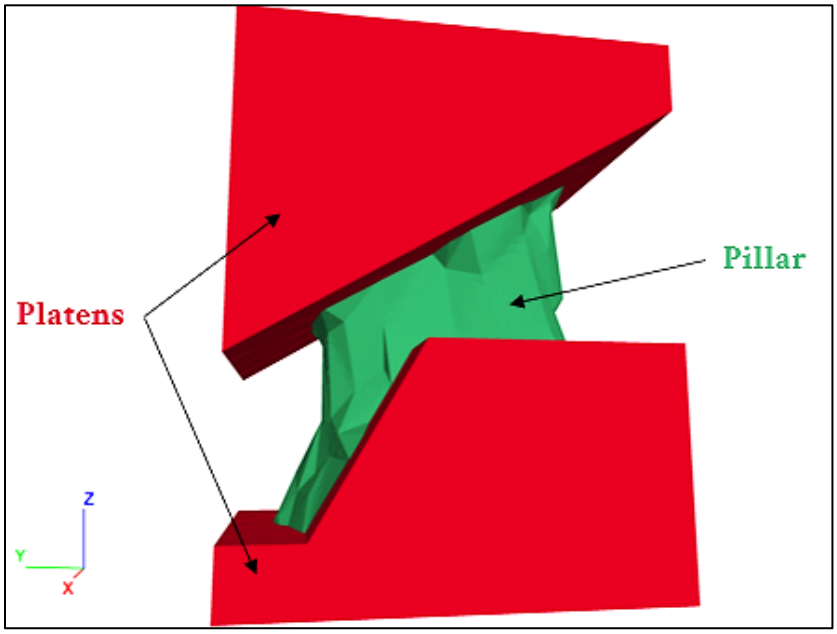

Figure 4.21 3DEC pillar model of Pillar-B with top and bottom platens.

4.4.2 Discrete Fracture Networks (DFNs)

In the case study mine, discontinuities embedded in the limestone rock mass play a huge role in deciding their behavior in varying stress conditions. Joints and fractures determine the rock mass strength along with the intact rock properties. since one cannot determine the distribution of joints inside the rock mass, the best possible way to recreate them is using discrete fracture networks (DFNs). In 3DEC, DFNs can be created by using the statistical information of joint size (trace length, size) and orientation (dip, dip direction) as provided in Table 4.1. As the determined values or input in the software code, 3DEC creates a stochastic network that best represents the real-life joint distribution. One of the cardinal parameters for deciding the spread of a DFN is fracture density. Fracture density is a measure of the spatial frequency of joints in a set and serves as a threshold condition for generating a DFN [22]. In this study, P_{32}, also defined as the area of fractures per unit volume of rock mass, was used to define the fracture density. The values of P_{32} are also provided in Table 4.1. Figure 4.22 shows how combinations of different joint networks constitute DFN simulating the real-life discontinuity network. Figure 4.23 shows the blocky nature of the stone pillar models after being cut by the DFNs.

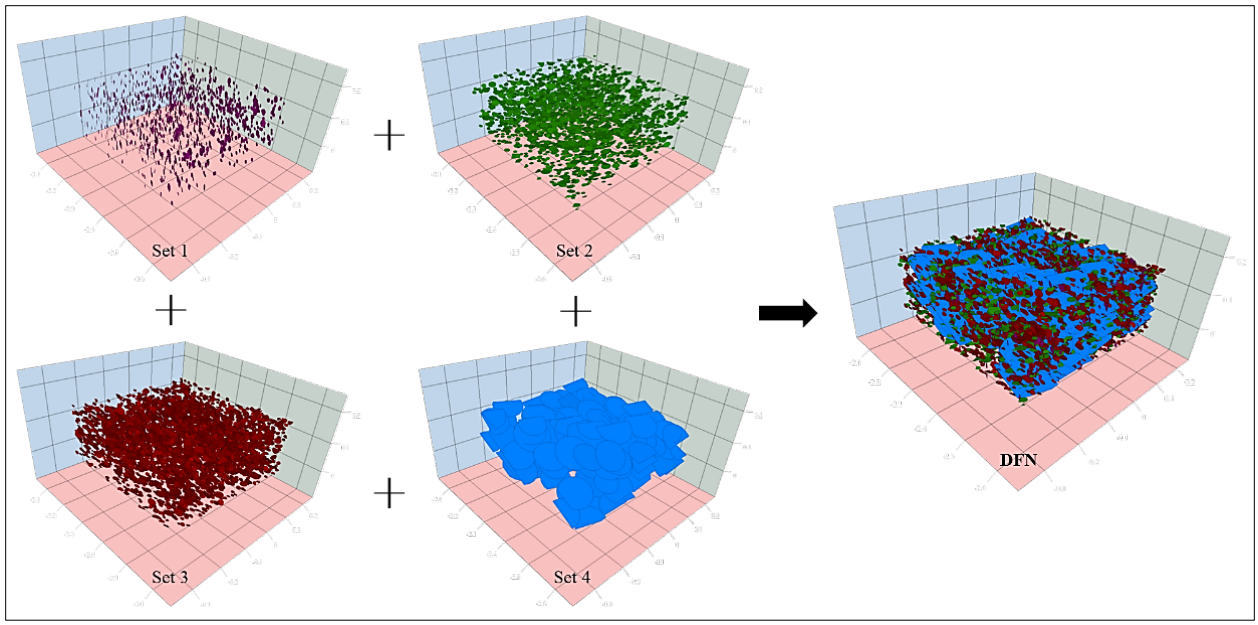

Figure 4.22 Combinations of different joint networks constitute a DFN in 3DEC [131].

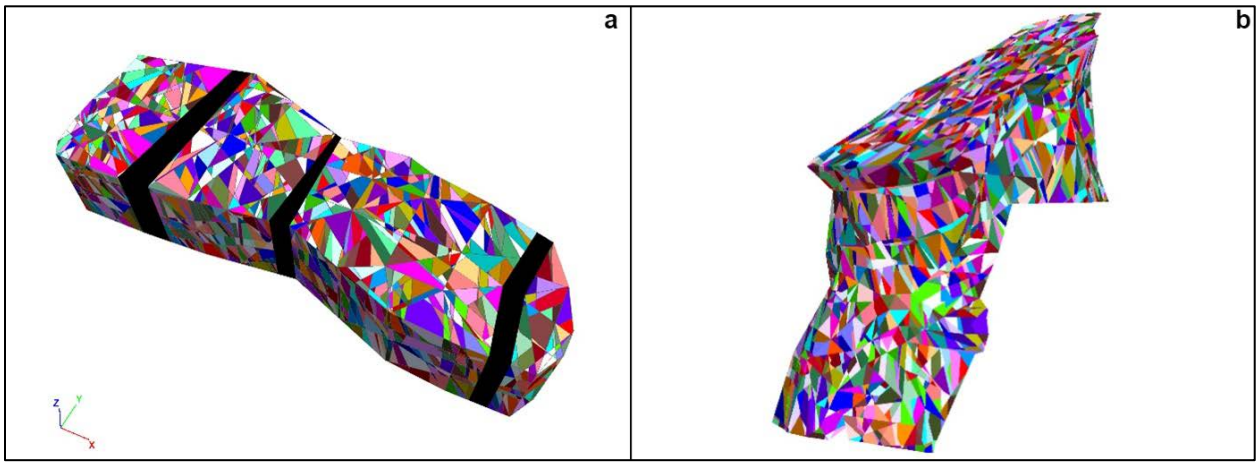

Figure 4.23 Final models for (a) Pillar-A and (b) Pillar-B, after being cut by the DFNs.

4.4.3 Initial Conditions and Geotechnical Properties

Based on the numerical modeling study performed in Section 3.3, the existing stresses were determined at each mining level of the case study mine. It was estimated that the current

stresses in the level of Pillar-A and Pillar-B range between 7-10 MPa. The same stress conditions were initialized in the pillar models before the progression of compressive load. Intact rock properties were measured for the limestone rock samples using borehole measurements and laboratory testing. Table 4.2 lists the physico-mechanical properties of intact rock and joints.

Table 4.2 Geotechnical properties of intact rock and joints.

Intact Rock Properties	
Density, ρ	2690 kg/m^3
Young's Modulus, E	52.25 GPa
Bulk Modulus, K	37.86 GPa
Shear Modulus, G	20.57 GPa
Poisson's Ratio, μ	0.27
Cohesion, c	12.53 MPa
Friction Angle, ϕ	36.73
Dilation Angle, ψ	24.5
Tensile Strength, τ	2.69 MPa
Joint Properties	
Joint Normal Stiffness	300 GPa
Joint Shear Stiffness	30 GPa
Joint Friction Angle	30^o
Joint Cohesion	0.0

In absence of the joint testing and stiffness measurements, values for essential properties were obtained using the research work performed by Bandis et al. [8] on similar types of limestone samples. Dry tight joints were considered with no infill. As measured in the field, the joint condition is considered slightly rough and the joint aperture data was not available. The karst cavities in pillar a were not assigned any properties as the material in there was

assumed to be a cohesionless mixture of clay, groundwater, and small rock fragments. During the numerical simulation, these zones were declared null zones.

4.4.4 Boundary Conditions

Axial compressive stresses were applied on the top and bottom faces of the pillar models. This was done by applying a constant velocity boundary in the vertical directions at the top and bottom faces at the rate of 5 micrometers per timestep. The pillars were compressed until ultimate yielding or failure was observed. The boundary conditions on the sides were kept free because of the presence of the unconfined sidewalls. However, the horizontal movement was restricted on the top and bottom faces by preventing any movement in the lateral directions barring axial movement. Figures 4.24(a) and 4.24(b) show how compressive velocity boundaries were applied to the pillar models. Pillar-B was confined using non-deformable rigid blocks like platens on the top and bottom because of the presence of non-planar faces. This is done to ensure a constant application of load with the time steps. Boundaries were fixed on the contact planes between Pillar B and its platens such that the shear movement is restricted along the contact planes. Platens were not needed for Pillar-A since it already has top and bottom planar faces.

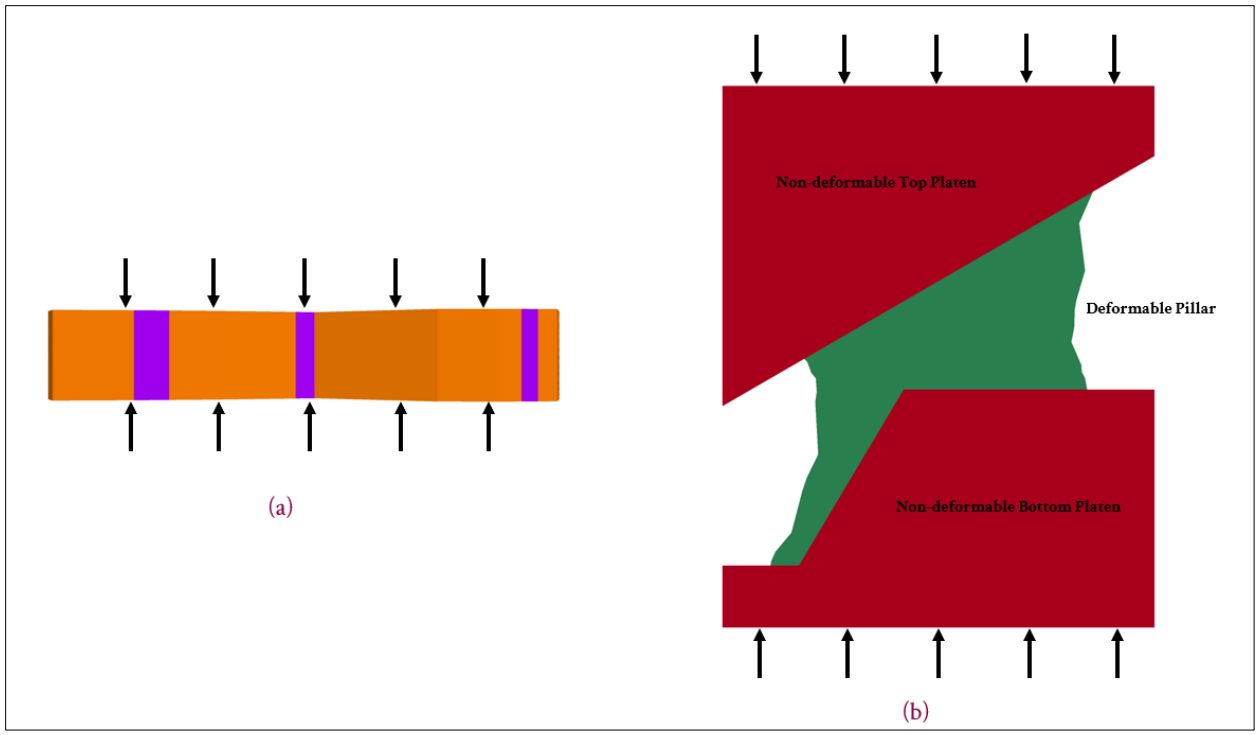

Figure 4.24 Application of axial compressive velocities to the pillar models.

4.5 Results

Each numerical modeling scenario was simulated till the yielding state of the pillar models was observed using the stress-strain plot for the Mohr-Coulomb constitutive model. The results for both the pillars are as follows:

4.5.1 Pillar-A Results

Pillar-A was compartmentalized into four zones based on where the karst cavities are running across the pillar width and splitting it. Figure 4.25 displays the four sub-divisions in different colors.

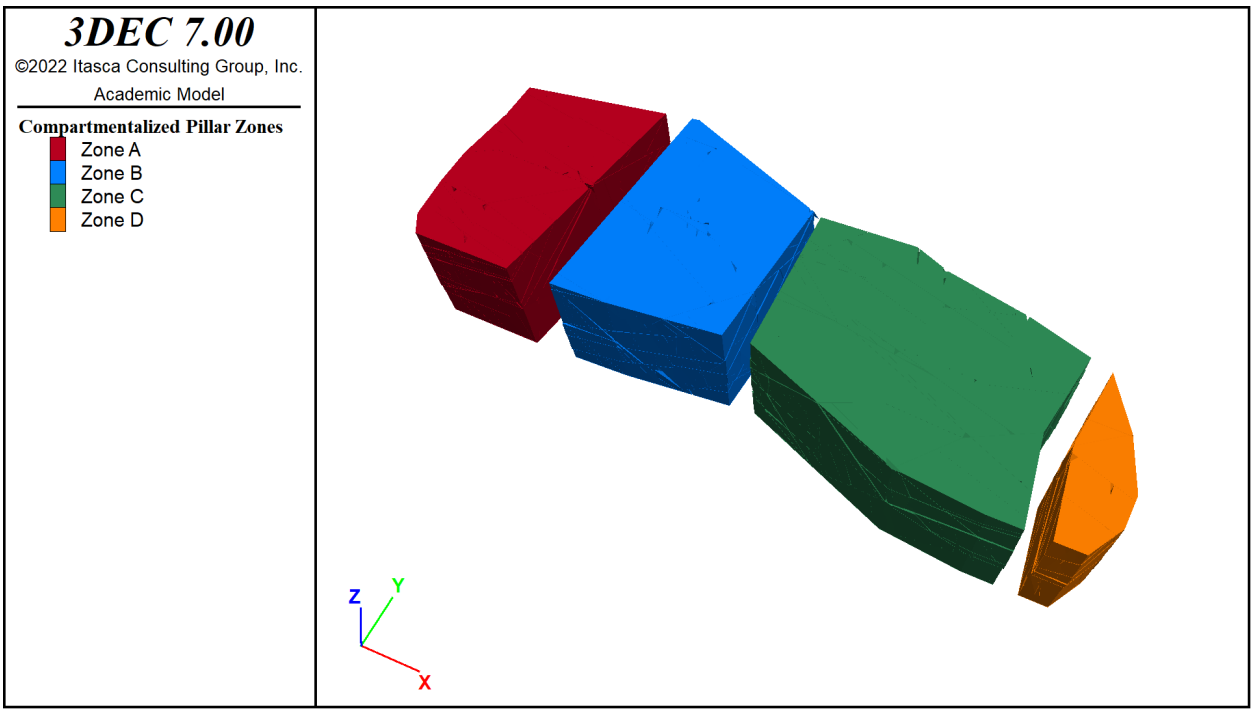

Figure 4.25 Pillar-A model is compartmentalized into four zones.

Since the pillar has planar top and bottom faces, the application of compressive velocity was simple when compared to Pillar-B. The stress-strain plots for all the zones along with the complete pillar are provided in Figure 4.26. As the load is gradually increased, it is observed that Zone-D displays an early failure at 9 MPa. Zone-D is the smallest zone amongst the four zones and has the least confinement of all. The total pillar yielding is observed at 58 MPa. Zone-A fails at around the same time as the total pillar failure. Zone-B and Zone-C display higher strength compared to the other zones and yield at 69 MPa and 78MPa, respectively. The primary reason behind this is expected to be higher confinement for both these zones on either side by Zone-A and Zone-D. The simulation cycle is stopped when the total pillar stress line plateaus. It is assumed that there is no further need to simulate the sub-divided zones once the complete pillar has yielded.

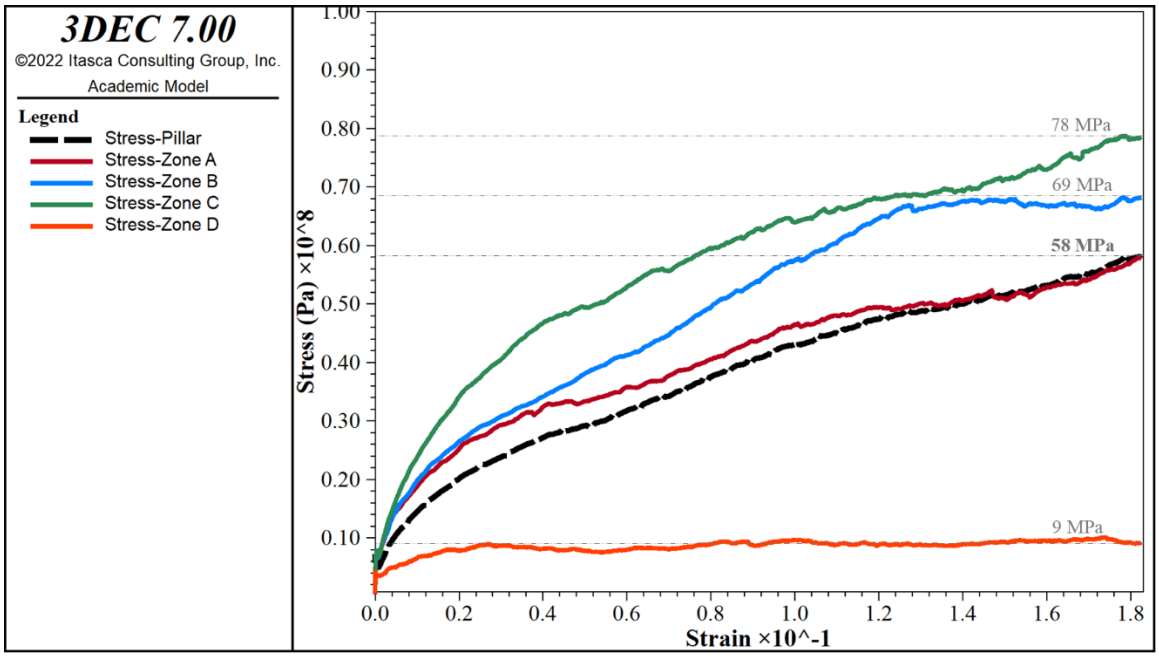

Figure 4.26 Axial stress vs. strain plots for Pillar-A and sub-divided four zones.

Figure 4.27 shows the deterioration of Pillar-A along with the stress-strain plot. The process of pillar failure and the deterioration and strength of its zones shows the behavior of the rock mass with increasing stress. Upon observing the complete pillar and the concerned zones, the areas for further improving the design of the pillar can be figured out. The mine management did not perform any numerical analysis for deciding the size of the pillar when the karst volumes were encountered while mining. The geologists and engineers went ahead with the decision to leave wider lateral dimensions and shorter height based on the experience of tackling ground control issues in the case study mine. From the axial stress vs strain plot, it becomes clear that Zone D has low strength and is not in a condition to take any further load. Comparing the strength of the pillar (9 MPa) to the existing stresses (7-10 MPa), one can estimate a low factor of safety of less than one. From a safety point of view, this section of the pillar might already be yielded and may prove hazardous in future mining operations. By assessing Pillar-A using this numerical modeling study, it may

be inferred that it is necessary to place ground control measures in effect using secondary support elements. Since the total pillar strength is much higher than the existing stresses, it may have been possible to completely extract Zone-D to reduce the risk of hazards. It is believed that because of the low height of the pillar, it sees a higher degree of damage when a load is applied to it. Despite containing karst volumes, Pillar-A demonstrates a higher strength compared to Pillar-B, primarily because of its wider base and low height.

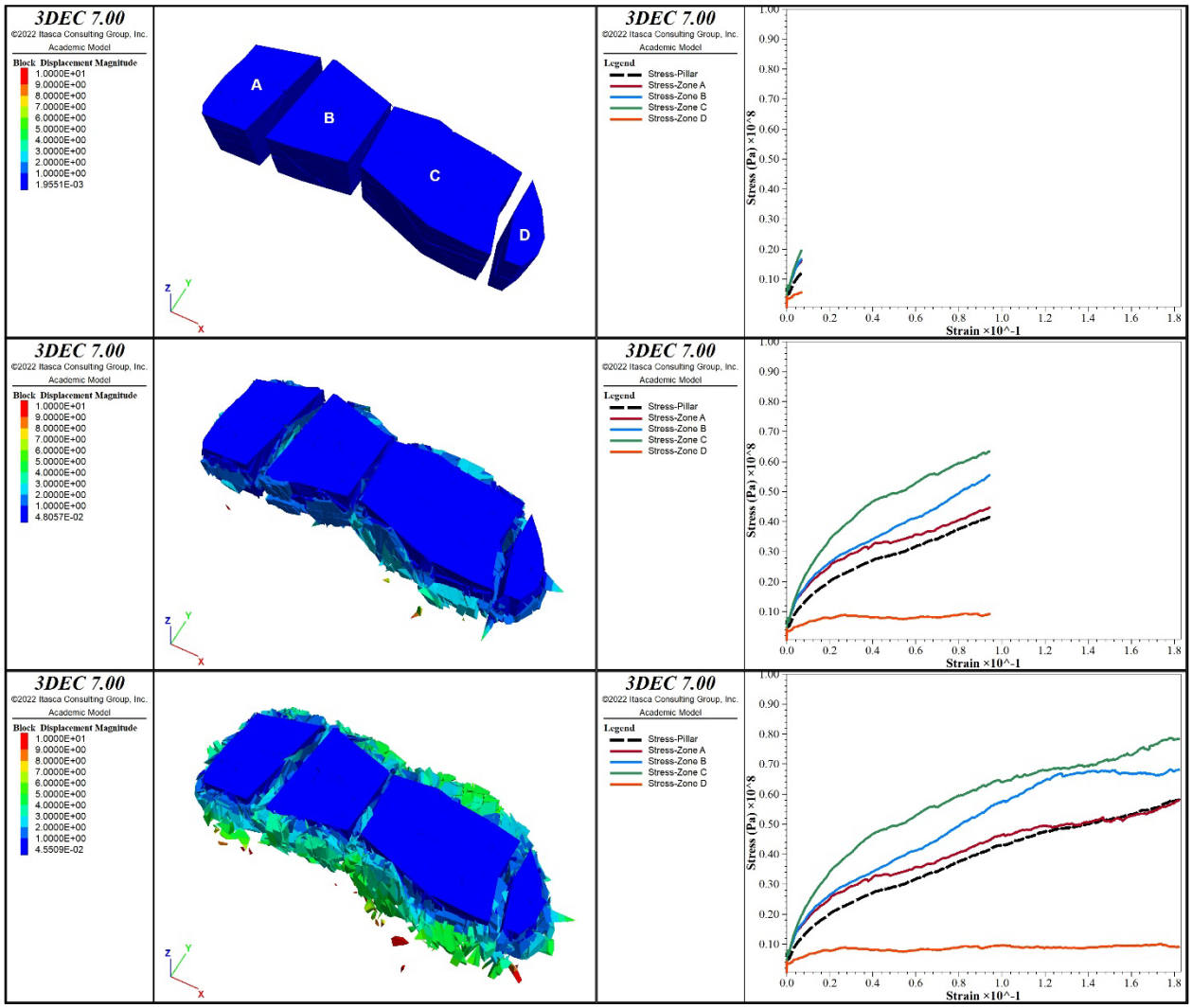

Figure 4.27 Displacement magnitude contour with axial stress-strain plots at different stages for Pillar-A and its zones.

4.5.2 Pillar-B Results

Pillar-B is subdivided into six almost equal zones. As for deciding the number of zones to divide a particular pillar in, it depends on which areas to analyze for stability. A good place to start is to compartmentalize fewer zones in the beginning and start prioritizing the areas showing symptoms of a possible hazardous incident. Also, the zones could be divided based on a possible redesigning of a pillar if any secondary recovery is planned in the future. Figure 4.28 shows the six compartmentalized zones of Pillar-B.

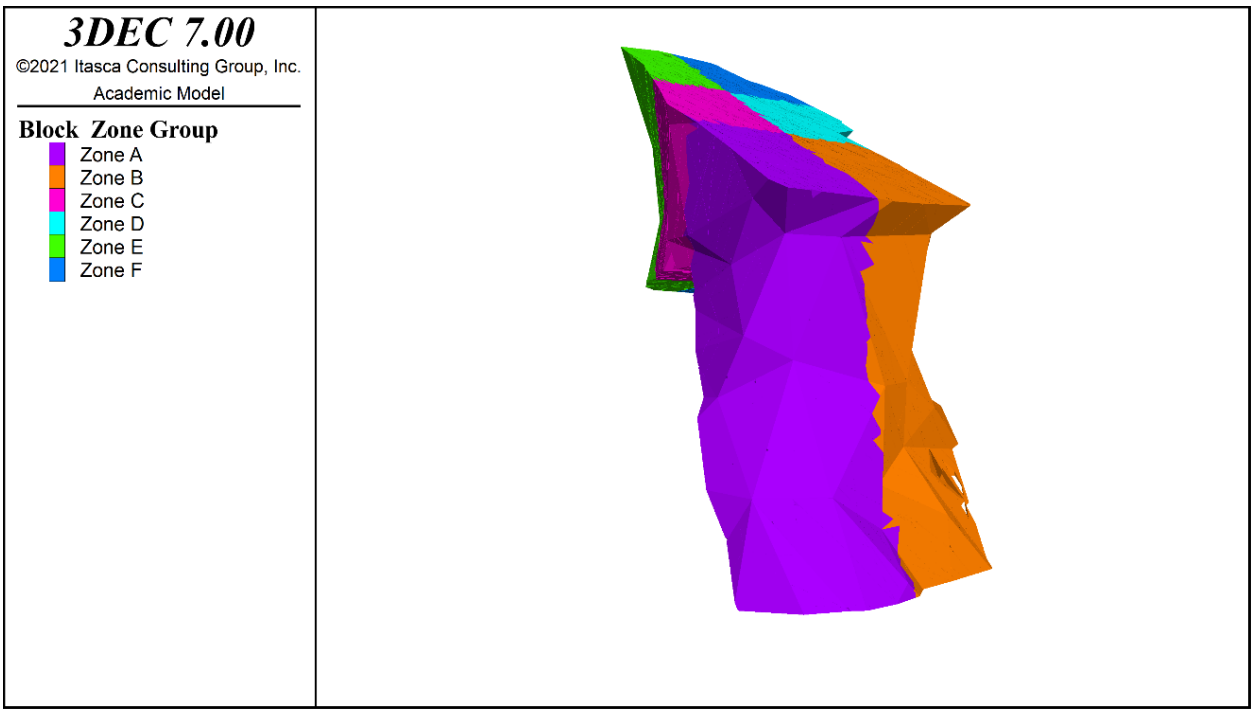

Figure 4.28 Pillar-B model is compartmentalized into six zones.

The stress-strain plots for Pillar-B and its compartmentalized zones are shown in Figure 4.29. The complete pillar yields at 45 MPa with zones A and E failing at the same strength. Zones B and F take a stress level of 49 MPa at the same point. Similar to what was observed for Pillar-A, the zones confined on either side i.e., Zone-C and Zone-D, display a

higher strength. They are projected to counter stresses higher than 88 MPa and 83 MPa, respectively. The simulation was stopped when the total pillar failure was observed.

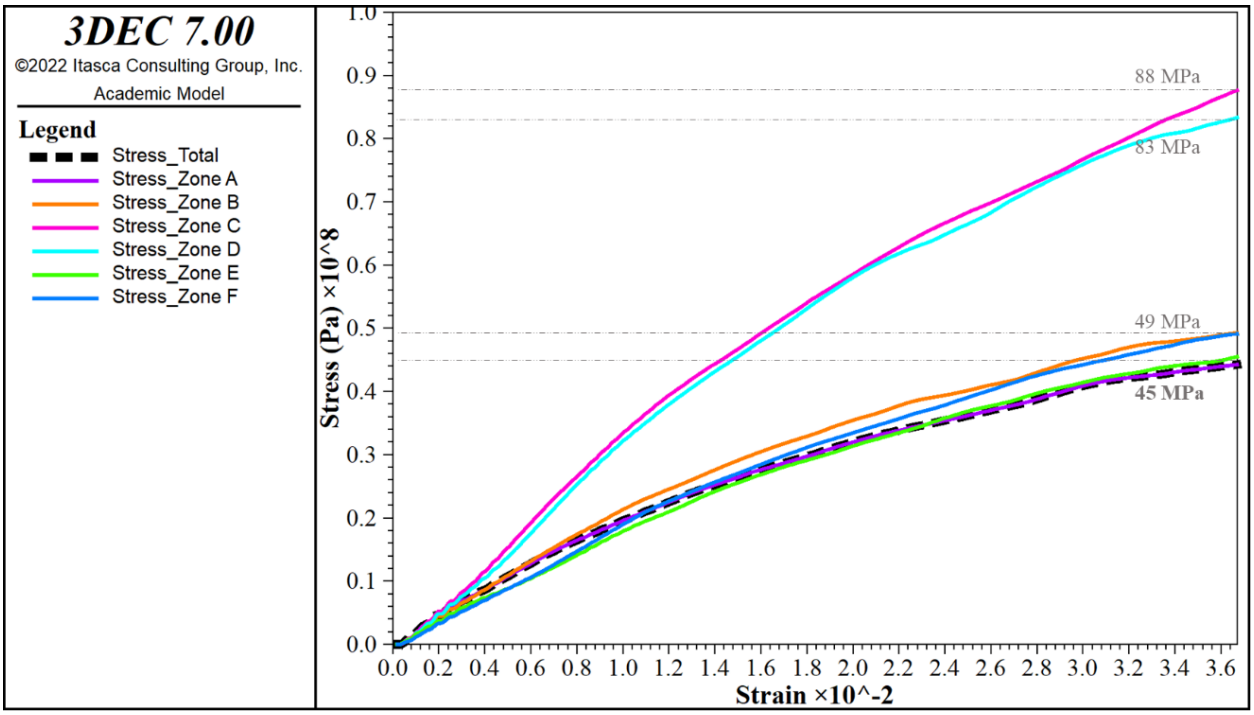

Figure 4.29 Axial stress vs. strain plots for Pillar-B and sub-divided six zones.

From the displacement magnitude contour for Pillar-B as shown in Figure 4.30, it may be concluded that although the scale shows a higher range of displacement, a similar condition is not observable from the contour images. Also, a comparable deterioration, as seen for Pillar-A, is not observed in this case. After much contemplation, it is interpreted that because of a higher volume compared to Pillar-A, Pillar-B has a higher distribution of large blocks. Because of a larger height, Pillar-B can contain a higher strain before showing such significant degradation. It should be noted that a large presence of discontinuities does not necessarily mean that a rock mass will behave as a discontinuum material. When the conditions lead to a high build-up of internal stresses or compressive stresses, rocks may behave in a continuum manner [19]. It is also possible that due to the presence of a high

amount of joint contact planes, Pillar-B behaves as a continuum rock mass compared to Pillar-A. It is understood that because of the wide range of the scale, the displacement contour images of the whole pillar block cannot display a true sense of movement. for this reason, a cross-section taken from the center of the pillar is plotted along with the joint-subcontact failures generated with the increasing load. This is shown in Figure 4.31.

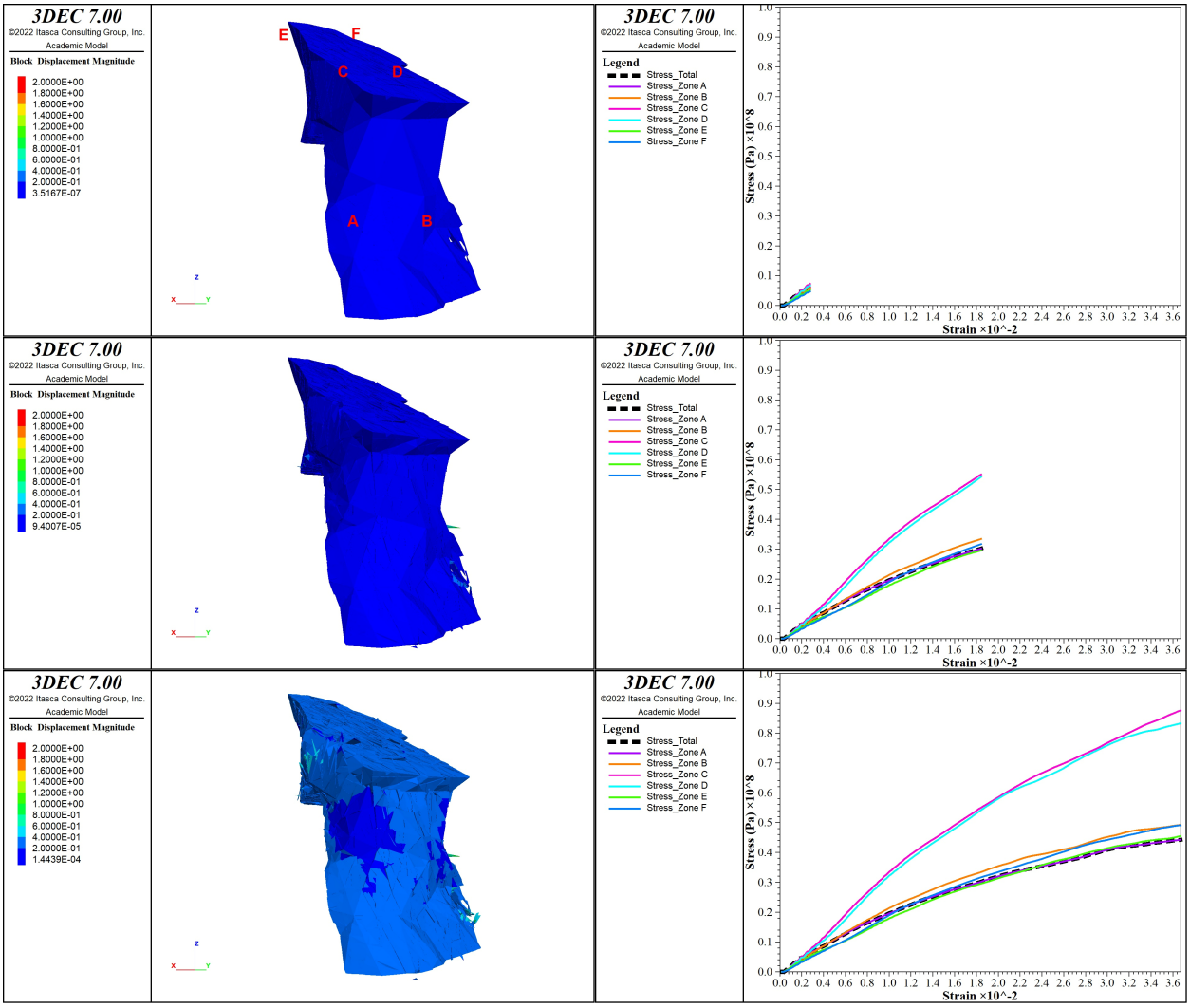

Figure 4.30 Displacement magnitude contour with axial stress-strain plots at different stages for Pillar-B and its zones.

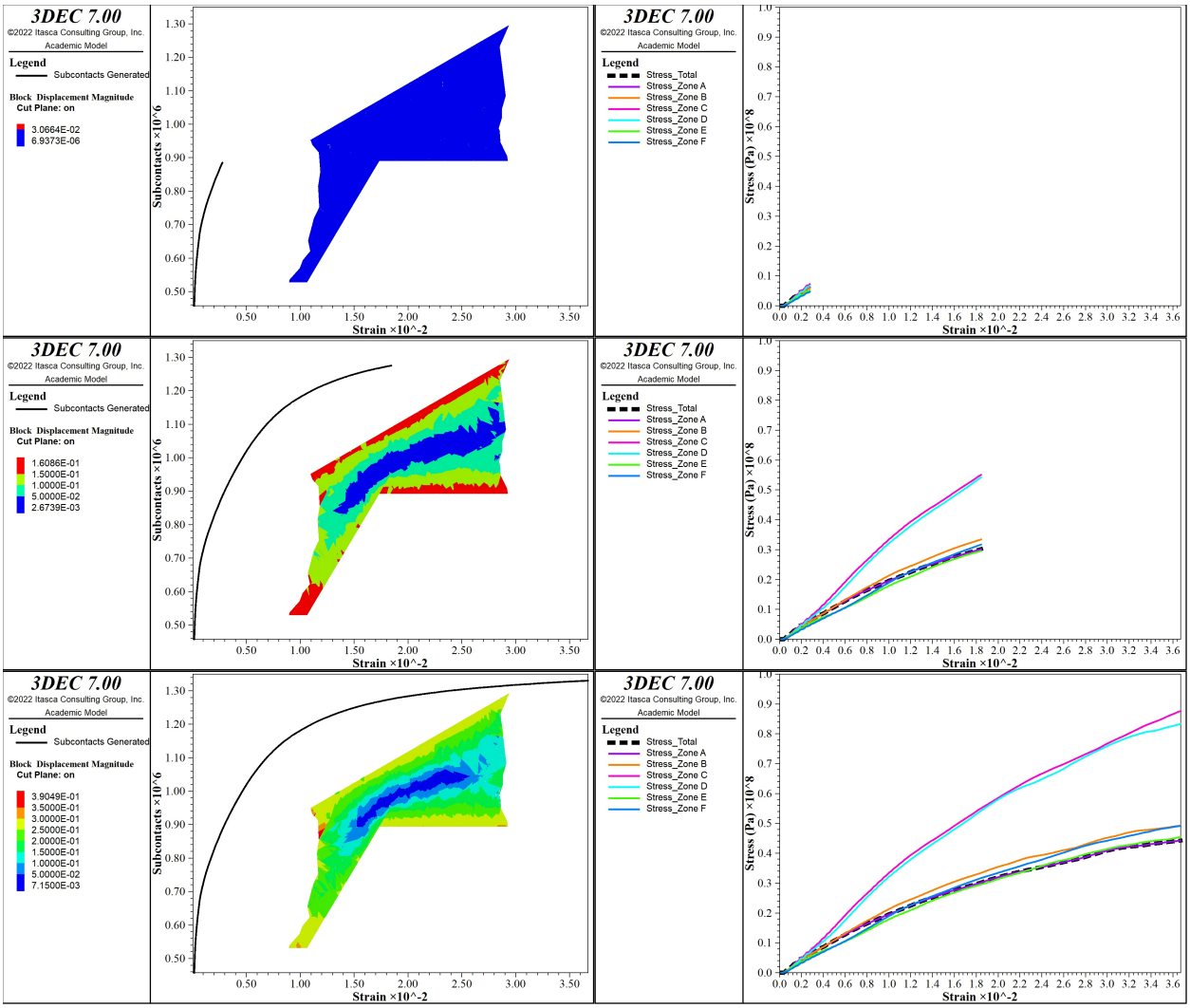

Figure 4.31 Displacement magnitude contour with joint-subcontact failures at different stages for Pillar-B.

Figure 4.31 clearly shows that the displacement in the center of the pillar is varying with increasing load along with the joint-subcontact plot showing the number of fractures generated during the degradation of the pillar at different stages.

4.6 Conclusions

This pillar compartmentalization study is important for stone mines where structural failures dominate the stress-based failures. It helps realize the importance of ground control in the necessary areas of a pillar or even certain roofs. This study also helps realize the important areas or sections of a pillar that a mine operator needs to focus on while redesigning the pillar for secondary recovery or bolstering it to secure the local stability around the pillar. Some of the important conclusions that can be made from the study are:

a) From the pilot studies, it was observed that different sections or zones of a pillar may behave differently with the application of stresses. The different behavior of zones, as well as that of the complete pillar, highly depends on the interaction of discontinuities with the stresses.

b) A combination of terrestrial, drone-based LiDAR survey, and photogrammetry survey proves extremely beneficial for capturing the pillar geometries as well as mapping the discontinuity network along with any karst cavities present in the rock mass.

c) Where the drone LiDAR surveys our most important in collecting the data for manual-virtual discontinuity mapping, the photogrammetry surveys can add useful information for visualization purposes. The only requirement for gathering data using photogrammetry surveys is the presence of ambient artificial lighting systems which are not compulsory for conducting the LiDAR surveys.

d) By compartmentalizing the pillar zones, one may analyze different regions based on the interaction with the stresses and the discontinuity placement in those zones. To decide the number of zones to divide the pillar in, it is important to prioritize the

areas or sections showing concern for potential ground failure. the zones can also be compartmentalized based on a possible secondary recovery in the future.

e) Discrete element modeling is an important tool for simulating the behavior of blocky limestone deposits owing to the presence of a vast network of joints, fractures, and discontinuities. A discrete fracture network can replicate the stochastic distribution of discontinuities pervading the rock mass. Since pillar behavior is largely dependent on the interaction of joints with the stresses, a study should be conducted to monitor changes in the response of different pillar zones with different realizations of DFNs.

f) Drone-based LiDAR surveys are most useful in mapping tall pillars, as they remove the risk associated with conducting traditional surveys using manual elevated work platforms or lifts. Mapping joints or fractures in the unreachable high areas of the pillar is convenient by using a drone-mounted mapping system.

g) Jones [74] speaks highly of the evolving mobile LiDAR technologies for mines and the vast possibilities of their role in underground geomechanics. With the increasing amount of stone mining operations going underground every year, it is important to implement a combination of intelligent surveying systems and numerical modeling for increasing the safety and stability of pillars and large underground stone excavations.

Chapter 5

Parametric Study of the Discrete Fracture Networks and Shear Strength Properties on Hard Rock Pillar Strength for Analyzing Local Stability[4]

5.1 Introduction

Numerous methods have been developed to assess and predict the response of hard rock pillars in underground hard rock mines over the last century. Most of these methods include back analysis by comparing stable and failed pillars in an area in a mine and deriving empirical equations using a sufficient amount of data [55], [88]. A good alternative to using the empirical approach for predicting rock failure mechanics is to use analytical methods which employ the principles of statistical methods and probability [142]. Esterhuizen [33] conducted a statistical investigation to estimate the strength of pillars in hard rock mines.

[4] A part of this chapter will be submitted for journal publication to the International Journal of Rock Mechanics and Mining Sciences upon review by the co-authors.

Griffiths et al. [52] proposed using Monte-Carlo simulations to estimate underground pillar stability, which is a type of probabilistic method.

For the past two decades, the mining industry and academic researchers have found increasing reliability and use of numerical methods for pillar design. Several researchers have used numerical modeling to either study the failure mechanisms or derive empirical pillar strength equations for hard rock underground mines [88], [100]. Esterhuizen [37] developed a pillar design methodology for slender stone pillars using a combination of empirical observations and numerical methods. Jessu & Spearing [70] investigated the effect of major discontinuities on the performance of inclined pillars in FLAC3D and calibrated their results using the empirical model suggested by Lunder & Pakalnis [88]. Several researchers at the National Institute of Occupational Safety and Health (NIOSH) Pittsburgh Research Laboratory have contributed to the literature for underground stone pillar assessment using various empirical and numerical method-based approaches to successfully develop design guidelines [30], [39], [62].

This chapter evaluates the effect of spatial density of discontinuities on the effect of pillar strength. Discrete Element Modeling (DEM) is performed in 3DEC with the help of a Discrete Fracture Network (DFN) representing the mapped field discontinuities. 3DEC simulates the rock mass as a discontinuous material with joints acting as boundary conditions separating the block assembly [64]. Discontinuum modeling software provides an excellent advanced geotechnical analysis for a blocky deposit such as limestone and helps understand the governing behavior of joints, fractures, and bedding planes on the rock mass. Although running a DEM simulation for a single large pillar, like those present in the case study mine, maybe informative, assessing the local stability of a model containing several pillars might be time-consuming as well as computationally intensive. For this purpose,

continuum modeling provides a much better alternative to quickly analyze the stability and understand the redistribution of stresses on a local scale. The research provided in this chapter discusses a simple procedure to calibrate a continuum model in FLAC3D to reflect the effect of discontinuities observed in the discontinuum model in 3DEC. The equivalent physico-mechanical properties in the continuum model are calibrated based on the rock mass behavior observed for the discontinuum model. The calibrated properties are used to analyze the stability of a local area consisting of multiple pillars recreated to replicate their design in the mine. A relationship is established between the spatial density of discontinuities in discontinuum models and the shear strength properties in continuum models to adapt future models based on the variation in the joint distribution in the rock mass.

5.2 Background

The case study mine is developed in a limestone deposit developed in an underground setting. A modified room-and-pillar method is employed on a multi-level scale to extract a 30^{o} dipping formation. A calcite-filled bedding plane parts the limestone deposit on the top plane. The pillars in the mine are designed to be inclined and rectangular with a base dimension of 24.5 m x 24.5 m with a height of 30.5 m (100 ft). The underground operation is also affected by the presence of karstic cavities, which have been the root cause of multiple ground control issues in the mine. Figure 5.1 shows the size of a pillar in the case study mine and Figure 5.2 shows one of the areas affected by the collapse of a karst void.

Figure 5.1 Massive pillar layout in the underground case study mine.

Figure 5.2 Ground failure caused due to collapse of karst void [18].

The interruptions caused by the karst cavities often require the mine management to employ ground control measures. These measures are mostly based on assessing the geotechnical conditions and experience of the geologist and mining engineers from their experience in countering such incidents in the past. Most of the major rock mass classification schemes such as the Q-system [10] and the Rock Mass Rating [14] do not include the effect of karst on carbonate rock mass. Therefore, geotechnical analysis of underground excavations in limestone deposits requires categorical geological assessment of the conditions and numerical modeling studies customized for both local as well as global stability analysis. These studies require geological observations and geotechnical data collection on a comprehensive basis. Widely used techniques such as manual-virtual discontinuity mapping using lidar or photogrammetry scans are paramount in gathering information about the discontinuity network as well as excavation geometry and tracking karst cavities (Chapter 4). Previous studies have been conducted adding the case study mine for mapping the karst voids using Ground-penetrating Radar (GPR) surveys and analyzing pillar behavior with varying stress levels [7], [105], [129].

5.3 Discontinuum Modeling

Several researchers have utilized discontinuum modeling to assess the behavior of fractured rock masses. For this study, 3DEC developed by Itasca Consulting Group was used to simulate the behavior of limestone rock mass pervaded with a discontinuity network [64]. Employing Discrete Fracture Networks (DFNs) in 3DEC presents a pragmatic option to simulate the invisible joint network within the rock mass. DFNs use statistical information gathered using geological mapping in the field to build a stochastic discontinuity network,

trying to replicate the field conditions. Cacciari & Futai [23] modeled a tunnel in a shallow, fractured rock mass, and presented a practical approach for generating the DFNs using terrestrial laser scanning. Cui et al. [28] investigated the fractured rock mass strength using DFN engineering in a scale-effect study.

5.3.1 Model Geometry and Boundary Conditions

As explained earlier, the pillars in the case study mine what designed to be 30.5 m tall with a base dimension of 24.5 m x 24.5 m. The case study mine is developed in a middle- to lower-Ordovician age limestone deposit. The hanging wall and footwall in the mine are excavated on strike with a horizontal roof which is subsequently slashed by blasting to the inclined contact with the overlying bedding strata. After the eventual stoping of the crosscuts connecting both the headings, the pillars are left arranged in an inclined fashion separating the roof and the floor. Figure 5.3 shows the layout of the case study mine.

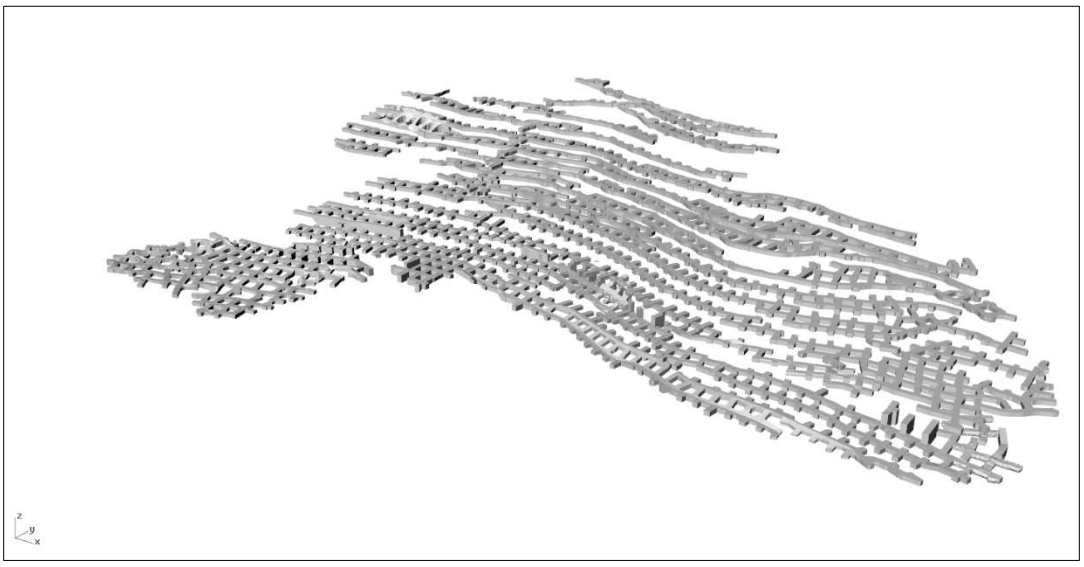

Figure 5.3 The multi-level room-and-pillar layout of the case study mine.

Since the 3DEC model is used to calibrate the properties of the continuum rock mass, a rectangular pillar model as shown in Figure 5.4 is used to understand the behavior of a pillar with variation in stress. The objective is to replicate the behavior for a continuum model, and in doing so, calibrate the properties that may be used for a local area model. The pillar behavior was observed with increasing compressive stress which was applied on the top and bottom inclined faces in the axial direction. The stress was applied in the form of positive velocity vectors on the bottom face and positive velocity vectors on the top face, thus compressing the pillar model in the z-direction. To avoid any horizontal movement along those planes, the boundaries were fixed in the x- and y-direction along the top and bottom faces of the model.

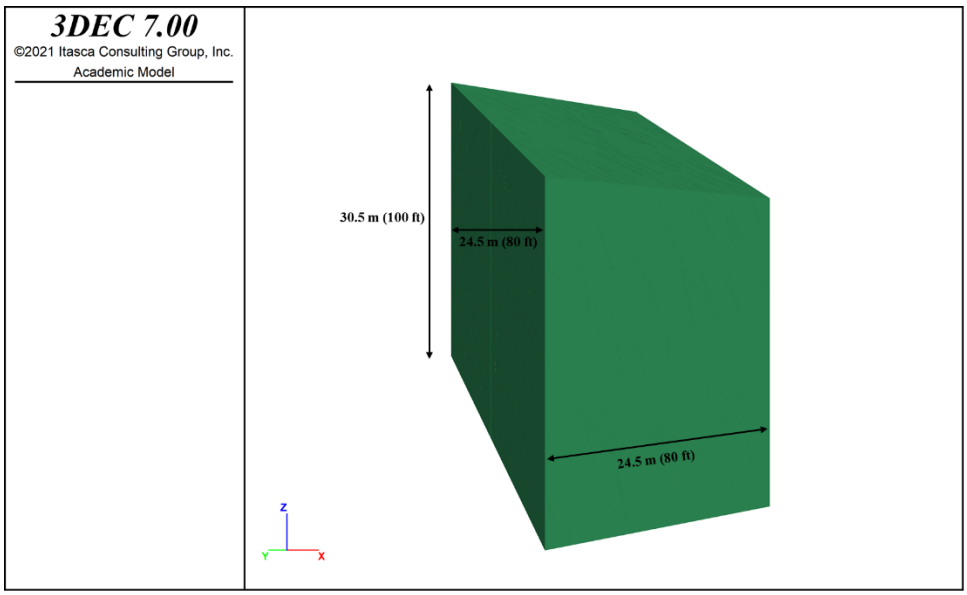

Figure 5.4 Pillar model created in 3DEC for discontinuum modeling.

Since the simulation replicates the procedure of a uniaxial compressive test, many works of literature suggest the application of a constant stress/displacement rate such that failure occurs within 5-10 mins of loading. This means for a relatively strong rock such as the one in the pillar model, a stress rate between 0.5-1 MPa/s or a displacement rate of 0.5-1

mm/min is recommended [5], [20]. But the sample types and sizes for these tests are also standardized and there will be too many variables governing the compressive behavior of a tall pillar with embedded discontinuities. Therefore, a separate study was conducted to analyze the appropriate rate for the applied uniform compressive velocity to the pillar. For this purpose, separate pillar models were simulated using separate velocities. The result of this study is shown in Figure 5.5.

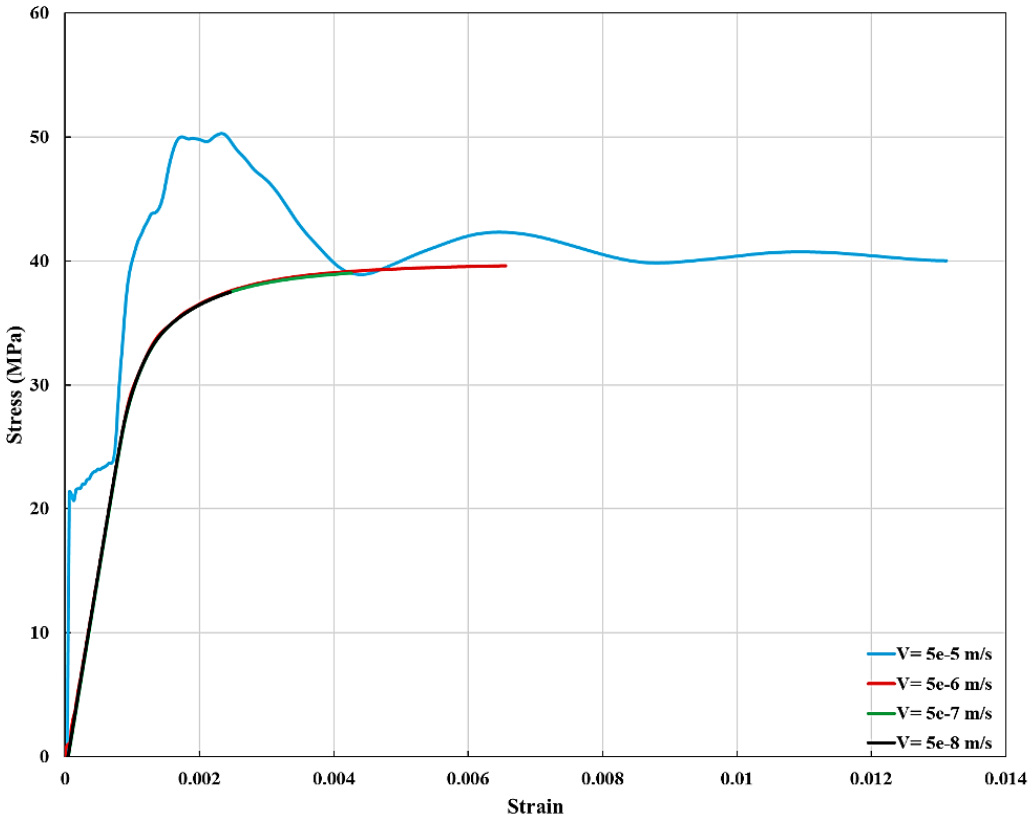

Figure 5.5 Simulation results for different velocity vector rates for the pillar model.

It can be observed from the previous figure that the compressive velocity vector rate is varied for four magnitudes starting from 5E-05 m/s to 5E-08 m/s, increased subsequently by a magnitude of 10. The stress-strain plot for the pillar model compressed with a velocity of 5E-05 m/s is quite abrupt and shows an exaggerated strength of the pillar due to the

mechanical shock transmitted to the model during compression. It is found that once the velocity magnitude reaches 5E-06 m/s or 5 µm/s, all the lower magnitudes follow the same stress-strain path, and the pillar fails the same stress without showing any abrupt spikes in the plots. It should be noted that when a velocity vector of magnitude 5 µm/s is applied to the pillar, it means that -2.5 µm/s is applied to the top face and +2.5 µm/s is applied to the bottom face. The sign convention represents the direction in which the velocity vectors are being applied. Using the result from this study, velocity vectors of the magnitude of 2.5 µm/s were used to compress the pillar model. The boundaries on the sides of the model were kept free as the sidewalls of the pillar would not be confined.

5.3.2 Physico-mechanical Properties

Table 5.1 lists the geotechnical properties of the intact rock and the joints that were used for the study. The properties were estimated by the mine management using laboratory testing and borehole measurements. There was no information regarding the joint properties at the site and the properties assigned to the joints are based on the work performed by Bandis et al. [8] on similar limestone rock samples.

Table 5.1 Physico-mechanical properties for intact rock and joints for discontinuum modeling.

Intact Rock Properties		**Joint Properties**	
Density, ρ	2690 kg/m^3	Joint Normal Stiffness	300 GPa/m
Bulk Modulus, K	37.86 GPa	Joint Shear Stiffness	30 GPa/m
Shear Modulus, G	20.57 GPa	Joint Friction Angle	30^o
Poisson's Ratio, µ	0.27	Joint Cohesion	0.0
Cohesion, c	12.53 MPa		
Friction Angle, ϕ	36.73		
Dilation Angle, ψ	24.50		

The rock mass was assigned Mohr-Coulomb constitutive behavior model to simulate the behavior of the deformable blocks along with the Coulomb-slip model assigned to the joints. The properties listed in Table 5.1 were adequate to define the characteristics of the pillar model when subjected to changes in stress levels.

5.3.3 Discrete Fracture Network (DFN)

During the past decade, a lot of researchers have presented several techniques for generating DFNs and using them for modeling geomechanical behavior, hydromechanical behavior, and analyzing the stability of excavations in naturally fractured rock masses [22], [28], [85]. However, literature is scarce on using DFNs for analyzing the behavior of limestone rock mass affected by karst voids. Research studies have been conducted by the author in the case study mine using LiDAR and photogrammetry mapping for generating DFN to evaluate the strength of pillars affected by karst voids. Also, attempts have been made to analyze redesigned pillar models for maximizing production while maintaining stability in the mine [128], [129]. The DFN used for the discrete element model was obtained from a former study conducted for the limestone mine. Here, the author performed manual-virtual discontinuity mapping for the LiDAR point clouds at different regions of the mine (Section 4.3.3). The joint mapping information obtained from the study found little to no variation in joint settings with an increase in depth. Since the local area simulated later in this study covers four levels in mine with no drastic changes in the joint orientation, size, and spatial density, a constant joint distribution/network was assumed for all the models simulated in this study. The statistical information used for generating the DFN is provided in Table

4.1. Figure 5.6 shows the pillar model as an assembly of blocks separated by the generated discrete fractures.

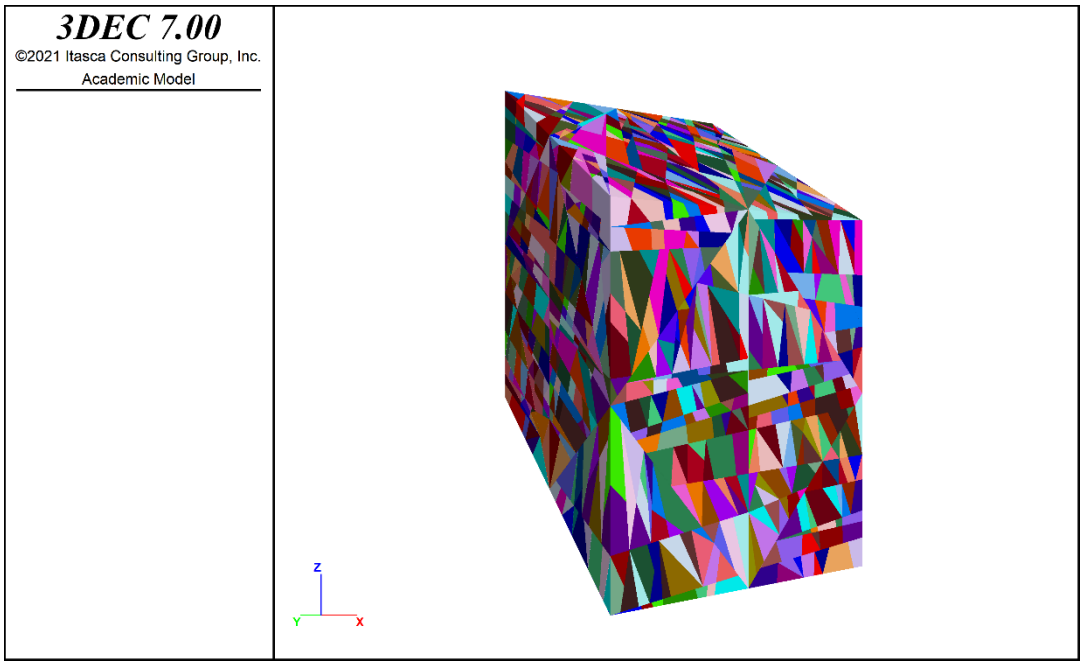

Figure 5.6 Pillar is shown as a jointed block assembly separated by the DFN.

5.3.4 Discontinuum Modeling Results

The discontinuum model for a single pillar took a total of 53 hours to complete the simulation. The simulations were carried out on a computer system equipped with a 6-core 8th generation i9 processor, 32 GB of RAM, and a max frequency of 4.8 GHz. The cycles were stopped when complete pillar yielding was indicated by the stress-strain plot. Figures 5.7 and 5.8 show the displacement magnitude for the pillar along with the stress-strain plot. The restriction of the horizontal movement of the top and bottom faces of the pillar is clear from the figure shown. It can be observed that the pillar has deteriorated completely and has yielded at a stress of 39 MPa. The 3DEC model not only displays the movement of

blocks along the discontinuities but also shows their rotation along with them. The block displacement magnitude scale is limited to a maximum ceiling of 10 m to prevent any distortion or confusion in viewing the relative displacement of blocks compared to each other.

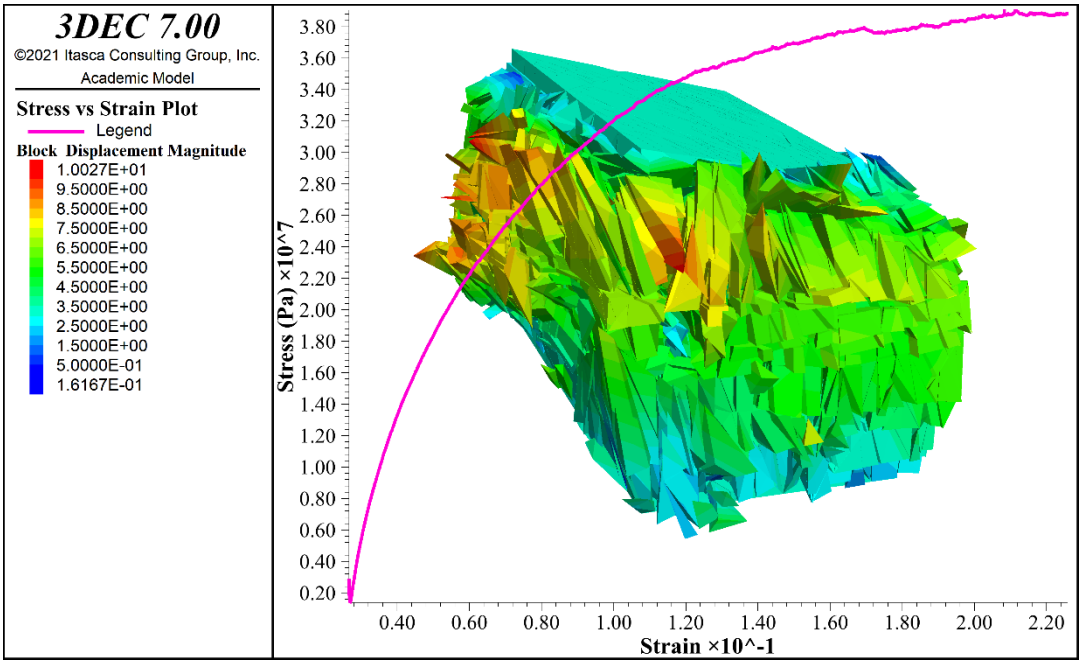

Figure 5.7 Displacement magnitude with the axial stress-strain plot for the discontinuum model.

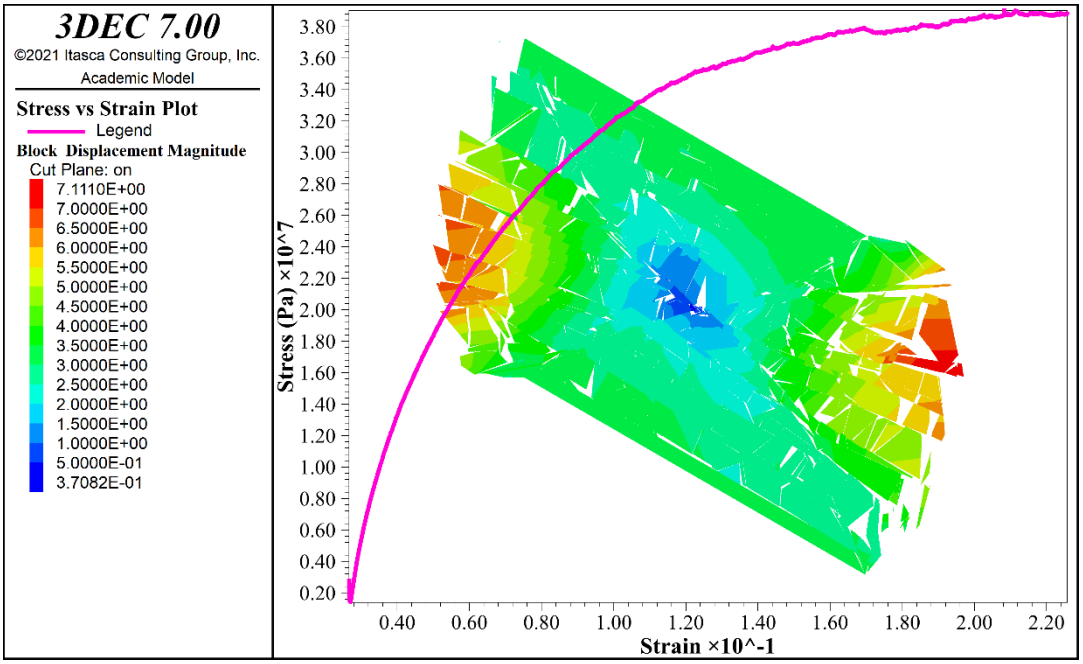

Figure 5.8 Displacement magnitude at mid-cross-section plane along with the axial stress-strain plot for the discontinuum model.

5.3.5 Variation of P_{32}

Further numerical simulations were performed for the discrete pillar model by varying the P_{32} value. This was done to understand the effect of the volumetric fracture density on the pillar strength. It is understood that by increasing the fracture density, the number of discontinuities within the pillar will also increase, thus resulting in a decrease in strength. Different P_{32} values for just one joint set of the pillar were tested by multiplying the original value by a factor 'δ' and the resultant pillar strengths were noted. The P_{32} values for all the joint sets were not varied, since this would result in extreme changes in pillar strength beyond the reasonable understanding. A similar process, as explained in the previous sections, was followed to numerically simulate the pillar by varying the P_{32} value of Joint Set (iii) and the resultant pillar strengths are presented in Table 5.2.

Table 5.2 Pillar strengths obtained for multiple P_{32} values for the joint set (iii).

δ	**P_{32}**	**Pillar Strength (MPa)**
0.25	0.053	132
0.5	0.106	75
1	0.211	39
2	0.422	22
3	0.633	12

5.4 Effect of Physico-Mechanical Properties on Pillar Strength

Physico-mechanical properties play an important role in deciding the performance of rock mass to changes in stress levels. This section discusses the effect of the shear strength properties (cohesion, friction angle, dilation angle) and elastic moduli (bulk modulus, shear modulus) on rock mass behavior. The influence of these properties will help translate and adjust the equivalent rock mass strength of a discontinuum pillar in continuum modeling software, in this case, FLAC3D. Similar to the previous section, a rectangular pillar model is constructed as shown in Figure 5.9 to understand the effect of all the properties. The variation in pillar strength or elastic moduli caused by the changes in the parameters is explained individually in the subsections.

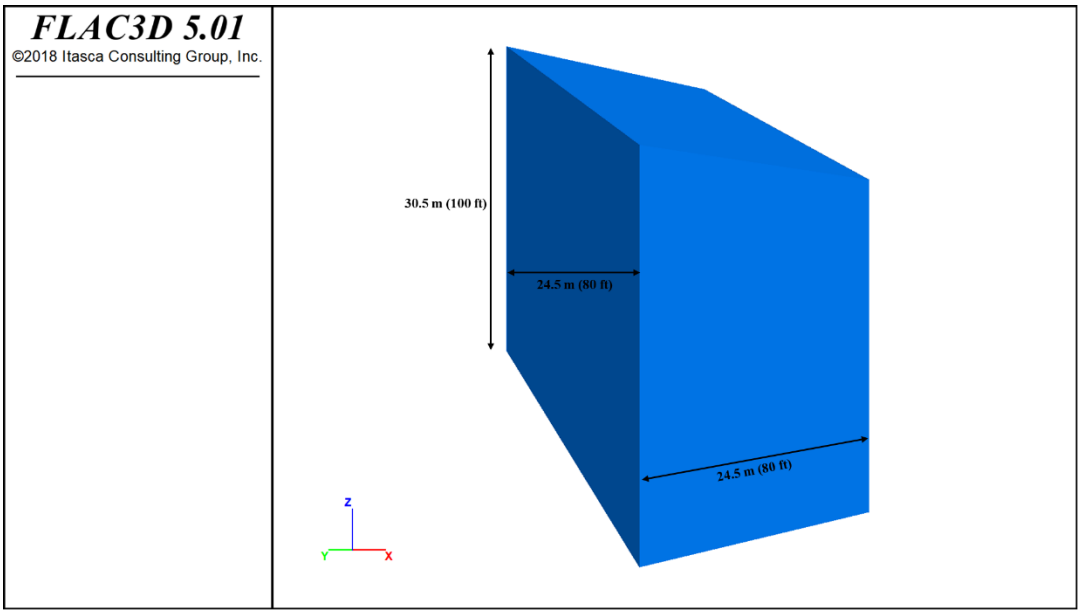

Figure 5.9 Pillar model created in FLAC3D for continuum modeling.

5.4.1 Effect of Shear Strength Properties

A substantial amount of research and information is present on determining and analyzing the shear strength of intact rock has been published during the past seventy years. Any attempt to discuss all the literature here would be inappropriate. In the context of this chapter, the shear strength properties of the intact rock are reflected concerning the Mohr-Coulomb theory [27]. The failure envelope for the Mohr-Coulomb criterion with a shear yield function and tension cutoff is implemented in FLAC3D or 3DEC. The stresses on the envelope are regulated by shear failure (non-associated flow rule), and tension failure (associated rule) [64]. A low shear strength implies a low cohesive strength or a reduced peak friction angle, or both, and consequently, a reduced dilation angle and asperity failure [102]. In this section, it was quite important to isolate the influence of the specific parameter whose effect on pillar strength is to be determined. Therefore, the elastic moduli properties were kept constant while varying the shear strength properties. At the same time, all the

other shear strength properties were kept constant while a particular property was being varied. It should be noted that the stress-strain plots while conducting this sub-study might not reflect the true strength of the pillar model. The plots are constructed to examine and correlate the variation in rock mass behavior while altering the parameters' values.

5.4.1.1 Cohesion (C)

Cohesion can be described as a form of stress that allows the rock particles to glue together. Based on the Mohr-Coulomb criterion, cohesion can be referred to as the shear strength under zero normal stress, or the intercept of the intact rock's failure envelope with shear stress [87]. To study the effect of cohesion on pillar strength, five values were selected and the results for the stress-strain values are presented in Figure 5.10. The friction angle and dilation angle values were kept constant at 37.86^{o} and 24.50^{o}, respectively.

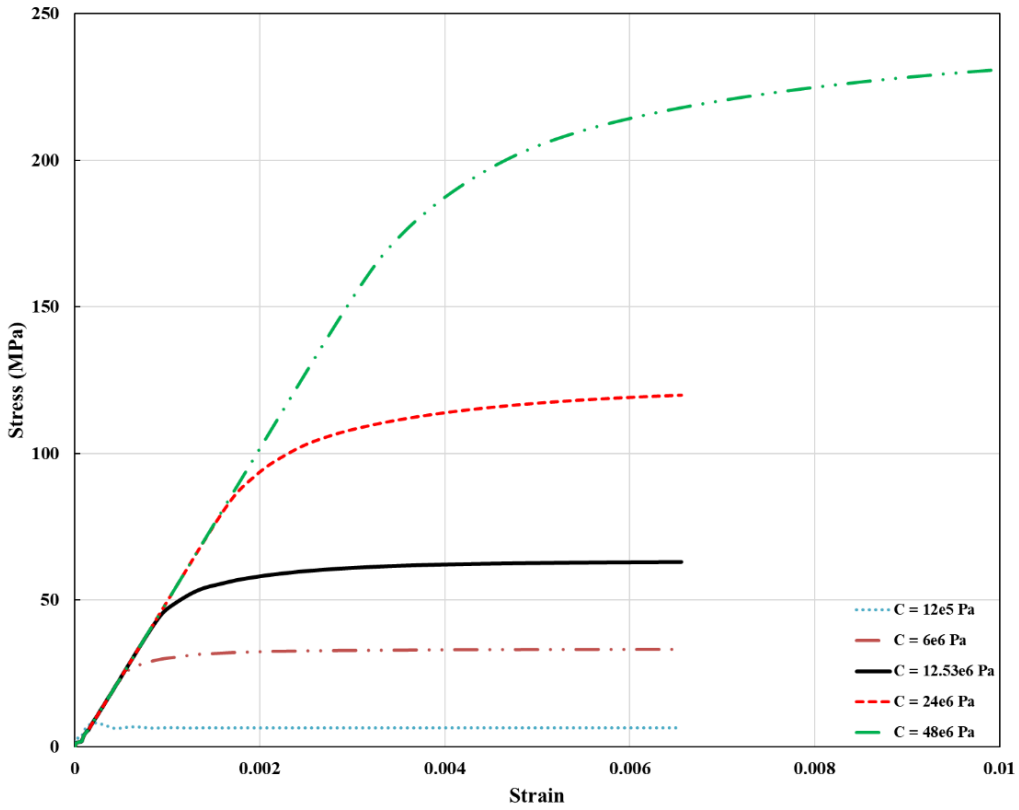

Figure 5.10 Variation in pillar strength with cohesion for continuum pillar model.

At the lowermost selected value of C = 1.2 MPa, the pillar strength is determined to be 6.5 MPa, which rises sharply to a value upwards of 200 MPa when the cohesive strength is increased to 48 MPa. The figure shows that cohesive force has an enormous effect on pillar strength.

5.4.1.2 Friction Angle (ϕ)

Friction angle can be defined as a shear strength property that describes the frictional shear resistance of rock granules with the application of normal stress [77]. Figure 5.11 shows the effect of friction angle on the variation of the pillar strength. Five values around the original

determined value of 37.86° were chosen for this study. The cohesion and dilation angle values were kept constant at 12.53 MPa and 24.50°, respectively. The stress-strain plots show a significant effect on the friction angle on pillar strength. At the lowest value of $\phi = 43°$, the pillar strength plateaus at 53 MPa, which later increases to 78 MPa at the highest test value of $\phi = 43°$.

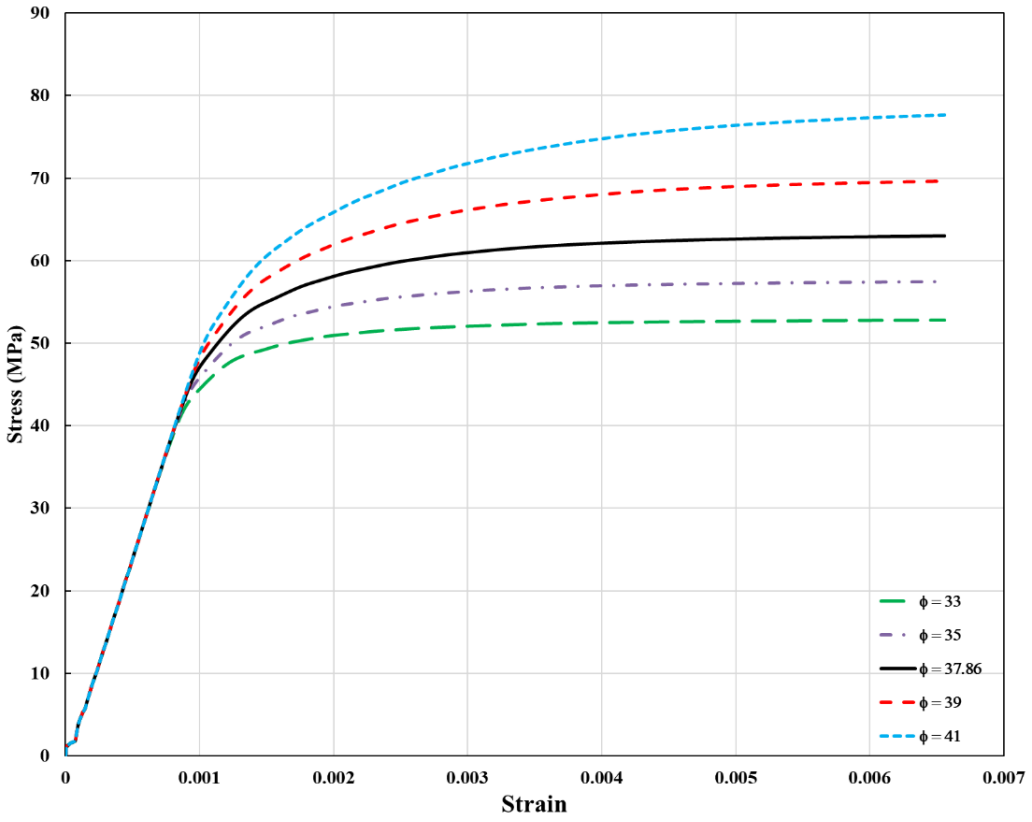

Figure 5.11 Variation in pillar strength with friction angle for continuum pillar model.

5.4.1.3 Dilation Angle (ψ)

For plastic material, like the one defined in this study, dilatancy or dilation can be defined as the variation in volume with the shearing of the material. The non-linearity of a Mohr-Coulomb failure envelope primarily occurs due to the change in packing of particles or

dilatancy which depends on confining stresses. For the Mohr-Coulomb constitutive model, dilation is defined as an angle that varies between the values of zero or friction angle (Rocscience). In this study, five values were selected including the default value of 24.5°. The variation in dilation angle has a modest effect on the final pillar strength. The pillar model fails at a strength of 62 MPa at the lowest value of $\psi = 20.5^{o}$. At the highest test value of $\psi = 20.5^{o}$, the pillar strength registers at 64 MPa. Figure 5.12 shows the effect of dilation angle on the variation of the pillar strength.

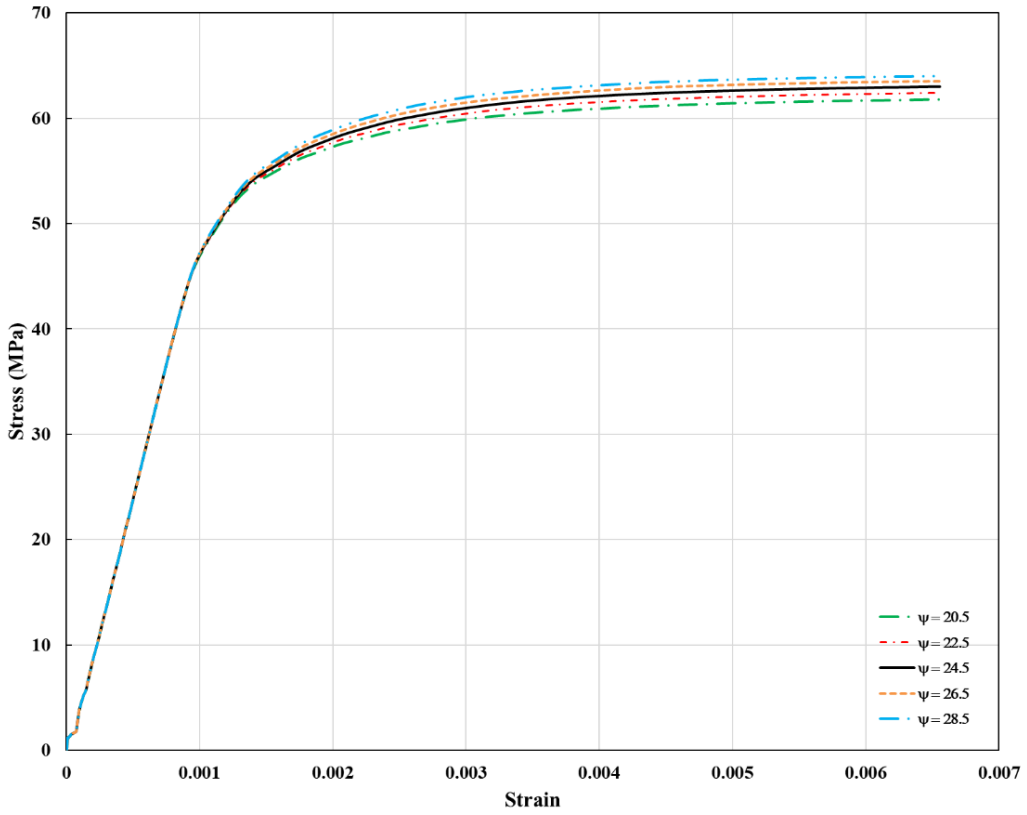

Figure 5.12 Variation in pillar strength with dilation angle for continuum pillar model.

5.4.1.4 Sensitivity Analysis for Shear Strength Properties

From sections 5.4.1.1, 5.4.1.2, and 5.4.1.3, it is observed that all the tested shear strength properties of cohesion, friction angle, and dilation angle are directly proportional to the pillar strength. Table 5.3 lists the estimated pillar strength values corresponding to the set parameter values for each property.

Table 5.3 Pillar strength values for shear strength properties.

Cohesion (MPa)	Pillar Strength (MPa)	Friction Angle (°)	Pillar Strength (MPa)	Dilation Angle (°)	Pillar Strength (MPa)
1.2	6.5	33	53	20.5	62
6	33	35	57.5	22.5	62.5
12.53	63	37.86	63	24.5	63
24	120	39	70	26.5	63.5
48	236	41	78	28.5	64

The sensitivity analysis of all the strength values for each parameter is shown in Figure 5.13. It is observed that pillar strength is most sensitive to cohesion or cohesive strength. The slope of the line for cohesion is the highest, followed by the friction angle and dilation angle. Dilatancy does not have a tremendous effect on the rock mass as expected for hard and brittle rock such as limestone. From the sensitivity analysis, it is recommended to use the most sensitive property (in this case, cohesion) for calibrating the rock mass strength as one would not need to vary the property value by a lot to adjust to the desired strength. The parameters which exhibit the lowest sensitivity may then be used to fine-tune the rock mass strength without causing a drastic variation in the shear strength properties.

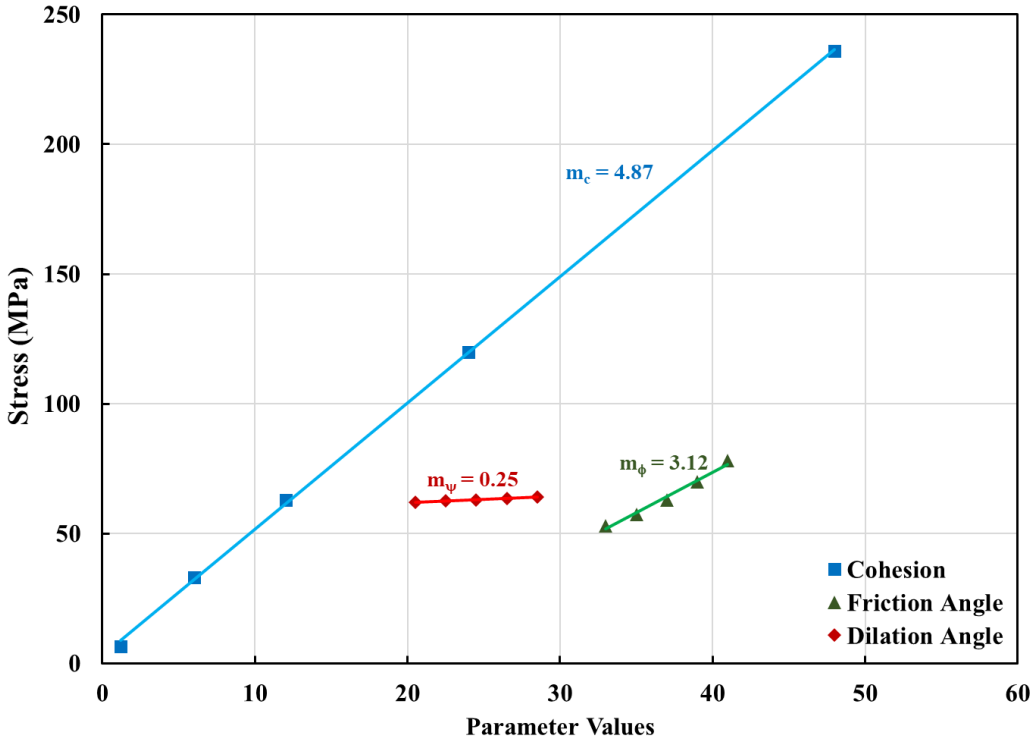

Figure 5.13 Sensitivity analysis plot for shear strength properties for the continuum pillar model.

5.4.2 Effect of Elastic Moduli

Although no rocks display linear elastic behavior, this is the most common way of representing the stress vs strain relationship for them. When tested through laboratory testing many rock samples exhibit a linear behavior to incremental changes in stress [69]. Many researchers assume linearity to apply the analytical stress-strain relationship to simplify complicated geomechanics. According to Jones & Ashby [72], elastic moduli (not to be confused with the modulus of elasticity) can be described as the resistance or stiffness of the rock material to elastic deformation. Mathematically, it can be defined as the linear ratio of the stress tensor to the strain tensor [12]. There are three primary types of elastic moduli: Young's Modulus (E), Bulk Modulus (K), and Shear Modulus (G). Two other elastic

moduli, namely Lame's first parameter ( ) and P-wave modulus (M) are not discussed in this study. The elastic moduli are one of the most important properties of the rock material that decide its behavior below the proportional limit. For a Mohr-Coulomb material in FLAC3D or 3DEC, the linear elasticity of the material can be fully described by any two elastic moduli. For this study, Bulk Modulus and Shear Modulus were chosen to define the rock zones. The analysis presented in the following sub-sections described the path of the rock material to its yielding state and not necessarily the ultimate strength of the pillar models. While varying the elastic moduli, the shear strength properties were kept constant. The objective here is to understand the variation in the compressible nature of the rock material and not estimate the accurate behavior of the rock mass.

5.4.2.1 Bulk Modulus (K)

The bulk modulus or K of a solid material can be described as its resistance to compression or as a ratio of the variation in stress to the relative change in volume. Figure 5.14 shows the variation in the stress-strain ratio or elasticity path with the different values of the bulk modulus. Five different values increased stepwise by the magnitude of 10 were tested and the slopes of the stress-strain plots were noted. As described earlier, this study aimed to study the linear section of the plots and not the yield region of the models.

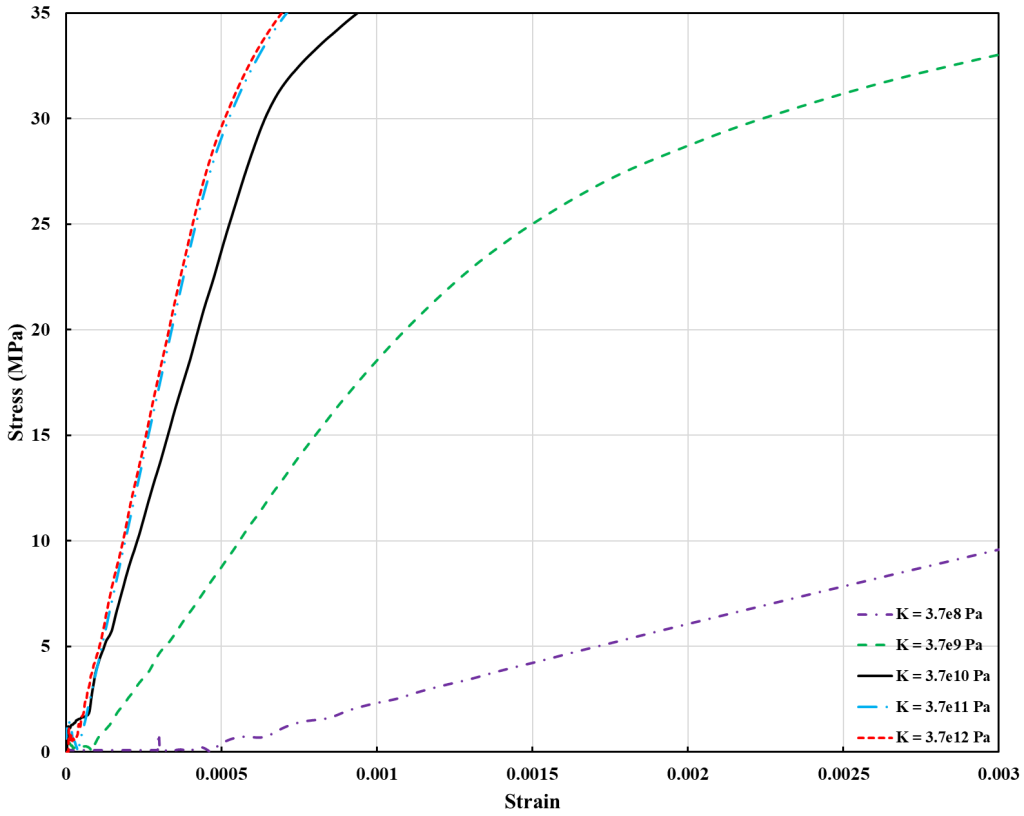

Figure 5.14 Variation in elasticity path with bulk modulus for continuum pillar model.

It may be observed that as the bulk modulus value is increased from K= 3.7E8 Pa to K= 3.7E12 Pa, the steepness or slope of the curve is increasing. This implies that as the value of K is increased, it takes less strain variation for the pillar to reach its ultimate strength, and the material becomes less compressive.

5.4.2.2 Shear Modulus (G)

The shear modulus or G of a solid material can be defined as its resistance to shear, or elastic shear stiffness, and is mathematically represented as the ratio of shear stress to the shear strain. The elasticity paths with the different values of shear modulus are depicted in Figure 5.15. Five different values of shear modulus were tested, and the stress-strain

behavior was plotted. There is little difference between the high slope values of the stress-strain plots for the values of G= 2E10 Pa, G= 2E11 Pa, and G= 2E12 Pa, which decreases drastically as the shear modulus is subsequently decreased by a magnitude of 10 for the two values of G= 2E9 Pa and G= 2E8 Pa. This shows that as the shear modulus is increased, there is less deformation of the rock when it experiences parallel shear forces on its opposite faces.

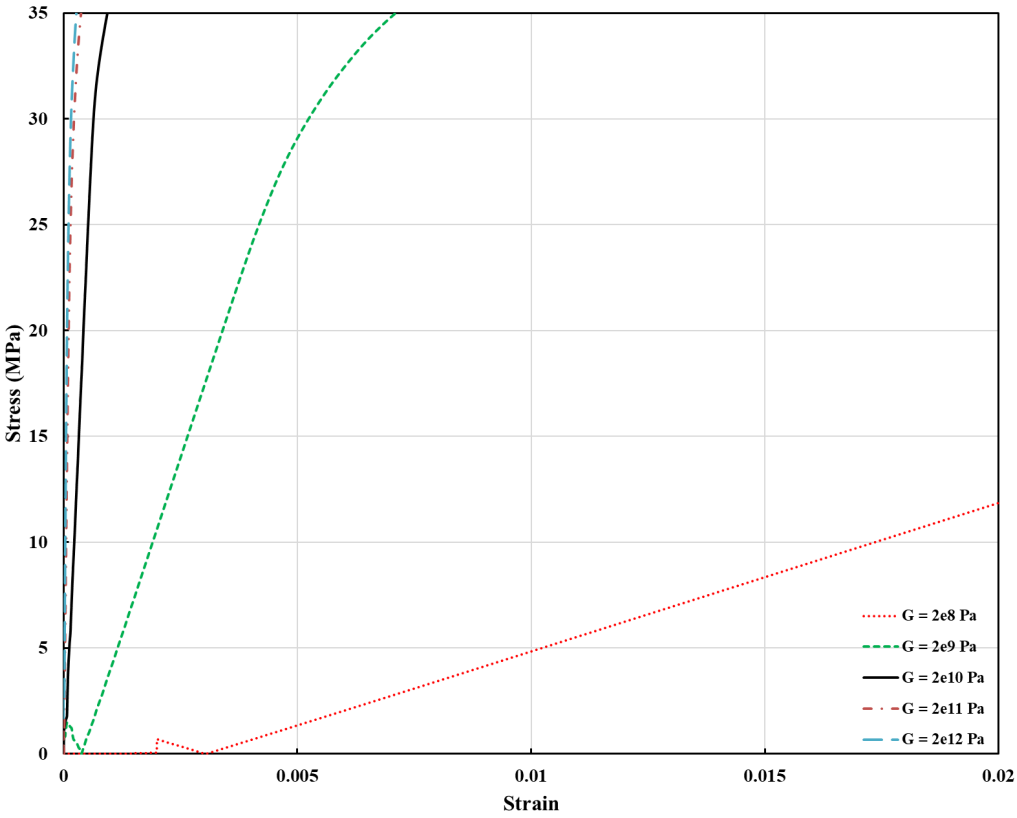

Figure 5.15 Variation in elasticity path with shear modulus for continuum pillar model.

5.4.3 Calibrated Values for Continuum Modeling

After understanding the effect of the parameters in the previous sections, it is important to translate the discontinuum model properties to continuum model properties to incorporate the weakening effect discontinuities embedded in the rock mass. For this purpose, three continuum models in FLAC3D were tested and the stress-strain profiles were matched against the one generated using the discontinuum model in 3DEC. The three different sets of values tested to calibrate the continuum model in FLAC3D are provided in Table 5.4 and they provided the closest match to the 3DEC model. The stress-strain profiles of these models are shown in Figure 5.16.

Table 5.4 Different sets of values were tested to calibrate the continuum model.

	ρ (kg/m³)	**G (MPa)**	**K (MPa)**	**C (MPa)**	**ϕ (°)**	**ψ (°)**
3DEC Model	2690	20590	37860	12.53	36.73	24.5
FLAC3D - A	2690	2059	3786	8.07	35.8	24.5
FLAC3D - B	2690	411.8	757.2	8.07	35.9	24.5
FLAC3D - C	2690	205.9	378.6	8.07	35.9	24.5

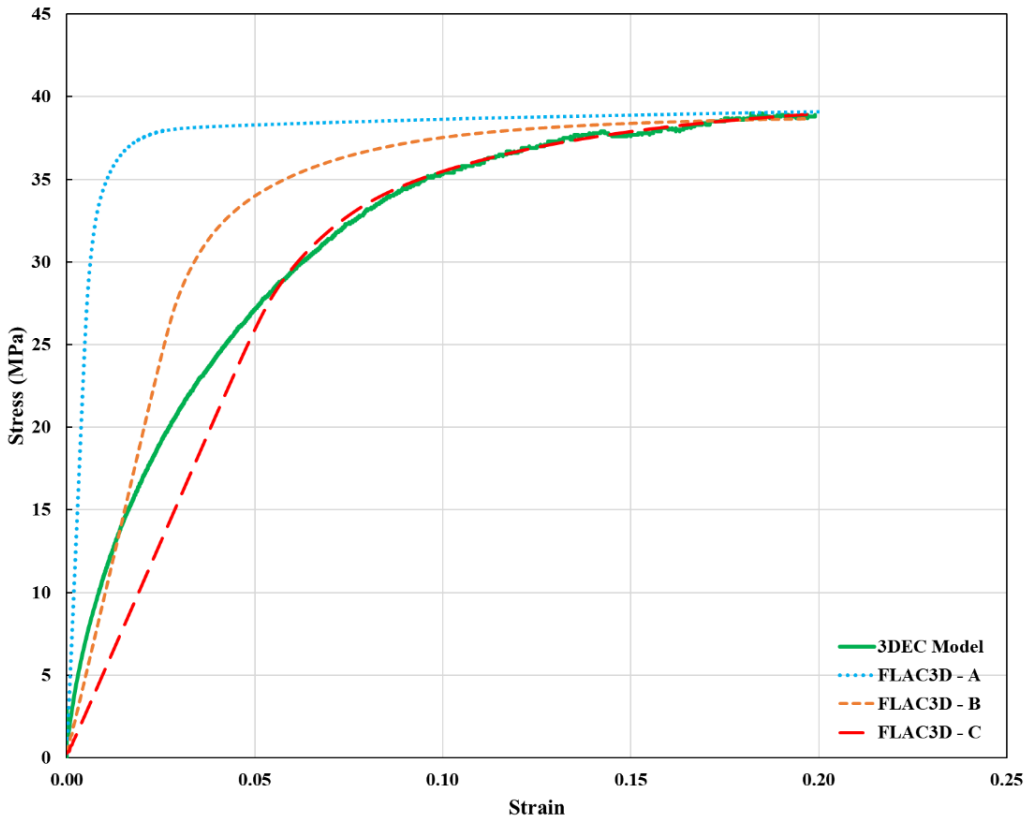

Figure 5.16. Stress-strain profiles of different continuum models to match the discontinuum model.

Identical shear strength properties were input for the three models as they were matched exactly to the maximum stress ceiling of 39 MPa as determined by the original 3DEC model with the lab measured intact rock properties and field mapped discontinuities. When comparing the different variations of the calibrated FLAC3D models, it was found that model A matched the stress-strain profile of the 3DEC model only during the initial stages of the simulation. The stress-strain profile of continuum model B complemented a considerable portion of the 3DEC profile during the pre-yield stages. Whereas the profile for continuum model C was analogous to the 3DEC profile during the pre-peak and post-peak stages. Therefore, the author decided to select the properties of model C for simulating the local area of the case study mine using continuum modeling in FLAC3D. The reasoning

behind this decision is that it is essential to replicate the pre-peak and post-peak behavior when the rock mass is in the yielding and failure stages. Figure 5.17 shows a comparison between the displacement magnitude contour of the 3DEC and the calibrated FLAC3D model.

The stress-strain profile of models simulated using FLAC3D followed a straight line rather than following the Mohr-Coulomb failure envelope during the pre-yield stages like 3DEC. The reason for this was that those continuum models do not exhibit block movement during the simulation and exhibit elastic-dominant behavior during the initial stages. Whereas in 3DEC, block movement and rotation in 3DEC begins at the start of the simulation cycle, and hence, it can follow the Mohr-Coulomb failure plot from the moment load is applied. The same is depicted in Figure 5.17 where the resultant displacement in both the models is comparable, but the 3DEC model looks visually compressed compared to the FLAC3D model.

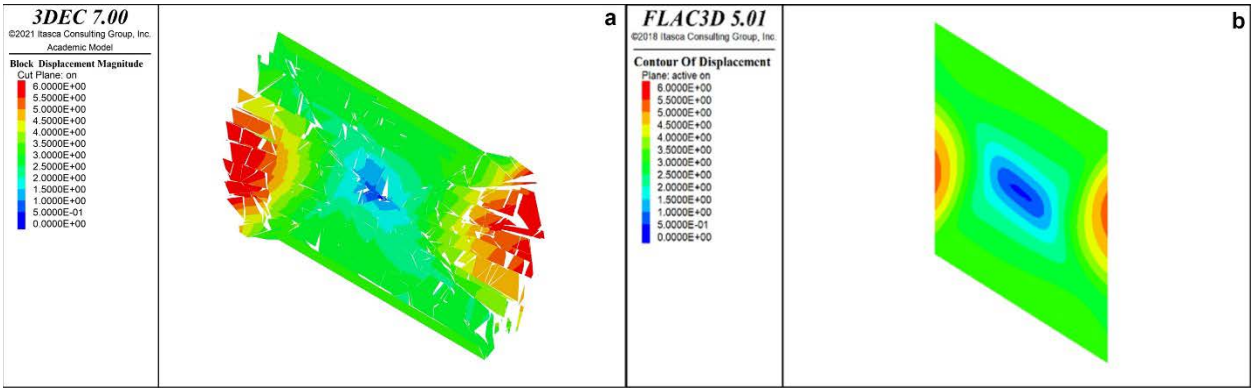

Figure 5.17 Displacement magnitude contour for original 3DEC model and calibrated FLAC3D model.

5.5 Local Stability Analysis using Continuum Modeling

Fast Lagrangian Analysis of Continua in 3 Dimensions (FLAC3D), developed by Itasca Consulting Group, is used to conduct numerical simulations by treating the rock mass as a continuum [67]. This program is based on an explicit finite volume method for computational purposes while incorporating the complex details of the constructed models. After accomplishing a successful calibration of a discrete, blocky, and jointed rock mass to continuum properties, a section of the mine was selected to analyze the local stability and confirm the results with geotechnical observations in the field.

5.5.1 Local Model Geometry

The mine area, including the pillars and development drives, for which the local stability analysis was conducted is highlighted in Figure 5.18. The area covers four levels in the case study mine. Mining operations in this area have faced obstacles in the past due to the presence of karst cavities. The ground control issues have led the mine operator to design oddly shaped pillars, some of which have not been benched to their full height and some are connected as double pillars to bolster local stability. Figure 5.19 shows the topography of the total model extent with the analysis area housed in it.

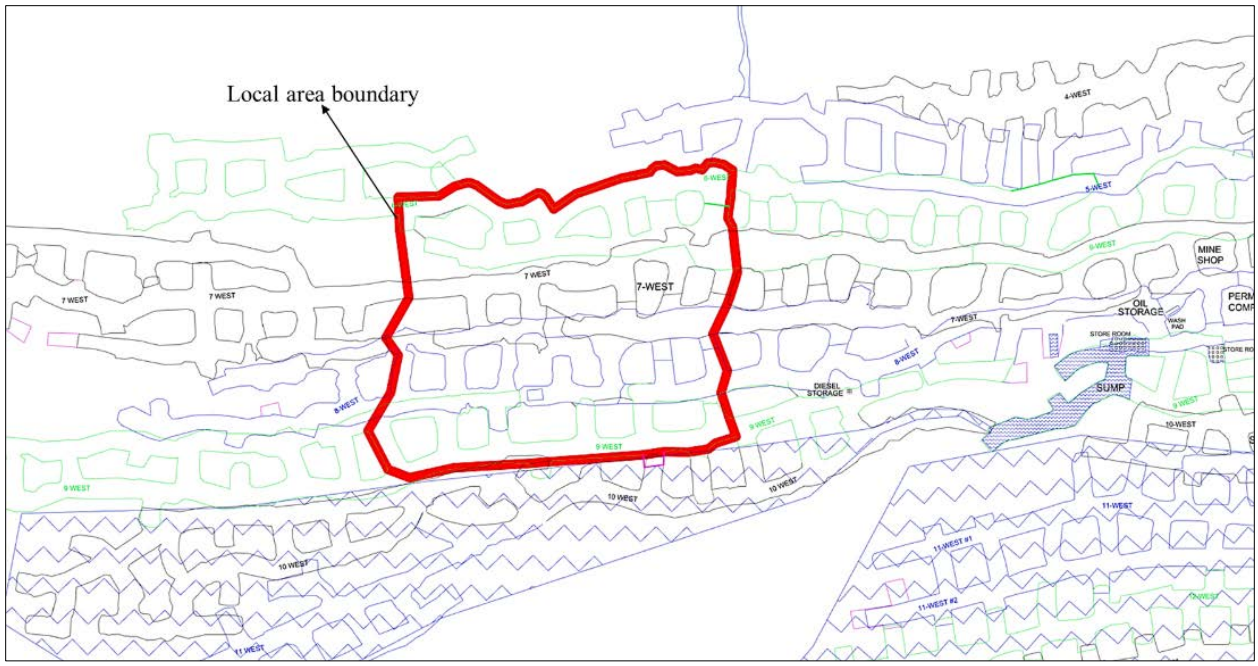

Figure 5.18 Highlighted boundary enclosing the area selected for stability analysis.

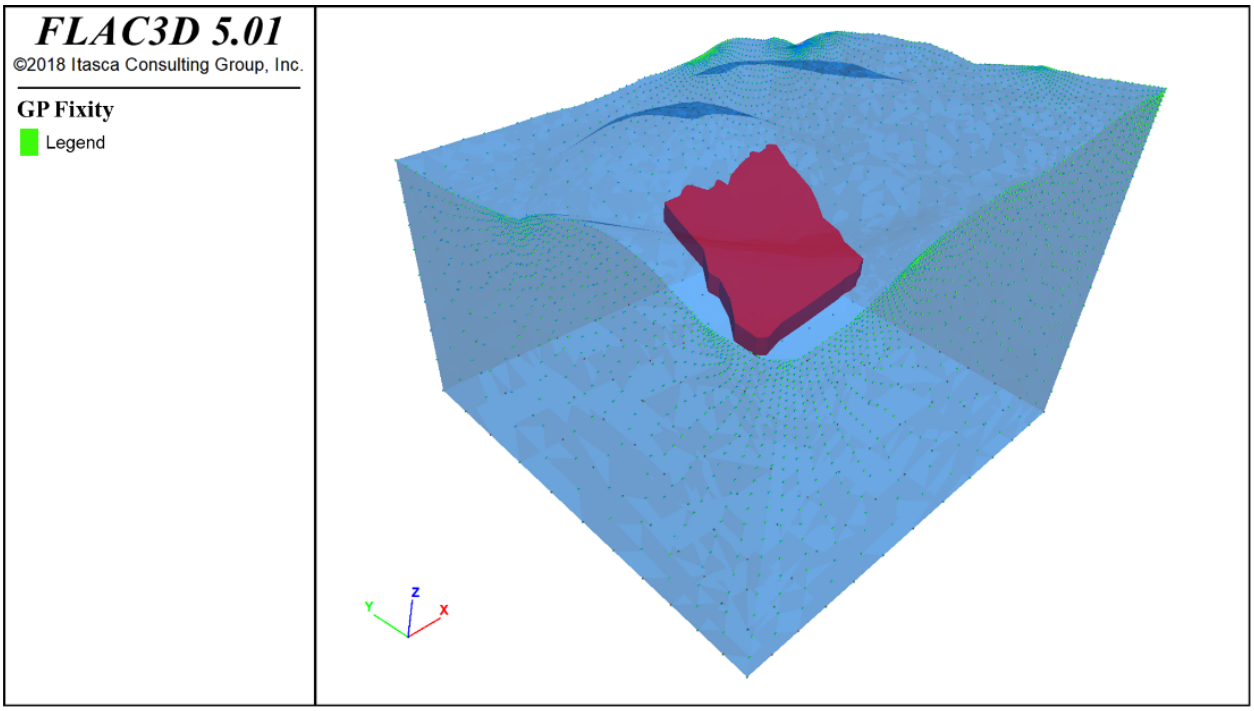

Figure 5.19 Topographical block with boundary conditions containing the analysis section.

5.5.2 Input Parameters and Mining Sequence

The physico-mechanical properties used for the rock mass are explained in detail in Section 5.4 of this chapter. The final calibrated and adjusted properties for all the rock types in the model are provided in Table 5.5.

Table 5.5 Calibrated geotechnical parameters for ore rock and host rock used in FLAC3D.

Rock Mass Properties	Orebody	Hanging wall	Foot wall
Density, ρ	2690 kg/m^3	2691 kg/m^3	2722 kg/m^3
Bulk Modulus, K	378.6 MPa	328.1 MPa	376.9 MPa
Shear Modulus, G	205.7 MPa	256.4 MPa	251.8 MPa
Poisson's Ratio, μ	0.27	0.19	0.21
Cohesion, C	8.08 MPa	4.19 MPa	11.19 MPa
Friction Angle, ϕ	35.93	51.01	36.87
Dilation Angle, ψ	24.50	34.40	24.88
Tensile Strength, τ	2.69 MPa	2.77 MPa	3.30 MPa

Figure 5.20 shows the recreated and simplified, yet identical dimensions of excavations including the drives, pillars, karst voids, and crosscuts left because of the benched stopes. The author attempted to simulate the mining sequence followed by the mine operator in the past. For this purpose, blasting advances ranging from 7 m to 10 m were simulated at a time and the model was allowed to reach equilibrium after each advance. The process of mapping and analyzing karst volumes is not explained in this study and the readers may refer to previous case studies conducted for the mine (Chapter 2). It is assumed that the karst voids run throughout the height of the deposit, thus assuming the worst-case scenario by overestimating the weakening volume.

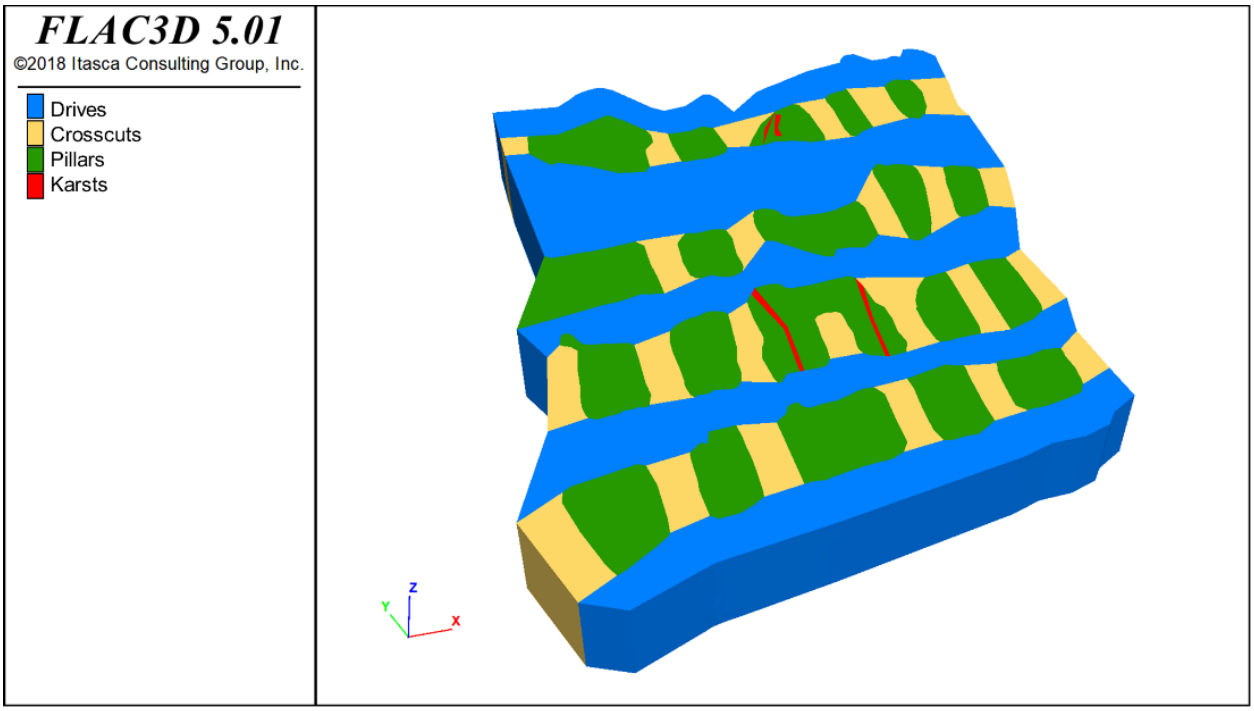

Figure 5.20 Local analysis area showing drives, crosscuts, pillars, and karst voids.

5.5.3 In situ Stresses and Boundary Conditions

In situ stress measurements were obtained by the mine management for multiple boreholes. An elevated vertical stress gradient of 0.0416 MPa/m was determined at the site and was used in the model with the vertical stress varying with depth depending on the topography. The horizontal stress was also assumed to change with depth and a gradient of 0.0143 MPa/m was determined. These measurements were found to be conforming with the prior findings by mine management for similar limestone environments in Kentucky [83] and Ohio [9].

As shown in Figure 5.19, the sides and bottom of the model's artificial boundary were fixed in all directions, and the topography at the top was kept free. Since the numerical model's boundaries are artificial, they have to be large enough to not affect any forces in the

simulated zone [130]. The model is allowed to reach equilibrium after each blasting advance is made and dynamic modeling is not used during this simulation.

5.5.4 Calibration of the model

Calibration of a numerical model is very important for replicating the evaluation of stresses and understanding the response of excavations to redistributed stress. Ideally, the numerical model needs to be calibrated using the field data of stress changes around the pillars of interest. Since the locations desired for taking the instrumentation data were not available due to the fieldwork time frame, the in situ state of the numerical model was calibrated with the in situ stress measurement data at the case study mine site. In situ stress measurement values were obtained by the mine management for multiple boreholes using a United States Bureau of Mines (USBM) Borehole Deformation Gage (BDG) in conjunction with the overcoring drilling technique [13], [61]. The diametrical borehole deformation during the overcoring process was continuously monitored to ensure that measured deformations are the result of elastic deformation and not peripheral movement. Out of multiple overcoring boreholes, maximum and minimum principal stress values were used for one borehole near the site of concern. Value for horizontal and vertical stress gradients in the numerical model are varied to approximately match the principal stress values at the site of the overcoring borehole to calibrate the in situ model. Figure 5.21 shows the measured and calculated stress values using the overcoring borehole method and the estimated values from the numerical model after calibration. Consequently, with the calibrated model and rock properties, the mining sequence followed at the mine is replicated to arrive at the current excavated state. It is assumed that after numerical simulation of the excavation

sequence, the redistributed stresses around and in the pillar resemble the approximate stress range estimated from the modeling results.

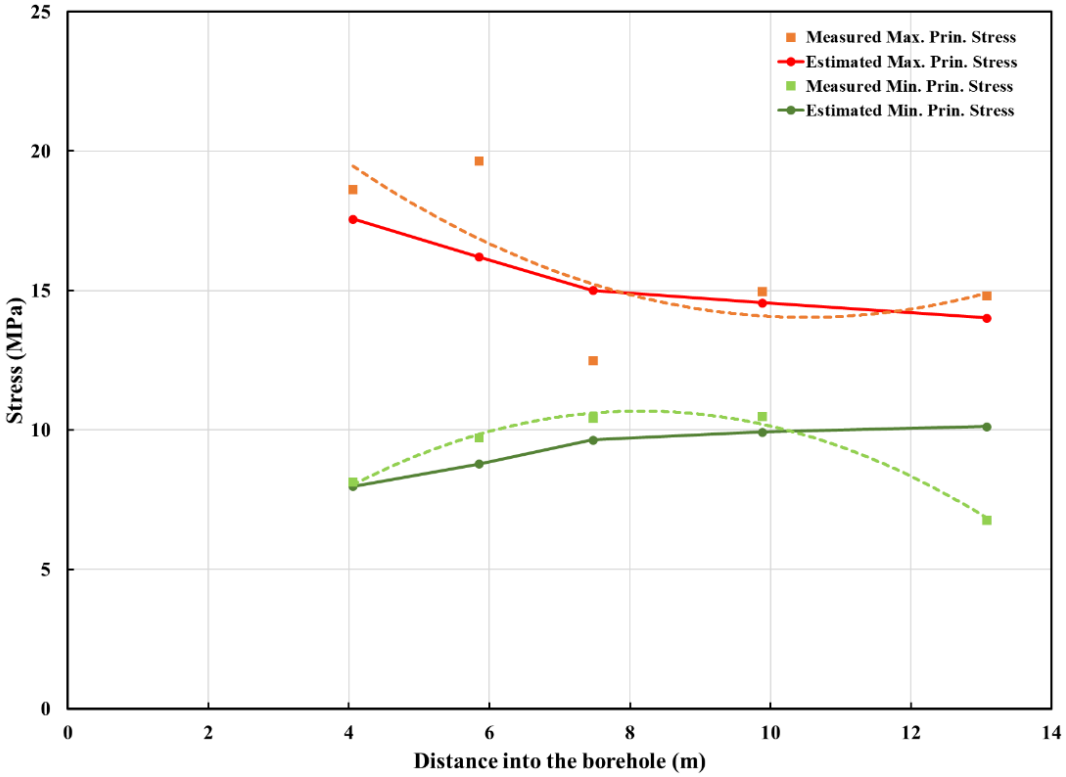

Figure 5.21 Plot for calibration of in situ model principal stresses vs distance in a borehole.

5.5.5 Analysis of Continuum Modeling Results

The different stages of the excavation sequencing followed to arrive at the current state of the local area selected for the stability analysis study are shown in Figure 5.22. The plot showing maximum unbalanced force registers a spike every time a blasting advance is made, and the model is allowed to reach equilibrium before another excavation is done.

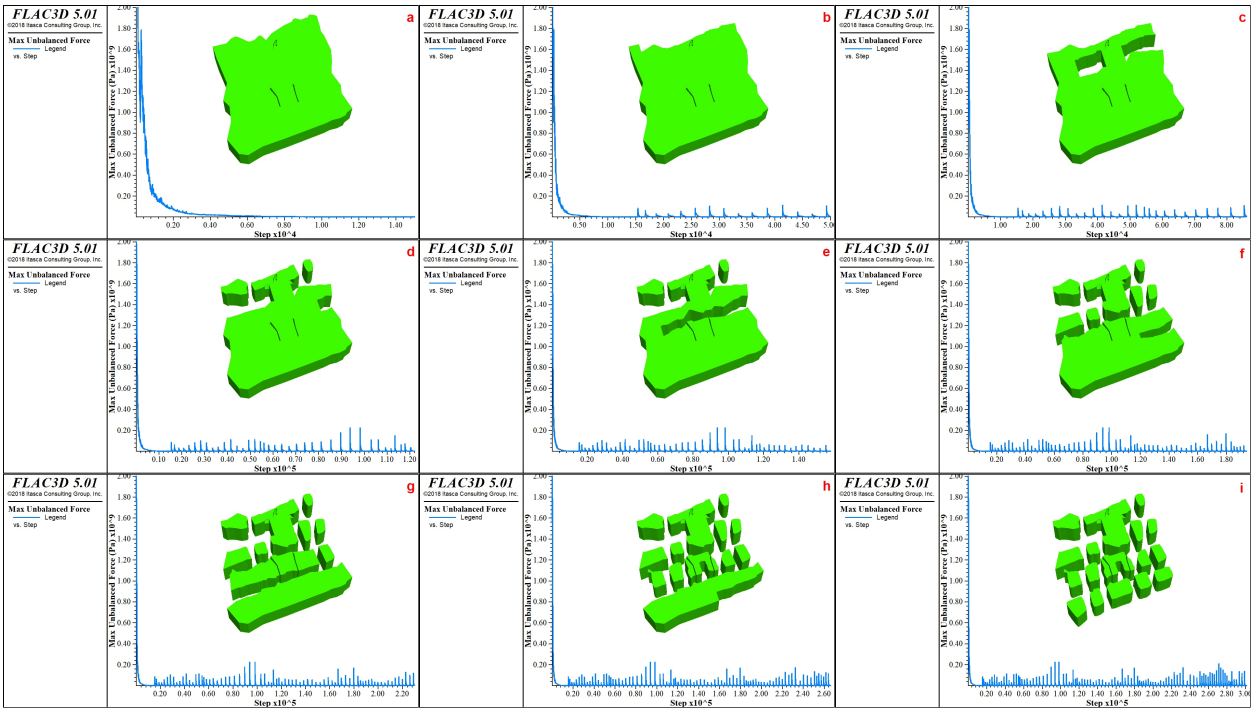

Figure 5.22 Excavation sequencing stages with the maximum unbalanced forces for the continuum modeling.

Figures 5.22(a) and 5.22(i) show the in situ and final stages of the numerical simulation, respectively. This continuum modeling study with FLAC3D does not only incorporate the calibrated properties estimated from the discontinuum modeling but also emphasizes two regions of the mine model where ground control issues have been encountered in the past.

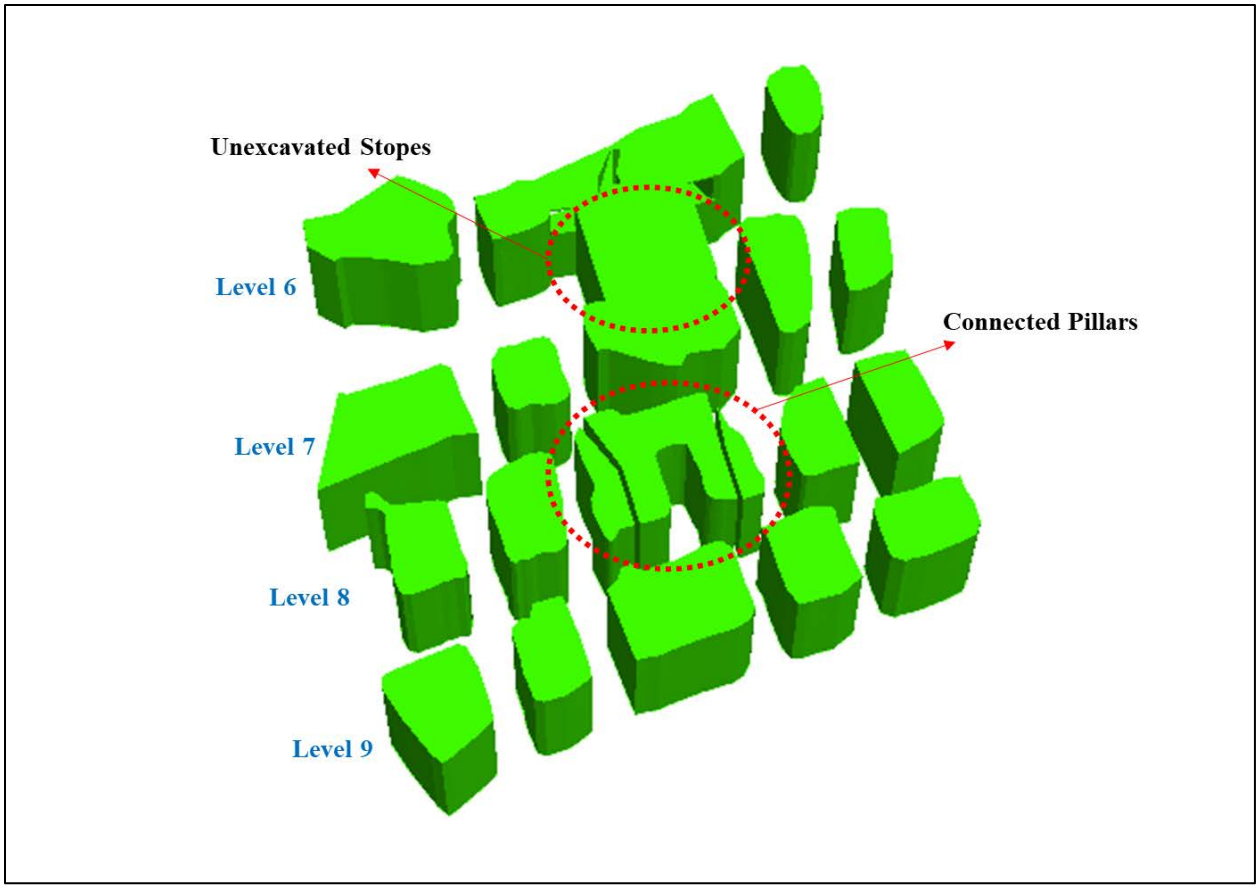

Figure 5.23 Current mined state of the mine model highlights the areas with ground control issues.

As depicted in Figure 5.23, the numerical model highlights two ground issues that were managed by taking appropriate measures by the mine management at the time. The first issue arose due to the collapse of a karst volume in Level 6 of the mine. To counter this situation, the subsequent stopes neighboring the pillar were not benched, thus leaving the pillar to a shortened height of 10 m as compared to the planned height of 30.5 m. Figure 5.24 shows the pillar model and the picture of the area at the mine level.

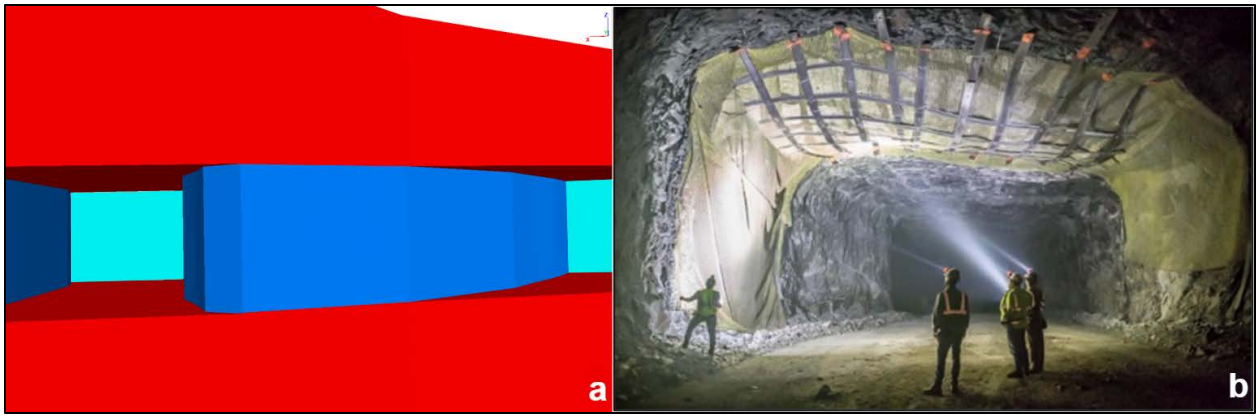

Figure 5.24 (a) Shortened height of the pillar in the numerical model; (b) Ground control measures installed to counter the instability caused by karst void collapse around the pillar.

Another ground control issue in the mine was met in Level 8, where another karst-affected pillar was discovered. The karst cavities, in this case, were not large, and only groundwater seepage was observed without any inrush of clayey-rocky material or collapse. This time, the management and operations group at the mine decided to leave a section of the part of the common crosscut intact between the two pillars, thus connecting them. This resulted in providing the extra stability that was maintained even when the rest of the crosscut was benched. The author made his best efforts to replicate this design implemented at the mine in the recreated model as shown in Figure 5.25. In previous studies conducted at the mine, the author suggested increasing the height of the pillar with karst in Level 6 by extracting its adjoining stopes [128]. Therefore, a separate scenario was simulated where the stopes were benched out in a proper sequence, thus extending the pillar to the regulation height of 30.5 m without changing its shape. All the analyses are presented in the continuing sections concerning the strength-to-stress ratio (Factor of Safety) and displacement magnitude around the excavations.

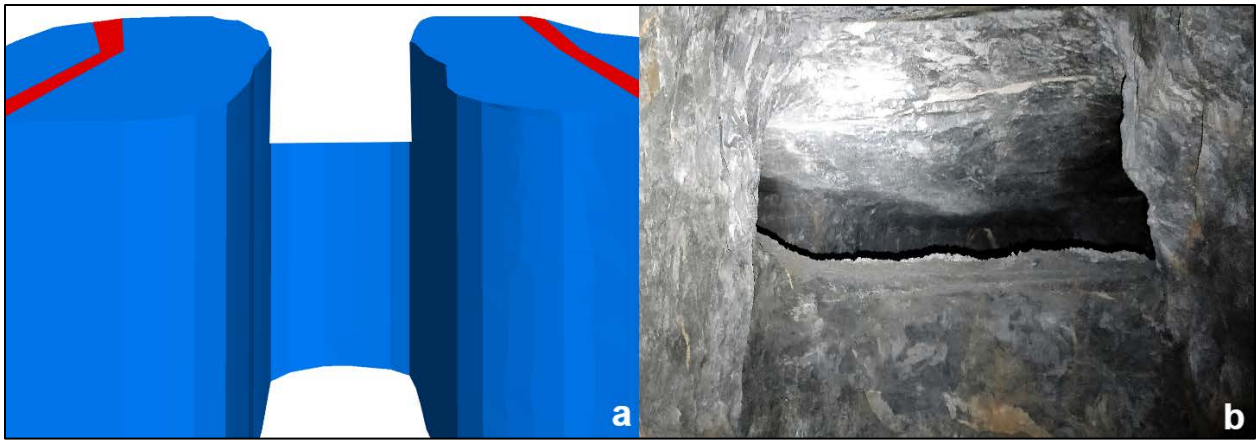

Figure 5.25 (a) Connected pillars with karst in the numerical model; (b) Picture of the connection zone in the mine.

5.5.5.1 Analysis of Strength-to-Stress Ratio

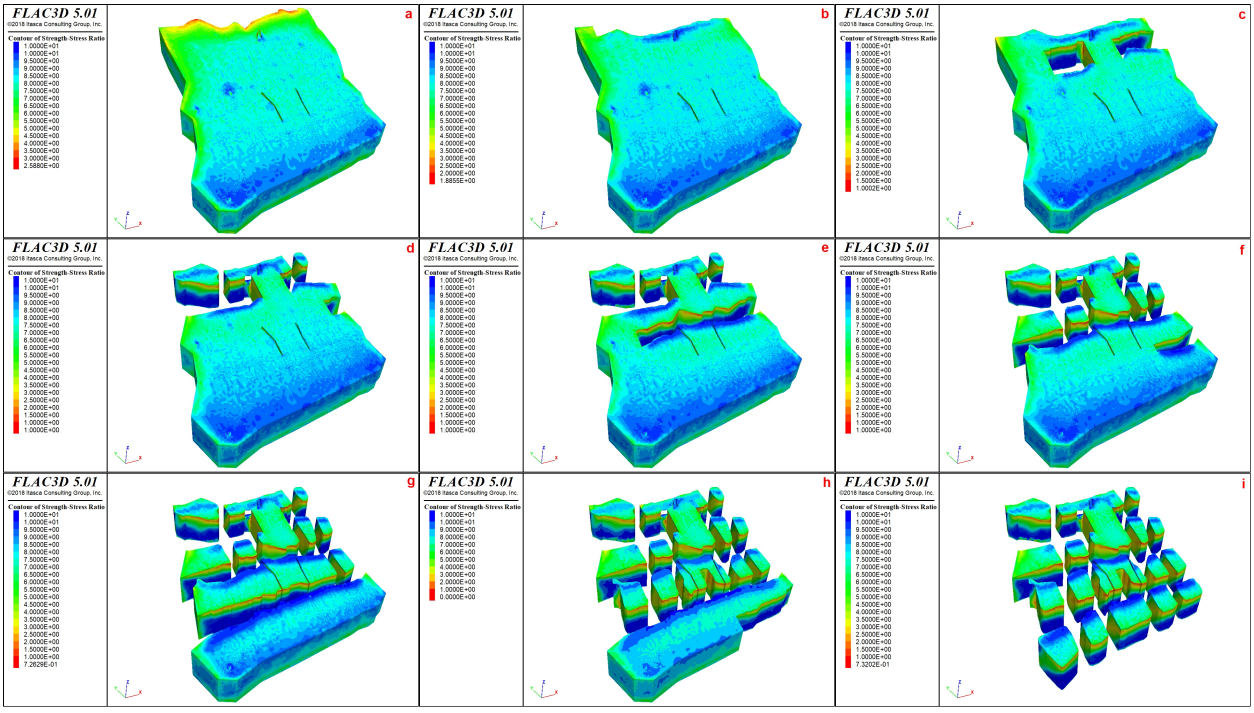

Figure 5.26 Strength-to-stress ratio for the current scenario with progressing excavation stages.

The strength-to-stress ratio for advancing excavation stages arriving at the current scenario of the mine is shown in Figure 5.26. It is observed that as the excavation progresses, there is a reduction in the strength-to-stress ratio, especially along the roof of the excavation. The bottom half of the pillar has a higher strength-to-stress ratio compared to the area adjoining the roof because of the presence of the horizontal drives supporting the bottom-rear half of the pillars. The comparison between the scenario of excavating the stopes around the karst-affected pillar in Level 6 is depicted in Figure 5.27.

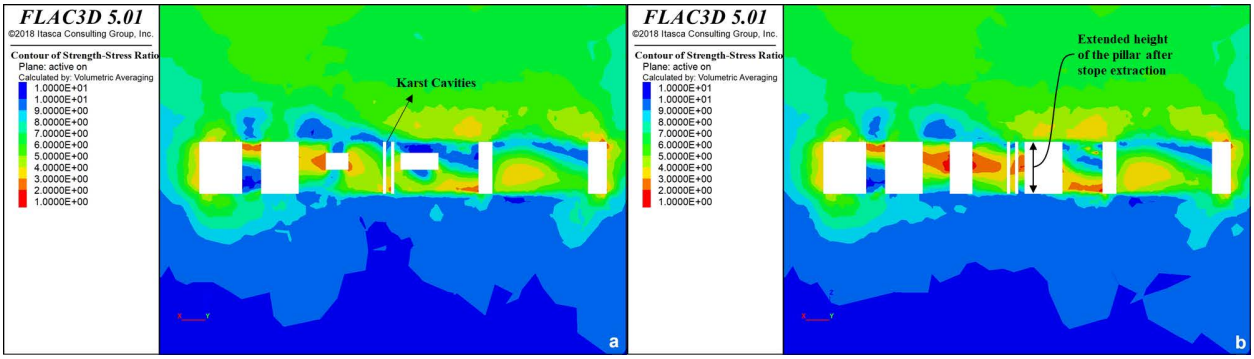

Figure 5.27 Strength-to-stress ratio around the karst pillar in level 6 during- (a)current situation; (b)benched stopes.

It can be inferred from the above Figure 5.27(a) that in the current situation, the strength-to-stress ratio for the karst-affected pillar predominantly lies in the range of about 4 to 7, which depicts high stability around it. When the stopes adjoining the pillar are excavated, as shown in Figure 5.27(b), there is a considerable production in the strength-to-stress ratio in the pillar. Especially, in the zones near the karst volumes, the ratio reduces below 3 but it still stays above 1.

5.5.5.2 Analysis of Displacement

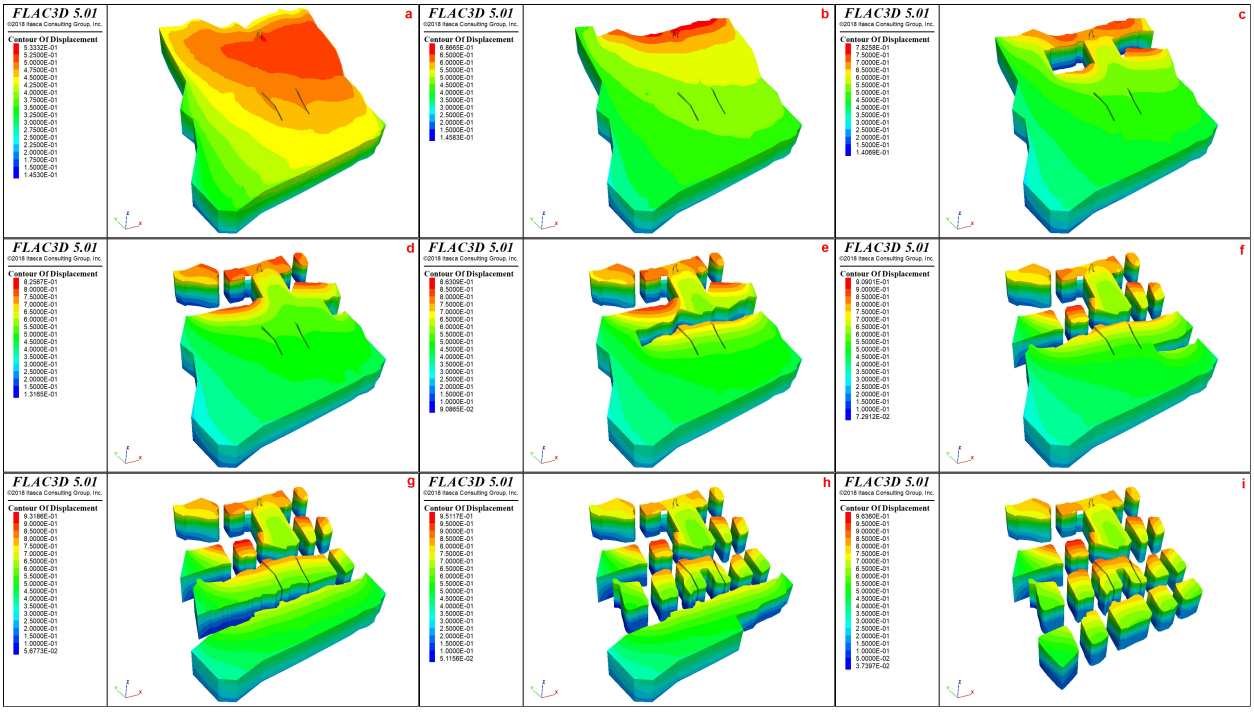

Figure 5.28 Displacement magnitude for the current scenario with progressing excavation stages.

Figure 5.28 displays the displacement magnitude around the excavation with advancing mining stages arriving at the current scenario of the mine. It is observed that as mining progresses, the magnitude of total displacement around excavation also increases due to the redistribution of stresses. The displacement around the roof is higher compared to that near the floor of the pillars or excavations. This is attributed to the extra support presented by the horizontal drives near the floor of the pillars and is consistent with the results obtained while assessing the strength-to-stress ratio near the excavations.

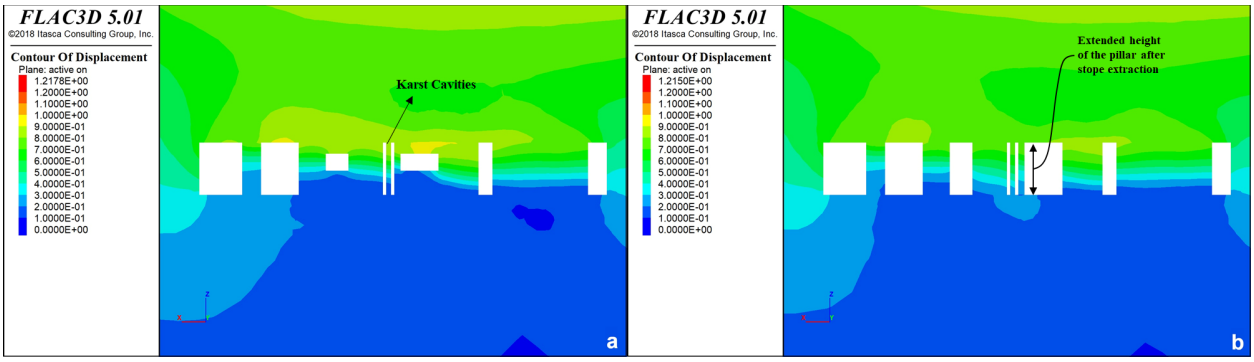

Figure 5.29 Displacement magnitude around the karst pillar in level 6 during- (a)current situation; (b)benched stopes

As the stopes near the karst-affected pillar in Level 6 are benched and completely excavated, a superior displacement is observed around the pillar compared to the current situation in the mine. The comparison between the two scenarios is shown in Figure 5.29.

5.6 Correlation Between P_{32} and Shear Strength Properties

One of the most important parameters in analyzing rock mass strength using discontinuum modeling is the incorporation of fracture intensity. Although modelers may create stochastic joint networks in software like 3DEC, it is essential to properly map discontinuities in the field and gather ample data for their reconstruction. The detailed class of fracture intensities was defined in 3-dimensions by Dershowitz & Herda [29] based on the dimensions of the discontinuity and the measurement region. These classes were defined in Fracman Manual by Golder Associates, and are represented in Figure 5.30.

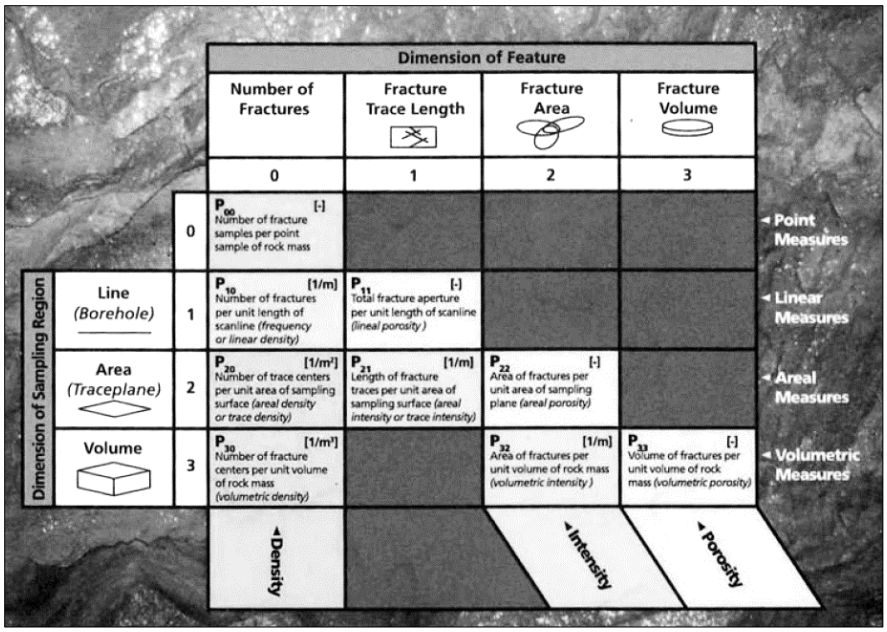

Figure 5.30 Fracture intensities explained in the P_{ij} system [48].

For this study, P_{32}, defined as the volumetric fracture density was utilized for creating the DFNs. The letter 'P' represents 'persistence', and the subscripts i=3 and j=2 define the dimensionality of the region and the joints, respectively. Therefore, P_{32} represents the area of fractures per unit volume of the rock mass. While conducting geological surveys at a site or using virtual point cloud mapping, joints interspersed in the rock mass cannot be measured practically. Only P_{10} or linear fracture intensity can be measured. Therefore, it becomes important to estimate and translate the fracture intensities in different dimensions. Many researchers have presented techniques and discussed methodologies for estimating fracture intensities and converting them to different dimensional intensities [23], [113], [123], [137], [138]. These techniques are not discussed in this dissertation.

Like physico-mechanical properties, joint networks are also not constant throughout the heterogenous rock mass. Therefore, for analyzing local-area or global stability for a mine site, it becomes important to include a variation of discontinuity network properties with

depth. This may be done by assigning different DFNs for different depth ranges when doing discontinuum modeling in software like 3DEC or using varying calibrated properties with depth for a continuum modeling software like FLAC3D.

This sub-study attempts to understand the correlation between the calibrated shear strength properties for a continuum model and the corresponding change in the volumetric fracture density (P_{32}). The common factor for establishing the correlation between the two factors is the pillar strength obtained for different shear strength properties as well as different values of P_{32}. Until now this research has discussed modifying and calibrating continuum model properties to include the weakening effect of a discontinuity network that is constant throughout the model. The main purpose of this sub-study is to understand the modification required in continuum modeling properties for a mine with a varying P_{32} with depth. This analysis does not apply to the continuum modeling performed in this chapter, since there was little to no variation observed in the joint sets throughout the local area selected for analyzing stability (Chapter 4). The relationship between the pillar strength and the parameters was determined using the trendline equations calculated using Tables 5.2 and 5.3. Table 5.6 shows the modeled values obtained for the calibrated properties of cohesion, friction angle, and dilation angles and P_{32} values using pillar strength values.

Different pillar strength values were selected for each parameter to maintain reasonable values for the shear strength properties. Using the pillar strength values for each shear strength property, a corresponding P_{32} value was determined. Despite using the different pillar strength values, the model equations were constant as derived from Table 5.3. From the values obtained in Table 5.6, the correlations between the shear strength properties and the P_{32} parameter were determined to be negative.

Table 5.6 Modeled values of different parameters calculated using different values of pillar strength.

Pillar Strength, S (MPa)	**Cohesion, C (MPa)** $C = 0.205S - 0.588$	**P_{32} (m^{-1})** $P_{32} = 9.755S^{-1.055}$	**Pillar Strength, S (MPa)**	**Friction Angle, ϕ (°)** $\phi = 0.316S + 16.693$	**P_{32} (m^{-1})** $P_{32} = 9.755S^{-1.055}$	**Pillar Strength, S (MPa)**	**Dilation Angle, ψ (°)** $\psi = 4S - 227.5$	**P_{32} (m^{-1})** $P_{32} = 9.755S^{-1.055}$
55	10.704	0.142	15	21.430	0.560	60	12.500	0.130
60	11.730	0.130	20	23.009	0.414	61	16.500	0.128
65	12.757	0.119	25	24.588	0.327	62	20.500	0.125
70	13.783	0.110	30	26.167	0.270	63	24.500	0.123
75	14.810	0.103	35	27.746	0.229	64	28.500	0.121
80	15.836	0.096	40	29.325	0.199	65	32.500	0.119
85	16.863	0.090	45	30.904	0.176	66	36.500	0.117
90	17.889	0.085	50	32.483	0.157	67	40.500	0.116
95	18.916	0.080	55	34.062	0.142	68	44.500	0.114
100	19.942	0.076	60	35.641	0.130	69	48.500	0.112
105	20.969	0.072	65	37.220	0.119	70	52.500	0.110
55	10.704	0.142	15	21.430	0.560	60	12.500	0.130

A strong negative correlation indicates that when the shear strength properties increase, the volumetric fracture density decreases. Therefore, an inversely proportional relationship can be established for varying the shear strength properties for a continuum model where fracture density is varying with depth. It is emphasized that thorough joint mapping surveying should be done for different sites at a mine to translate the discontinuum effect of varying DFNs to continuum models. Figure 5.31 shows the correlation determined for the shear strength properties and the corresponding P_{32} values.

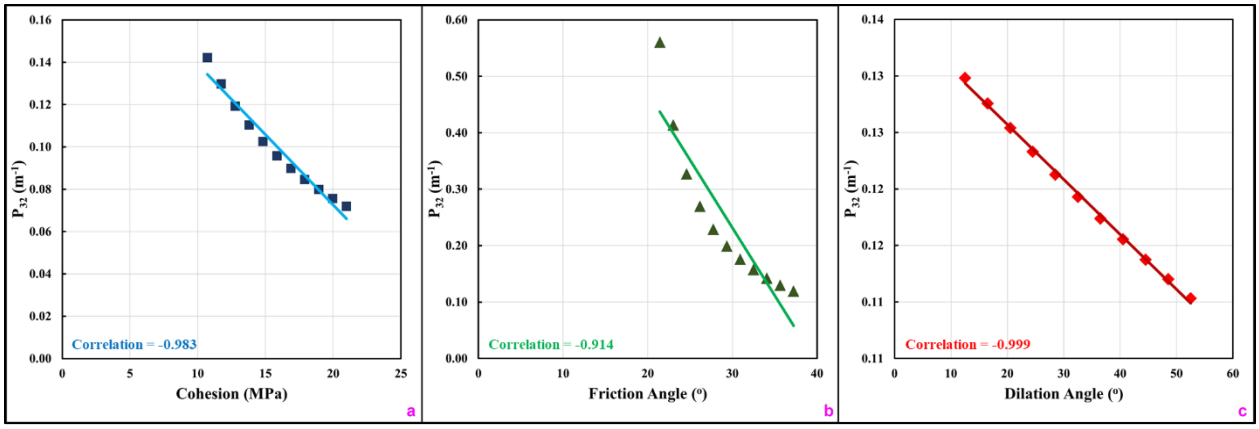

Figure 5.31 Correlation was determined for the shear strength properties and the corresponding P_{32} values.

5.7 Conclusions and Scope

This research presents a parametric study to understand the benefits and shortcomings of the discontinuum and continuum modeling simulations. The discontinuum modeling is effective for replicating the behavior of a blocky rock mass such as limestone, where discontinuities have a prominent effect on the strength of rock mass. It has the advantage of establishing a stochastic joint network created using geological mapping data. Whereas continuum models treat rock mass as a fracture-less entity but can still be adjusted to incorporate their effect with the correct calibration of physico-mechanical properties. This study makes an effort to translate the weakening effect of joints and fractures from discontinuum models to continuum models. It does that by studying the effect of shear strength properties and elastic moduli on the strength of rock mass and modifying them to incorporate the influence of a Discrete Fracture Network (DFN) on pillar strength. The following conclusions can be drawn from this research:

a) Discontinuum modeling using 3DEC provides one of the most accurate ways of determining pillar strength by representing fractured rock masses as an assembly of discrete blocks connected by the discontinuities represented by a DFN.

b) The volumetric fracture density or P_{32} has a profound effect on pillar strength. It can be estimated with the help of geological mapping of joint sets or using manual virtual point cloud mapping obtained using laser scanning or photogrammetry.

c) Shear strength properties play a major role in deciding rock mass behavior. Pillar strengths were compared by varying the properties including cohesion, friction angle, and dilation angle. A subsequent sensitivity analysis revealed that cohesion or cohesive strength has the highest effect on rock mass behavior followed by friction angle and dilation angle.

d) While the shear strength properties decide the ultimate strength of the pillar, elastic moduli define the rock mass behavior in terms of the stress-strain relationship before the yielding zone of the pillar. The bulk and shear modulus properties of the intact rock mass were also adjusted to calibrate the continuum model in FLAC3D.

e) The parametric and sensitivity analyses were cardinal to calibrate the continuum model and replicate the behavior of a discrete, jointed rock mass as observed during discontinuum modeling in 3DEC. Using the adjusted properties, a local area of the case study mine was numerically simulated.

f) It was observed that continuum modeling using FLAC3D is most effective when analyzing large sections of a mine. The total simulation time for a single pillar in 3DEC was 52 hours, whereas the local area model included multiple pillars and headings, and was simulated in 28 hours. This validates that continuum modeling

may prove less computationally intensive and takes considerably less time compared to a full-scale discrete element model in 3DEC.

g) The study was successful in analyzing the stability of a local area in the mine. The simulated model consisted of multiple pillars and heading and imitated the mining sequence that was implemented in the field. The model was highly useful in analyzing the ground control issues that the mine has faced due to the prevalent karstic network in the mine deposit. This also helps understand any alternative scenario that the mine management could have implemented to optimize ore recovery while improving safety.

This research also discusses the relationship between the shear strength properties and the varying spatial fracture density with depth. There was a strong negative correlation between the two domains. This was expected because when the high shear strength results in a higher rock mass strength, a higher fracture density leads to a decrease in the pillar strength. This finding could not be implemented in for the local-area analysis as all the mine levels in it were found to have similar joint distribution. Nevertheless, the results will be very useful for evaluating the behavior of excavations in a large, global mine model with a joint network varying with depth. In many multi-level underground mines, the physico-mechanical properties of rock mass are observed to vary with a change in mining depth. By understanding the relationship between the variation in properties or the Geological Strength Index (GSI) of the rock mass with depth, further studies could be conducted to understand the scaling of properties and subsequent calibration for such a model. This research will also be useful in analyzing improved alternative designs for existing underground stone or metal mines, which may later be implemented to enhance secondary recovery while maintaining ground stability.

Chapter 6

Stochastic Analysis using Finite Volume Modeling for Variation of Pillar Dimensions with Depth for a Karst-Prone Hard Rock Mine[5]

6.1 Introduction

The global limestone market stood at US$58.5 billion in 2020, with the United States accounting for 27% of the market share. It is projected to reach a target of US$65.3 billion in the year 2027, growing even in midst of the COVID-19 pandemic [148]. At present, 109 underground stone mines are operating in the country, with a majority of them expected to reduce the production burden of the surface mines as the resources deplete [111].

With the increasing investments and research efforts to meet the market demand, optimizing the extraction of valuable resources becomes necessary. Although the economic recovery is essential, preventing risks and ensuring the safety of miners should be the cardinal objective of the mining operations. Ground control in underground operations is a complex task compared to surface mines. Hence, it is important to improve the local and

[5] The prepared manuscript for this chapter will be submitted for journal publication to the Journal of Rock Mechanics and Rock Engineering upon review by the co-authors.

global stability in an underground mine. According to the Mine Safety and Health Administration (MSHA), 15% of all injuries at underground mines are caused due to falls of ground since 2000. In terms of occupational fatalities at all underground mines, this number grows to about 31%, and 39% for underground stone mines [108].

Since 2015, five incidents of massive pillar collapses have occurred in four underground stone mines located in Pennsylvania and Tennessee (MSHA, 2021). Although these collapses did not result in any direct injuries, they were responsible for generating air blasts that resulted in three serious injuries. Pillars are the backbone of a room-and-pillar mining operation. Any weakening of these structures can not only compromise the regional stability but also has a causal effect like subsidence and air blasts which are capable of harming miners working far away from the hazard site. Zipf [147] used the term 'catastrophic pillar failure (CPF)' to describe the phenomena of multiple pillar failure for hard rock metal mines. Mark et al. [96] discussed the mechanics of massive pillar collapses in form of a domino effect, where the breaking of pressure arch causes the failure of an array of adjacent pillars. Multiple researchers have discussed the safe practices for designing underground stone pillars and emphasized having a prevention approach for maintaining stability [35], [62], [80], [93]. All these studies have commonly discussed the significance of parameters including extraction ratio, width-to-height ratio, containment or barrier pillars, strata stresses, or geological features like discontinuities in assessing the stability of excavations.

Kortnik [81] presented the techniques and devices used for optimizing the mining of natural stone blocks in Slovenian mines using continuous instrumentation monitoring of high safety pillars. The National Institute for Occupational Safety and Health (NIOSH) published pillar and roof span guidelines for underground stone mines which mentioned empirical, analytical, and numerical approaches for estimating pillar performances [40]. The circular covered a

wide range of topics for geotechnical characterization, heading orientation, pillar design, roof horizon, span selection, stress measurements, and monitoring for analyzing the stability of underground mines.

In the past, several authors have published literature that discusses numerical investigations of groundwater inrush from karst collapse pillars for underground coal deposits [90], [92], [143]. There is also a vast amount of literature available for geological and laboratory investigations followed by geomechanical modeling for underground carbonate deposits [1], [3], [45], [86], [91], [95], [115]. But no scholarly articles or case studies are available for optimizing ore recovery or improving pillar design through numerical analyses for a karst-affected underground stone mine. The research discussed in this chapter attempts to understand optimizing pillar design for a case study stone mine using continuum modeling. The objective of suggesting improvised design over the existing room-and-pillar layout of the mine is to improve ore recovery while maintaining safe working conditions. The research dovetails the importance of ground control through pillar design while including karst voids in the numerical model based on geological surveys conducted at the site. The study may be useful to understand the effective use of stochastic analysis for estimating the feasibility of mining or secondary recovery in stone mines with a dominating discontinuity network and prevalent karst terrane.

6.2 Background

6.2.1 Geologic Setting of the Deposit

The case study mine is a lime-feedstock mine located in the Five Oaks limestone formation, which produces high calcium limestone. The geologic structure of the mine area is in an

anticline-syncline pair in a middle- to lower-Ordovician-age limestone deposit. The room-and-pillar mining method is modified to extract ore from the 30° formation dip. The development through rooms and crosscuts is about 12.8 m wide and 8 m high. After the top and bottom headings are mined, rooms are benched to a height of 30.5 m, leaving massive pillars with a square base dimension of 24.5 m x 24.5 m. The bedding plane parting at the top of the deposit is filled with calcite in most parts of the mine and is removed to leave a generally inclined roof. Figure 6.1 shows the massive, inclined pillars in the case study mine.

Figure 6.1 Tall, inclined pillars in the case study mine.

The multi-level room-and-pillar mine has a corkscrew-designed ramp that branches off and divides the mine into east and west sections. Figure 6.2 shows the layout of the mine with the highlighted area showing the region selected for numerical modeling in this chapter. The highlighted zone spans eight levels from top to bottom and across nine pillars on each level. In the mine operator's terminology, these levels are numbered starting from Level 6 through Level 13.

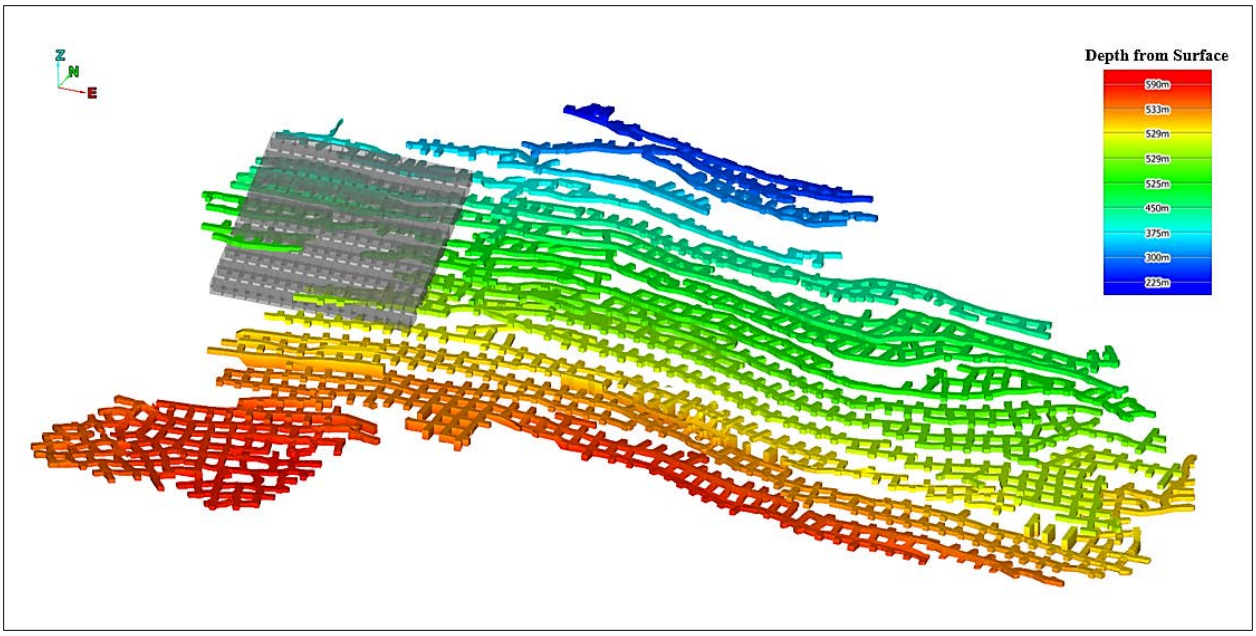

Figure 6.2 Highlighted area in gray showing the simulated area in the case study mine.

6.2.2 Karst Terrane

An extensive joint and fracture network in brittle carbonate deposits allow the movement of groundwater through them, which leads to erosion of rock. Over time, excessive erosion leads to the formation of clay-filled voids or 'karsts' [47]. The case study mine has a prevalent network of karst cavities which has been responsible for many ground failure incidents with no injuries to mining personnel, fortunately. In the past, the development of headings or benching of pillars with these voids has disrupted the mining operations and has been economically detrimental to the mine operator. The management often resorted to secondary ground support through the installation of mesh, roof bolts, or grouting for countering the collapse of sidewalls or roofs at the mine. Figure 6.3 shows the karst openings at the mine and the ground control measures.

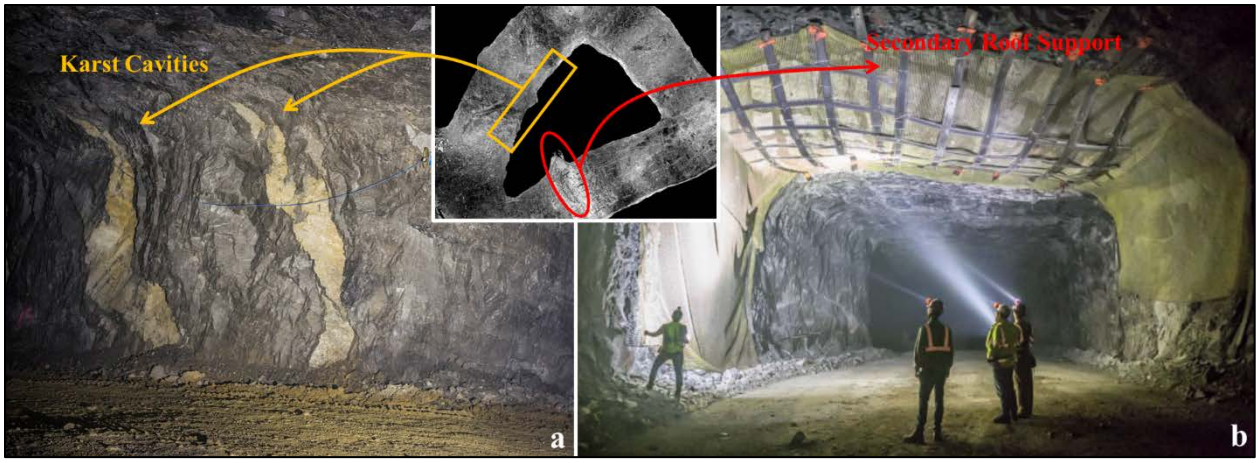

Figure 6.3 (a) Karst cavities in a pillar; (b) Secondary ground supports installed as a countermeasure.

6.3 Pillar Design Using Empirical and Analytical Approaches

The design of safety pillars for underground mines using empirical and analytical approaches has been studied by many researchers. The majority of empirical relationships have been derived using back analysis of case histories providing ample data to establish equations. Almost all the successful pillar design equations have been established by comparing failed and stable pillars in the same geological setting. Similar to coal pillar designs, empirical equations for hard rock pillars have been developed using dimensions of pillars, the factor of safety, and physico-mechanical properties of intact rock backed by laboratory testing [55], [76], [82], [88], [125]. For understanding the pillar design for the case study mine, the equation based on pillar confinement developed by Lunder & Pakalnis is used [88]. This empirical approach was based on the 178 case histories of pillars in the Canadian hard rock mines. The authors classified the pillars based on their factor of safety and approach can be stated as:

$$S = K^{*}UCS^{*} (C_1 + C_2^{*}) \quad (9)$$

where S is the ultimate pillar strength (MPa), K is the rock mass strength size factor, UCS is the uniaxial compressive strength of the intact rock (MPa), C_1 and C_2 are the empirical rock mass constants and κ (kappa) is the friction term which can be calculated as:

$$= \tan\left(\cos^{-1}\left[\frac{1-C_{pav}}{1+C_{pav}}\right]\right) \quad (10)$$

where C_{pav} is the average pillar confinement and can be determined as,

$$C_{pav} = C_p\left\{\log\left(\frac{W}{H}+0.75\right)\right\}^{1.4\frac{W}{H}} \quad (11)$$

where C_p is the coefficient of pillar confinement, W is the pillar width, and H is the pillar height. The values for C_1, C_2, K, and C_p were set to be 0.68, 0.52, 0.44, and 0.46, respectively. These values are based on the research by Esterhuizen [37] based on pillar performances in underground limestone mines in the eastern United States. Based on the pillar dimensions in the mine, the width-height ratio of the pillars is calculated to be 0.8.

A popular alternative to empirical equations is using analytical approaches, which have become common to perform risk analysis and the failure probability of pillars. The analytical methods are based on physics and mathematical principles combining the mechanical behavior of materials and static equilibrium [79]. These are used to establish the strength-to-stress ratio (factor of safety) for the pillars for different pillar geometries. However, these methods fail to describe the failure mechanics of the rock mass and the geotechnical variation in rock conditions across different deposits or in a mine. Lunder & Pakalnis [88] suggested the possibility of analyzing pillar stress using the tributary area method and

conducting extensive computational analysis for determining the factor of safety [19]. Figure 6.4 shows a cross-section through square-base pillars in a dipping flat deposit, similar to that of the case study mine.

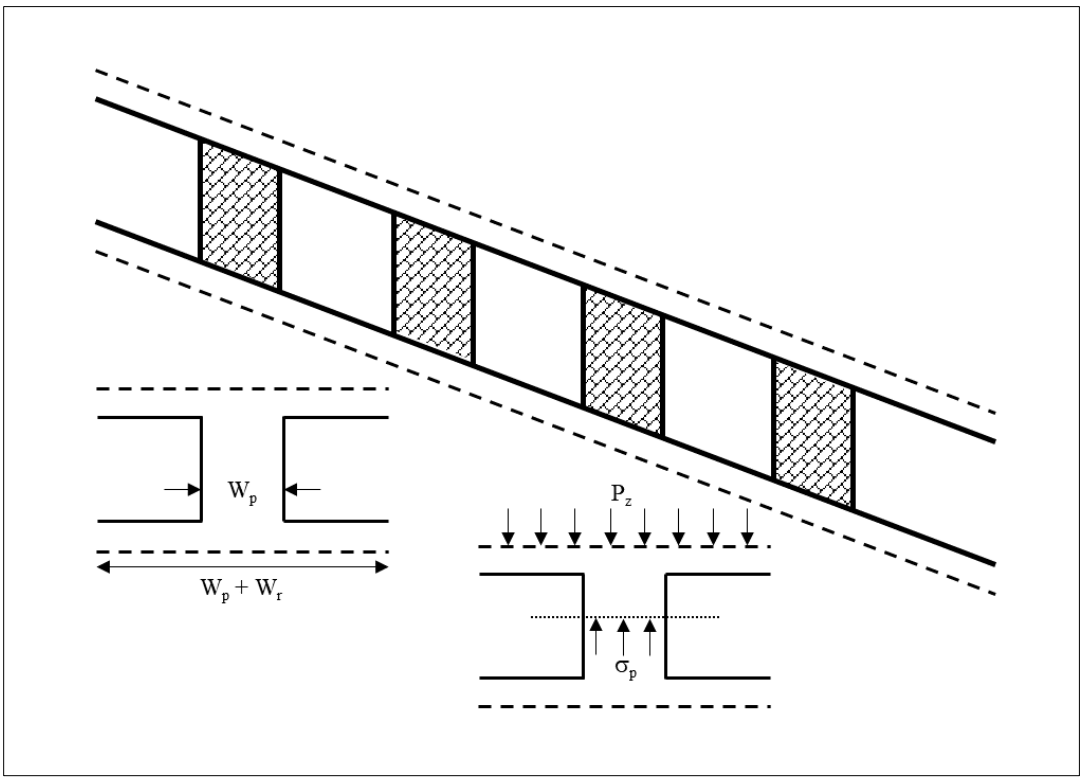

Figure 6.4 Cross-section of a uniform dipping deposit mined using the room-and-pillar method for calculating pillar stresses (Modified after Brady & Brown [19])

The equation to estimate the average axial stress in a pillar as shown in Figure 6.4 can be approximated as [140]:

$$_{p} = (\ \ .g.h)*\left\{\frac{(W_{r1}+ W_{p1}).(W_{r2}+ W_{p2})}{(W_{p1}* W_{p2})}\right\} = P_{z}*\left\{\frac{(W_{r1}+ W_{p1}).(W_{r2}+ W_{p2})}{(W_{p1}* W_{p2})}\right\} \quad (12)$$

where,

W_{r1} - the room's width (m),
W_{r2} - the room's length (crosscut), (m)

W_{p1} - the pillar's width, (m),
W_{p2} - the pillar's length, (m),
 - the density of overburden strata, (kg/m^3),
g - the acceleration due to gravity, (m/s^2),
h - the overburden thickness, (m),
P_z - the axial normal component of the in situ stress field, (MPa).

The relationship in equation 12 compares the post-mining axial stress levels to the variation in overburden and extraction ratio in the mine. The tributary area theory is based on the effect of overburden load on the stresses in a pillar, and their association with the area supported by the pillar and the area of the pillar.

To consider the variation in overburden thickness over each mining level caused due to the undulated topography, an average overburden thickness was considered for each level. This was based on the topographic contour existing above each level as shown in Figure 6.5.

Based on the dimensions of the pillars in the mine, a laboratory tested uniaxial compressive strength of 160 MPa, and a density value of 2690 kg/m^3, the strengths and average stresses on pillars in each level are calculated and mentioned in Table 6.1.

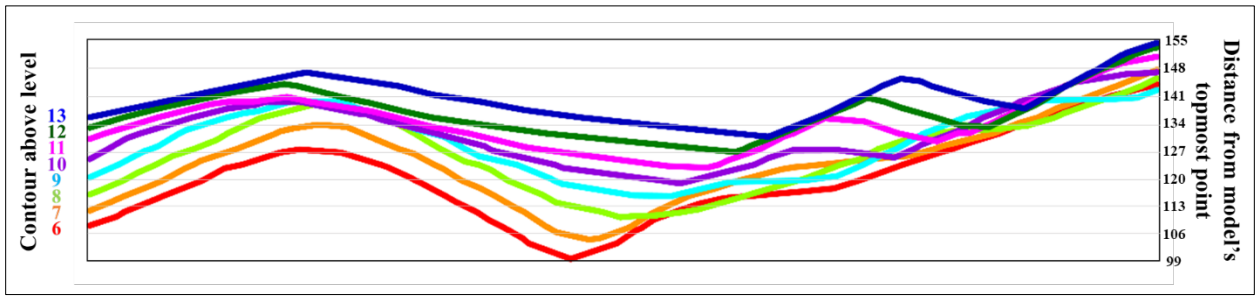

Figure 6.5 Topographic contours above each mining level and their relative distance from the model's topmost point.

Table 6.1 Average stresses and strength of pillars calculated using analytical and empirical methods.

Mine Level	**Tributary Area Stresses (MPa)** (Wagner & Frömmer Equation [140])	**Pillar Strength (MPa)** (Lunder & Pakalnis Equation [88])	**Factor of Safety**
6	10.38	57.21	5.51
7	12.64	57.21	4.53
8	14.64	57.21	3.91
9	16.68	57.21	3.43
10	18.84	57.21	3.04
11	20.83	57.21	2.75
12	23.01	57.21	2.49
13	25.14	57.21	2.28

Lunder and Pakalnis [88] classified the pillars with FOS less than 1 as failed, those with FOS between 1 and 1.4 were considered unstable, and the pillars with FOS greater than 1.4 were classified as stable. Esterhuizen et al. [43] suggested a FOS of greater than 1.5 as reasonable, based on the research of case histories for the design of room-and-pillar workings in limestone mines in the Eastern and Midwestern United States. The S-Pillar software and related literature developed by NIOSH recommend having a minimum FOS of 1.8 for underground pillars [36]. Based on Table 6.1, the regulation-size pillars in the case study mine should have a decent factor of safety (FOS). However, these equations do not factor in the presence of discontinuities and karst voids in the mine, the interaction of which is responsible for triggering ground-related issues. For this reason, it is important understand the rock mass behavior using the numerical methods which are explained in detail in the next section.

Figure 6.6 shows the average factor of safety achieved for each level using the analytical models and the numerical simulations explained later in Section 6.5.1 of this dissertation. It is observed that the empirical and analytical equations highly overestimate the FOS for

the pillars, especially in the shallower levels. It is believed that any design consideration made by overestimating a pillar's strength may prove dangerous, as the real strength may not be able to counter the redistributed stresses.

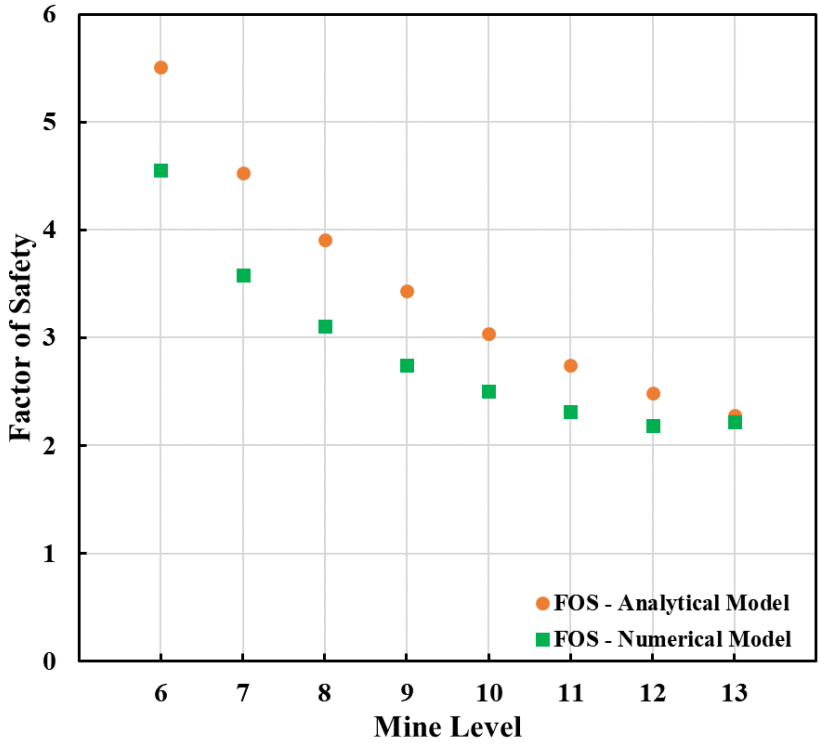

Figure 6.6 A comparison between the factor of safety estimated using analytical and numerical models.

6.4 Finite Volume Modeling with FLAC3D

Numerical modeling techniques are highly effective for estimating variation in stresses and strain for a rock mass. Although they are computationally intensive, they can accommodate minute details which are important for assessing a particular model. The numerical methods can also capture complex phenomena of rock mass such as non-linear material behavior, large strain or displacement, yield or failure zones, hydrogeological factors, and simulate the

effect of discontinuities on overall stability. All these factors provide numerical methods an edge over the other techniques for planning safety pillars in underground excavations.

For this study, FLAC3D (Fast Lagrangian Analysis of Continua in 3 Dimensions), developed by Itasca Consulting Group, was used. This software uses explicit finite-volume modeling to simulate rock mass as a continuum material. Although limestone is best represented as a discrete block assembly featuring an extensive joint and fracture network, a successful calibration of the rock mass to continuum properties was achieved in Chapter 5. This helps reduce the simulation time as well as computational burden and is useful in analyzing the local and global stability using the numerical model.

6.4.1 Model Geometry

The recreated and simplified model for the case study mine is shown in Figure 6.7. The simulated model spans eight levels from top to bottom and across nine regulation-size pillars on each level. The pillars are vertically aligned along their axis with an inclined top and bottom face. They have a square base dimension of 24.5 m x 24.5 m, and a height of 30.5 m. The footwall and hanging wall drives are equal in dimensions and are approximately 12.8 m wide and 8 m tall. The model reflects the ideal excavation dimensions that were planned by the mine management.

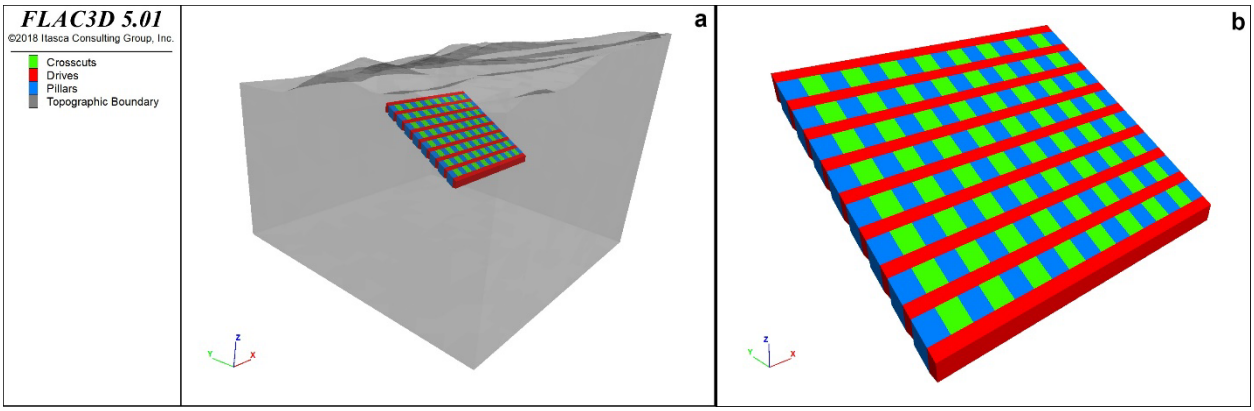

Figure 6.7 Simulated section of the mine within the topographic boundary showing crosscuts, drives, and pillars.

6.4.2 Boundary Conditions and In Situ Stresses

The sides and bottom of the model's artificial boundary in Figure 6.7(a) were fixed in all directions. Boundaries were not applied to the topographical surface on the top. Also, the artificial boundaries on the side were far enough from the deposit domains to avoid any influencing forces in the simulated zone.

In situ stresses were estimated by the mine operator using measurements from multiple boreholes. Borehole Deformation Gage (BDG) in accordance with the United States Bureau of Mines (USBM) overcoring drilling technique was used to obtain subsurface stress measurements [13], [60]. A vertical stress gradient of 0.0416 MPa/m and a horizontal stress gradient of 0.0143 MPa/m was estimated for the site and was applied to the in situ condition of the model. The maximum principal in situ stress was found to be near-vertical and is not typical of most in situ measurements made in North America [53], [56], [57]. This high vertical stress gradient as compared to a general stress gradient of 0.0265 MPa/m was found to be conforming with the prior findings in similar limestone environments [83], [9]. The

sign convention used during the study is negative for the compressive stresses and positive for the tensile stresses.

6.4.3 Physico-mechanical Properties

The geotechnical properties of the ore rock and host rocks are provided in Table 5.5. The properties were estimated by calibrating the discontinuum model properties that include the effect of discontinuities on the strength of the rock mass. A detailed process for calibration of properties to be used for continuum modeling is provided in Chapter 5.

Mohr-Coulomb constitutive model was assigned to simulate the behavior of the continuum rock mass. The model. FLAC3D implements the failure envelope for the Mohr-Coulomb criterion with a shear yield function and tension cutoff rule.

6.4.4 Excavation Sequence

This mining process in this research attempts to follow the ideal mining sequence planned and followed by the mine operator. To achieve this, the drives are excavated 10 m or 30 ft in a single advance and the model was allowed to reach equilibrium before another planned advance. The stopes are benched in two advances, thus leaving a 30.5 m or 100 ft high pillar. Dynamic modeling to simulate the blasting vibrations is not planned for this study. Also, it is assumed that no overbreak is generated during blasting. Figure 6.8 shows the mining sequence used to simulate the numerical model along with the maximum unbalanced forces in the model.

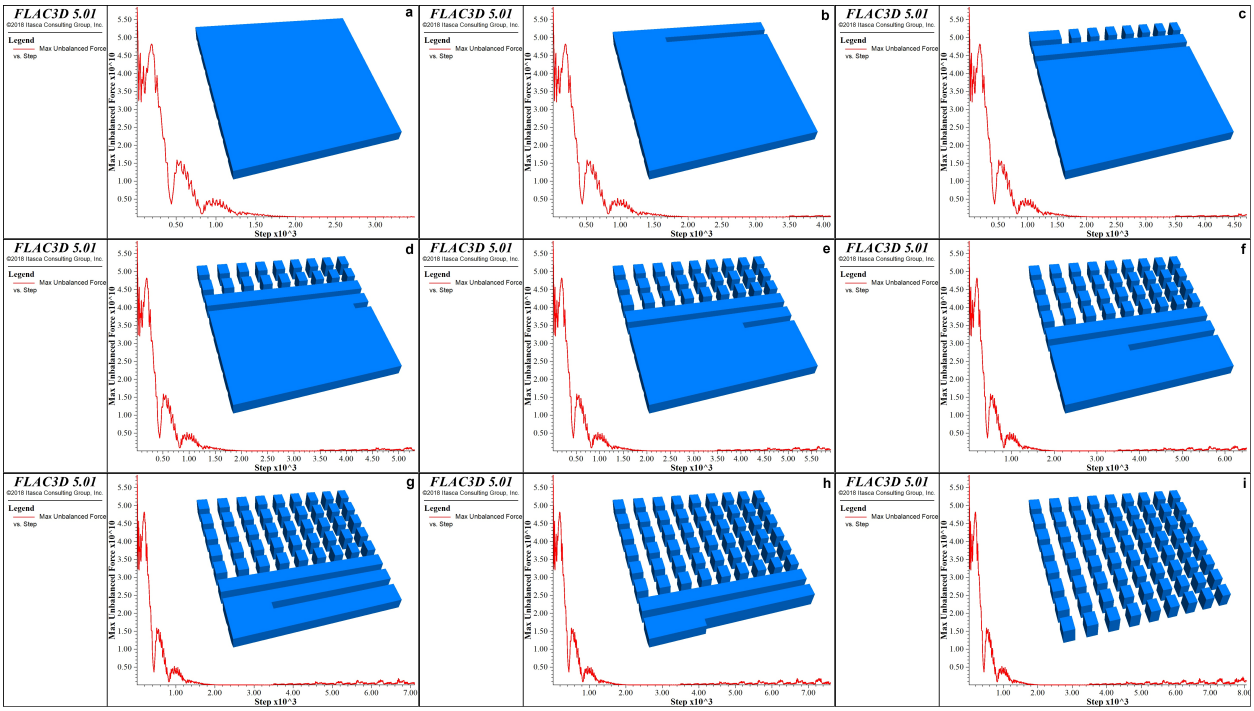

Figure 6.8 Different simulation stages show the replicated excavation sequence at the mine.

6.5 Karst-Free Mine Model Simulation

This section simulates the mine model by assuming no presence of any karst cavities in the deposit. The results achieved from this simulation will serve as a benchmark and can be compared to later models simulated with karsts to understand the effect of cavities on the strength of the pillars.

6.5.1 Original Room-and-Pillar Layout

The existing, ideal room-and-pillar layout of the mine is shown in Figure 6.9. For ease of identification, each level is labeled from 6 to 13, and each column of pillars across these levels is labeled from A to I.

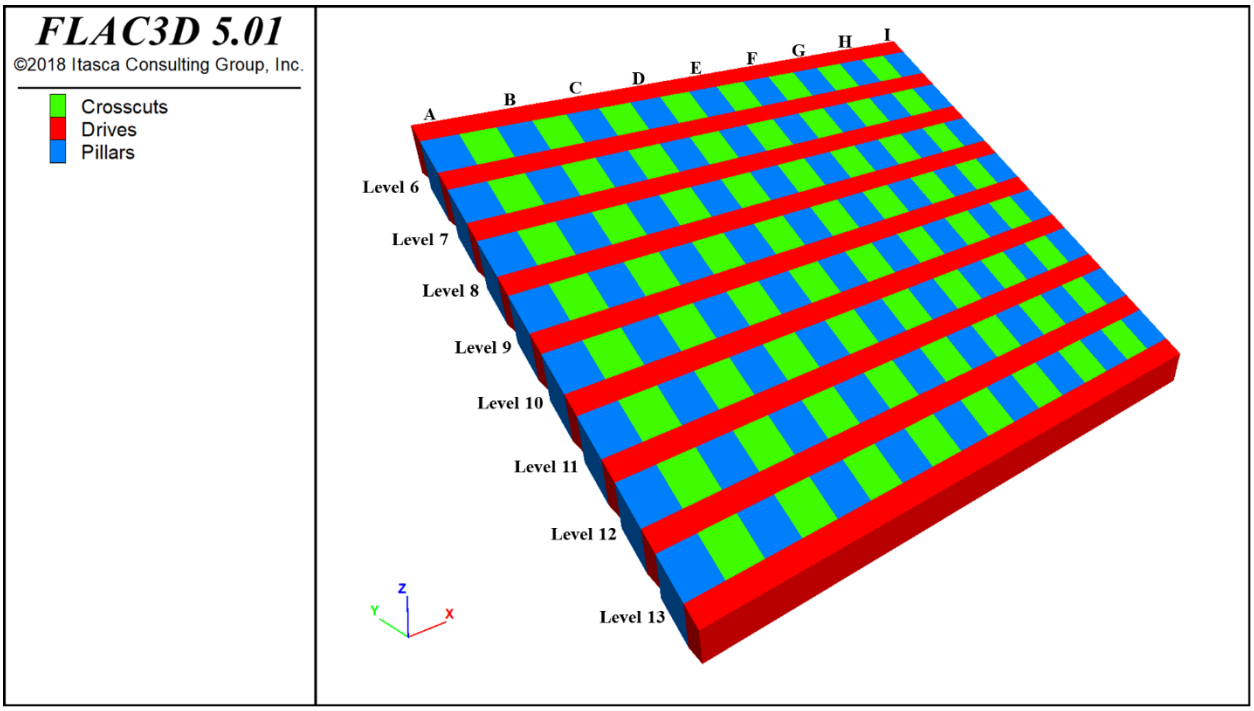

Figure 6.9 Original room-and-pillar layout of the mine showing the crosscuts, drives, and pillars.

Figures 6.10 and 6.11 show the pre-mining and post-mining contours of axial stresses and FOS across the deposit, respectively. It may be observed that Figure 6.10 shows the redistributed vertical stresses after the complete excavation through the deposit and the corresponding behavior is observed in Figure 6.11.

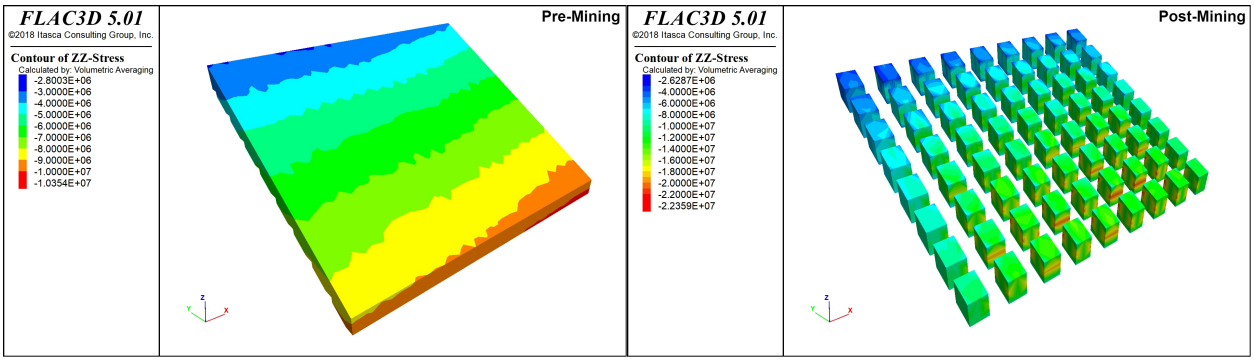

Figure 6.10 Contour of vertical stresses for pre- and post-mining state, respectively for karst-free original model.

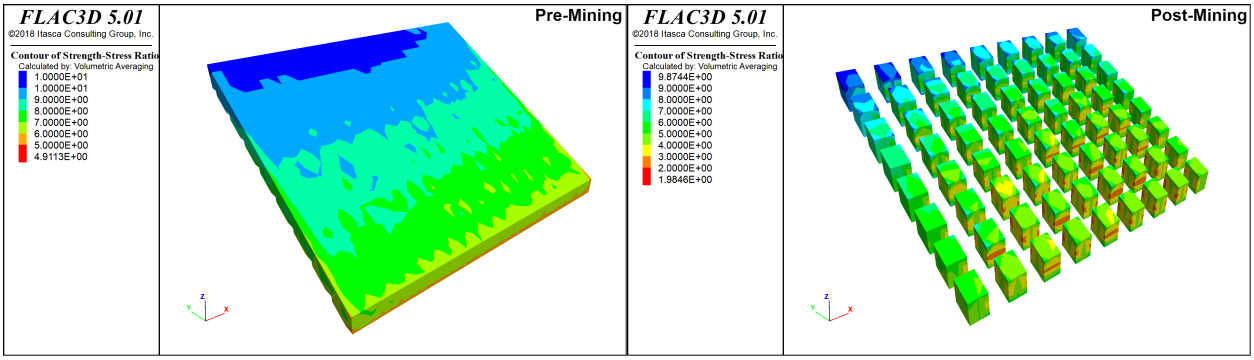

Figure 6.11 Contour of factor of safety for pre- and post-mining state, respectively for karst-free original model.

6.5.2 Modified Room-and-Pillar Layout

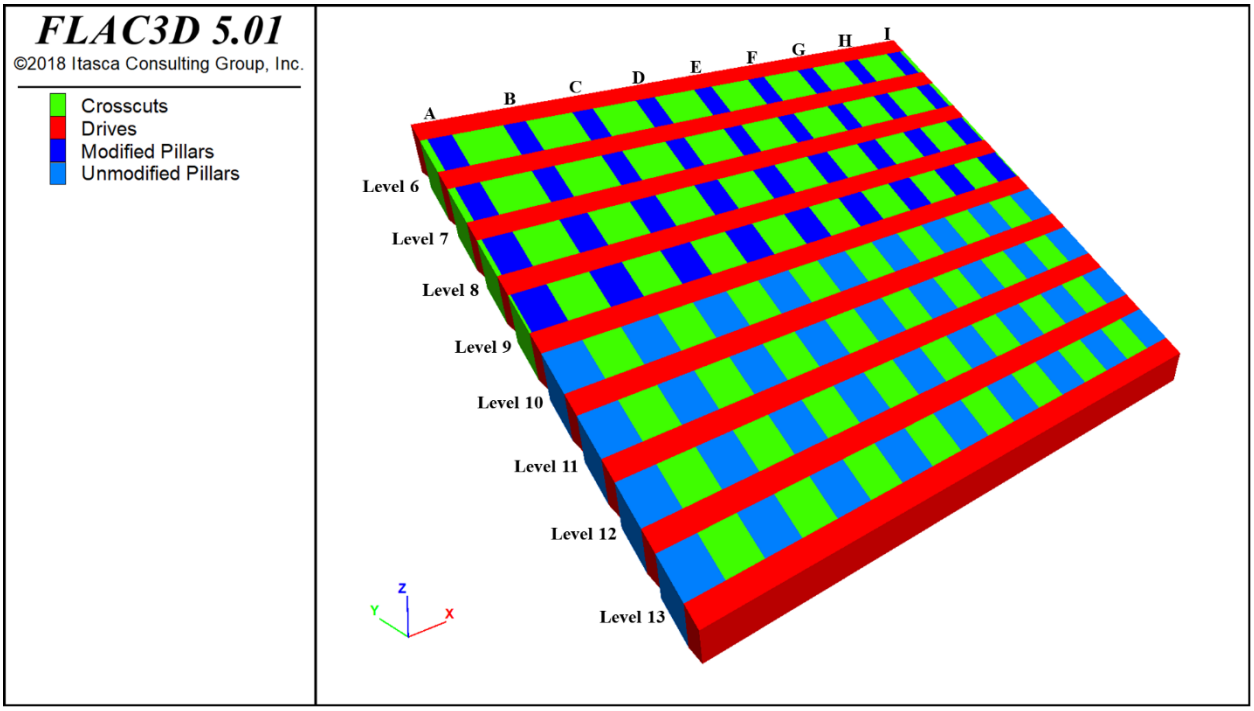

Figure 6.12 Modified karst-free room-and-pillar layout of the mine showing the crosscuts, drives, and pillars.

Figure 6.12 shows the modified room-and-pillar layout of the case study. As observed from the figure, only the dimensions of the pillars in the top four levels have been modified. The modification has been introduced by reducing the width of the pillar along the strike of the orebody. This changes the previously existing base dimensions of the pillar to a rectangular base dimension with the width along the dip kept constant at 24.5 m. The height of all the pillars is kept constant at 30.5 m or 100 ft. The original and modified dimensions of the pillars in each level are mentioned in Table 6.2.

Table 6.2 Originally planned pillar dimensions compared to modified pillar dimensions.

Mine Level	Original Pillar Dimensions			Modified Pillar Dimensions		
	Width along strike (m)	Width along Dip (m)	Height (m)	Width along strike (m)	Width along Dip (m)	Height (m)
6	24.5	24.5	30.5	15.25	24.5	30.5
7	24.5	24.5	30.5	15.25	24.5	30.5
8	24.5	24.5	30.5	18.3	24.5	30.5
9	24.5	24.5	30.5	21.35	24.5	30.5
10	24.5	24.5	30.5	24.5	24.5	30.5
11	24.5	24.5	30.5	24.5	24.5	30.5
12	24.5	24.5	30.5	24.5	24.5	30.5
13	24.5	24.5	30.5	24.5	24.5	30.5

6.5.2.1 Width-to-Height (W/H) Ratio

When the performance of pillars is analyzed using the tributary area method as described in Section 6.3, it is determined that the strength of a pillar is dependent on its bulk volume as well as its shape [19]. Many researchers have studied the effect of geometric shapes on a pillar's strength [54], [124]. Wagner [139] conducted a study on the design of pillars in coal mines and suggested that for pillars with an irregular shape, the operating area is of the

most importance. The operating area was defined as the area derived by the pillar dimensions normal to its axis. It was proposed that pillar strength is substantially affected by the relative dimensions of its operating area. This was used to estimate the effective width (W_{eff}) of irregular-shaped pillars, which could be stated as:

$$W_{eff} = \frac{4A_p}{C} \tag{13}$$

where C is the circumference of the pillar and A_p is the pillar operating area. Based on the above formula, the effective width-to-height ratios of the modified pillars in the case study mine are provided in Table 6.3.

Table 6.3 Effective Width-to-Height ratios for modified pillars.

Mine Level	**Width along strike, W_s (m)**	**Width along Dip, W_d (m)**	**Height, H (m)**	**Pillar Operating Area, A_{op} (sq. m)**	**Effective Width, W_{eff} (m)**	**Effective Width-to-Height Ratio, (W_{eff}/H)**
6	15.25	24.50	30.50	373.63	18.80	0.62
7	15.25	24.50	30.50	373.63	18.80	0.62
8	18.3	24.50	30.50	448.35	20.95	0.69
9	21.35	24.50	30.50	523.08	22.82	0.75
10	24.5	24.50	30.50	600.25	24.50	0.80
11	24.5	24.50	30.50	600.25	24.50	0.80
12	24.5	24.50	30.50	600.25	24.50	0.80
13	24.5	24.50	30.50	600.25	24.50	0.80

6.5.2.2 Justification for Modification

The decision behind the modification of pillars in the top four levels is based primarily on two factors: (i) Maintaining a threshold factor of safety and, (ii) Avoiding buckling for

slender pillars. As mentioned before many studies suggest maintaining a minimum factor of safety of 1.5 for the pillars. Since this deposit has an extensive karst network, there should be a conservative margin when deciding FOS values for designing pillars. This is to prevent any sudden ground collapse issues in the future if any karst cavity is discovered in a pillar structure. Figure 6.13 shows the average factor of safety determined for pillars in each level for the original and modified FLAC3D models. It was decided to keep the FOS values to a minimum of 2 for the pillars.

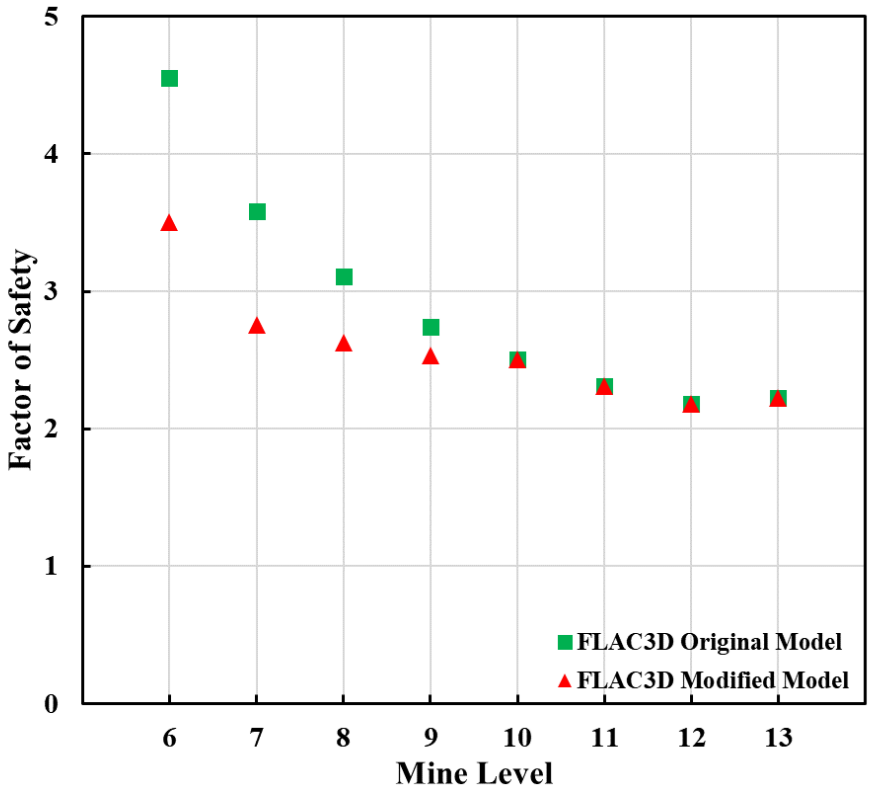

Figure 6.13 Comparison between the factor of safety estimated for karst-free original and modified numerical models.

Many researchers have studied the safety issues caused due to slender pillars in a hard rock mine [37], [88], [114]. Different works of literature have different definitions for slender pillar dimensions, but most of them describe observing a drastic change in pillar strength for

pillars with a W/H ratio of 0.5. Therefore, despite having a high average factor of safety of 3.5, the effective W/H ratio of the pillar is not decreased to less than 0.62. It can also be observed that the FOS values for the lower four levels are the same because no modification was introduced in these levels. The FOS of pillars is calculated using the average stress on each pillar and the strength of the pillars of different dimensions using continuum modeling in FLAC3D. The average FOS values for pillars in each level are then obtained by taking the average of the values for each level.

Figure 6.14 shows the pre-mining and post-mining contours of axial stresses across the deposit. The redistributed vertical stresses after the complete excavation are higher than those shown in Figure 6.10. The corresponding lowering of FOS values owing to the higher stresses can be observed in Figure 6.15.

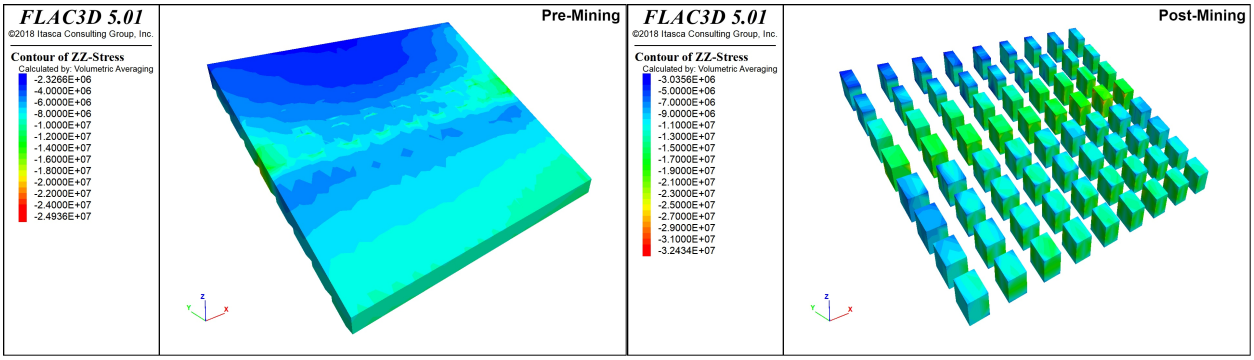

Figure 6.14 Contour of vertical stresses for pre- and post-mining state, respectively for karst-free modified model.

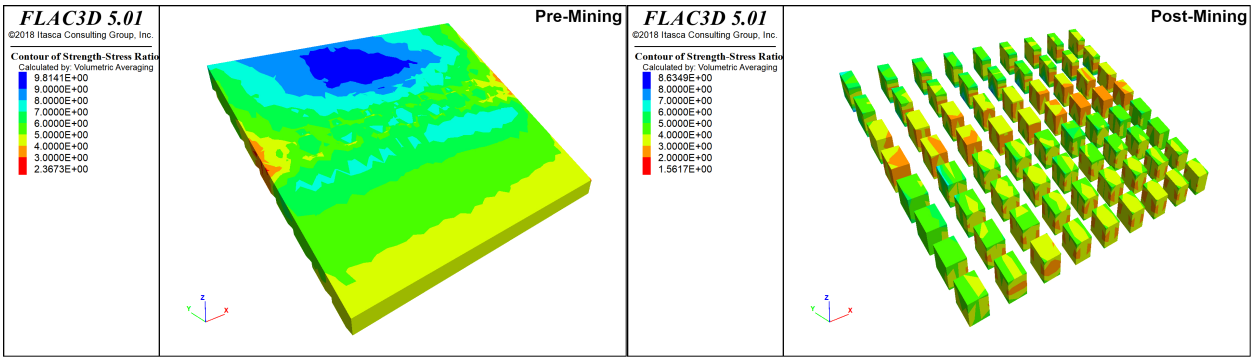

Figure 6.15 Contour of factor of safety for pre- and post-mining state, respectively for karst-free modified model.

6.5.3 Results & Analysis for Karst-free Simulations

6.5.3.1 Analysis of Stresses

Figures 6.16 and 6.17 show the different stresses estimated for each level using the original and modified models, respectively. In both the figures, it was observed that the vertical stresses on the pillars closely follow the maximum principal stress plot which is in agreement with the input stress gradients in the models.

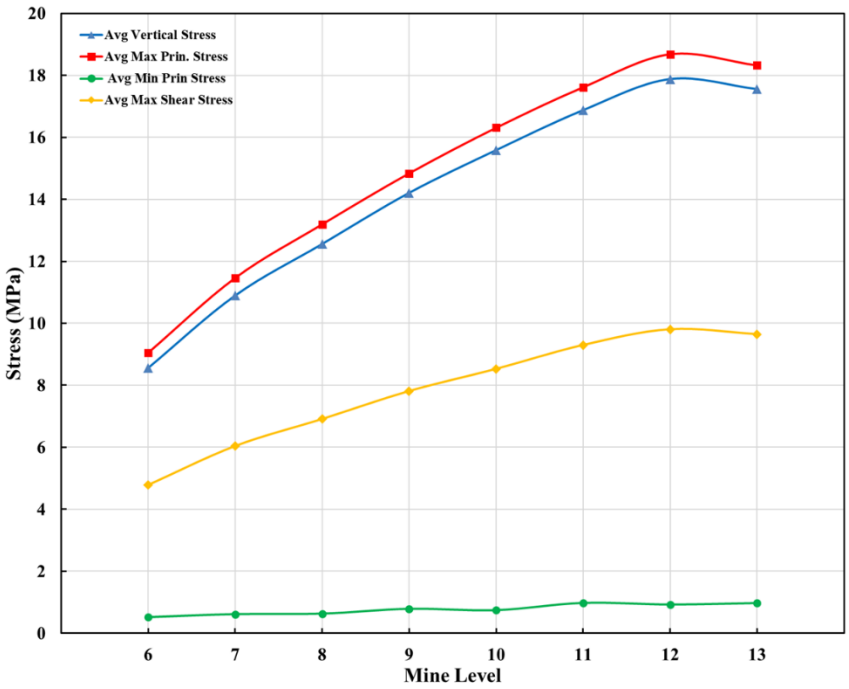

Figure 6.16 Distribution of various stresses averaged for each mine level for karst-free original model.

It is observed that in Figure 6.17, the redistributed stresses in the top four levels consisting of the modified pillars increase substantially as compared to Figure 6.16. This agrees with the phenomenon that these pillars will observe higher stresses due to the availability of less material to support the roof strata. The plot also exhibits the stresses approaching the values for the lower-level pillars, although they are still higher than the original model.

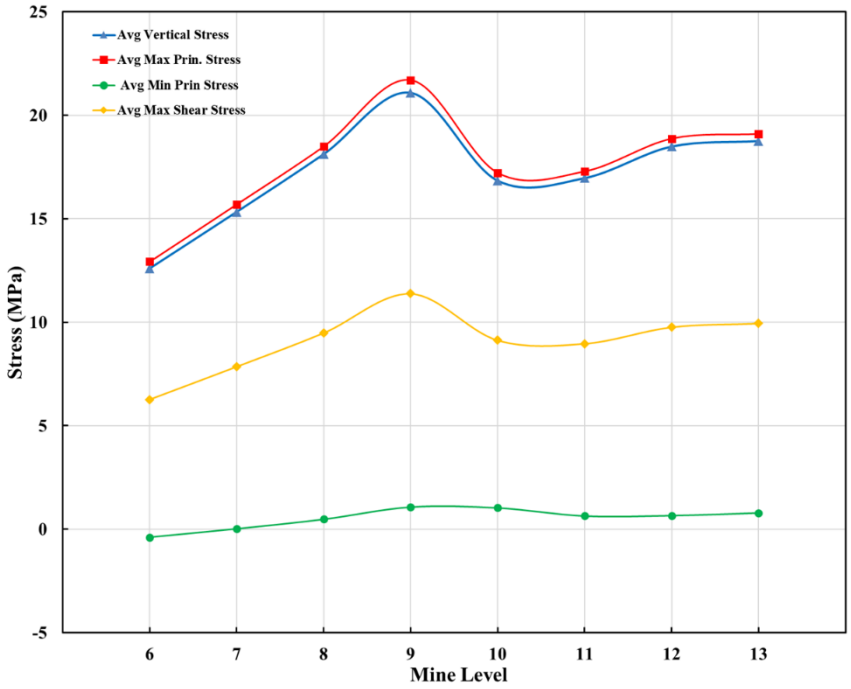

Figure 6.17 Distribution of various stresses in pillars across each mine level for karst-free original model.

It is also important to observe the variation of pillars across each column (A to I) to understand the change in stresses based on the pillar location near the abutment of the center of the model. For the original model, the axial pillar stresses along the vertical direction are shown in Figure 6.18. The plot contradicts the tributary area method which states that each pillar is responsible for carrying its share of the overburden load. However, it is clear from the plot that pillars near the center columns carry a higher tributary load as compared to the pillars in the end columns. This may be explained by the formation of a pressure arch formed by the overburden stresses. When the vertical stresses are high in a strong overburden/host rock, a pressure arch can develop and create a tributary area load along the central pillars while shielding the abutment pillars. In most cases, a build-up of a pressure arch can transfer enough load from the abutment pillars and stabilize the

formation. Figure 6.19 depicts a similar scenario, however, with high vertical stresses observed by the modified pillars for the top four levels due to higher redistributed stresses.

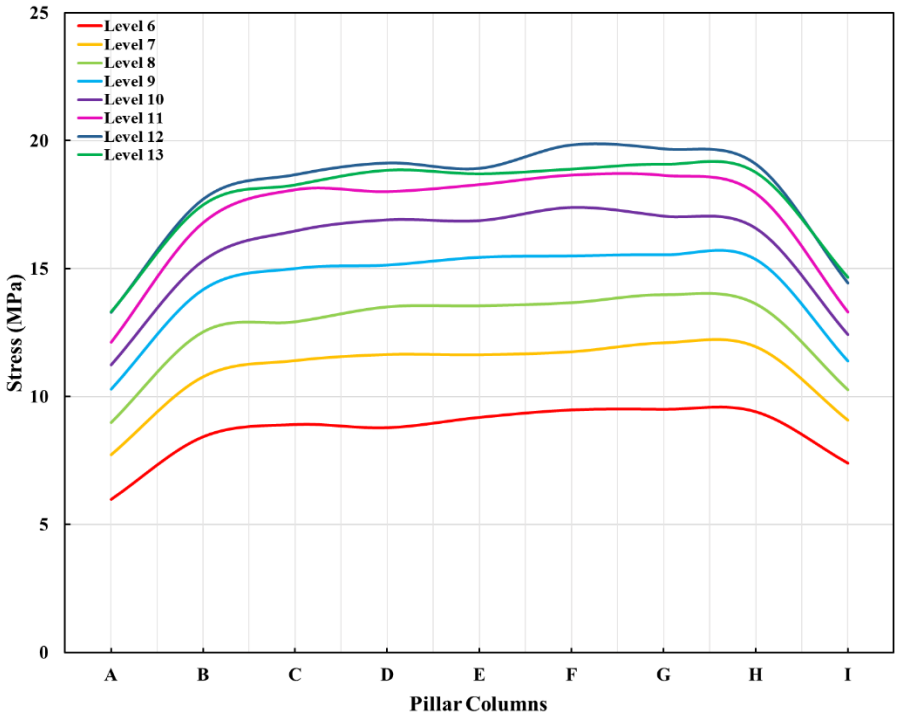

Figure 6.18 Distribution of vertical stresses across each pillar column for the karst-free original model.

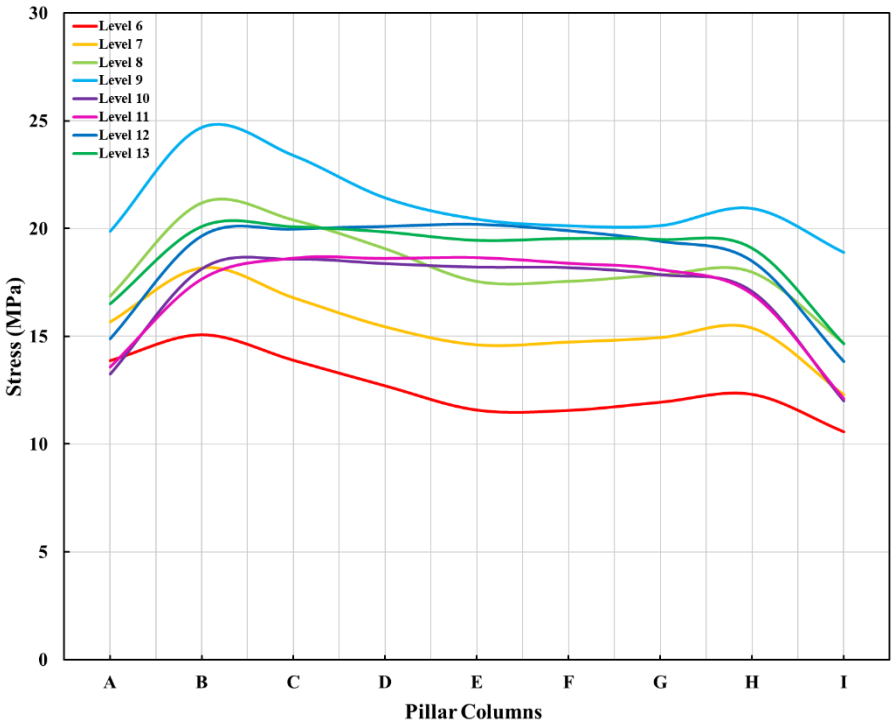

Figure 6.19 Distribution of vertical stresses across each pillar column for the karst-free modified model.

6.5.3.2 Analysis of Strength-to-Stress Ratio (FOS)

A special function was compiled in FISH, an in-built language in FLAC3D, to estimate the FOS (strength-stress ratio) from the simulated models in FLAC3D. The program was able to read data at more than 2500 points within the boundaries of 72 pillars for the original and modified models. The data gathered was used to estimate the normal distribution for the factor of safety values obtained at the points within the pillars.

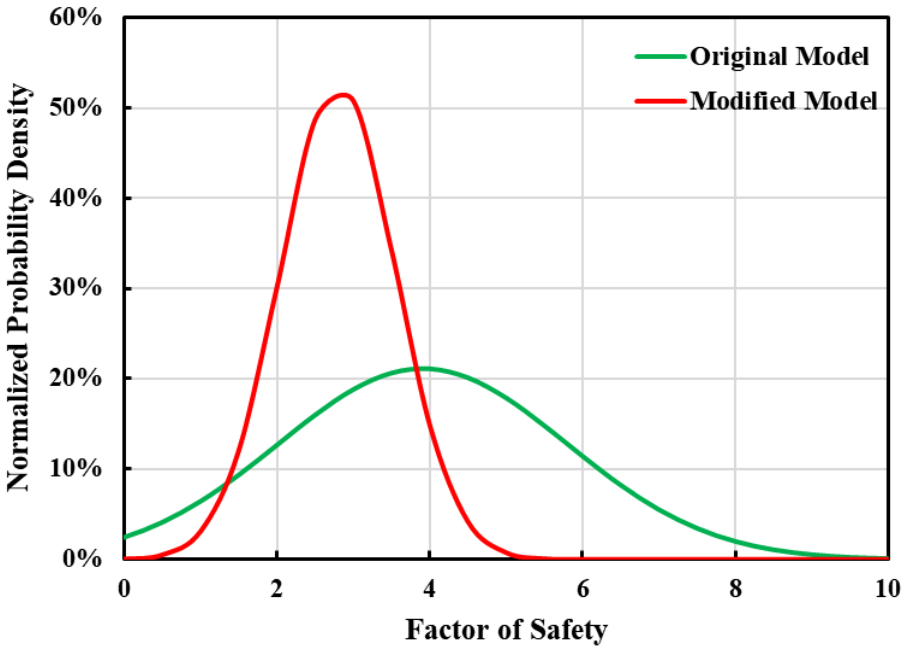

Figure 6.20 Normalized probability density plot of FOS values for karst-free original and modified numerical models.

The normal distribution plot for the modified model, as shown in Figure 6.20, could be compared to see the shift in the distribution of FOS values when compared to the original model. This helps to visualize the probability of a zone within all the pillars having a particular FOS value for both numerical models. To assist the quantification or the shift in FOS after modifying the pillar design for the mine, Figure 6.21 shows the box plot depicting the mean, median, quartiles, and range of the FOS values. It should be noted that the FOS values depicted in this plot do not depict the ultimate or average values of the pillar, but rather they note the values at different individual points. This is important in making inferences about the transition of values within pillar zones as they are modified.

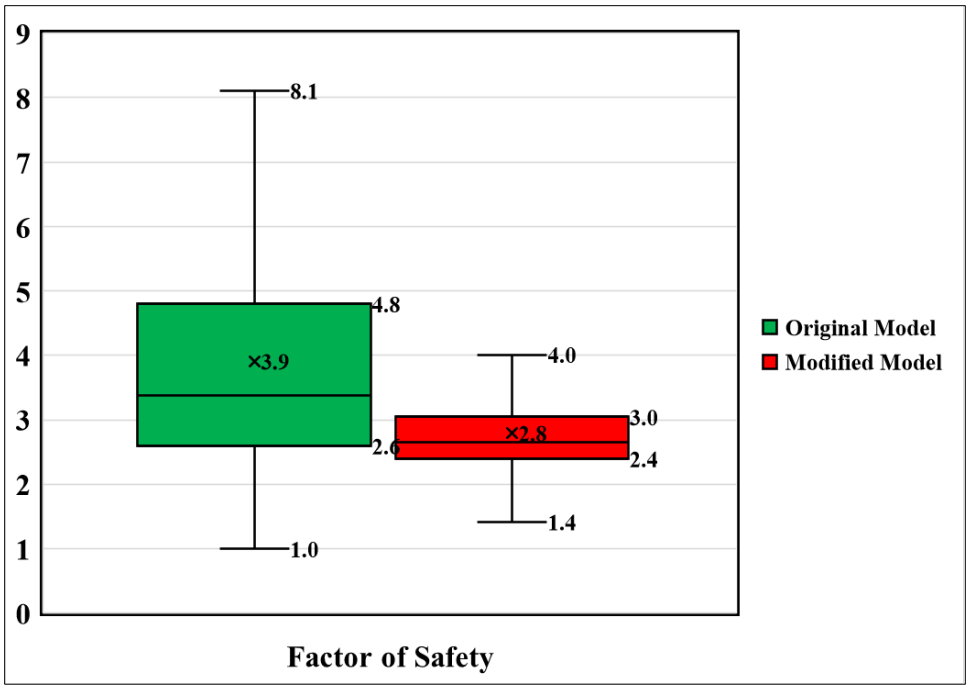

Figure 6.21 Box plot for FOS values for karst-free original and modified numerical models.

6.6 Karst-Prone Mine Model Simulation

This section simulates the mine model by assuming the presence of any karst cavities in the deposit. The results achieved from this simulation are compared to the previous models simulated without karsts to understand the effect of these voids on the strength of the pillars. Interaction of the discontinuity network with karst voids in the immediate roof or sidewalls can lead to ground collapse, thus posing a risk to the safety of miners and operations. A comprehensive survey for identifying all the karst cavities in the region selected for modeling is nearly impossible. Therefore, a stochastic distribution of karst cavities based on random positioning in the ore deposit was done to understand their effect on the stresses and the FOS of pillars.

6.6.1 Methodology

Figure 6.22 depicts a pillar from the numerical model meshed using tetrahedral zones in Griddle software [68]. The minimum dimension for meshing was set to zero, while the maximum mesh dimension was 2 m. Allotting these values allowed to generate a fine mesh that would allow more control over generating the shapes of the voids.

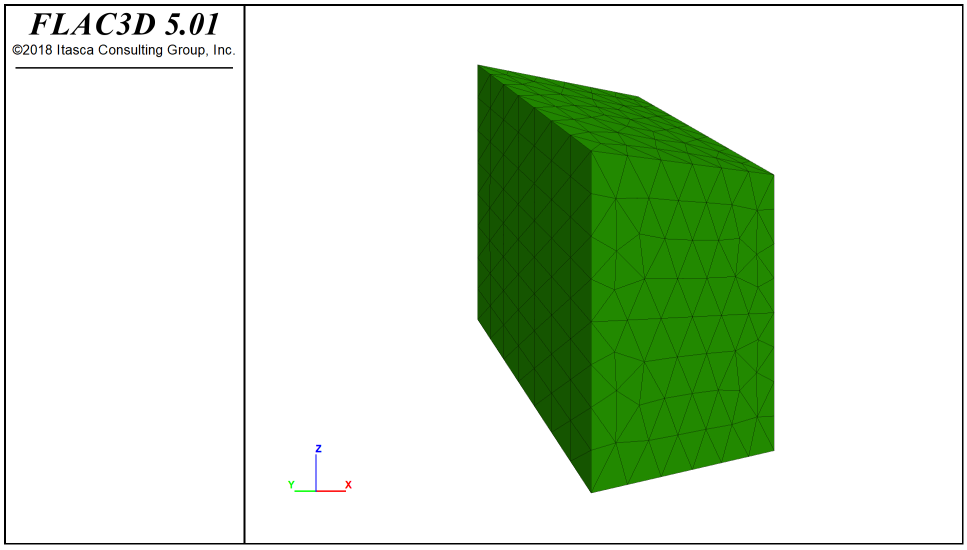

Figure 6.22 Pillar model with tetrahedral mesh elements.

Using the earlier research studies and surveys conducted at the mine (Chapters 2, 4, & 5), preliminary data were collected for the total volume of pillars surveyed and the void volumes encountered in the survey zone. The details of the survey are provided in Table 6.4.

Table 6.4 Field survey data used in estimating the distribution of karst in the orebody.

Source	Data Type	Pillar Volume (m^3)	Karst Volume (m^3)	Total Survey Volume (m^3)	Karst/Pillar Volume %
Chapter 2	Single Pillar	5358.89	482.30	5841.19	9.00
Chapter 4	Single Pillar	7532.85	970.03	8502.88	12.88
Chapter 5	Local Area	488402.87	6278.53	1457688.84	1.29
					Average= 7.72%

Including survey data from the single pillars adds a high bias to the data as these pillars were selected primarily because of the presence of karst in them. The local area survey presents a much more realistic extent of the presence of karst voids in the deposit. Although the survey data is scarce and there is a high possibility of variation over an extended survey zone, the estimated average value highly overestimates the karst voids, thus introducing more weakened zones during the analysis. This results in simulating a worst-case scenario for the deposit by underestimating the strength in rock mass in more voids. Based on the survey, the parameters for karst volumes embedded in the numerical models are presented in Table 6.5.

Table 6.5 Input parameters for generation of karst volumes in the numerical models.

	Total Pillars	Total Pillar Volume (m^3)	Orebody Volume (m^3)	Karst Volume (m^3)
Original Model	72	1306020.10	3745799.97	100824.75
Modified Model	72	1130354.71	3745799.97	100824.75

The karst volumes were simulated as null zones in FLAC3D. The reason behind this was assuming that the voids are filled with cohesionless material that does not contribute to the strength of the rock mass. Despite having a low volume of pillars in the modified model due to smaller dimension pillars, it was assumed that the karst volumes will be the same as the original model.

The karst cavities are assigned to the tetrahedral zones in the orebody, similar to the ones shown in Figure 6.22. This adds to the simplicity of introducing cavities in the fractured limestone deposit while the tetrahedral blocks imitate the pinching-expanding shape behavior of voids in the field. A pseudo-random number generator function was used to select the tetrahedral zones and any adjoining zones were combined into a bigger void. A pseudorandom sequence of numbers is useful in this case as it appears to be random, despite having produced inside a completely deterministic orebody volume and void shapes. For this study, the randomly selected void zones were limited in a way such that the largest dimension of the combined karst cavity does not exceed twice the largest dimension of a pillar in the excavation. The process of stochastically assigning karst helps to realize the feasibility of mining a deposit ridden with such cavities. It also aids in understanding the effect of voids on pillar strength and the appropriate designs and ground control measures that might be adopted during the excavation process. Twenty models with different randomly sequenced positioning of karst voids were simulated for each scenario, i.e., the original pillar layout and the modified pillar layout.

6.6.2 Original Room-and-Pillar Layout

Figure 6.23 shows one of the twenty simulated numerical models including random positioning of karst volumes along with the pillars. All models were simulated using the mining sequence as explained in Section 6.4.4. The pre-mining and post-mining contours of axial stresses and FOS across the karst-ridden deposit are shown in Figures 6.24 and 6.25, respectively. When compared to Figures 6.14 and 6.15, it may be observed that the average factor of safety of pillars has decreased, especially in the vicinity of the karst voids.

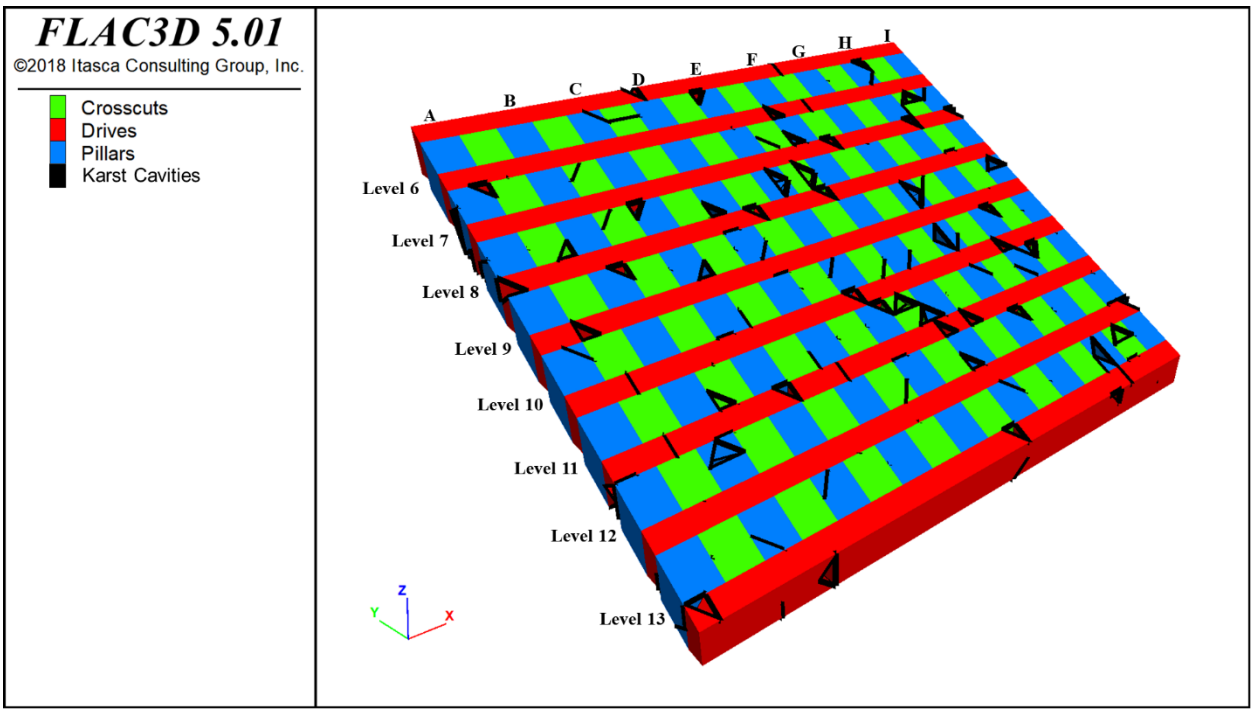

Figure 6.23 Original room-and-pillar layout of the mine showing the crosscuts, drives, pillars, and karst cavities.

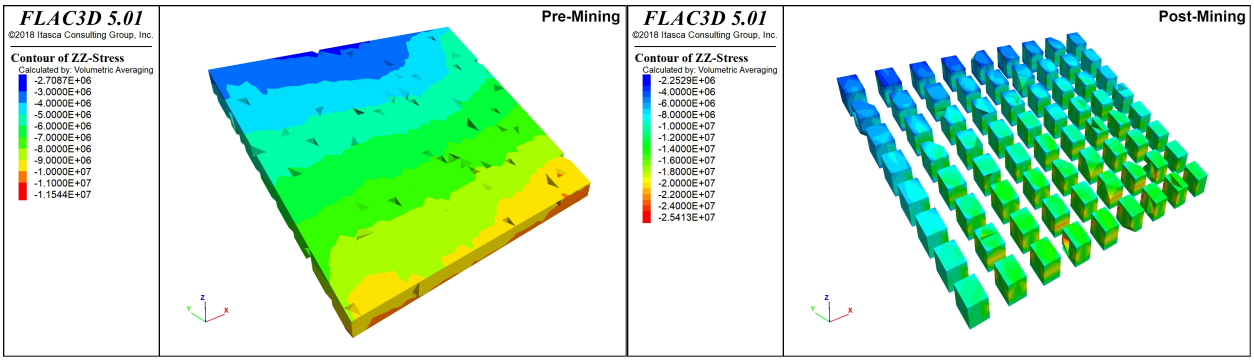

Figure 6.24 Contour of vertical stresses for pre- and post-mining state, respectively for karst-prone original model.

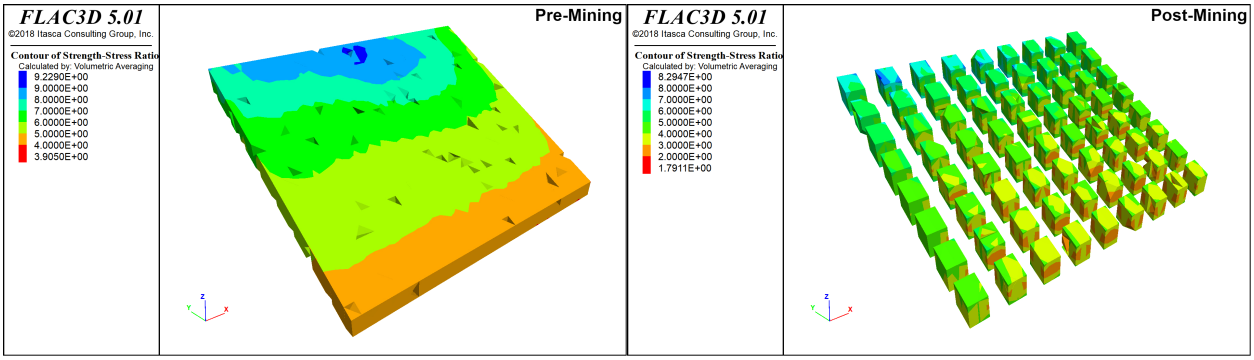

Figure 6.25 Contour of factor of safety for pre- and post-mining state, respectively for karst-prone original model.

6.6.3 Modified Room-and-Pillar Layout

One of the twenty simulated models for the modified room-and-pillar layout for the karst-ridden deposit is depicted in Figure 6.26. The dimensions of modified pillars on the top four levels of the layout are the same as the model for the karst-free deposit.

Similar to the observations during the karst-free models, the modified karst-prone model has a higher magnitude of redistributed stresses in the upper four levels as evident from

Figure 6.27. The contours for FOS, as shown in Figure 6.28, are lower in the modified levels when compared to the original model from the previous section.

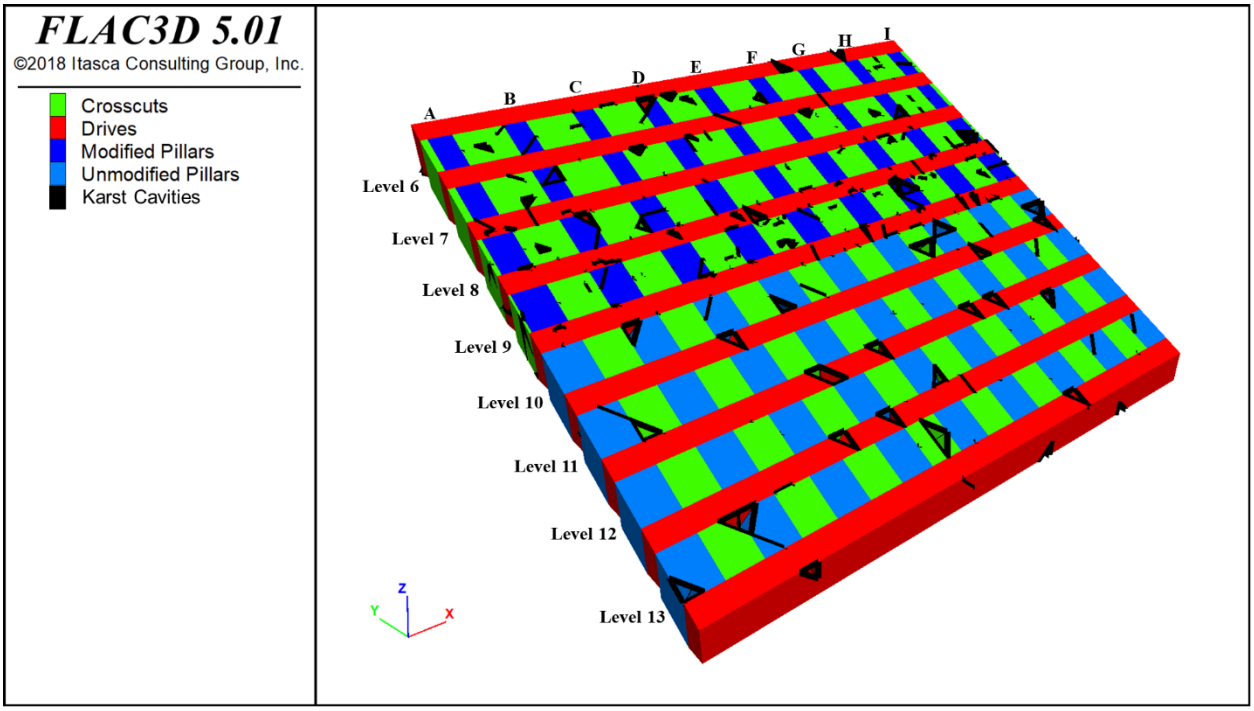

Figure 6.26 Modified room-and-pillar layout of the mine showing the crosscuts, drives, pillars, and karst cavities.

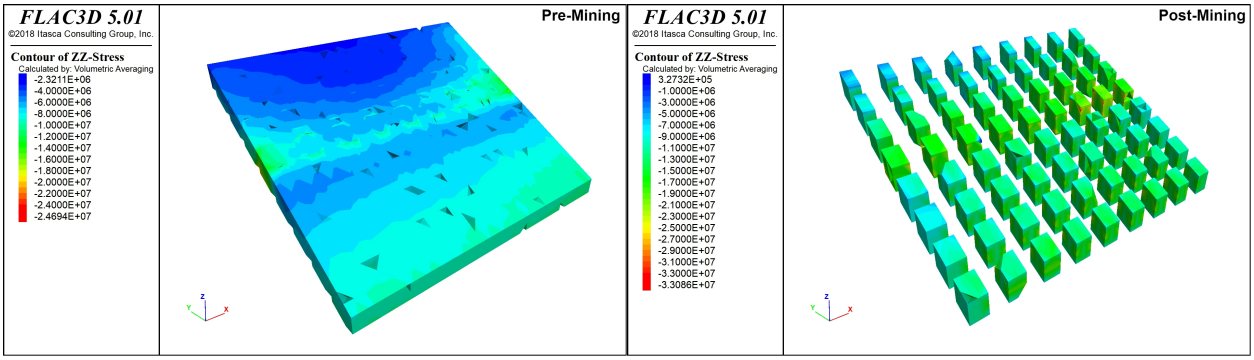

Figure 6.27 Contour of vertical stresses for pre- and post-mining state, respectively for karst-prone modified model.

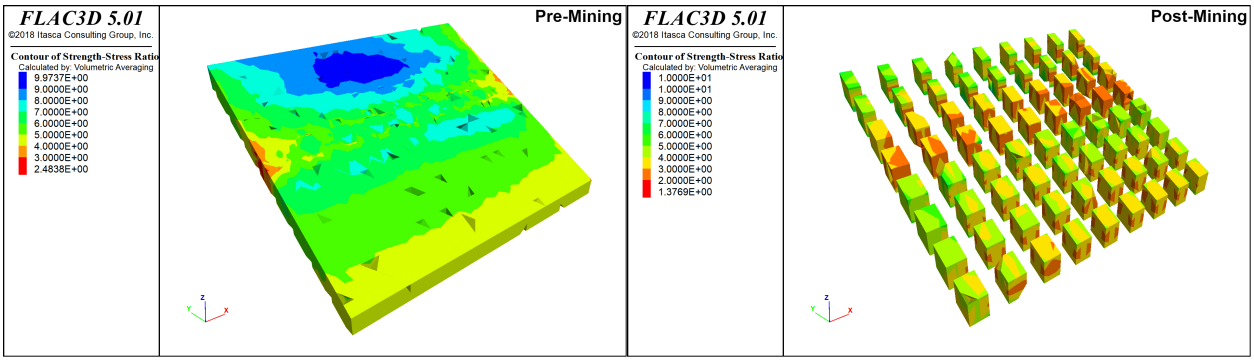

Figure 6.28 Contour of factor of safety for pre- and post-mining state, respectively for karst-prone original model.

6.6.4 Result & Analysis for Karst-Prone Simulations

6.6.4.1 Analysis of Stresses

The analyses shown in this section are for the layouts shown in Figures 6.23 and 6.26, which are one of the twenty models for original and modified layouts, respectively. The results are similar to the multiple plots obtained for the numerous models, all of which cannot be shown here. Figures 6.29 and 6.30 show the different stresses estimated for each level using the original and modified karst-prone models, respectively. Similar to the karst-free models, it was observed that the vertical stresses are neighboring the maximum principal stresses.

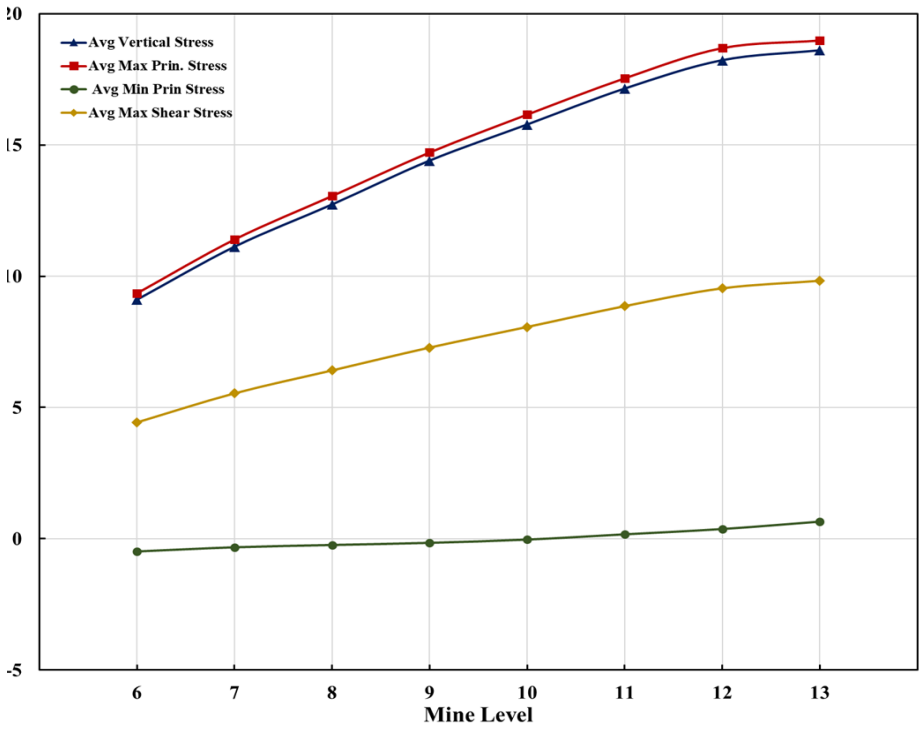

Figure 6.29 Distribution of various stresses averaged for each mine level for karst-prone original model.

Figure 6.30 shows that the redistributed stresses in the top four modified levels increase considerably as compared to the stresses in Figure 6.29. Like Figure 6.17, the same is expected here due to these pillars bearing higher redistributed stresses to support the roof. The plot depicts the stresses transitioning back to the trend followed by the original model for the lower four levels.

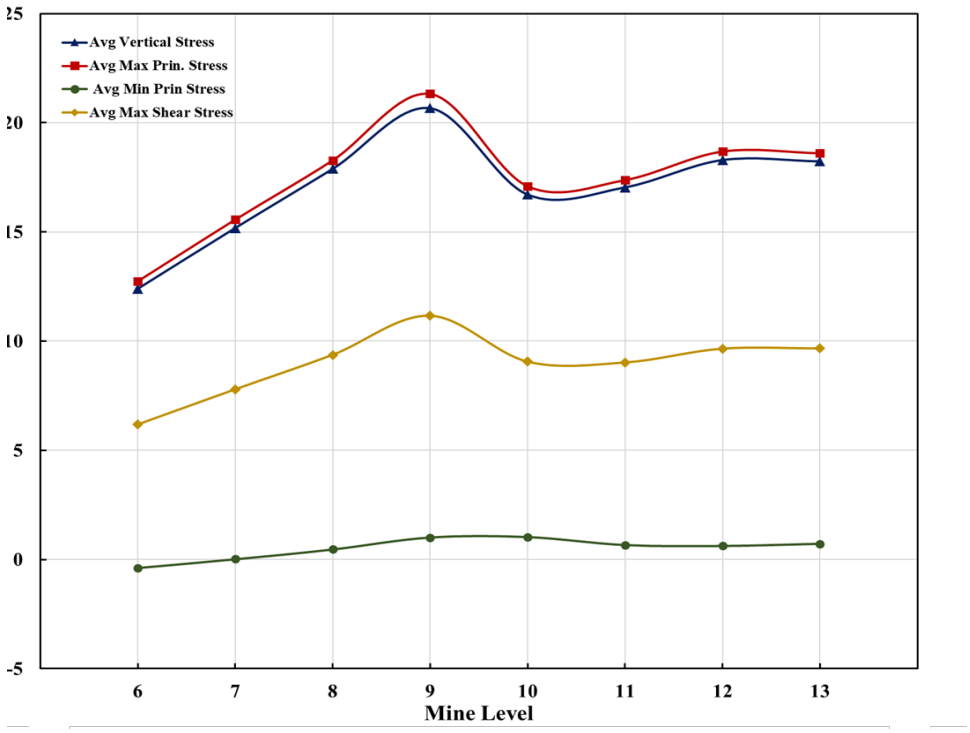

Figure 6.30 Distribution of various stresses in pillars across each mine level for karst-prone original model.

The variation in vertical stresses across the pillars in a single column (from A to I) is observed for each level in Figure 6.31 (original model) and Figure 6.32 (modified model). Apart from the pressure arch phenomenon observed in these plots, some interesting results are observed. When the plot for Level 13 in Figure 6.31 is observed, a lot of fluctuation is observed in pillars in the same column. The same trend is observed for levels 8 and 9 in Figure 6.32 for the modified numerical model. After further examination, it is noticed that these fluctuations in axial stresses are caused by the high presence of karst voids in the pillars across the noted mine levels. As confirmed by previous studies (Chapter 2), the presence of cavities in pillars leads to a noticeable reduction in overall strength. This may lead the structures to yield at a lower stress level and transfer the bearing load to the surroundings. These phenomena often lead to cascading pillar failures where the neighboring

pillars are unable to withstand the sudden release of stresses due to the failure of one pillar. It can also be observed in Figure 6.32 that high vertical stress is taken by the modified pillars as compared to the unmodified pillars in the lower four levels.

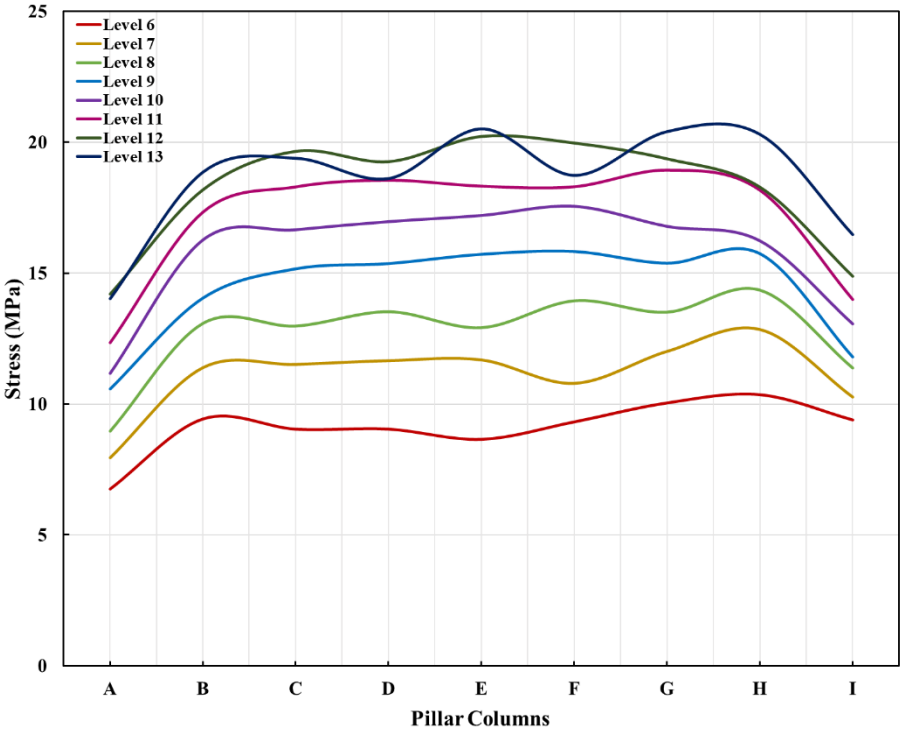

Figure 6.31 Distribution of vertical stresses across each pillar column for the karst-prone original model.

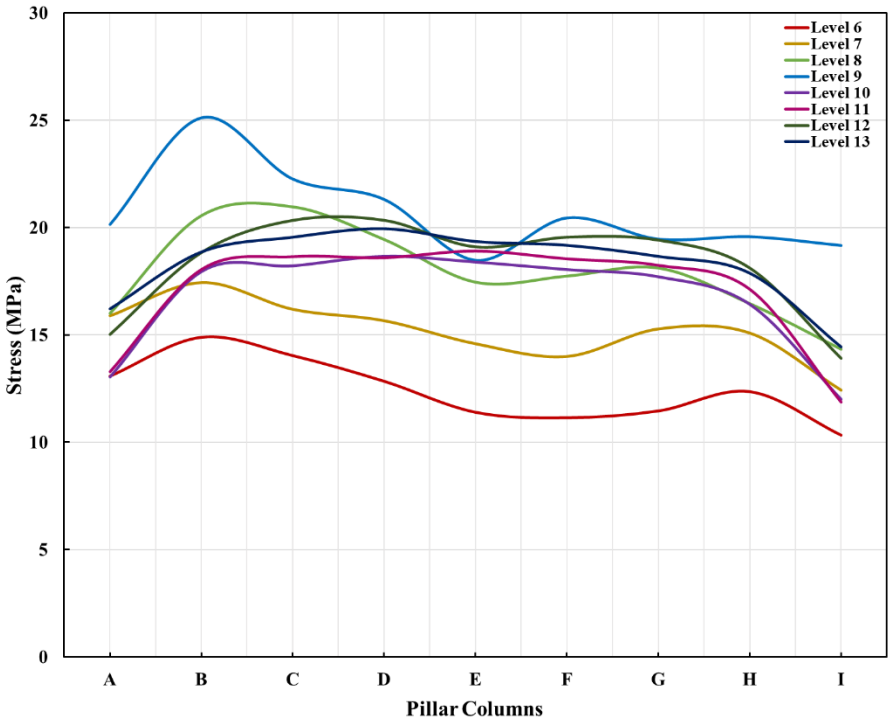

Figure 6.32 Distribution of vertical stresses across each pillar column for the karst-prone modified model.

6.6.4.2 Analysis of Strength-to-Stress Ratio (FOS)

For each of the twenty models with original and modified layouts with randomly arranged karst voids, the FOS values were recorded at more than 2500 points. This amounted to about 50000 data points for each layout. The data set was used to plot the normal distribution plot to determine the probability density function for different values of FOS between 0 and 10. Figure 6.33 helps visualize the shift in the probability density plot when the modified pillar design is introduced.

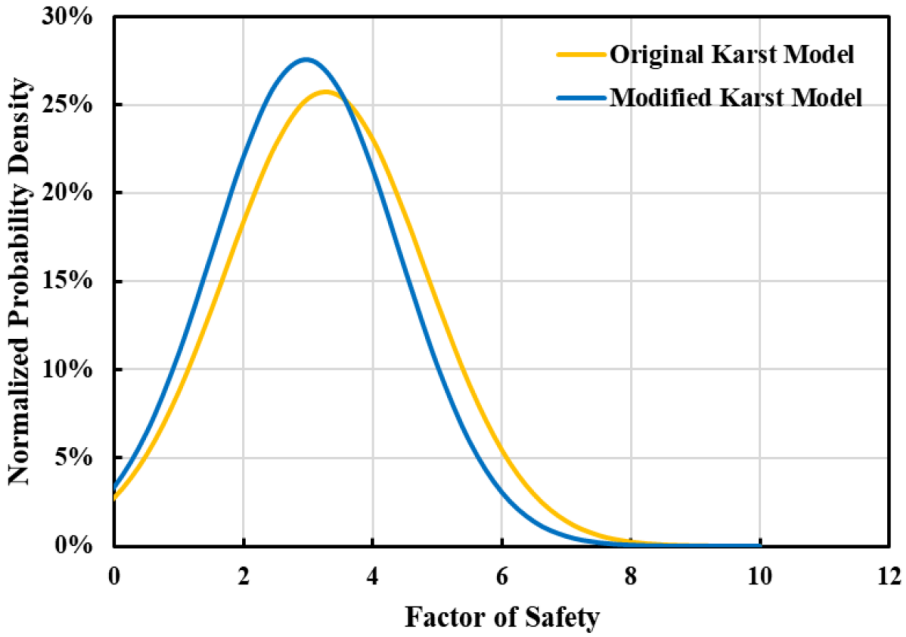

Figure 6.33 Normalized probability density plot of FOS values for karst-prone original and modified numerical models

Interestingly, a substantial shift between the mean point of the two plots is not observed when compared to Figure 6.20. Despite introducing slimmer pillars in the modified layout, the two probability density plots resemble each other. The same could be observed in Figure 6.34 which shows the distribution of the FOS values in the box plot format. Instead of observing a decrease in the lower range value for the modified layout, a higher value is obtained when compared to the lower range value of the original layout.

A primary reason for the similarity in the normal distribution plot for the two layouts might be the presence of karst voids. Before modifying the pillars, the cavities result in a loss of FOS values in the pillar zones. It might be possible that there is a higher presence of randomly distributed cavities in the pillars of the original model and lower in those for the modified model. It is believed that this phenomenon would not be observed if more stochastic models are run for each layout with the random karst voids positioning.

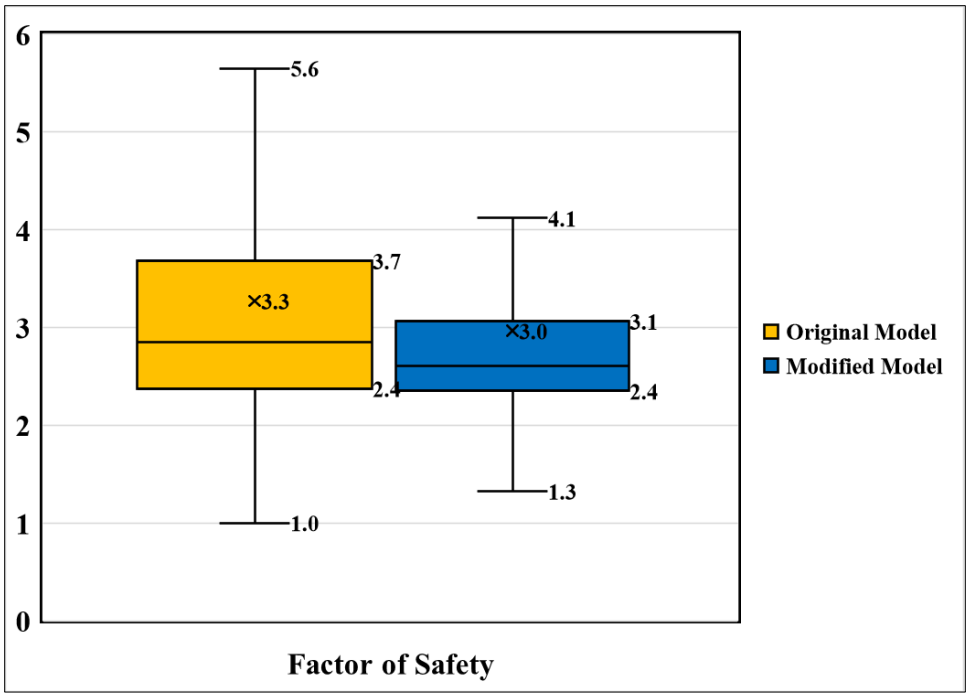

Figure 6.34 Box plot for FOS values for karst-free original and modified numerical models.

6.7 Conclusions & Scope

This chapter presents an insight into the process of optimizing pillar design in underground mines for optimizing production while minimizing safety risks. The research was based on a room-and-pillar limestone mine that faced frequent ground control issues, such as roof/sidewall collapse and an inrush of groundwater with clay-rocky material from the inherent karst cavities in the deposit. However, the principles and techniques explained here can be applied to other hard rock deposits, not only to understand the pillar design framework but also to assess the feasibility of secondary recovery.

According to the United States Geological Survey (USGS), during the past ten years, the total annual weighted average price for all types of limestone products (high-calcium quicklime, hydrate, dolomitic quicklime, crushed stone products, etc.) increased by

US$40.60 per metric ton. The case study mine is a high-calcium lime feedstock mine. If we consider a weighted average price for high-calcium lime at a conservative price of US$100 per metric ton (the weighted average for all types of lime in the US is $136.50 per metric ton), the enhanced recovery from the modified pillar model would amount to about US$48 million.

Apart from increasing recovery, this study also discusses the importance of maintaining stability for a karst-prone underground mine. A detailed numerical study of the stress regimes and comparing shifts in factor of safety values of different zones in the mine is useful in planning a safe production. In this study, the shift is visualized using normal distribution plots for FOS values in the pillar zones for the original as well as the modified models. An effort is made to design pillars so that a minimum desired strength-to-stress ratio is always maintained. As shown in Figure 6.35, the mine has slender pillars placed in different locations and levels and based on the field inspections, the performance of these pillars has been satisfactory in the past and no ground issues have been observed in their vicinity.

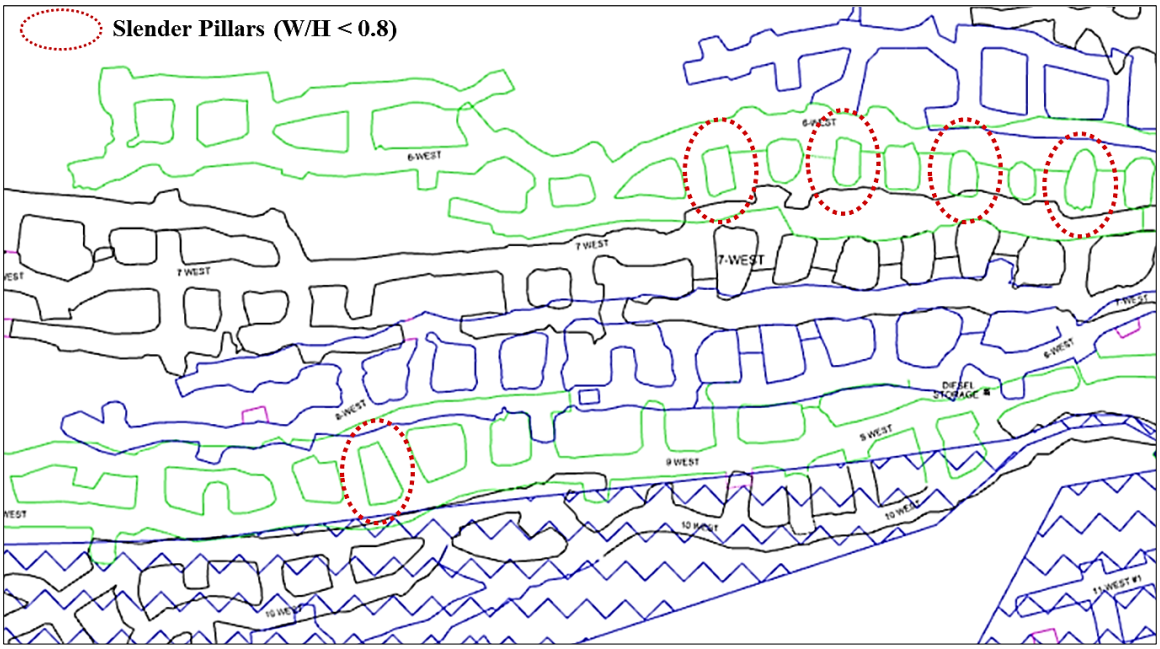

Figure 6.35 Highlighted locations show the presence of slender pillars in the case study mine.

The research uses an ideal layout of the case study mine, and the exact results may not be perfectly applied to mining operations because of the imperfect excavations in the real world. But the methodological approach is optimized for the deposit and may favor similar hard rock operations.

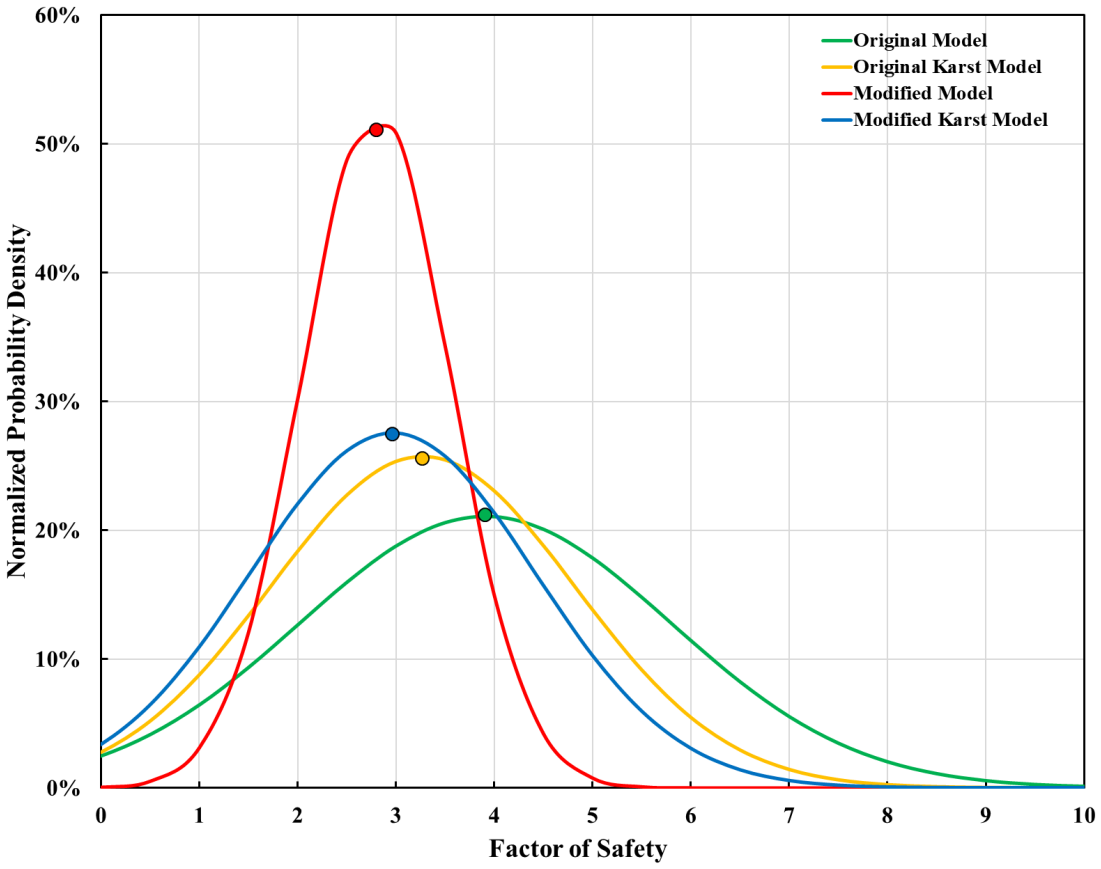

Figure 6.36 Normal distribution plots for comparing karst-free and karst-prone scenarios for the original and modified models in terms of factor of safety.

A stochastic approach to utilizing finite volume modeling is highly effective in observing the effect of weak cavities in underground excavations. This is true for both the original and the modified pillar layouts. The placement of karst voids as unstable zones has proved a viable solution by using a pseudo-random number generator function. It is recommended that a thorough geological and geophysical analysis of the site is valuable for reducing the unknown variables for the placement of the voids. Non-invasive geophysical techniques such as Ground-penetrating Radar (GPR) are a great mode of identifying the presence of subsurface voids. Multiple models with random voids placement are numerically simulated using FLAC3D and provide great insights into the weakening effect of karsts on structural

strength and redistribution of stresses. This also displays the advantages of numerical modeling over analytical methods which cannot factor in the geotechnical complexities of the rock mass. Figure 6.36 shows a comparison between normal distribution plots for all the scenarios simulated during this study. The shift in the skewness of the plots can be visualized and a basic observation of the effect of different variations could be understood. The results obtained from this modeling research are useful for interpreting the need for the optimizing design of pillars for a hard rock mine. Varying pillar dimensions with depth is an excellent way to counter the increasing stresses. Introducing modifications to the design and dimensions of pillars and headings affected by karsts is an effective way to increase local stability and prevent hazardous working conditions. In the past, the mine management has modified pillar dimensions to counteract any discovered karst cavities.

The study could be an effective benchmark to understand the feasibility of planning mining operations requiring unorthodox ground control management. This research primarily analyzes the effect of voids within the pillars. It would be interesting to study the combined effect of such instabilities within the roof or floor of the excavations. The study could also be extended to simulate the presence of big faults or fractures through the deposit and the hydrogeological challenges associated with them. This could be accomplished using a hybrid approach by integrating finite volume and discrete element modeling.

Chapter 7

Conclusions & Scope of the Research

7.1 Summary and Conclusions

Four incidents of massive pillar collapses have occurred in different underground stone mines in the US since October 2020 [108]. Stable pillars are the backbone of room-and-pillar mining operations. Any deterioration of these structures can not only compromise regional stability, but a propagation effect can cause damage to multiple neighboring pillars and jeopardize global stability. Pillar failure incidents also have a causal effect like subsidence and air blasts which are capable of hurting miners working far away from the accident site. To prevent such future accidents and raise awareness, Mine Safety and Health Administration (MSHA) has introduced the "Pillar Collapse Initiative" to provide mine operators with multiple resources at their disposal.

This dissertation demonstrates a numerical modeling approach-based framework which integrates discontinuum modeling, stochastic continuum modeling, and geotechnical field mapping for the optimization of pillar design beginning from a single pillar to a global mine scale. This research aims to help realize the role of improving excavation design, particularly pillars, for improving stability and production in underground stone mines. Underground mine operators must come beyond following conservative and traditional design approaches and standards. For many small underground mining operations, a limited budget may impede their capability to implement these changes. But when we focus on the bigger objective of improving productivity while maintaining safety, it becomes clear that the

suggested techniques can help bridge the gap to implementing the changes. The modeling approach and techniques during this research were based on a case study stone mine but could provide a pragmatic framework for safe and efficient extraction of ore from other large-opening hard rock mines. Figure 7.1 displays the basic framework, methodology, and techniques presented in this dissertation. The essential summary and conclusions of the research can be stated as follows:

- Karst-related safety incidents endanger the safety of the mine workers and mine machinery in stone mining operations. Insufficient literature makes it difficult to quantify the impacts on pillar stability caused by the presence of karst cavities. This research quantifies this effect for different scenarios to better understand the reduction in strength of pillars with karsts. This is important while encountering karsts or other instability issues in pillars and headings.

- Modifying the design of karst-affected pillars and assessing the resulting performance is essential to understanding the improvisation necessary to maintain stability without compromising production. Discrete element modeling (DEM) coupled with the use of Discrete Fracture Networks (DFNs) can help gather accurate pillar behavior to improve upon the existing design.

- Analyzing separately compartmentalized pillar zones is important for stone mines where structural failures dominate the stress-based failures. It helps realize the importance of ground control in the necessary areas of a pillar or even certain roof sections. It also helps realize the important areas or sections of a karst-ridden pillar that needs ground control measures or while remining a pillar for secondary recovery.

- LiDAR and photogrammetry surveys are vital in collecting the statistical mapping data for discontinuities, which is imperative for formulating the DFNs. The

photogrammetry surveys can also add useful information for visualization purposes. Ground-penetrating Radar (GPR) surveys may be time-consuming but provide invaluable data for the extent or spread of cavities within the rock mass. Drone-based surveys are exceptional for mapping unreachable high sections of tall pillars which are common in stone mines and remove the risk associated with conducting traditional surveys.

- Discontinuum modeling using 3DEC was effective for replicating the behavior of a blocky rock mass such as limestone and implementing a stochastic joint network in form of DFNs. Parametric and sensitivity analyses of shear strength, elastic moduli, and joint spatial density play a vital role to translate the behavior of a discrete, jointed rock mass to continuum material. Continuum modeling using FLAC3D is most effective when analyzing large sections of a mine. This allows speedy simulations of an alternative scenario for optimizing ore recovery while improving safety.

- A stochastic approach to utilizing finite volume modeling (FVM) is highly effective in analyzing global-scale models incorporated with weak cavities in underground excavations. This research also helps visualize the "shift" in the stress regimes and factor of safety (FOS) of different zones which is useful in planning a safe production. A probabilistic analysis of the stochastic placement of unstable zones in a deposit provides a good starting point for a mining strategy and helps develop a pre-feasibility plan including various ground control measures during the life of a karst-affected mine.

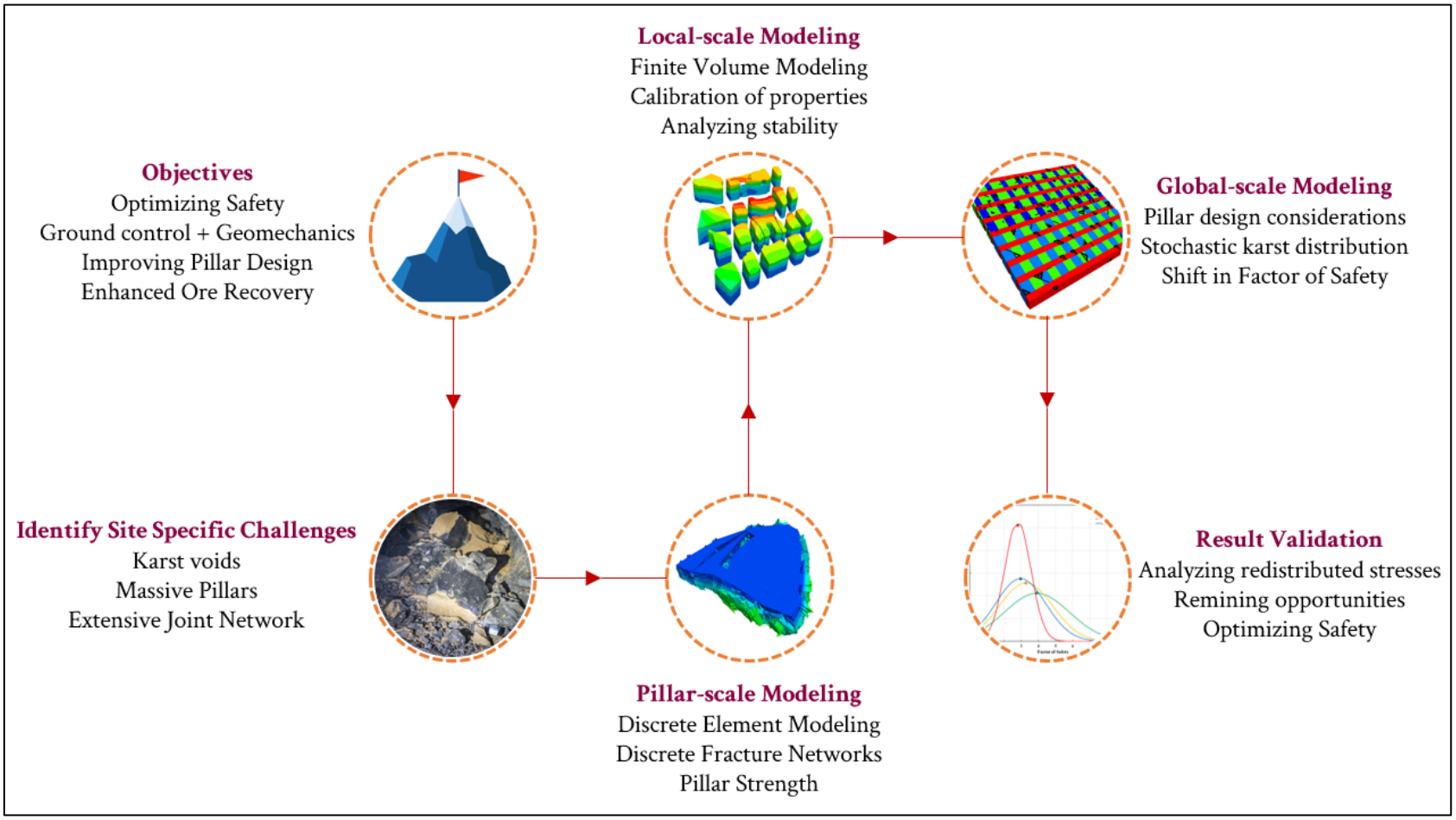

Figure 7.1 Flowchart depicting the basic framework, methodology, and techniques presented in this dissertation.

7.2 Scope of the Research

This dissertation begins with examining a single pillar in the mine to visualize optimization on a global scale. It identifies the site-specific ground control challenges, which in this case, is the presence of karsts. Finally, it proposes a comprehensive methodology for boosting local and global stability by mitigating exposure to rockfall-related hazards and improving the safety of miners. Based on the doctoral research conducted and exploration of ongoing advancements, the following research areas could be pursued further to promote ground control and safety in underground stone mining operations:

- With the increasing amount of stone mining operations going underground every year, it is important to implement a combination of intelligent surveying systems for gathering accurate data. The use of cross-borehole ground penetrating radar (XBGPR), continuous monitoring using interferometric radar systems, or even low-budget extensometer surveillance could help the operators understand the precursors to ground fall.

- Further research should be conducted on establishing a relationship between the joint spatial density with depth and the physico-mechanical properties of the rock mass. This will help improve the calibration of numerical models with depth and apply appropriate constitutive properties based on the dominance of stress- or structurally-controlled mechanics. A similar study could be done to understand the lateral variation of the joint distribution.

- The stochastic analysis study using FVM could be an effective benchmark to understand the feasibility of planning mining operations requiring unconventional ground control management. This study did not incorporate several variables such

as overbreak due to blasting and a detailed analysis of the effect of karsts on the roof or floor. A hybrid dynamic modeling approach using DEM and FVM could help achieve accurate results and factor in various data for unknown variables which could not be obtained during this research.

- One of the major safety issues that originate due to the opening of karst cavities is the continuous outflow of groundwater. Mine operators need to undertake measures to prevent this flow such as grouting the voids or regularly pumping the water out of the mine. This adds to the financial burden incurred by the operators to ensure the smooth functioning of operations. The research did not consider the hydrogeological effect on the strength of pillars in the case study mine. The joint sets surveyed in the mine are tight with dry conditions. Further studies should be done to incorporate the strength reduction of rock mass in mines with water inflow in the joint network.
- Most of the small underground operations do not have a dedicated ground control management plan which restricts speculative measures in the event of a ground-related hazard. The principles identified through this research can be adapted to develop such plans and enable adherence to procedural guidelines to combat ground fall incidents for underground hard rock mines.

The proposed research is valuable for improving pillar design, excavation practices, and prioritizing health and safety in karst-affected underground mines. The techniques discussed here would enable enhancing ore recovery while mitigating hazards in underground stone and large-opening mines.

Bibliography

[1] M. Alber and J. Heiland, "Investigation of a Limestone Pillar Failure Part 1: Geology, Laboratory Testing and Numerical Modeling," *Rock Mech. Rock Eng. 2001 343*, vol. 34, no. 3, pp. 167–186, 2001, doi: 10.1007/S006030170007.

[2] G. F. Andriani and M. Parise, "Applying rock mass classifications to carbonate rocks for engineering purposes with a new approach using the rock engineering system," *J. Rock Mech. Geotech. Eng.*, vol. 9, no. 2, pp. 364–369, Apr. 2017, doi: 10.1016/J.JRMGE.2016.12.001.

[3] G. F. Andriani and M. Parise, "On the applicability of geomechanical models for carbonate rock masses interested by karst processes," *Environ. Earth Sci.*, vol. 74, no. 12, pp. 7813–7821, Dec. 2015, doi: 10.1007/S12665-015-4596-Z.

[4] A. P. Annan and J. L. Davis, "Impulse radar sounding in permafrost," *Radio Sci.*, vol. 11, no. 4, pp. 383–394, Apr. 1976, doi: 10.1029/RS011I004P00383.

[5] ASTM, "Standard Test Method for Unconfined Compressive Strength of Intact Rock Core Specimens," vol. 95, no. D2938-95, pp. 1–3, 2002.

[6] L. A. Ayres da Silva, A. L. M. Ayres da Silva, and E. C. Sansone, "The shape effect and rock mass structural control for mine pillar design," in *ISRM International Symposium - EUROCK 2013*, Oct. 2013, pp. 563–567. doi: 10.1201/b15683-94.

[7] J. G. Baggett, "A Study of Ground Penetrating Radar Methods in an Underground Stone Mine to Improve Ground Control," Virginia Tech, 2019.

[8] S. C. Bandis, A. C. Lumsden, and N. R. Barton, "Fundamentals of rock joint deformation," *Int. J. Rock Mech. Min. Sci.*, vol. 20, no. 6, pp. 249–268, Dec. 1983, doi: 10.1016/0148-9062(83)90595-8.

[9] J. Barrix, B. McGunegle, S. J. Bauer, D. E. Munson, and M. P. Hardy, "In situ stress measurements and their implications in a deep Ohio mine," 2005.

[10] N. Barton, R. Lien, and J. Lunde, "Engineering classification of rock masses for the design of tunnel support," *Rock Mech. Felsmechanik Mécanique des Roches*, vol. 6, no. 4, pp. 189–236, Dec. 1974, doi: 10.1007/BF01239496.

[11] B. F. Beck, "Sinkholes and the Engineering and Environmental Impacts of Karst (2005)," Sep. 2005. doi: 10.1061/9780784407967.

[12] F. Beer, E. Johnston, J. DeWolf, and D. Mazurek, *Mechanics of Materials*, 7th ed. McGraw-Hill, 2015.

[13] D. Bickel, "Rock Stress Determinations from Overcoring: An Overview," 1993.

[14] Z. T. Bieniawski, "The Rock Mass Rating (RMR) System (Geomechanics Classification) in Engineering Practice," *Rock Classif. Syst. Eng. Purp.*, pp. 17-17–18, Aug. 1988, doi: 10.1520/stp48461s.

[15] Z. T. Bieniawski and W. L. Van Heerden, "The significance of in situ tests on large rock specimens," *Int. J. Rock Mech. Min. Sci. Geomech. Abstr.*, vol. 12, no. 4, pp. 101–113, Apr. 1975, doi: 10.1016/0148-9062(75)90004-2.

[16] R. Bishop, "Applications and Development of Intelligent UAVs for the Resource Industries," Virginia Tech, 2022.

[17] R. Bishop, J. Monsalve, J. Baggett, A. Soni, and N. Ripepi, "A comparison of laser scanning and photogrammetry in an underground limestone mine," in *2019 SME Annual Conference and Expo and CMA 121st National Western Mining Conference*, 2019, no. Preprint 19-095. doi: 10.13140/RG.2.2.11354.16320.

[18] R. E. Bishop, "Applications of Close-Range Terrestrial 3D Photogrammetry to Improve Safety in Underground Stone Mines to Improve Safety in Underground Stone Mines," 2020.

[19] B. H. G. Brady and E. T. Brown, *Rock mechanics for underground mining*, 2nd ed. Springer Science & Business Media, Inc., 1993.

[20] E. T. Brown, "Rock characterization testing and monitoring. ISRM suggested methods.," *Rock Charact. Test. Monit. ISRM Suggest. methods.*, 1981.

[21] D. Bunting, "Chamber pillars in deep anthracite mines," *Trans AIME*, vol. 42, pp. 236–245, 1911.

[22] P. P. Cacciari and M. M. Futai, "Mapping and characterization of rock discontinuities in a tunnel using 3D terrestrial laser scanning," *Bull. Eng. Geol. Environ.*, vol. 75, no. 1, pp. 223–237, Feb. 2016, doi: 10.1007/S10064-015-0748-3.

[23] P. P. Cacciari and M. M. Futai, "Modeling a Shallow Rock Tunnel Using Terrestrial Laser Scanning and Discrete Fracture Networks," *Rock Mech. Rock Eng.*, vol. 50, no. 5, pp. 1217–1242, May 2017, doi: 10.1007/s00603-017-1166-6.

[24] C. Caselle, S. Bonetto, C. Comina, and S. Stocco, "GPR surveys for the prevention of karst risk in underground gypsum quarries," *Tunn. Undergr. Sp. Technol.*, vol. 95, p. 103137, Jan. 2020, doi: 10.1016/J.TUST.2019.103137.

[25] M. Cauvin, T. Verdel, and R. Salmon, "Modeling Uncertainties in Mining Pillar Stability Analysis," *Risk Anal.*, vol. 29, no. 10, pp. 1371–1380, Oct. 2009, doi: 10.1111/J.1539-6924.2009.01237.X.

[26] J. Chen, "Karst Collapse in Cities and Mining Areas, China," 1988.

[27] C. A. Coulomb, "Essai sur une application de maximis et minimis à quelques de statique, relatives à l'Architecture," *Mémories del Mathématique Phys. Present. à l'Académie R. des Sci.*, vol. 7, pp. 343–387, 1773.

[28] Z. Cui, Y. Zhang, Q. Sheng, and L. Cui, "Investigating the Scale Effect of Rock Mass in the Yangfanggou Hydropower Plant with the Discrete Fracture Network Engineering Approach," *Int. J. Geomech.*, vol. 20, no. 4, Feb. 2020, doi: 10.1061/(ASCE)GM.1943-5622.0001584.

[29] W. S. Dershowitz and H. H. Herda, "Interpretation of fracture spacing and intensity," in *33rd U.S. Symposium on Rock Mechanics, USRMS*, Jun. 1992, pp. 757–766. doi: 10.1016/0148-9062(93)91769-f.

[30] D. . Dolinar and G. . Esterhuizen, "Evaluation of the effect of length on the strength of slender pillars in limestone mines using numerical modeling," in *26th International Conference on Ground Control in Mining*, 2007, pp. 304–313.

[31] D. Dolinar and G. Esterhuizen, "Evaluation of the effect of length on the strength of slender pillars in limestone mines using numerical modeling," in *Proceedings of the 26th international conference on ground control in mining*, 2007, pp. 304–313.

[32] D. Elmo and D. Stead, "An integrated numerical modelling-discrete fracture network approach applied to the characterisation of rock mass strength of naturally fractured pillars," *Rock Mech. Rock Eng.*, vol. 43, no. 1, pp. 3–19, Feb. 2010, doi: 10.1007/s00603-009-0027-3.

[33] G. S. Esterhuizen, "Variability considerations in hard rock pillar design," in *International Journal of Rock Mechanics and Mining Sciences & Geomechanics Abstracts*, 1993, vol. 31, no. 2, pp. 4–5. doi: 10.1016/0148-9062(94)93101-1.

[34] G. S. Esterhuizen, D. R. Dolinar, and J. L. Ellenberger, "Pillar strength in underground stone mines in the United States," *Int. J. Rock Mech. Min. Sci.*, vol. 48, no. 1, pp. 42–50, 2011, doi: 10.1016/j.ijrmms.2010.06.003.

[35] G. S. Esterhuizen, D. R. Dolinar, and J. L. Ellenberger, "Pillar strength in underground stone mines in the United States," *Int. J. Rock Mech. Min. Sci.*, vol. 48, no. 1, pp. 42–50, 2011, doi: 10.1016/J.IJRMMS.2010.06.003.

[36] G. S. Esterhuizen and M. M. Murphy, "S-Pillar (Version 1.2)." U.S. Department of Health and Human Services, Centers for Disease Control and Prevention, National Institute for Occupational Safety and Health, Office of Mine Safety and Health Research., 2011.

[37] G. S. Esterhuizen, "An evaluation of the strength of slender pillars," in *Society for Mining Metallurgy and Exploration*, 2007, vol. 320, p. 69.

[38] G. S. Esterhuizen, D. R. Dolinar, and J. L. Ellenberger, "Pillar strength and design methodology for stone mines," *Proc. 27th Int. Conf. Gr. Control mining. Morgant. WV West Virginia Univ.*, no. 9, pp. 241–253, 2008.

[39] G. S. Esterhuizen, D. R. Dolinar, and J. L. Ellenberger, "Pillar and Roof Span Design in Stone Mines," *Department Of Health And Human Services, NIOSH*, May 2011. http://stacks.cdc.gov/view/cdc/23444 (accessed Sep. 21, 2021).

[40] G. S. Esterhuizen, D. R. Dolinar, J. L. Ellenberger, and L. J. Prosser, "Pillar and roof span design guidelines for underground stone mines," National Institute for Occupational Safety and Health (NIOSH), Pittsburgh, PA, 2011.

[41] G. S. Esterhuizen and J. L. Ellenberger, "Effects Of Weak Bands On Pillar Stability In Stone Mines: Field Observations And Numerical Model Assessment," in *26th International Conference on Ground Control in Mining*, 2007, pp. 320–326.

[42] G. S. Esterhuizen, A. T. Iannacchione, J. L. Ellenberger, and D. R. Dolinar, "Pillar Stability Issues Based on a Survey of Pillar Performance in Underground Limestone Mines," in *Proceedings of the 25th International Conference on Ground Control in Mining*, Aug. 2006, pp. 354–361.

[43] G. Esterhuizen, D. Dolinar, and J. L. Ellenberger, "Pillar Strength and Design Methodology for Stone Mines," *27th Int. Conf. Gr. Control Min.*, pp. 241–253, 2008.

[44] Z. Fang and J. P. Harrison, "Development of a local degradation approach to the modelling of brittle fracture in heterogeneous rocks," *Int. J. Rock Mech. Min. Sci.*, vol. 39, no. 4, pp. 443–457, Jun. 2002, doi: 10.1016/S1365-1609(02)00035-7.

[45] N. L. Fazio *et al.*, "A three-dimensional back-analysis of the collapse of an underground cavity in soft rocks," *Eng. Geol.*, vol. 228, pp. 301–311, Oct. 2017, doi: 10.1016/J.ENGGEO.2017.08.014.

[46] S. Fekete, M. Diederichs, and M. Lato, "Geotechnical and operational applications for 3-dimensional laser scanning in drill and blast tunnels," *Tunn. Undergr. Sp. Technol.*, vol. 25, no. 5, pp. 614–628, Sep. 2010, doi: 10.1016/J.TUST.2010.04.008.

[47] S. Frisia and A. Borsato, "Chapter 6 Karst," *Dev. Sedimentol.*, vol. 61, no. C, pp. 269–318, 2010, doi: 10.1016/S0070-4571(09)06106-8.

[48] Golder Associates, "FracMan Manual."

[49] L. Gongyu and Z. Wanfang, "Sinkholes in karst mining areas in China and some methods of prevention," *Eng. Geol.*, vol. 52, no. 1–2, pp. 45–50, Mar. 1999, doi: 10.1016/S0013-7952(98)00053-2.

[50] D. Goodman, "Ground Penetrating Radar Imaging Software GPR-SLICE." 2018.

[51] M. Grasmueck, "3-D ground-penetrating radar applied to fracture imaging in gneiss," *Geophysics*, vol. 61, no. 4, pp. 1050–1064, 1996, doi: 10.1190/1.1444026.

[52] D. V. Griffiths, G. A. Fenton, and C. B. Lemons, "Probabilistic analysis of underground pillar stability," *Int. J. Numer. Anal. Methods Geomech.*, vol. 26, no. 8, pp. 775–791, Jul. 2002, doi: 10.1002/NAG.222.

[53] B. Haimson, "Deep stress measurements in three Ohio quarries and their comparison to near-surface tests," Aug. 1982.

[54] M. Hardy and J. Agapito, "Pillar design in underground oil shale mines," in *The 16th US Symposium on Rock Mechanics (USRMS)*, 1977, pp. 257–266.

[55] D. G. F. Hedley and F. Grant, "Stope-and-pillar design for Elliot Lake Uranium Mines," *Can. Min. Metall. Bull.*, vol. 65, no. 723, p. 37, 1972.

[56] G. Herget, "High stress occurrences in the Canadian Shield," Aug. 1982.

[57] E. Hoek and E. Brown, "Underground Excavations in Rock," *Inst. Min. Metall. London*, pp. 95–101, 1980.

[58] E. Hoek, P. K. Kaiser, and W. F. Bawden, *Support of underground excavations in hard rock*. CRC Press, 2000.

[59] C. T. Holland and F. L. Gaddy, "Some aspects of permanent support of overburden on coal beds," in *Proceedings of the West Virginia Coal Mining Institute*, 1957, pp. 43–65.

[60] V. Hooker and D. Bickel, *Overcoring equipment and techniques: used in rock stress determination*. 1974.

[61] V. E. Hooker and D. L. Bickel, *Overcoring Equipment and Techniques Used in Rock Stress Determination*, vol. 8618, no. 8618. US Bureau of Mines, 1974. doi: 10.1016/0148-9062(74)90409-4.

[62] A. T. Iannacchione, "Analysis of pillar design practices and techniques for US limestone mines," *Trans. Inst. Min. Metall. Sect. a-Mining Ind.*, vol. 108, pp. 152–160, 1999.

[63] M. A. Idris, D. Saiang, and E. Nordlund, "Stochastic assessment of pillar stability at Laisvall mine using Artificial Neural Network," *Tunn. Undergr. Sp. Technol.*, vol. 49, pp. 307–319, Jun. 2015, doi: 10.1016/J.TUST.2015.05.003.

[64] Itasca Consulting Group, "3DEC." Minneapolis, Minnesota, USA, 2021.

[65] Itasca Consulting Group, "Universal Distinct Element Code (UDEC)." Minneapolis, Minnesota, USA, 2021.

[66] Itasca Consulting Group, “Particle Flow Code (PFC).” Minneapolis, Minnesota, USA, 2021.

[67] Itasca Consulting Group, “Fast Lagrangian Analysis of Continua in 3 Dimensions (FLAC3D).” Minneapolis, Minnesota, USA, 2018.

[68] Itasca Consulting Group, “Griddle.” 2020.

[69] J. Jaeger, N. Cook, and R. Zimmerman, *Fundamentals of rock mechanics*, 4th ed. Blackwell Publishing, 2009.

[70] K. V. Jessu and A. J. S. Spearing, “Performance of inclined pillars with a major discontinuity,” *Int. J. Min. Sci. Technol.*, vol. 29, no. 3, pp. 437–443, May 2019, doi: 10.1016/j.ijmst.2018.09.006.

[71] L. Jing and J. A. Hudson, “Numerical methods in rock mechanics,” *Int. J. Rock Mech. Min. Sci.*, vol. 39, no. 4, pp. 409–427, Jun. 2002, doi: 10.1016/S1365-1609(02)00065-5.

[72] D. R. H. Jones and M. F. Ashby, “Elastic Moduli,” in *Engineering Materials 1*, 5th ed., Butterworth-Heinemann, 2019, pp. 31–47. doi: 10.1016/B978-0-08-102051-7.00003-8.

[73] E. Jones and D. Beck, "The use of three-dimensional laser scanning for deformation monitoring in underground mines.” 13th AusIMM Underground Operators’ Conference.

[74] E. Jones, "Mobile LiDAR for underground geomechanics: learnings from the teens and directions for the twenties," in *UMT 2020: Proceedings of the Second International Conference on Underground Mining Technology*, 2020, pp. 3–26. doi: 10.36487/ACG_repo/2035_0.01.

[75] A. E. Kehew, "General geology for engineers," pp. xv, 447 p., 1988.

[76] M. R. Von Kimmelmann, B. Hyde, and R. J. Madgwick, "Use of Computer Applications At Bcl Limited in Planning Pillar Extraction and the Design of Mining Layouts.," in *Int. Soc. Rock Mech. Symposium*, 1984, pp. 53–63. doi: 10.1016/0148-9062(85)92716-0.

[77] J. W. Koloski, S. D. Schwarz, and D. W. Tubbs, "Geotechnical properties of geologic materials," *Eng. Geol. Washingt.*, vol. 1, no. 78, pp. 19–24, 1989.

[78] J. Kortnik, "Optimization of the high safety pillars for the underground excavation of natural stone blocks," *Acta Geotech. Slov.*, vol. 6, no. 1, pp. 34–48, 2009.

[79] J. Kortnik, "High safety pillars design for underground excavation of natural stone blocks," *J. Civ. Eng. Constr. Technol.*, vol. 3, no. 6, Jun. 2012, doi: 10.5897/JCECT12.054.

[80] J. Kortnik, "Optimization of the high safety pillars for the underground excavation of natural stone blocks," *Acta Geotech. Slov.*, vol. 6, no. 1, pp. 35–48, 2009.

[81] J. Kortnik, "Stability assessment of the high safety pillars in Slovenian natural stone mines," *Arch. Min. Sci.*, vol. 60, no. 1, pp. 403–417, 2015, doi: 10.1515/amsc-2015-0027.

[82] N. Krauland and P. E. Soder, "Determining Pillar Strength from Pillar Failure Observation.," *Eng. Min. J.*, vol. 188, no. 8, pp. 34–40, 1987, doi: 10.1016/0148-9062(88)93093-8.

[83] G. Kuhnhein and R. Ramer, "The Influence of Horizontal Stress on Pillar Design and Mine Layout at Two Underground Limestone Mines," in *Proceedings of the 23rd International Conference on Ground Control in Mining*, 2004, pp. 311–319.

[84] E. L. Kuniansky, D. J. Weary, and J. E. Kaufmann, "The current status of mapping karst areas and availability of public sinkhole-risk resources in karst terrains of the United States," *Hydrogeol. J.*, vol. 24, no. 3, pp. 613–624, Nov. 2016, doi: 10.1007/S10040-015-1333-3/FIGURES/4.

[85] Q. Lei, J. P. Latham, and C. F. Tsang, "The use of discrete fracture networks for modelling coupled geomechanical and hydrological behaviour of fractured rocks," *Comput. Geotech.*, vol. 85, pp. 151–176, May 2017, doi: 10.1016/J.COMPGEO.2016.12.024.

[86] P. Lollino, V. Martimucci, and M. Parise, "Geological survey and numerical modeling of the potential failure mechanisms of underground caves," *Geosystem Eng.*, vol. 16, no. 1, pp. 100–112, Mar. 2013, doi: 10.1080/12269328.2013.780721.

[87] N. Lu and W. J. Likos, "Origin of Cohesion and Its Dependence on Saturation for Granular Media," *Poromechanics V - Proc. 5th Biot Conf. Poromechanics*, pp. 1669–1675, 2013, doi: 10.1061/9780784412992.197.

[88] P. J. Lunder and R. C. Pakalnis, "A determination of the strength of hard-rock mine pillars," *CIM Bull.*, vol. 90, no. 1013, pp. 51–55, 1997.

[89] P. Lunder, "Hard Rock Pillar Strength Estimation -an Applied Empirical Approach," University of British Columbia, 1994. doi: 10.14288/1.0087520.

[90] D. Ma and H. Bai, "Groundwater inflow prediction model of karst collapse pillar: a case study for mining-induced groundwater inrush risk," *Nat. Hazards*, vol. 76, no. 2, pp. 1319–1334, 2015, doi: 10.1007/s11069-014-1551-3.

[91] D. Ma, H. Bai, X. Miao, H. Pu, B. Jiang, and Z. Chen, "Compaction and seepage properties of crushed limestone particle mixture: an experimental investigation for Ordovician karst collapse pillar groundwater inrush," *Environ. Earth Sci.*, vol. 75, no. 1, pp. 1–14, Jan. 2016, doi: 10.1007/S12665-015-4799-3/FIGURES/13.

[92] D. Ma, X. Cai, Q. Li, and H. Duan, "In-situ and numerical investigation of groundwater inrush hazard from grouted karst collapse pillar in longwall mining," *Water (MDPI)*, vol. 10, no. 9, p. 1187, Sep. 2018, doi: 10.3390/w10091187.

[93] D. F. Malan and J. A. L. Napier, "The design of stable pillars in the Bushveld Complex mines: A problem solved?," *J. South. African Inst. Min. Metall.*, vol. 111, no. 12, pp. 821–836, 2011.

[94] Maptek Ltd., "PointStudio - Point cloud modeling and analysis." 2021.

[95] D. Marchetti, G. Avanzi, N. Sciarra, M. Calista, and L. Piaggi, "Pillar sizing and stability analysis by numerical modeling for underground stone quarrying," May 2021.

[96] C. Mark, F. Chase, and R. Zipf, *Preventing massive pillar collapses in coal mines*. Public Health Service, Centers for Disease Control and Prevention, National Institute for Occupational Safety and Health, 1997.

[97] C. Mark and F. E. Chase, "Analysis of Retreat Mining Pillar Stability (ARMPS)," in *Proceedings of the new technology for ground control in retreat mining, NIOSH IC 9446*, Nov. 1997, pp. 17–34.

[98] C. Mark and M. Gauna, "Preventing roof fall fatalities during pillar recovery: A ground control success story," *Int. J. Min. Sci. Technol.*, vol. 27, no. 1, pp. 107–113, Jan. 2017, doi: 10.1016/J.IJMST.2016.09.030.

[99] T. Marshall, L. Prosser, A. Iannacchione, and M. Dunn, "Roof Monitoring in Limestone-Experience with the Roof Monitoring Safety System (RMSS)," in *Proceedings of the 19th International Conference on Ground Control in Mining*, 2000, pp. 185–191.

[100] C. D. Martin and W. G. Maybee, "The strength of hard-rock pillars," *Int. J. Rock Mech. Min. Sci.*, vol. 37, no. 8, pp. 1239–1246, Dec. 2000, doi: 10.1016/S1365-1609(00)00032-0.

[101] R. C. McDowell and A. P. Schultz, "Structural and stratigraphic framework of the Giles County area, a part of the Appalachian Basin of Virginia and West Virginia," *US Geological Survey Bulletin*, vol. 1839 E. 1990.

[102] H. Melin, "Controlling parameters for normal and shear behaviour of rock fractures-a study of direct shear test data from SKB," 2012.

[103] R. Metsger, "Mining problems in a karst valley—technical and social," *Bull. Assoc.*, 1979.

[104] T. Miyoshi, D. Elmo, and S. Rogers, "Influence of data analysis when exploiting DFN model representation in the application of rock mass classification systems," *J. Rock Mech. Geotech. Eng.*, vol. 10, no. 6, pp. 1046–1062, Dec. 2018, doi: 10.1016/J.JRMGE.2018.08.003.

[105] J. J. Monsalve, J. G. Baggett, A. Soni, N. Ripepi, and J. Hazzard, "Stability analysis of an underground limestone mine using terrestrial laser scanning with stochastic discrete element modeling," Jun. 2019.

[106] J. Monsalve, "Integrating Laser Scanning with Discrete Element Modeling for Improving Safety in Underground Stone Mines," Virginia Tech, Blacksburg, 2019.

[107] J. J. Monsalve, A. Pfreundschuh, A. Soni, and N. Ripepi, "Automated Discontinuity Extraction Software Versus Manual Virtual Discontinuity Mapping: Performance Evaluation in Rock Mass Characterization and Rockfall Hazard Identification," *Mining, Metall. Explor. 2021 383*, vol. 38, no. 3, pp. 1383–1394, Mar. 2021.

[108] MSHA, "Mine Safety and Health Administration." 2021.

[109] J. Muaka *et al.*, "Modelling hard rock jointed pillars using a distinct element and discrete fracture network approach considering the effect of a clay-filled shear structure," in *Deep Mining 2017: Eighth International Conference on Deep and High Stress Mining*, Mar. 2017, pp. 311–328. doi: 10.36487/ACG_REP/1704_22_MUAKA.

[110] G. Napa-García and V. Navarro Torres, "Applicability of failure strain for the stability evaluation of square pillars in room and pillar mining," *UMT 2017 First Int. Conf. Undergr. Min. Technol.*, pp. 557–565, Oct. 2017, doi: 10.36487/ACG_REP/1710_45_NAPA-GARCIA.

[111] National Institute for Occupational Safety and Health, "Mine and Mine Worker Charts," *Centers for Disease Control and Prevention*, 2021. https://wwwn.cdc.gov/niosh-mining/MMWC

[112] H. Ninanya, N. Guiguer, E. A. Vargas, G. Nascimento, E. Araujo, and C. L. Cazarin, "Analysis of water control in an underground mine under strong karst media influence (Vazante mine, Brazil)," *Hydrogeol. J. 2018 267*, vol. 26, no. 7, pp. 2257–2282, May 2018, doi: 10.1007/S10040-018-1785-3.

[113] E. B. Niven and C. V Deutsch, "Relating Different Measures of Fracture Intensity," *CCG Annu. Rep.*, vol. 12, 2010.

[114] L. Obert and W. Duvall, *Rock Mechanics and the design of structures in rock*, vol. 650. New York: Wiley, 1967.

[115] M. Parise and P. Lollino, "A preliminary analysis of failure mechanisms in karst and man-made underground caves in Southern Italy," *Geomorphology*, vol. 134, no. 1–2, pp. 132–143, Nov. 2011, doi: 10.1016/J.GEOMORPH.2011.06.008.

[116] M. Pierce, "An introduction to random disk discrete fracture network (DFN) for civil and mining engineering applications," *ARMA e-Newsletter*, pp. 3–8, 2017.

[117] Y. Potvin, M. Hudyma, and H. Miller, "Design guidelines for open stope support," *Bull Can Min Met.*, vol. 82, pp. 53–62, 1989.

[118] C. Pritchard and D. Hedley, "Progressive pillar failure and rockbursting at Denison Mine," in *Proceedings of 3rd International Symposium on Rockbursts and Seismicity in Mines, Kingston. Rotterdam: AA Balkema*, 1993, pp. 111-J6.

[119] Robert McNeel & Associates, "Rhinoceros 3D." 2020.

[120] D. Roberts, D. Tolfree, and H. McIntire, "Using confinement as a means to estimate pillar strength in a room and pillar mine," May 2007.

[121] Rocscience, "Documentation-Strength Properties." https://www.rocscience.com/help/rs3/documentation/geology-excavation/materials/define-material-properties/strength-parameters/strength-properties (accessed Apr. 01, 2022).

[122] Rocscience Inc., "Dips - Graphical and Statistical Analysis of Orientation Data." 2021.

[123] S. Rogers, D. Elmo, G. Webb, and A. Catalan, "Volumetric Fracture Intensity Measurement for Improved Rock Mass Characterisation and Fragmentation Assessment in Block Caving Operations," *Rock Mech. Rock Eng.*, vol. 48, no. 2, pp. 633–649, Mar. 2015, doi: 10.1007/S00603-014-0592-Y/FIGURES/21.

[124] M. Salamon and A. Munro, "A study of the strength of coal pillars," *J. South. African Inst. Min. Metall.*, vol. 68, no. 2, p. 67, 1967.

[125] J. Sjöberg, "Failure modes and pillar behaviour in the Zinkgruvan mine," in *33rd U.S. Symposium on Rock Mechanics, USRMS 1992*, Jun. 1992, pp. 491–500. doi: 10.1016/0148-9062(93)93204-b.

[126] B. A. Slaker, M. M. Murphy, and T. Miller, "Analysis of extensometer, photogrammetry and laser scanning monitoring techniques for measuring floor heave in an underground limestone mine," *Trans. Soc. Mining, Metall. Explor. Inc*, vol. 344, no. 1, p. 31, Jan. 2018, doi: 10.19150/TRANS.8746.

[127] B. Slaker, M. Murphy, and J. Winfield, "Tracking convergence, spalling, and cutter roof formation at the pleasant gap limestone mine using LiDAR," 2019.

[128] A. Soni, J. Monsalve, R. Bishop, and N. Ripepi, "Modified Design of Pillar based on Estimated Stresses and Pillar in an Underground Limestone Mine,". In Press. *Manuscript Submitted for Publication.*

[129] A. Soni, J. J. Monsalve, R. Bishop, N. Ripepi, and J. G. Baggett, "Estimating Strength of Pillars with Karst Voids in a Room-and-Pillar Limestone Mine," *Mining, Metall. Explor.*, pp. 1–14, 2022.

[130] A. Soni, S. R. Naik, and N. Ripepi, "Stability analysis of drives excavated in paste-filled stopes for underhand mining," Jun. 2019. 53rd U.S. Rock Mechanics/Geomechanics Symposium. New York, NY.

[131] A. Soni, J. Monsalve, and N. Ripepi, "Analysis of Pillar Strength and Design in a Karst-affected Underground Stone Mine," 2022. 56th U.S. Rock Mechanics/Geomechanics Symposium. Santa Fe, NM.

[132] Statista, "U.S. crushed stone production 2011-2021," 2021. https://www.statista.com/ (accessed Mar. 02, 2022).

[133] M. Sturzenegger, M. Yan, D. Stead, and D. Elmo, "Application and limitations of ground-based laser scanning in rock slope characterization," 2007. doi: 10.1201/NOE0415444019-c4.

[134] H. Sun *et al.*, "Characterization of shallow karst using electrical resistivity imaging in a limestone mining area," *Environ. Earth Sci. 2017 7622*, vol. 76, no. 22, pp. 1–9, Nov. 2017, doi: 10.1007/S12665-017-7112-9.

[135] A. Tomory, J. Carvalho, and M. Kowalczyk, "Logistic Regression in Hard Rock Pillar Design," Jun. 2014.

[136] A. Vakili, "An improved unified constitutive model for rock material and guidelines for its application in numerical modelling," *Comput. Geotech.*, vol. 80, pp. 261–282, Dec. 2016, doi: 10.1016/J.COMPGEO.2016.08.020.

[137] I. Vazaios, N. Vlachopoulos, and M. S. Diederichs, "Integration of Lidar-Based Structural Input and Discrete Fracture Network Generation for Underground Applications," *Geotech. Geol. Eng.*, vol. 35, no. 5, pp. 2227–2251, Oct. 2017, doi: 10.1007/S10706-017-0240-X.

[138] N. Vlachopoulos, I. Vazaios, B. Forbes, and C. Carrapatoso, "Rock Mass Structural Characterization Through DFN–LiDAR–DOS Methodology," *Geotech. Geol. Eng.*, vol. 38, no. 6, pp. 6231–6244, Dec. 2020, doi: 10.1007/S10706-020-01431-1.

[139] H. Wagner, "Pillar design in coal mines," *J. South. African Inst. Min. Metall.*, vol. 80, no. 1, pp. 37–45, 1980, doi: 10.10520/AJA0038223X_1290.

[140] H. Wagner and T. Frömmer, "Changing the mining method in an Austrian magnesite mine," *Min. Sustain. Dev.*, pp. 211–215, 2005.

[141] R. K. Wattimena, "Predicting the stability of hard rock pillars using multinomial logistic regression," *Int. J. Rock Mech. Min. Sci.*, vol. 71, no. 71, pp. 33–40, 2014, doi: 10.1016/j.ijrmms.2014.03.015.

[142] A. H. Wilson, "An hypothesis concerning pillar stability," *Min Eng (London)*, vol. 131, no. 141, pp. 409–417, 1972.

[143] B. Yao, Z. Chen, J. Wei, T. Bai, and S. Liu, "Predicting Erosion-Induced Water Inrush of Karst Collapse Pillars Using Inverse Velocity Theory," *Geofluids*, vol. 2018, 2018, doi: 10.1155/2018/2090584.

[144] Y. Zhang, "Modelling hard rock pillars using a Synthetic Rock Mass approach ," Simon Fraser University, Vancouver, 2014.

[145] J. Zhou, X. B. Li, X. Z. Shi, W. Wei, and B. B. Wu, "Predicting pillar stability for underground mine using Fisher discriminant analysis and SVM methods," *Trans. Nonferrous Met. Soc. China*, vol. 21, no. 12, pp. 2734–2743, Dec. 2011, doi: 10.1016/S1003-6326(11)61117-5.

[146] J. Zhou, X. Li, and H. S. Mitri, "Comparative performance of six supervised learning methods for the development of models of hard rock pillar stability prediction," *Nat. Hazards*, vol. 79, no. 1, pp. 291–316, Oct. 2015, doi: 10.1007/S11069-015-1842-3/FIGURES/7.

[147] R. Zipf, "Pillar Design to Prevent Collapse of Room-And-Pillar Mines," *Undergr. Min. Methods Eng. Fundam. Int. Case Stud.*, Jan. 2001.

[148] "Limestone - Global Market Trajectory & Analytics," 2021.

Appendices

Appendix A

This research is a part of the capacity building project "Ground control research for improving safety performance in underground stone and other large opening mines: Design, Monitoring and Risk management".

The project is funded by the National Institute for Occupational Safety and Health (NIOSH) Mining Program under Contract No. 200-2016-91300.

Appendix B

The following manuscript was accepted for publication by the Mining, Metallurgy & Exploration journal, titled "Effect of Karst Voids on Pillar Strength in an Underground Limestone Mine"

Mining, Metallurgy & Exploration
https://doi.org/10.1007/s42461-022-00594-0

REVIEW

Estimating Strength of Pillars with Karst Voids in a Room-and-Pillar Limestone Mine

Aman Soni[1] · Juan J. Monsalve[1] · Richard Bishop[1] · Nino Ripepi[1] · Jonathan G. Baggett[2]

Received: 19 September 2021 / Accepted: 29 March 2022

Abstract

Underground limestone deposits are prone to karst void formations due to the dissolution of carbonate rocks. These deposits offer permeable conditions to groundwater flow leading to the formation of a network of void spaces or cavities. The cavities can accommodate unconsolidated sediments and groundwater. Interaction of these voids with a prevalent discontinuity network may lead to ground control problems during mining operations. This paper presents a numerical estimation of the effect of karst voids on the strength of pillars in an underground room-and-pillar limestone mine. It is shown that these voids may contribute to a considerable decrease in pillar strength. Mining advances into such formations may lead to a sudden inrush of groundwater or unconsolidated sediments. Apart from posing a safety hazard, this may also disrupt the pre-planned mine operations and design of the headings and pillars. The procedure for estimation of pillar strength using numerical modeling may provide a viable approach to design the future pillars detected with karst voids. Previous studies performed at the case study mine used ground-penetrating radar (GPR) to map the karst boundaries inside the pillar. Apart from the LiDAR scans used to map the discontinuity network around the pillars, some approximations were made to account for the inadequate discontinuity characterization data. Distinct-element modeling (DEM) is used to simulate the presence of voids and discontinuities in the form of discrete fracture networks (DFN). An effort is made to understand the importance of pillar design and dimensions in an underground limestone mine with karst voids to prevent local instability related to pillar failures.

Keywords Pillar strength · Pillar design · Karst · 3DEC · DEM · DFN · GPR · Ground control

1 Introduction

Over the past decade, underground stone mining operations in limestone deposits have become more common in the eastern USA. Compared to slope stability efforts in surface operations, ground control operations in underground mining are more complicated and require more engineering and training. Currently, there are 110 underground stone mines in the USA majority of which employ room-and-pillar mining methods to extract limestone for crushed stone products (NIOSH, 2021). Despite employing fewer miners than coal mines, stone mines experience a higher number of reportable injuries. Since 1983, about 12% of all the reported injuries in the stone mining industry are because of rock falls from the roof or pillar ribs (MSHA, 2021).

Compared to other rock types, limestone mines have a higher potential to encounter karst voids at some point during their excavation operations. This is due to the prevalent karstic network developed in the limestone rock masses [1]. These cavities are formed over a long time by the dissolution of carbonate rocks and can be unforeseen until encountered due to mining activities. The hindrance of karsts in the mining operations has been well documented by [2]. The disruption of mining operations while encountering karst cavities often requires potential ground control measures beyond the typical scope of a ground control management plan (GCMP) constituted for the mine. Even the rock mass classification schemes, such as the Rock Mass Rating (RMR) from Bieniawski and the Q-system from Barton, do not classify the karst-affected carbonate rock mass, and therefore the analysis of such cases requires geological analysis of the underground conditions [3].

✉ Aman Soni
amansoni@vt.edu

[1] Mining and Minerals Engineering, Virginia Polytechnic Institute & State University, Blacksburg, VA, USA

[2] Rio Tinto Corporation, Salt Lake City, UT, USA

Published online: 21 April 2022

This paper evaluates the stability of a pillar (designated Pillar-X) with the presence of a karst void in an underground limestone mine. The case study mine is a multi-level room-and-pillar underground limestone mine. The pillar in question, i.e., Pillar-X, lies at a depth of about 180 m from the surface. The study discusses the methods which were utilized in determining the karst boundaries inside the suggested Pillar-X, using ground-penetrating radar (GPR). The size of Pillar-X was left to be bigger than the intended pillar dimensions to counter any local instability issue which may have been suspected by the mine management. The mine has experienced ground control issues such as roof and rib failures in the past. The karst cavities, filled with unconsolidated clayey-rock material, may interact with the immediate roof or ribs in the mine drives, or even around a pillar. The interaction is also dominated by the discontinuity network, which is a typical feature of a naturally fractured limestone deposit. Any karst voids which extend beyond the pillar into the roof and floor will also adversely affect the pillar stability. The potential loading issues caused by the extension of voids beyond the pillar and their interaction with the discontinuities are not discussed in this paper. To study the stability of Pillar-X, a 3-dimensional numerical modeling tool 3DEC was used. This software utilizes a finite-difference distinct element method (DEM) to simulate the condition of an underground excavation. The DEM is useful in characterizing the presence of discontinuous media in the rock mass. The pillar model is framed using the rock material and joint properties that were measured by the mine management and confirmed using laboratory testing. LiDAR scans of the pillar were used for discontinuity mapping of the pillar and assessing the different joint sets using Maptek's I-Site point-cloud processing software. Since all of the joints' characteristics cannot be measured inside Pillar-X, a discrete fracture network (DFN) was employed to create a virtual network system which is the closest possible representation to a real-world joint system. Different scenarios were created to account for the irregularities found in the GPR surveys. For each scenario, the pillar model was analyzed for its strength based on a constant compressive velocity applied to it. The analysis characterizes the significant reduction in the pillar strength in the different scenarios, each with increased karst void volume. The paper also discusses the importance of pillar design in the presence of karst cavities to maximize ore extraction as well as maintain local and global stability in a stone mine.

2 Background

2.1 Case Study Mine

The case-study mine is situated in a region with synclinal Ordovician limestone. The limestone deposit hosts an extensive network of interconnected karst cavities. These cavities are formed over several years due to the dissolution of limestone rock by the flow of groundwater or weak carbonic acid through the vast fracture network of a limestone deposit. The orebody is 30 m thick and dips at approximately 30° towards the southeast as visible from the outcrop. The levels of the mine are connected by a corkscrew ramp. Each level has an east and west section branching off of the corkscrew ramp; at present, each branch contains a footwall and hanging wall tunnel separated by 24.5 m × 24.5 m × 30.5 m rectangular pillars left after complete extraction from the eventual stoping, and tunnels are approximately 8.5-m tall and 14-m wide.

2.2 Pillar Location and Geometry

The pillar being analyzed in this paper, named Pillar-X for this study, is shown in Figs. 1 and 2. After the discovery of karst voids in Pillar-X, the stopes around it were not completely excavated, leaving the pillar height to be 9.5 m as opposed to the intended pillar height of 30.5 m after the complete extraction of stope from the adjacent levels. During the initial preparation of the stope around the pillar, the mine workers faced a safety incident of ground collapse from the side-wall which opened up to the karst cavity.

The spillage of wet clay along with the rock boulders did not result in any injuries but it hampered the operations in that region and required additional mucking and rehabilitation of ground support. Figure 3 shows the material collapse in the mine due to the opening up of the karst cavity. The mine management employed temporary ground support measures such as plastic mesh pinned up with steel straps to prevent heading damage due to clayey-rock material and groundwater seepage. Furthermore, grouting was done as a permanent ground control measure to prevent any suspected local instability issues. Figure 4 shows the temporary ground controls measure taken around the pillar.

2.3 GPR Investigative Study

Ground-penetrating radar (GPR) surveys could be effective in detecting dielectric boundaries within a solid structure, such as rock mass or concrete pillars [4]. GPR's advantage to map bedrock depth and soil stratigraphy [5] and mapping fractures in gneissic rocks [6] amongst other works has been well renowned. At the case study mine, investigative work was conducted to detect the shape of any karst void(s) in Pillar-X via a dense grid of 3-dimensional GPR survey [4].

The authors used a 3-sq. m tarp marked with gridded survey lines and shot locations. Figure 5 shows the authors surveying the underground case study mine.

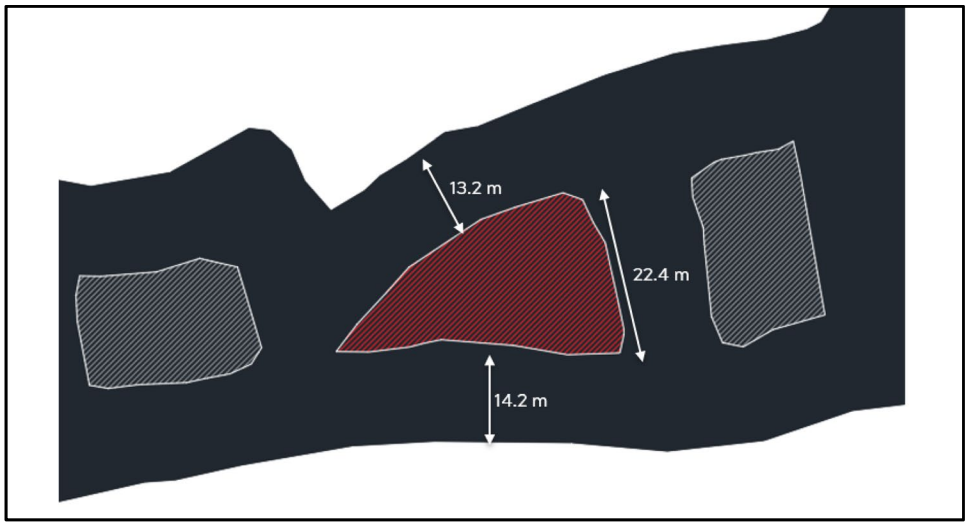

Fig. 1 Plan view of Pillar-X in the underground mine

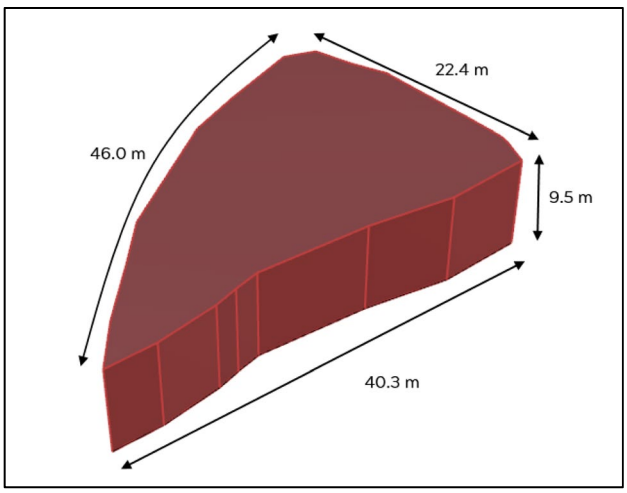

Fig. 2 Perspective view of Pillar-X in the underground mine

Fig. 3 Material collapse from karst void in the case study mine (Credits: R. Bishop)

Fig. 4 Ground support around Pillar-X (Credits: R. Bishop)

The survey was conducted on a total of 8 tarp positions along the ~ 46-m length along one side of Pillar-X. The survey was not extended along the 40.3 m length because of the mesh installed on the collapsed pillar rib to block any inflow of consolidated segments. This prevented any additional data collection for delineating the karst cavity boundaries, considering how groundwater and clayey material attenuate the signals. A 250-MHz antenna was selected by the authors as this frequency showed a penetration depth of greater than 20 m and resolution was favorable to obtain surface reflections. To extract reflection events and ultimately convert these to either points or iso-surfaces, GPR Slice software was used by the authors. The iso-surfaces from all tarp survey grids identified the commonalities and surface trends, as seen in Fig. 6a and b.

The clusters of these iso-surfaces or points were connected to form meshes to produce representative surfaces of the karst void boundary. The plan view of the

Fig. 5 3D GPR survey conducted along the Pillar-X

Fig. 7 Iso-surface meshes created from the reflection points

iso-surface mesh reflection boundary of the karst void inside the pillar is shown in Fig. 7.

Conductive mediums, such as wet clays and water which fill the karst void, highly attenuate the GPR wave energy. Limestone rock is dry, homogenous, and a resistive medium for GPR waves, and is ideal for strongly transmitted and reflected signals [7]. Since the conductive medium inside the void produced reflections, the authors could not propose a closed void volume, which in terms of delineating void boundaries, would be an ideal case. Figure 8 shows a plan view of the approximated karst volume to area projection by the authors [4].

However, the GPR results from this study investigated the surfaces along the pillar sidewalls only. Therefore, there is no information regarding the continuation of discovered cavities above or below the survey window along the pillar. However, accounts from the mining personnel who performed the ground control measures at the site suggest the continuation of void in the immediate roof of the pillar. Also, the physical testing of the void fill material, as indicated by the observed characteristics of reflected radar signals, was not performed. To compensate for the missing information, the karst cavity was assumed to be continuous across the height of the pillar. This will always underestimate the pillar strength as it will possess a larger void volume filled with weak material. Also, different scenarios were considered to include all possibilities for cavity shapes that may affect the pillar strength. These scenarios involved varying the size of karst volume ranging from the approximated volume to a worst-case scenario, where the outer boundaries of the iso-surface reflections were considered with no limestone rock mass in between. These cases are explained further in the sections.

3 Distinct Element Modeling in 3DEC

3DEC is a three-dimensional numerical modeling code developed by Itasca Consulting Group [16]. This software is based on the distinct element method (DEM) for simulating the response of the discontinuum network in rock masses such as joints and fractures. The software represents discontinuous media as an assembly of discrete blocks and the discontinuities between them as boundary conditions. For this study, individual blocks are set as deformable material

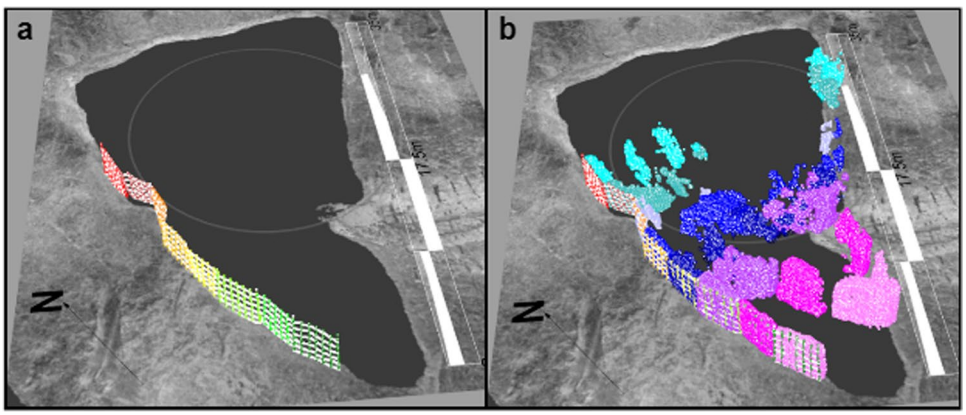

Fig. 6 **a**, **b** Reflection points obtained from the GPR survey along one side of the pillar [4]

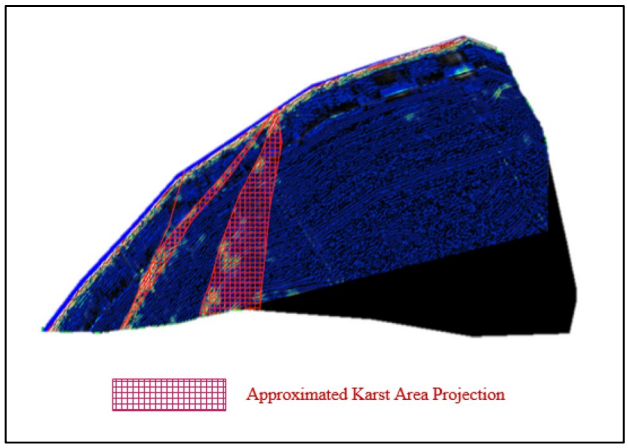

Fig. 8 Plan view of an approximate karst area projected from the iso-surface meshes [4]

and are meshed as finite different zones. The displacements along the joints and rotation of blocks facilitate us to observe the behavior of the pillar under increasing load.

Pillar strength in stones mines has been studied by many researchers. [8, 9, 11] have suggested methods of estimating the pillar strength and supplemented it with numerical models. [12] addressed the pillar design issues that are typically faced in underground mines. DEM has frequently been used as a tool to analyze rock mass behavior, however, there is a lack of published research on analyzing pillar strength with karst voids detected using underground mining GPR applications.

4 Pillar Model Generation

4.1 Pillar-X Model Scenarios

For this study, three different scenarios were considered in which the pillar geometry was kept constant. However, the karst void volume was varied to simulate the effect of increasing void volume on pillar strength. The karst voids in the cases were assumed to be empty to underestimate any insignificant support provided by the clayey-rock material present inside the void. The constructed Pillar-X model dimensions were estimated by the LiDAR scans obtained around the pillar. The three scenarios are described in detail below:

i. *Scenario 1* — In this case, the Pillar-X was assumed to be a solid limestone pillar without any karst voids. To assess the effect of karst voids on pillar strength, it is important to model a benchmark pillar strength value. In this case, it was done by simulating the case in which a solid pillar is subjected to increasing compressive stresses until failure is achieved. Figure 9 shows the geometry of the solid pillar. The volume of the original pillar is ~ 5580 cu.m.
ii. *Scenario 2* — In this scenario, the karst voids were created analogous to the iso-surface boundaries as suggested by the GPR study as shown in Fig. 8. The karst voids were assumed to run throughout the height of the pillar. This scenario simulates a most likely case which is suggested by the authors of this paper and also the authors that conducted the GPR study. Figure 10 shows the geometry of the pillar and karst void. The volume of the empty karst void simulated in scenario 2 is roughly 482 cu.m, constituting roughly 9% of the total volume.
iii. *Scenario 3* — In this case, Pillar-X is simulated with the karst voids having the largest volume. It is assumed that the outer boundaries of the GPR iso-surfaces form the shape of the void and there is no hard-rock wedge dividing the void as present in scenario 2. The simulated pillar model of this case is shown in Fig. 11. The karst void in scenario 3 has the largest void volume of about 1009 cu.m, constituting roughly 18% of the total volume.

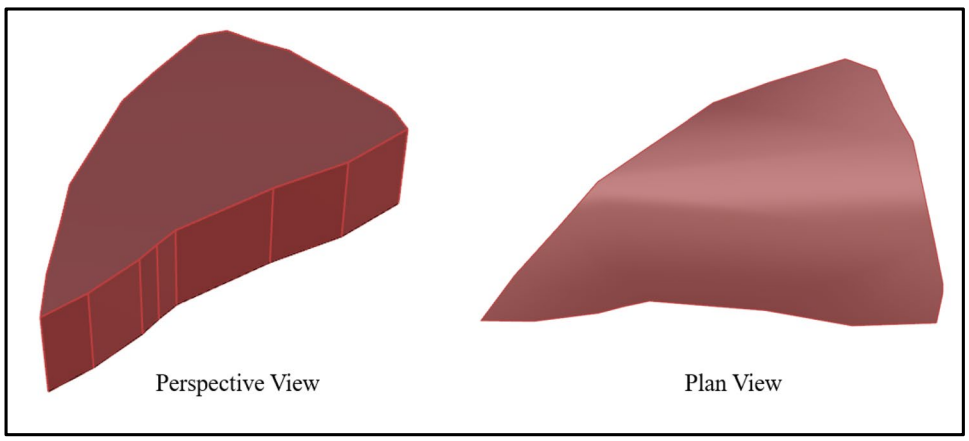

Fig. 9 Simulated Pillar-X model in scenario 1

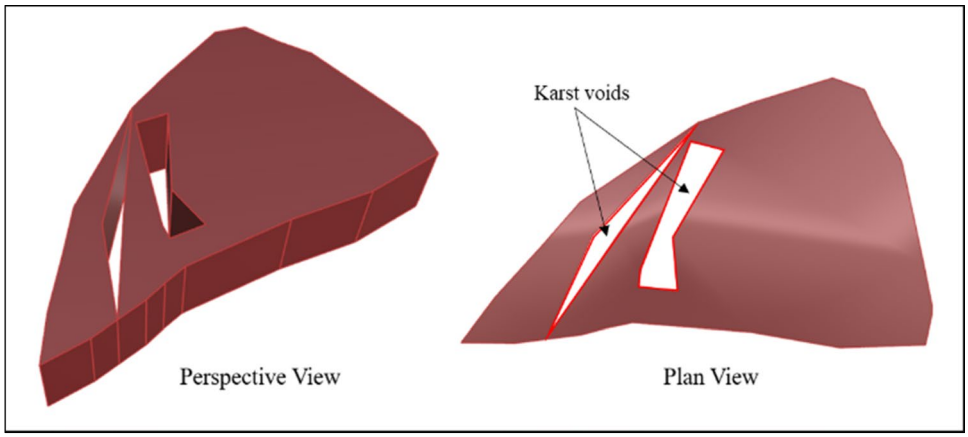

Fig. 10 Simulated Pillar-X model in scenario 2

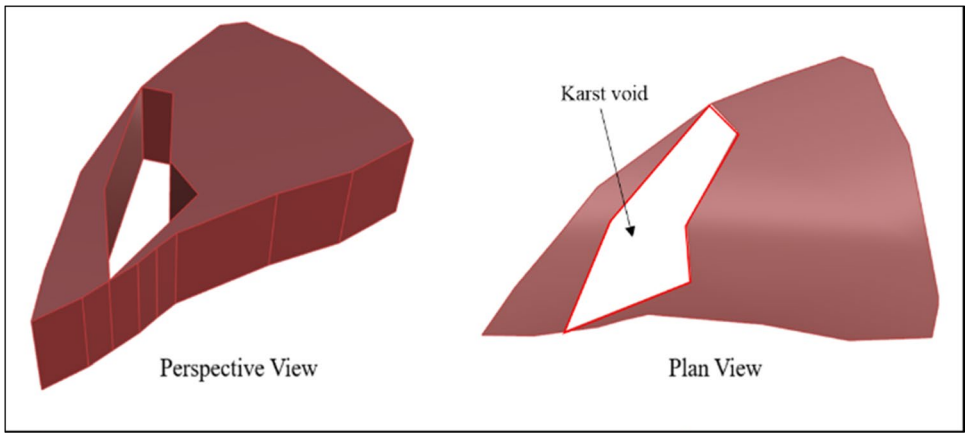

Fig. 11 Simulated Pillar-X model in scenario 3

4.2 Physico-mechanical Properties

The physico-mechanical and geotechnical properties for the rock mass and joints used in the numerical model were measured by the mine management using geotechnical borehole measurements and laboratory testing. The calculated values for joint shear stiffness and joint normal stiffness are based on the work performed by [13, 14]. The properties are listed in Table 1. The lithology of the synclinal Ordovician limestone deposit in the ore body was characterized as Five Oaks limestone [15]. The elastic-isotropic constitutive model is used to represent rock behavior in the numerical model. The authors believe that the strain softening/hardening model could have been the ideal model to simulate the Pillar-X model, but due to the absence of detailed properties, the elastic-isotropic model state was simulated. This constitutive model characterizes the pillar to reflect reversible deformations upon unloading, i.e., the stress–strain laws are linear and path-independent. The Coulomb slip joint constitutive model is assigned to represent the physical response of rock joints. The model simulates the displacement of the discontinuities by weakening cohesive and tensile strength when shear or tensile failure begins [16].

Table 1 Physico-mechanical properties for rock mass and joints

Rock mass properties	
Density	2690 kg/m^3
Bulk modulus, K	37.86 GPa
Shear modulus, G	20.57 GPa
Poisson's ratio	0.27
Joint properties [13]	
Joint normal stiffness	300 GPa/m
Joint shear stiffness	30 GPa/m
Joint friction angle	30°
Joint cohesion	0.0

4.3 Boundary Conditions

For assessing the pillar strength, compressive stresses axially along the z-axis to the pillar. Since the pillar is not supported by any material on the sides, no boundary conditions

were applied to the model sides. Fixed boundaries were applied to the top and bottom face of the pillar to prevent any movement and ensure constant stress application with time steps. The load was applied to the pillar model in each scenario using an applied velocity on the top and bottom. It is assumed that only the compressive stress or the vertical stress is being imparted along the axis of the pillar, thus compressing the pillar. No shear stresses are applied on the top and bottom face of the pillar model. The magnitude of the velocity applied was about 0.5 mm/s. Each scenario was cycled until failure of the pillar model in each scenario was observed.

4.4 Discontinuity Mapping

An important aspect of the numerical modeling of Pillar-X was to account for the discontinuity network affecting it. Joints play a major role in deciding the strength of a rock mass and detailed knowledge of them would help to simulate accurate conditions. A preliminary investigation was conducted at the case study mine which describes obtaining the LiDAR scans and virtually mapping the discontinuity network around the area from the scans [14]. Maptek I-Site, a point cloud processing and modeling software, was used to extract the discontinuities and different parameters such as joint orientation, fracture density, and size of joints in different joint sets. Figure 12 shows the plan view of the structural mapping performed around Pillar-X. Four discontinuity sets were defined from the mapped discontinuities. Figure 13 shows the process of structural discontinuity mapping in the I-Site.

5 Discrete Fracture Network

After sufficient information on the structural features was collected from the LiDAR scans, the data were classified into four joint sets. Extracted data included size information (trace length and area) and orientation information (dip, dip direction, and strike). All this information is used by 3DEC to generate DFNs which simulate a close representation of the geological structures in a rock mass. This fracture network is a set of discrete, planar, finite-size fracture disks, which intersect the model to generate a set of blocks that constitute a simulated jointed rock mass. These disks are created based on statistical data of the joint characteristics, such as orientation, size, and density, measured in the field [17], or in this case, measured virtually from LiDAR point clouds. Table 2 summarizes the statistical data of the joint properties for each joint set used in the modeling study.

One of the important parameters for generating DFNs is fracture density, which is a measure of the spatial frequency of discontinuities in a joint set. This parameter serves as a threshold condition while generating DFNs in 3DEC [10]. For this study, fracture density was defined as the area of fractures per unit volume of the rock mass or P_{32}. The DFN model is calibrated using the P_{32} values of the four joint sets measured in the DFNs for the model. Since the fractures per unit volume in the pillar cannot be measured practically through field mapping, P_{10}, also known as linear fracture intensity values are measured.

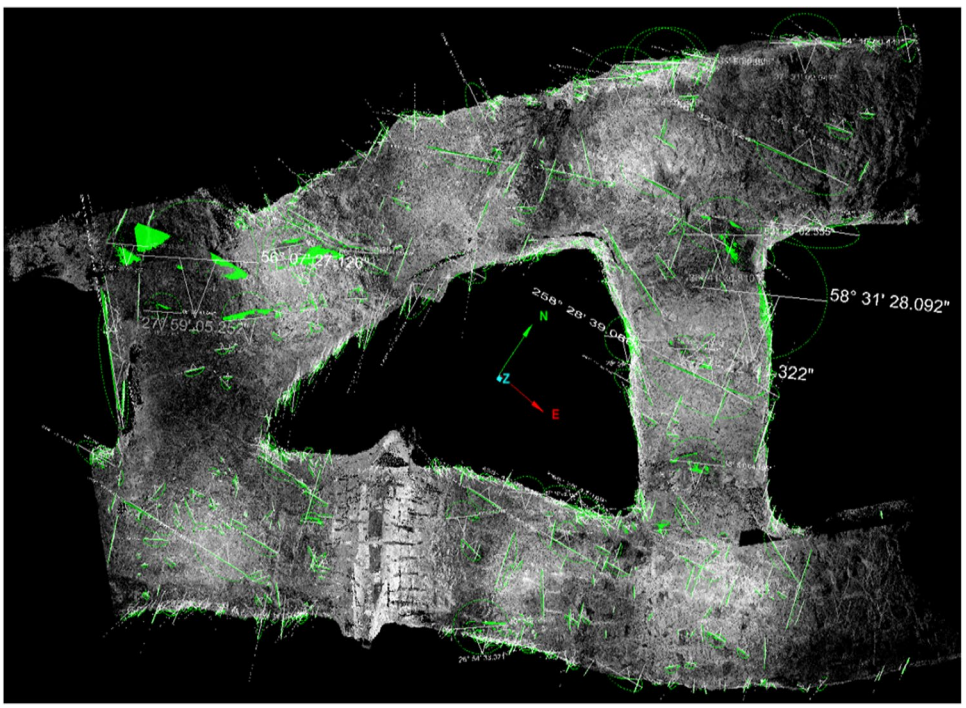

Fig. 12 Virtual discontinuity mapping from LiDAR scans around the Pillar-X [14]

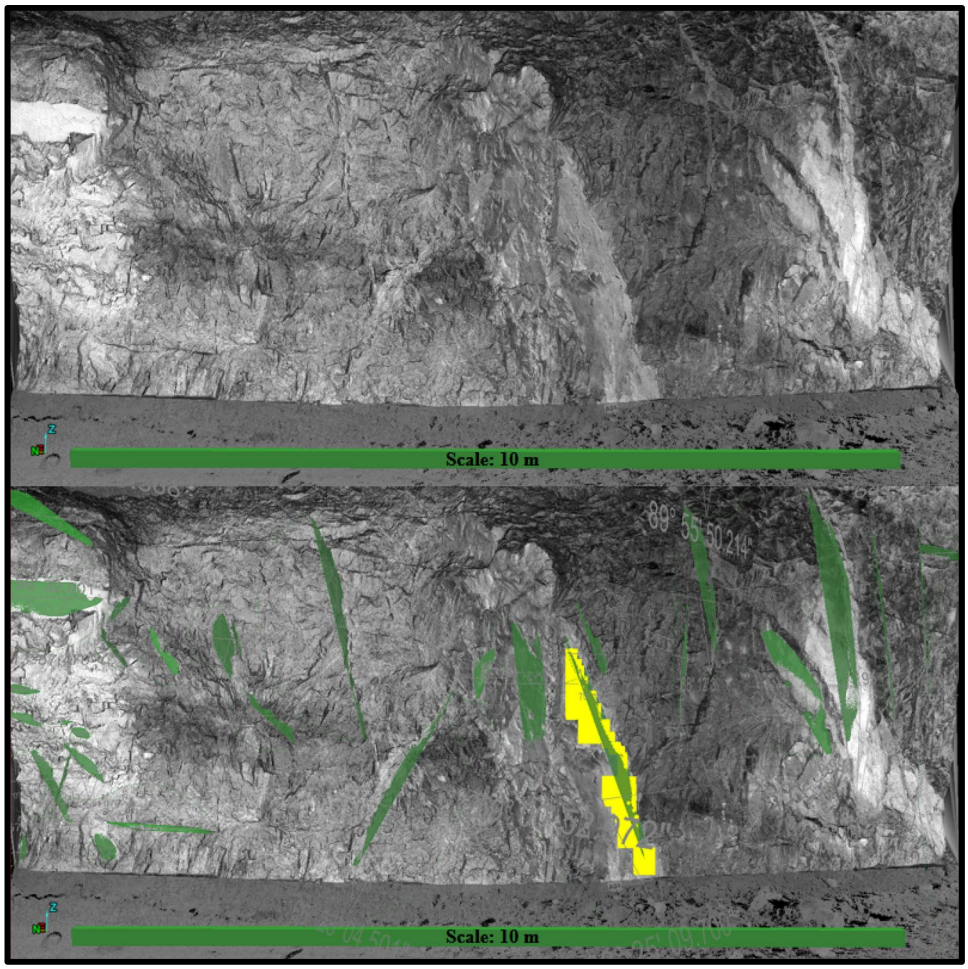

Fig. 13 Discontinuity mapping from LiDAR scans in Maptek I-Site [14]

Table 2 Statistical data for each joint set used to generate discrete fracture networks

	Joint sets		S1	S2	S3	S4 (bedding)
Parameters	**Orientation**	**Dip (°)**	88	68	75	29
		Dip direction (°)	255	348	21	144
		K (Fisher distribution)	103.9	102.4	69.5	197.3
	Size	**Distribution**	Log-normal	Log-normal	Log-normal	Log-normal
		Mean	0.353	0.318	0.018	0.778
		Standard deviation	0.659	0.772	0.749	0.934
	Density	**P_{32} (joint area/volume)**	0.045	0.095	0.181	0.227

P_{10} is defined as the number of fractures measured along scanlines [18]. The P_{32} value is set in the numerical model such that the fractures are generated in the model yield the P_{10} value equivalent to the one mapped in the field using virtual discontinuity mapping from LiDAR scans. Figure 14 shows the DFNs of different joint sets merged to form a combination of simulated fracture networks which was used to cut the Pillar-X model in all scenarios.

6 Results and Analysis

The numerical modeling analysis for the three scenarios was performed to observe the deterioration of the pillar with increasing stress levels. It should be noted that the stress levels are plotted versus the axial strain along the pillar. Since a constant velocity boundary was applied to the top and bottom surface planes of the pillar model, visualizing stress with axial strain would also indicate the

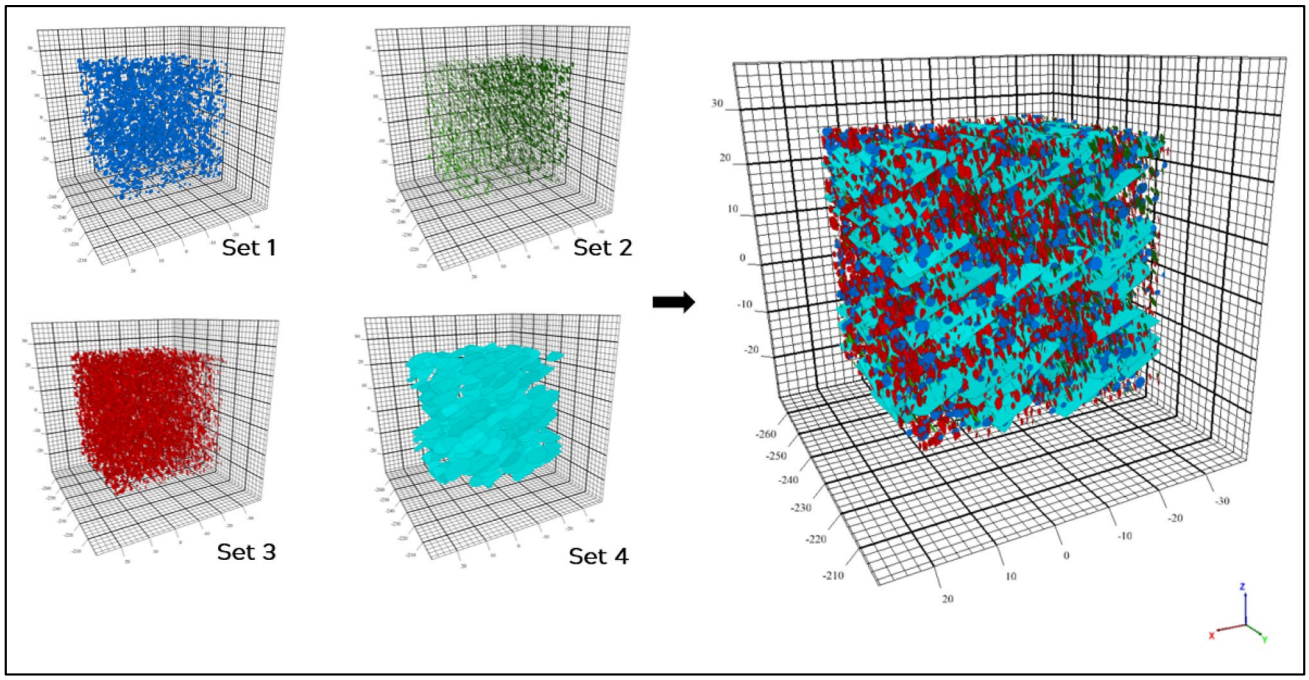

Fig. 14 DFNs of different joint sets merged to form a combination fracture network in 3DEC

modulus of the rock mass with discontinuities. The analyses are explained below:

i. *Scenario 1* — In scenario 1, numerical modeling was performed to the original pillar model without the presence of karst voids in it. The pillar model was cut from the discrete fracture network as explained in the previous section. The model was then subjected to increasing stress levels until yielding occurs and ultimately failure is achieved. Figure 15 shows the deterioration of the pillar with increasing stress levels. It is observed that as the compressive stress increases, an increase in rock boulder failure and spalling from the sidewall occurs. The observed spalling is due to the increase in tensile stresses along the sidewall of the pillar. Also, major weakening occurs due to the simulated increase in compressive stresses. It is inferred that a combination of these stresses leads to the ultimate failure of the pillar rock mass yielding at its ultimate strength. Simulating a solid pillar model without karsts allows us to make a comparison as to what is the effect of the introduction of cavities in the pillar has on its strength. It is visible that the pillar fails when the applied stress magnitude reaches ~ 54 MPa. Even before the stress value reaches at failure level, at around ~ 43 MPa, the sidewall of the pillar looks to have significantly deteriorated.
ii. *Scenario 2* — Figure. 16 shows the condition of Pillar-X in scenario 2 with the increase in stresses. It shows the simulation of the pillar with the suggested karst voids. It is observed that the ground failure from the sidewall has increased in this scenario for the same stresses in scenario 1. Pillar-X yields and ultimately failure occurs at around 43 MPa. This shows that the strength of the pillar has reduced although not too much, but still proves that the presence of karst cavities reduces the pillar strength. The spike observed in the stress–strain curve is attributed to simulation error that may have been generated due to a massive rock block separating from the pillar.
iii. *Scenario 3* — Simulation of Pillar-X with the worst-case of assuming the biggest karst void is performed in scenario 3. Figure 17 shows that the breakage of material and spalling has increased significantly compared to other scenarios. With increasing stress levels, the pillar yields and fails at a highly reduced value of ~ 28 MPa. This suggests that with increasing karst void volume, the deterioration increases as the strength of the pillar decreases significantly.

7 Conclusions

This study simulates the presence of karst voids in a pillar in an underground limestone mine. Different results are achieved when testing the strength of Pillar-X in three different scenarios of varying karst cavity volume. The

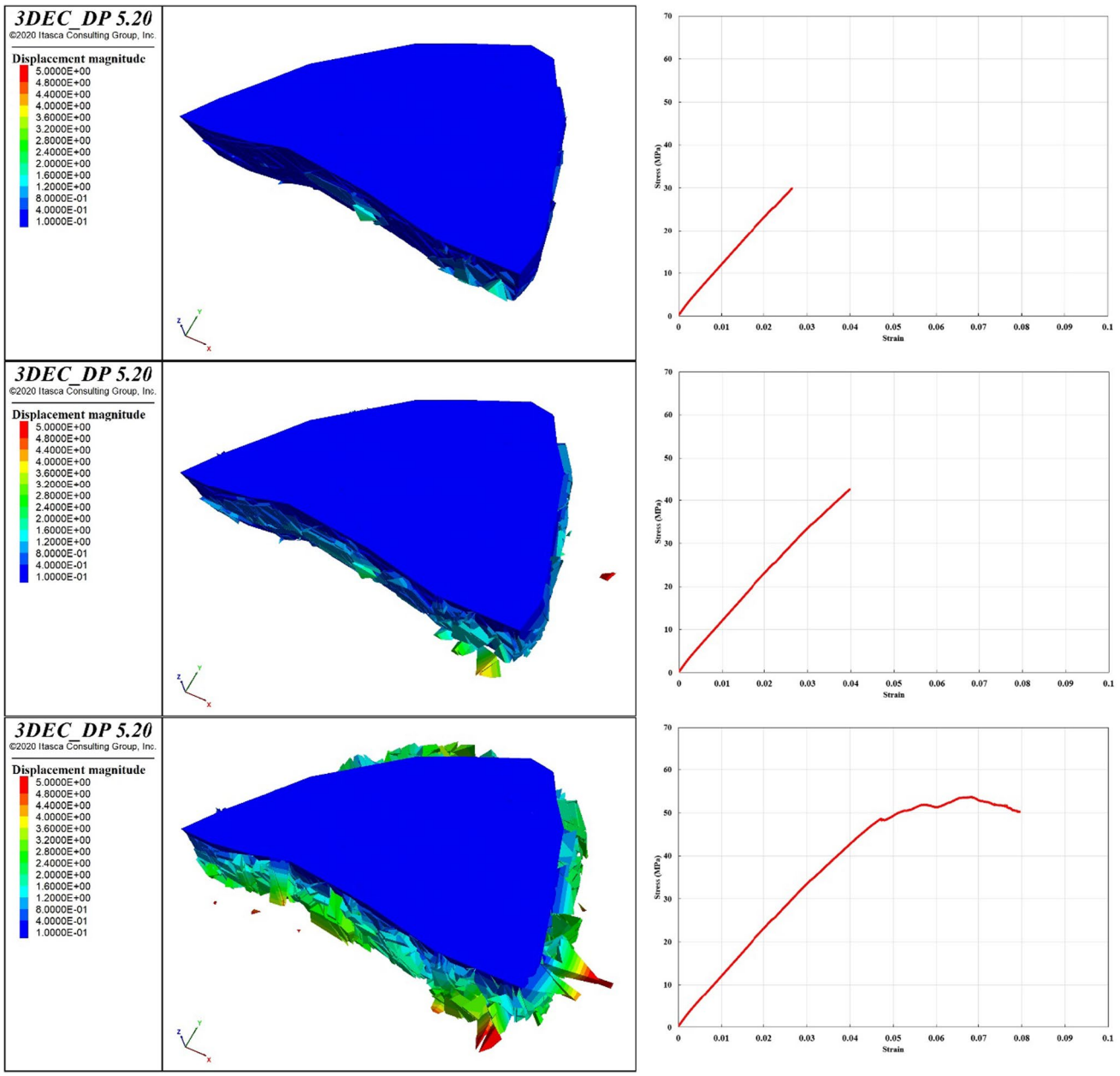

Fig. 15 Deterioration phases of Pillar-X with increasing stress levels in scenario 1

miners in the case study mine have had many encounters with karst-related safety incidents during excavation operations. This study is important to design the pillar and headings for future mining operations and the use of numerical modeling to assess local stability with the presence of karsts. The following conclusions can be drawn from this study:

i. Karst-related safety incidents are quite common in stone mining operations. The karst voids, filled with rocky-clayey material, may interact with the immediate roof and fracture network resulting in ground collapse. This may endanger the safety of the mineworkers and mine machinery.
ii. To assess the strength of Pillar-X, different scenarios were simulated. The solid pillar with no karst voids failed at ~ 54 MPa showing the highest strength of all three scenarios. Stress was applied to the top and bottom face of the pillar in the form of constant velocity in 3DEC. Deterioration of the pillar was observed with increasing compressive stresses plotted against the axial strain.

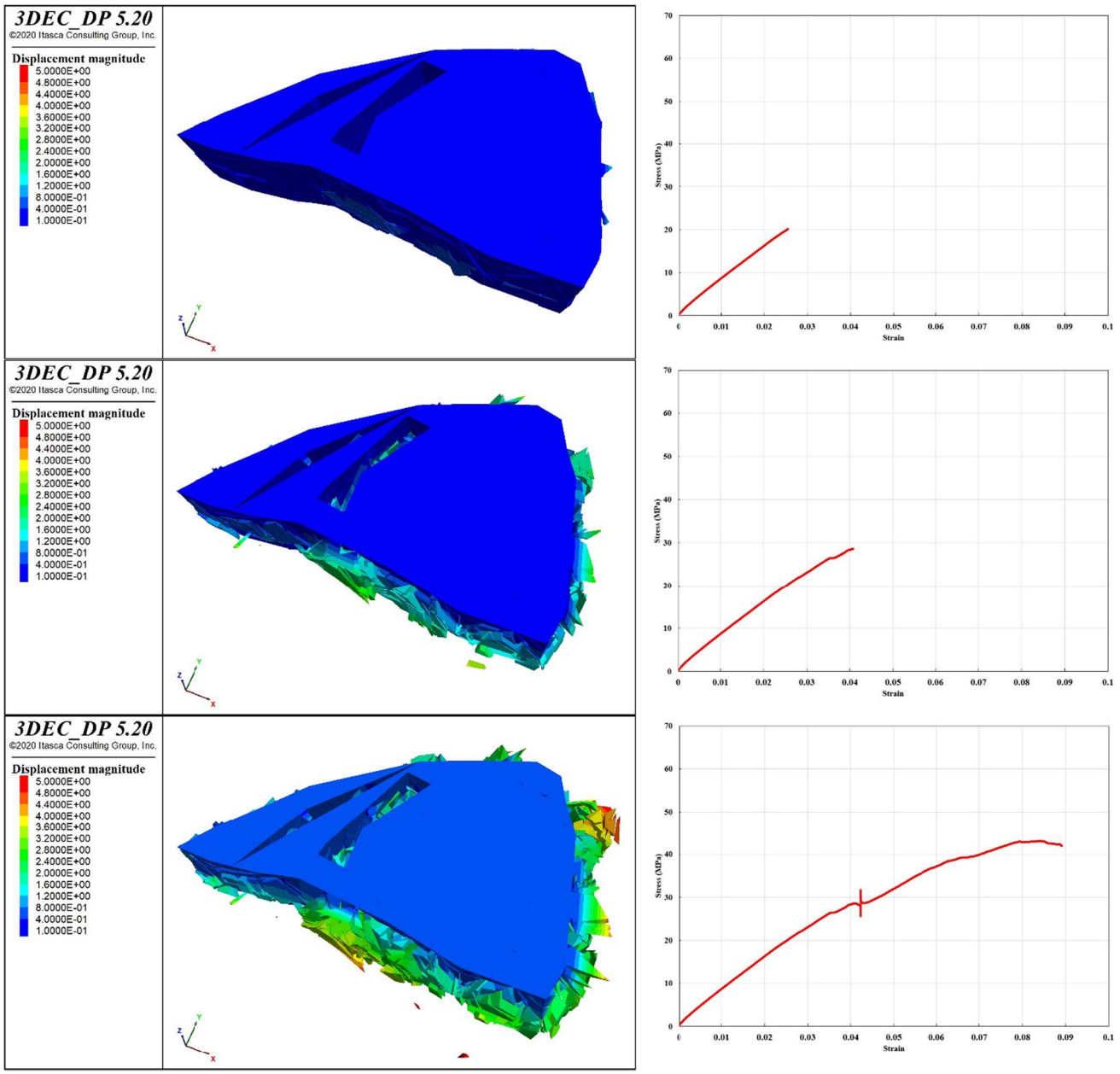

Fig. 16 Deterioration phases of Pillar-X with increasing stress levels in scenario 2

iii. The pillar with the suggested karst voids in scenario 2 yielded and ultimately failed at ~ 43 MPa. It showed a reduced strength as compared to the original pillar in scenario 1 indicating a reduction in strength due to the presence of karst inside.

iv. The worst-case scenario with the biggest karst void showed the least strength of all the models. With a failure stress level of ~ 28 MPa, the pillar deteriorated too much as compared to the previous scenarios.

v. The numerical modeling study suggested that as the void volume inside the pillar increases, the ability of the pillar to withstand higher stresses decreases. Figure 18 shows a comparison of all the scenario models with increasing stress with time steps.

Concluding numerical modeling research to this study, which is published as a separate article, has been conducted at the case study mine. The study estimates the redistributed compressive stresses in and around the pillar to be in the range of ~5–8 MPa. Looking at the strength of the pillar scenarios, it may be inferred that despite the presence of karsts, the pillar can withhold higher stresses than the current stress

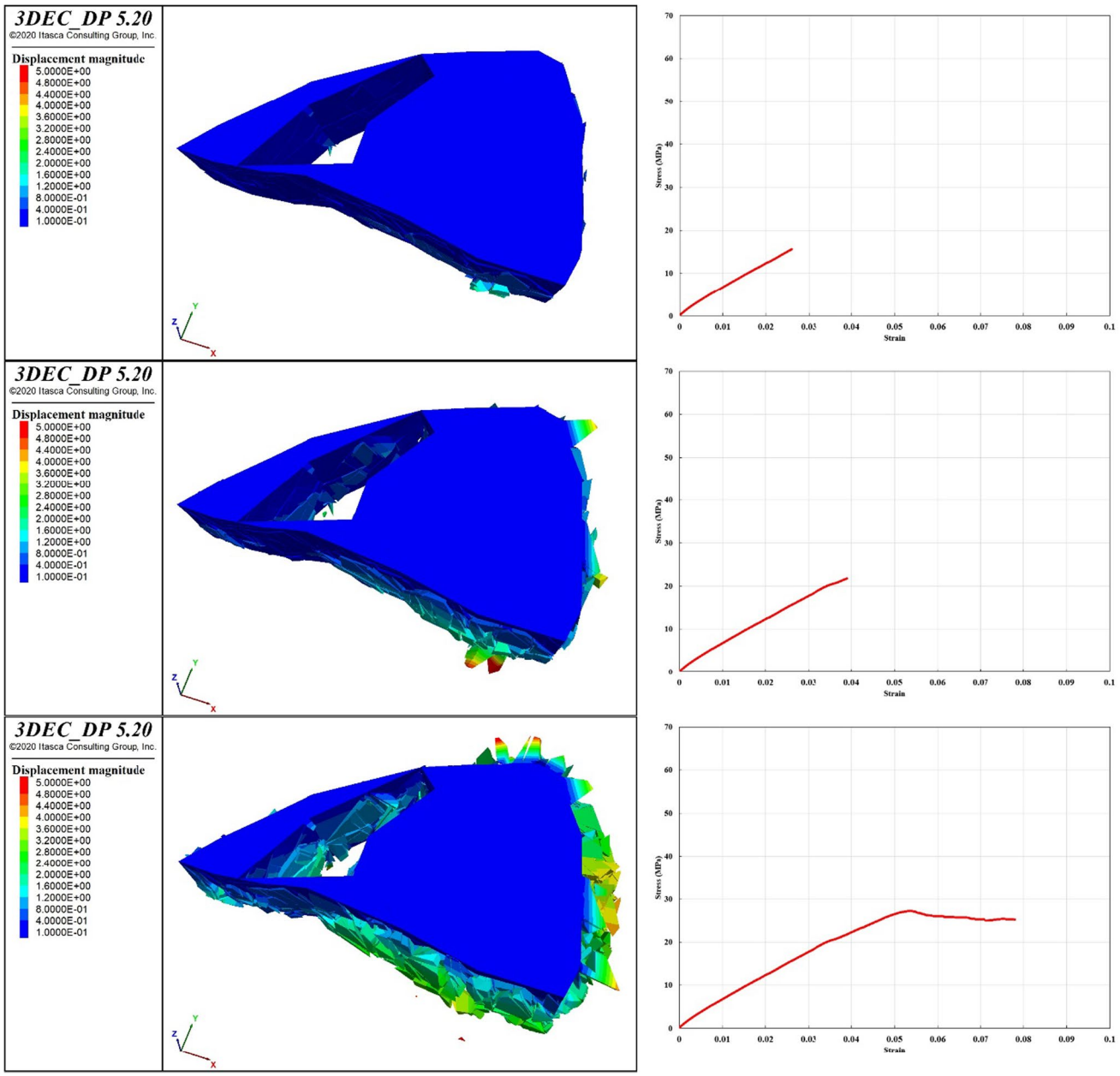

Fig. 17 Deterioration phases of Pillar-X with increasing stress levels in scenario 3

condition. Although the mine management would not like to design the pillar within their desired Factor of Safety limit so that the stresses would not reach anywhere near the yielding point where substantial deterioration may occur. In this case, the numerical modeling allows picturizing the ground condition at the stress level at which the maximum limestone could be mined around the pillar without compromising the safety of the mine-workers or machinery.

8 Scope of the Study

This paper summarizes the numerical modeling analyses performed on the Pillar-X in a multi-level room-and-pillar underground limestone mine. Insufficient research exists to understand the impacts on pillar stability caused by the presence of karst voids. This study quantifies this effect in different scenarios, each with increasing the cavity volume

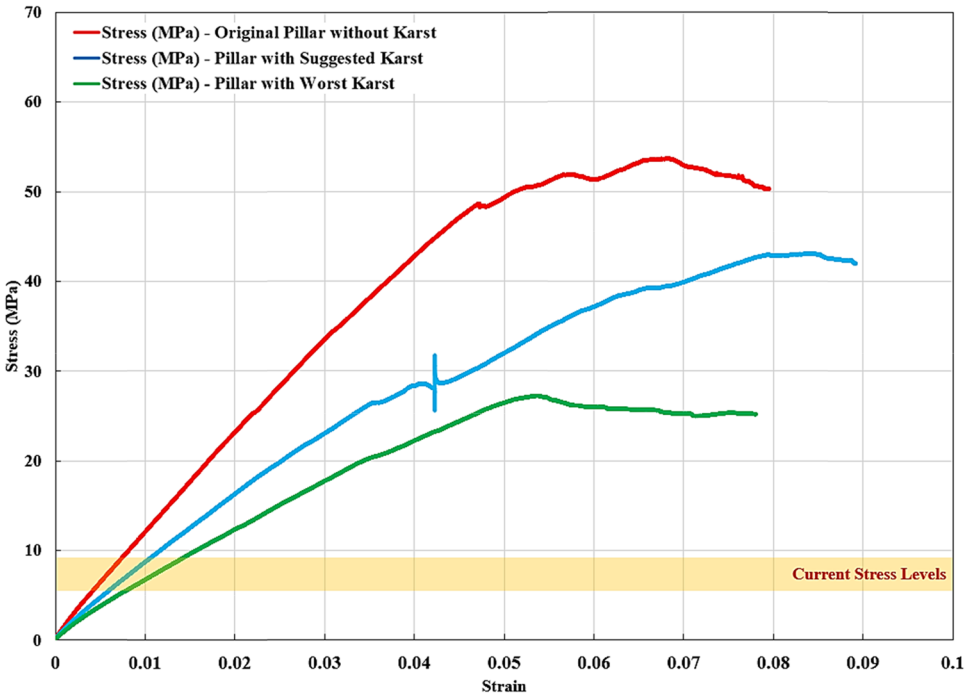

Fig. 18 Increasing stress with time steps for all scenarios along with estimated stress levels in the pillar

to better understand the reduction in strength of a pillar with increasing compressive stresses. For this study, it is assumed that the compressive stress or vertical stress is imparted along the axis of the pillar, thus compressing the pillar. Even with the presence of the karst voids, the pillar could face higher stresses than the suggested current stress level of ~5–8 MPa existing in and around the pillar. Hence, it may be inferred that there is room for improvement regarding the pillar design. It could be concluded that more ore could have been taken out of the pillar without compromising its safety. The picturization of pillar deterioration with the increase in stresses allows us to decide the pillar strength at which the mine management would be comfortable with the pillar condition. And further improvements in design could be made until satisfaction is achieved with the pre-decided factor of safety of the pillar. The authors are currently working towards simulating models using different constitutive models to have a comprehensive idea about the plastic behavior of the rock mass. This would allow us to further refine the pillar design and compare the results of this study to another one where the plastic behavior of the rock mass dominates. Since the pillars and headings around Pillar-X were designed based on its width dimensions, optimizing material extraction could only be done while modifying the pillar along its axis. The authors suggest extracting the stopes on the subsequent levels, which were not excavated thus leaving the pillar with its shortened height. A separate study is underway to suggest appropriate modifications to the pillar given its strength and existing stress levels.

At higher depths, the redistributed stress acting on the pillars is highly likely to increase. In this case, the numerical model would be an effective tool to reconsider the current rectangular design of the pillars in the case study mine. Also, if any karst cavities are encountered, pillar or heading design could be varied and analyzed using 3DEC as a distinct element modeling tool to enclose the voids in the pillar while maintaining its stability. This study could also be important in helping with the secondary recovery from the remnant pillars in the mine to maximize ore extraction from the mine. Finally, when combined with karst-detection technologies such as probing or geophysical methods, numerical DEM could be effective to suggest any design changes while stoping and/or advancing while maintaining local as well as global mine stability.

Acknowledgements The authors would like to thank Dr. James Hazzard and Itasca Consulting Group for their support and guidance during this study.

Author Contribution Not applicable.

Funding This work is funded by the National Institute for Occupational Safety and Health (NIOSH) Mining Program under Contract No. 200–2016-91300. Views expressed here are those of the authors and do not necessarily represent those of any funding source.

Data Availability Not applicable.

Code Availability Not applicable.

Declarations

Ethics Approval Not applicable.

Consent to Participate Not applicable.

Consent for Publication Not applicable.

Conflict of Interest The authors declare no competing interests.

References

1. Kuniansky EL, Weary DJ, Kaufmann JE (2016) The current status of mapping karst areas and availability of public sinkhole-risk resources in karst terrains of the United States. J Hydrogeol 24(3):613–624
2. Gongyu Li, Wanfang Z (1999) Sinkholes in karst mining areas in China and some methods of prevention. J Engineering Geology 52(1–2):45–50
3. Andriani GF, Parise M (2017) Applying rock mass classifications to carbonate rocks for engineering purposes with a new approach using the rock engineering system. J Rock Mech Geotech Eng 9(2):364–369
4. Baggett JG (2019). A Study ofGround Penetrating Radar Methods in an Underground Stone Mine to Improve Ground Control (Master Thesis, Virginia Tech).
5. Davis JL, Annan A (1989) Ground-penetrating radar for high-resolution mapping of soil and rock stratigraphy. Geophysical prospecting Res 37(5):531–551
6. Grasmueck M (1996) 3-D ground-penetrating radar applied to fracture imaging in gneiss. Geophys 61(4):1050–1064
7. Annan AP, Davis JL (1976) Impulse radar sounding in permafrost. Radio Sci 11(4):383–394
8. Esterhuizen GS, Dolinar DR, Ellenberger JL (2011) Pillar strength in underground stone mines in the United States. Int J Rock Mech Min Sci 48(1):42–50
9. Esterhuizen GS, Dolinar DR., Ellenberger JL, Prosser LJ (2011) Pillar and roof span design guidelines for underground stone mines
10. Cacciari PP, Futai MM (2016) Mapping and characterization of rock discontinuities in a tunnel using 3D terrestrial laser scanning. Bull Eng Geol Env 75(1):223–237
11. Esterhuizen GS, Dolinar DR, Ellenberger JL (2008) Pillar strength and design methodology for stone mines. In Proceedings of the 27th international conference on ground control in mining. Morgantown WV: West Virginia University (241–253)
12. Iannacchione AT (1999) Pillar design issues for underground stone mines.
13. Bandis S, Lumsden A, Barton N (1983) Fundamentals of rock joint deformation. Int J Rock Mech Min Sci Geomechanics 20(6):249–268. Pergamon
14. Monsalve JJ, Baggett JG, Soni A, Ripepi N, Hazzard J (2019) Stability analysis of an underground limestone mine using terrestrial laser scanning with stochastic discrete element modeling. In 53rd US Rock Mechanics/Geomechanics Symposium. OnePetro
15. McDowell RC, Schultz AP (1990) Structural and stratigraphic framework of the Giles County area, a part of the Appalachian Basin of Virginia and West Virginia (No. 1839-E)
16. 3DEC Version 5.2 (2019) User's manual. Itasca Consulting Group, Minneapolis, Minnesota
17. Pierce M (2017) An introduction to random disk discrete fracture network (DFN) for civil and mining engineering applications. ARMA e-Newsletter 20:3–8
18. Miyoshi T, Elmo D, Rogers S (2018) Influence of data analysis when exploiting DFN model representation in the application of rock mass classification systems. J Rock Mechanics Geotech Eng 10(6):1046–1062

Appendix C

The following manuscript was accepted for publication by the American Rock Mechanics Association for the 56th US Rock Mechanics/Geomechanics Symposium, titled "Analysis of Pillar Strength and Design in a Karst-affected Underground Stone Mine"

ARMA 22–924

Analysis of Pillar Strength and Design in a Karst-affected Underground Stone Mine

Soni, A., Monsalve, J., and Ripepi, N.
Virginia Polytechnic Institute and State University, Blacksburg, Virginia, USA

ABSTRACT: Underground stone mines are often prone to karst formations created by the gradual erosion of carbonate rocks due to groundwater flow. The prevalent fracture network in these stone deposits offers favorable conditions for acidic dissolution, which leads to the formation of large karst cavities. The interaction of these cavities with the extensive presence of discontinuities is the major cause of ground control problems encountered during stone mining operations. This paper presents a case study for analyzing the effect of the karst cavity on the strength of a pillar in an underground room-and-pillar stone mine. Numerical analyses show that the presence of these voids in a pillar contributes to a considerable decrease in load-bearing capacity. Any development through excavation or blasting into the affected areas may pose a safety hazard to the miners. Apart from that, this may also disrupt production and burden the pre-planned mine operations. The study for estimating pillar strength using numerical modeling could provide a pragmatic approach to designing future pillars affected by karsts. The shape and volume of the karst cavities inside the concerned pillar were approximated using ground-penetrating radar (GPR) surveys. LiDAR scans were performed to map the discontinuity network around the pillars, and Discrete Fracture Network (DFN) technique was implemented to simulate the joint network in the pillar's rock mass. The behavior of the pillar with the increase in axial compressive stress was observed with the help of Distinct-element modeling (DEM) using 3DEC software. The pillar's rock mass is simulated using Elastic and Mohr-Coulomb constitutive models. Two scenarios are presented to assess the pillar strength with and without the presence of karst. Pillar strength is compared to the estimated current stress levels to understand the potential for improvement in the pillar design. The research emphasizes the importance of pillar design while maximizing safety and production in underground stone mines with karst cavities to prevent pillar instability or local roof failures.

1. INTRODUCTION

Over the past decade, the demand for crushed stone and limestone products has been increasing annually. To meet this demand, over 1500 million metric tons of crushed stone were mined in the United States alone in 2021 (Statista, 2021). As surface deposits deplete, underground stone mining operations are becoming more common in the eastern United States. Currently, there are 109 active underground stone mining operations in the U.S. to extract crushed stone products (NIOSH, 2022). Since October 2020, four incidents of massive pillar collapses have occurred in underground stone mines. Fortunately, the incidents did not result in any injuries or loss of lives (MSHA, 2021). Compared to surface operations, underground stone mining operations require more effort towards ground control and safety.

Limestone deposits have a higher secondary porosity due to the presence of joints, faults, and bedding planes. Groundwater flow through these channels causes the dissolution of fractured rock leading to the formation of karst cavities. Most underground stone mines encounter karstic networks during excavation operations (Kuniansky et al., 2016). These cavities can be unforeseen until discovered due to mining activities. Gongyu et al. (1999) have documented problems caused by karsts in some of the mining operations in China. The classification of these karst-affected limestone rock masses is beyond the typical scope of rock mass classification schemes, including the Q-system from Barton and the Rock Mass Rating (RMR) system from Bieniawski. The analysis of such cases requires a geological examination of underground conditions and unconventional solutions (Andriani and Parise, 2017).

This paper analyzes the strength of a karst-affected pillar in an underground stone mine. The case study mine is operated as a multi-level room-and-pillar underground mine. Ground-penetrating radar (GPR) surveys were conducted by Baggett et al., (2019), to delineate the karst boundaries in the pillar. Due to suspected local instability issues, the pillar was left with highly conservative dimensions by the mine operator without any further study. The mine has experienced ground control issues in the past due to the opening up of multiple karst cavities.

The interaction of karst voids with the natural fractures and discontinuities in the mine may have destabilized the pillars along with the immediate roof. This can adversely affect local stability and cause potential loading issues in neighboring pillars. To study the stability of the pillar, the finite-difference distinct element method (DEM) was applied with the help of the numerical modeling tool 3DEC. The software was able to simulate the presence of discontinuous media in the rock mass. This was implemented using a discrete fracture network (DFN), which imitates the real-world joint distribution inside the pillar. The parameters for defining the DFN were obtained using LiDAR scans on and around the pillar. Manual virtual discontinuity mapping was carried out to estimate the joint sets, characteristics, and distribution. The stability of the pillar was estimated with and without karst cavities present inside it. This gives a definite idea of the effect that voids have on the strength of the pillar. This paper also discusses any improvement in the pillar design to maximize ore extraction while maintaining the same safe working conditions. This is done by comparing the pillar strength to the current redistributed stresses at the working level where the pillar is located.

2. CASE STUDY MINE

2.1. Geology and Mining Method

The mining operation is implementing a multi-level room-and-pillar method to extract a 30 m thick orebody that is dipping at ~30° towards the southeast. The deposit is situated in a region with synclinal Ordovician limestone. It hosts a vast network of interconnected cavities. The karstic network is formed due to the dissolution of carbonate rock by the groundwater flow through the omnipresent fractures and fissures. Each mine level has two sections bifurcating towards east and west, emerging off of the corkscrew declining ramp. Also, each level contains a hanging wall and footwall tunnel separated by 24.5 m x 24.5 m x 30.5 m rectangular pillars, left after complete extraction from the eventual benching. The tunnels are approximately 30 m tall and 12.8 m wide after the stopes are excavated.

2.2. Pillar Location and Karst Issues

The location and shape of the pillar being analyzed in this study are shown in Figure 1. During the initial benching of the stope around the pillar, the operation encountered ground collapse from the sidewall which opened up to a karst cavity. After the discovery of karst voids in the pillar, the mine management decided not to go ahead with the complete benching of the stopes. This resulted in the pillar height left to be 9.5 m as opposed to the pillar design height of 30.5 m after the complete benching of stope from the adjoining levels. Figure 2 shows the ground collapse encountered around the pillar.

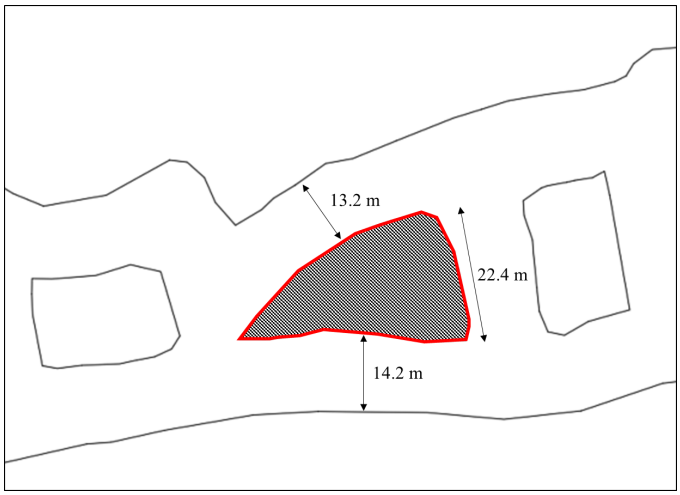

Fig. 1. Plan view of the pillar location in the case study mine.


Fig. 2. Ground collapse from karst cavity in the case study mine pillar (Bishop, 2020).

The sudden collapse and inrush of clay and rock boulders did not cause any injuries but hindered the local excavation operations. The mine management employed several ground support measures such as roof bolts and meshes supported with steel straps to prevent future ground issues. Furthermore, the cavity was filled with grout to stabilize the weakened section of the pillar.

2.3. Delineating Karst Cavities

At the mine, investigative Ground-penetrating radar (GPR) surveys were conducted by Baggett et al. (2019) to detect the shape and boundaries of karst cavities in the pillar. The surveys were conducted using a 250 MHz antenna along a dense 3-dimensional grid, and a signal infiltration depth of 20-25 meters was achieved to obtain karst surface reflections. The surface reflections were converted to iso-surfaces, which in turn were used to identify commonalities and boundary trends. The plan view of the reflection boundary of the karst void, represented as clusters of the iso-surfaces or points, is shown in Figure 3.

Fig. 3. Iso-surface meshes (shown in green) were created from the GPR survey.

Since the conductive medium inside the void, such as clay and water produces reflections, the authors could not propose a definitive closed void volume, which in terms of delineating void boundaries, would be an ideal case. Figure 4 shows a plan view of the approximated karst void area projected by the authors using the GPR survey.

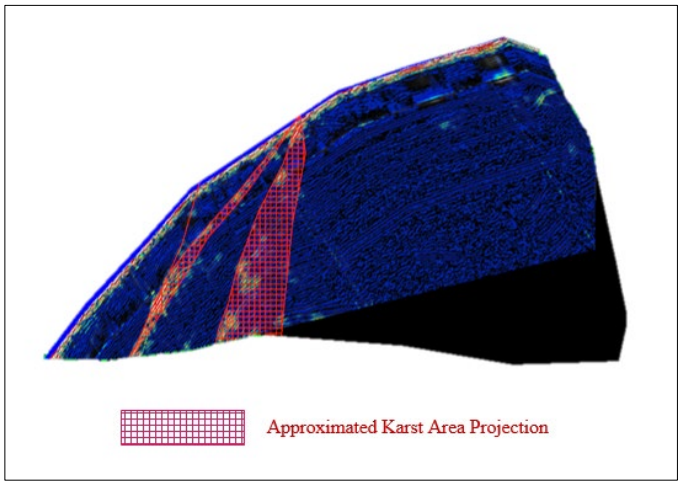

Fig. 4. Plan view of an approximate karst area projected from the iso-surface meshes (Baggett et al., 2019).

The results from the GPR provided little to no information regarding the continuation of karst voids inside the pillar. Geotechnical observations from the mine geologists and surveyors suggest the presence of the discovered voids throughout the height of the pillar. To compensate for the missing information and consider a worst-case scenario, the karst cavity is assumed to be running throughout the pillar. This will result in the largest possible shape of the cavities along the pillar height and will disregard any pinching and expanding of cavities inside the pillar volume. Figure 5 shows the recreated model simulated as the pillar with the proposed karst volumes contained inside it.

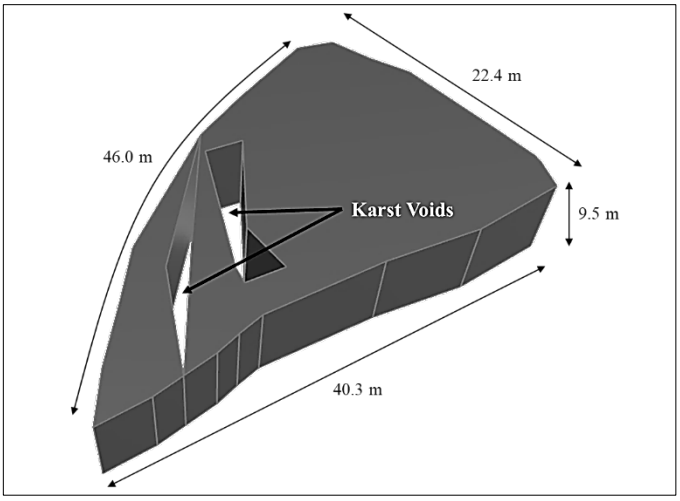

Fig. 5. Karst voids inside the pillar in the case study mine.

3. DISTINCT ELEMENT MODELING (DEM) WITH 3DEC

3DEC is a three-dimensional numerical modeling code based on the distinct element method (DEM). This software is developed by Itasca Consulting Ltd. and represents discontinuous media as an assembly of discrete blocks separated by the discontinuity network. For this study, individual blocks are treated as deformable material and are meshed as finite different elements. The rotation of blocks and their displacement along the discontinuities allow us to observe the behavior of the pillar with increasing stresses.

Pillar strength in stones mines has been investigated by many researchers. Iannacchione, A. T. (1999) addressed the importance of stable pillar design to prevent ground failure issues that are typically faced in stone mines. Esterhuizen et al. (2011) suggested methods for estimating the pillar strength and demonstrated the use of numerical models in verifying their designs.

3.1. Manual Virtual Discontinuity Mapping

A significant aspect of simulating the pillar behavior was to map the discontinuity network affecting it. Discontinuities play a vital role in deciding the strength of a rock mass. Since one cannot measure the joint distribution beyond the surface of the pillar and inside it, a thorough mapping would help to simulate accurate conditions. For this purpose, LiDAR surveys were performed at the site to map the joint distribution on and around the pillar. Figure 6 shows the plan view of the discontinuity mapping performed around the pillar. Maptek I-Site was used to process the point clouds and map the discontinuities.

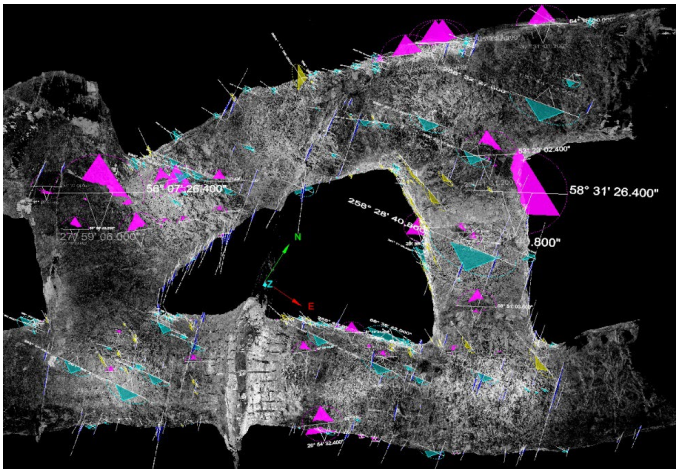

Fig. 6. Discontinuity mapping using LiDAR scans around the pillar (Monsalve et al., 2019).

Different joint parameters such as orientation, fracture density, and size were determined for different joint sets. Four discontinuity sets were determined from the mapped joints. Figure 7 shows the stereonet generated from the discontinuity mapping data.

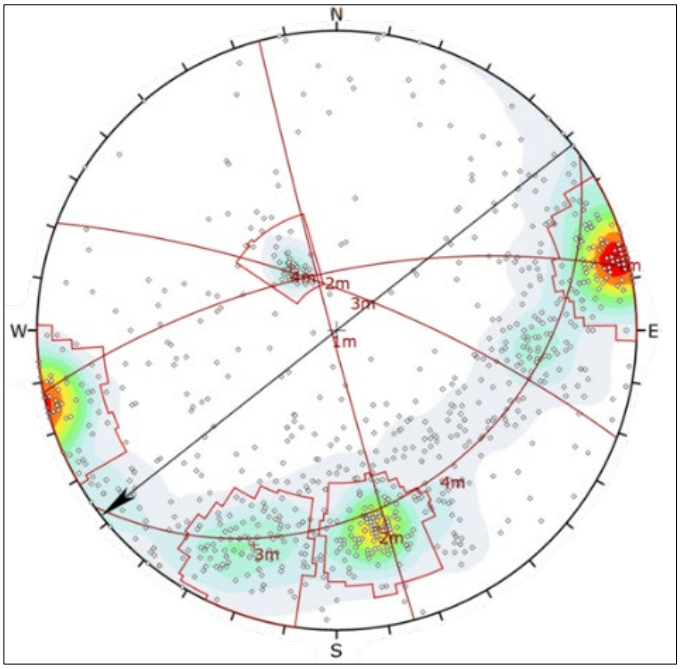

Fig. 7. Stereonet generated from the joint mapping data showing the presence of four joint sets.

3.2. Discrete Fracture Network (DFN)

Using the structural mapping information collected from the LiDAR scans, the joints were classified into four sets. The mapping data included statistical data of the joint characteristics, such as orientation, size, and density, measured virtually from LiDAR scans. The data file is input in 3DEC to generate the DFN which simulates a real-life distribution of the geological features in the pillar rock mass.

The software generates the DFN as a set of discrete, planar, finite-size fracture disks, which dissects the pillar model to generate blocks constituting a jointed rock mass. Table 1 summarizes the statistical data of the joint distribution for each joint set used in the modeling study. The fracture density of the DFN is the threshold condition to generate the spatial distribution of joints in 3DEC (Cacciari and Futai, 2015). The fracture density for this study was defined as the area of joints per unit volume of the rock mass or P_{32}. Since the joints cannot be mapped in terms of volume using the LiDAR scans or field surveys, the DFN model is calibrated using P_{10} values.

P_{10} is the linear fracture intensity or the number of fractures measured along scanlines (Miyoshi et al., 2018). The P_{32} values of the four joint sets in the DFN are varied to imitate their P_{10} values in the field. Figure 8 shows the combined DFN of four joint sets merged and used to cut the pillar model. Figure 9 shows the pillar displayed as a group of joined blocks after being cut by the DFN, to represent the real rock mass.

Table 1. Statistical survey data for joint sets for generating the discrete fracture network.

	JOINT SETS →		Set A	Set B	Set C	Set D
PARAMETERS	Orientation	Dip [°]	29	75	68	88
		Dip Direction [°]	144	21	348	255
		K (Fisher Distribution)	197.3	69.5	102.4	103.9
	Size	Distribution	Log-normal	Log-normal	Log-normal	Log-normal
		Mean	0.778	0.018	0.318	0.353
		Standard deviation	0.934	0.749	0.772	0.659
	Density	P_{32} (joint area/volume)	0.227	0.181	0.095	0.045

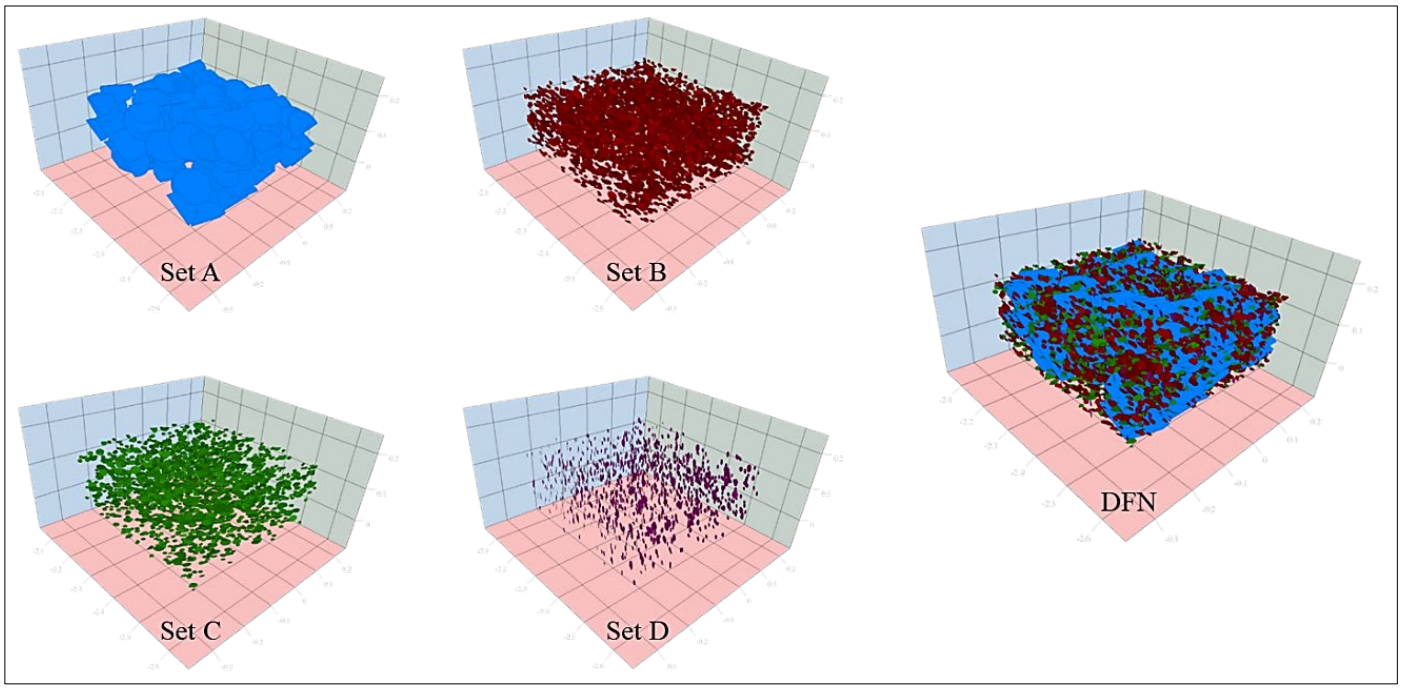

Fig. 8. DFNs of all the joint sets combined to form a stochastic fracture network in 3DEC.

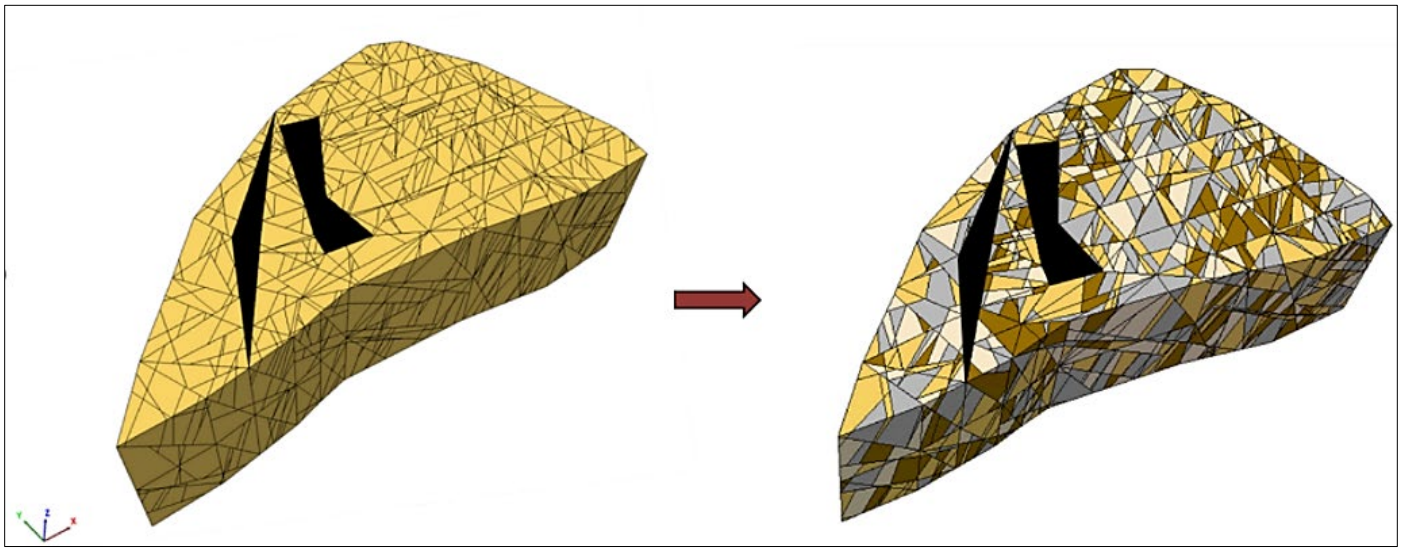

Fig. 9. Pillar with karsts with the discrete fracture network (Soni et al., 2022).

4. NUMERICAL MODELING PARAMETERS

4.1. Pillar Model Scenarios

To quantify the effect of karst presence in the pillar volume, two different scenarios were considered. While keeping the geometry the same, the pillar model was numerically simulated with and without the presence of estimated karst voids in it. The karst volumes in the pillar were found to be filled with a mixture of clayey-rocky material which exhibited little cohesive strength. Therefore, in the numerical models, these voids were assumed to be hollow to underestimate any insignificant support provided by the void material. The dimensions of the pillar were estimated by the LiDAR scans and that of the voids using the GPR study. The two scenarios are described below:

(i) Scenario 1- For this scenario, the pillar was assumed to be a solid stone pillar without any karst cavities. To estimate the weakening of strength caused by the presence of cavities, it is important to understand the solid pillar's strength. Figure 10 shows the model of the solid pillar used for numerical simulation.

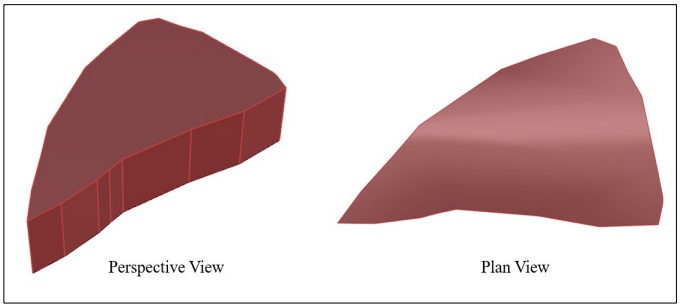

Fig. 10. Pillar model without karst voids.

(ii) Scenario 2- In this case, the voids were modeled and assumed to exist through the height of the pillar. This scenario simulates the pillar model in its existing condition. Figure 11 shows the model of the pillar with karst voids. The volume of the karst cavities accounts for roughly 9% of the total pillar volume.

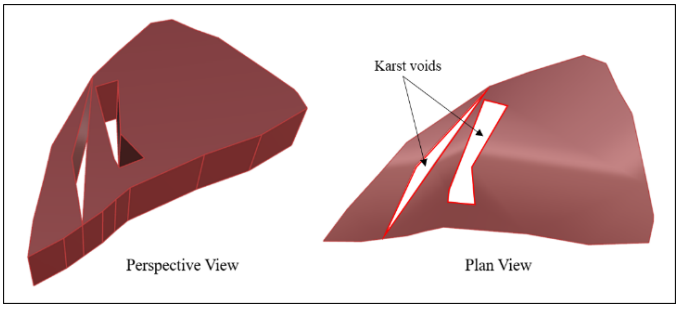

Fig. 11. Pillar model without karst voids.

4.2. Intact Rock and Joint Properties

The geotechnical properties of the intact rock used for numerical modeling were determined by the mine operator using geotechnical borehole measurements and rock laboratory testing. The joint properties are obtained from the research study performed by Bandis et al. (1983) on limestone samples. Assuming zero cohesion based on this study underestimates the joint strength. The authors believe that in absence of conclusive properties, it is advisable to avoid overestimation of mechanical properties and pillar strength. Both the intact rock and joint properties are provided in Table 1. The lithology of the synclinal Ordovician limestone deposit was characterized as Five Oaks limestone by McDowell and Schultz (1990). Elastic-Isotropic and Mohr-Coulomb constitutive models were used to represent rock behavior for both scenarios. For both the constitutive models, Coulomb-slip joint constitutive model was assigned to simulate the behavior of discontinuities.

4.3. Boundary Conditions

Compressive stresses are applied axially at the pillar to the top and bottom faces of the pillar. The boundaries on the unconfined sidewalls of the pillar were kept free. The boundaries on the top and bottom planes of the pillar were fixed in the lateral directions to prevent any shear movement.

Table 2. Geotechnical properties for rock mass and joints.

INTACT ROCK PROPERTIES	
Density, ρ	2690 kg/m^3
Bulk Modulus, K	37.86 GPa
Shear Modulus, G	20.57 GPa
Poisson's Ratio, μ	0.27
Cohesion, C	12.53 MPa
Friction Angle, ϕ	36.73
Dilation Angle, ψ	24.5
JOINT PROPERTIES (Bandis et. al, 1983)	
Joint Normal Stiffness, jkn	300 GPa/m
Joint Shear Stiffness, jks	30 GPa/m
Joint Friction Angle, J_ϕ	30^o
Joint Cohesion, J_C	0.0

This also ensured a constant application of load with the numerical cycle. In each scenario, a constant load per time step was applied to the pillar model in form of applied velocity at the rate of 5 mm/s at the top and bottom. It is assumed that the load compressing the pillar is imparted only in the form of axial stresses along the pillar. Each scenario was simulated till the failure state of the pillar model was achieved for each constitutive model.

5. RESULTS

The numerical models for the two scenarios were analyzed to observe and compare the deterioration of the pillar with increasing stress levels. It should be noted that the stresses are plotted versus the strain along the axis of the pillar models. Since a constant velocity boundary was applied to the top and bottom surface planes of the pillar model, visualizing stress with axial strain would also indicate the modulus of the rock mass with discontinuities. The results in detail are explained below:

5.1. Elastic Pillar Models

The pillar model was numerically simulated with and without karsts, with the rock mass following the Elastic constitutive model. Figures 12 and 13 show the deterioration of the pillar without and with voids, respectively. The displacement contours show an increase in rock boulder failure and spalling activity from the sidewall with an increase in compressive stresses. The deterioration occurs primarily due to the increase in tensile failures along the pillar rib. With increasing compressive stresses, the pillar without voids shows its ultimate strength at ~54 MPa. Simulating the pillar model with cavities allows us to assess the effect of karsts on pillar strength. The pillar model with karst voids yielded at ~43 MPa. The spike observed in the stress-strain plot for this scenario is attributed to a massive rock block separating from the pillar, which may lead to a sudden stress activity. As expected, this shows a significant reduction in pillar strength with the introduction of the suggested karst volumes. The presence of cavities leads to a 20% reduction in overall pillar strength.

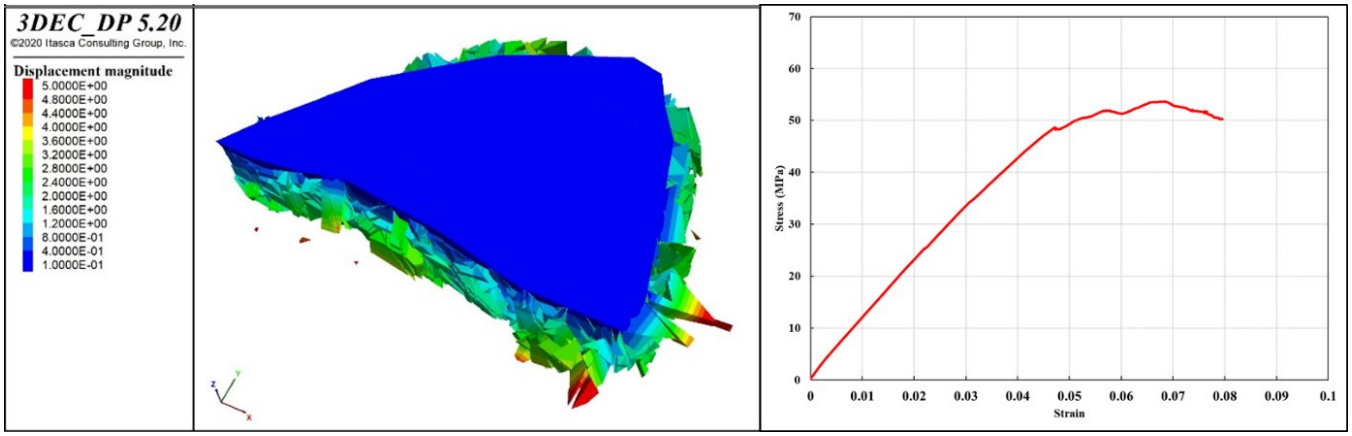

Fig. 12. Displacement contour and Stress vs Strain plot for Elastic pillar without karsts.

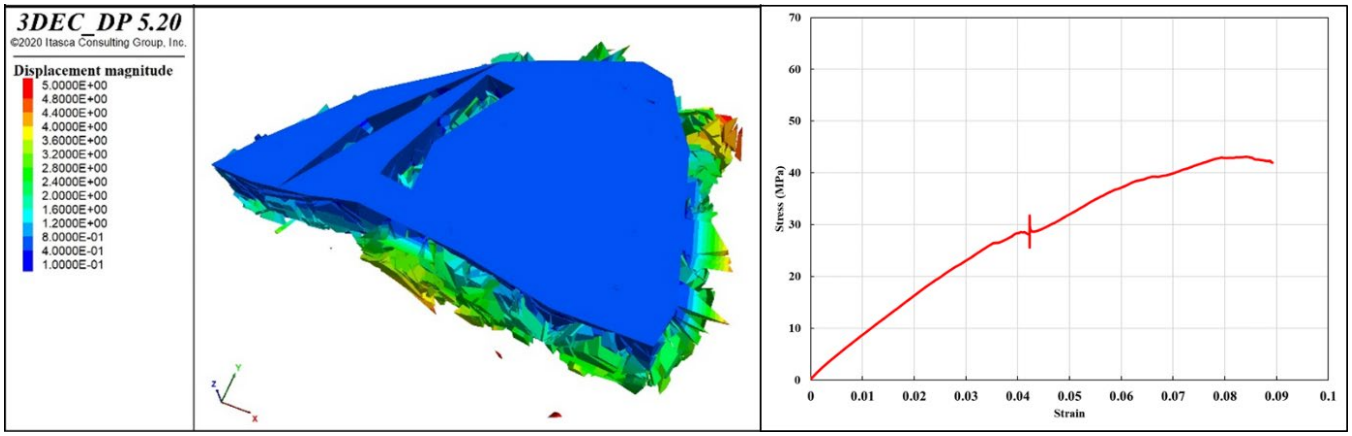

Fig. 13. Displacement contour and Stress vs Strain plot for Elastic pillar with karsts.

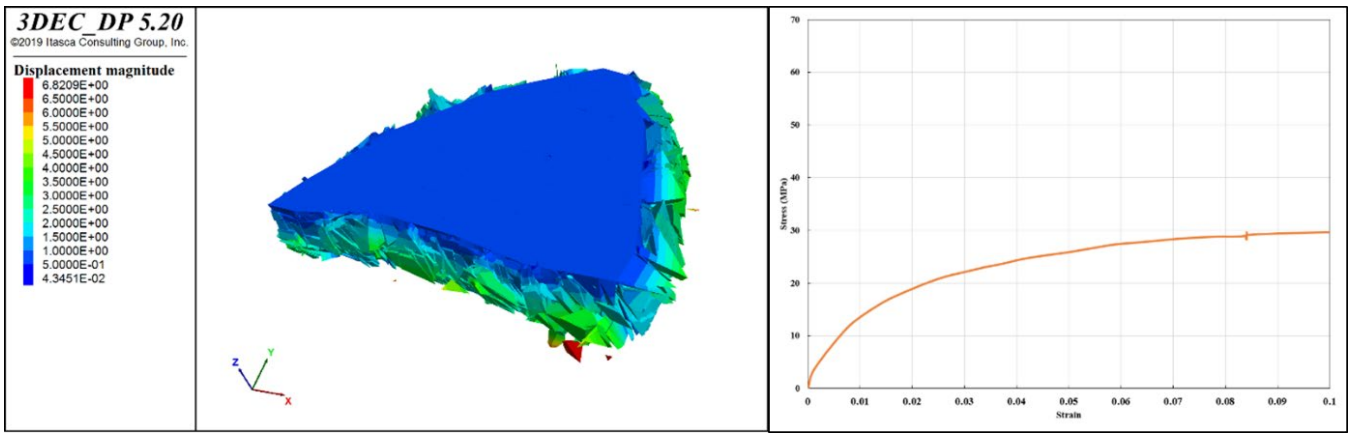

Fig. 14. Displacement contour and Stress vs Strain plot for Mohr-Coulomb pillar without karsts.

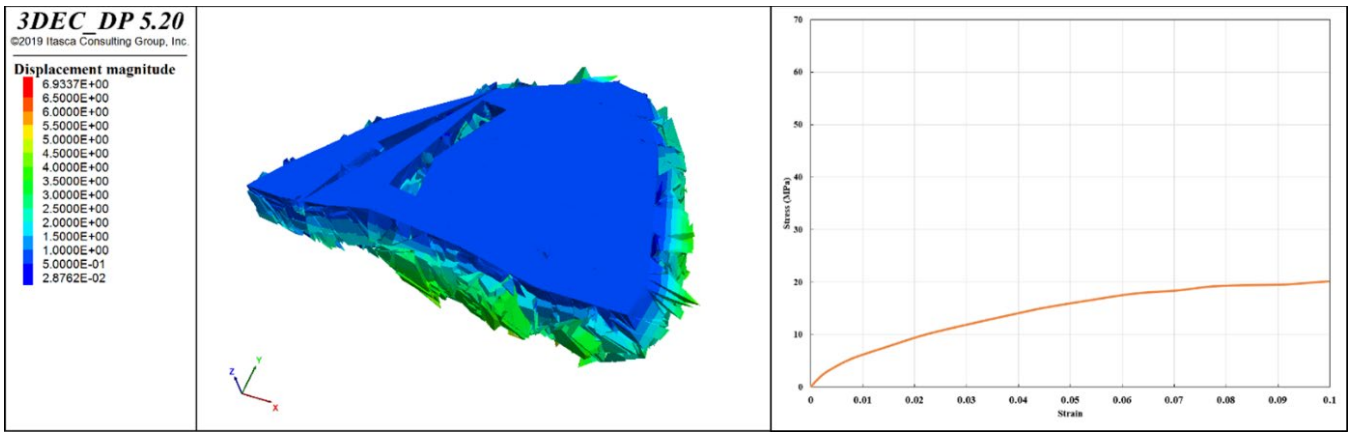

Fig. 15. Displacement contour and Stress vs Strain plot for Mohr-Coulomb pillar with karsts.

5.2. *Mohr-Coulomb Pillar Models*

Subsequently, the pillar models were simulated with the rock mass set to follow the Mohr-Coulomb behavior. Figure 14 shows the simulation results for the pillar model without cavities. The ultimate strength of the pillar is estimated to be ~30 MPa. The pillar model here shows less deterioration when compared to the Elastic model with the same conditions. The degree of block failure may be due to an increase in the plastic behavior of the rock mass. The Mohr-Coulomb pillar model with the voids yields at ~20 MPa. Figure 15 displays the magnitude of block failure along the sidewall for the pillar model with voids along with its stress-strain plot. Comparing the two scenarios still shows that the presence of karst cavities reduces the pillar strength, but for Mohr-Coulomb criteria, the pillar strength reduces by almost 33%. Therefore, the effect of cavities is significantly higher for a Mohr-Coulomb rock mass when compared to the Elastic pillar model.

5.3. *Current Stress Regime*

This study analyzes the behavior of a pillar in the case study mine with increasing stresses. Insufficient research exists to understand the effect of karst cavities on limestone pillar strength. Therefore, this quantification is done using different scenarios to understand the role of these voids on the pillar behavior. The study also understands the difference in pillar strength when the rock mass is simulated as Elastic versus Mohr-Coulomb constitutive model. Another numerical modeling research related to this paper, and currently submitted for publication as a separate article, has been conducted at the case study mine. The study evaluates the redistributed stresses in the mine level where the pillar is situated. Figures 16(a) and 16(b) show the contour of pre-, and post-excavation axial stresses in the global mine model, respectively.

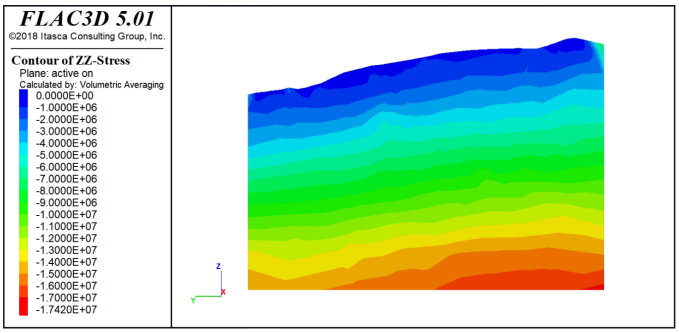

Fig. 16(a). Contour of global stresses (in Pa) before mining.

The redistributed stresses around the concerned site are estimated to be in the range of ~3-8 MPa when the model is simulated as a Mohr-Coulomb rock mass. If the pillar strength results are taken into the account, it may be predicted that with the presence of voids, the pillar can withstand higher stresses than the current stress condition.

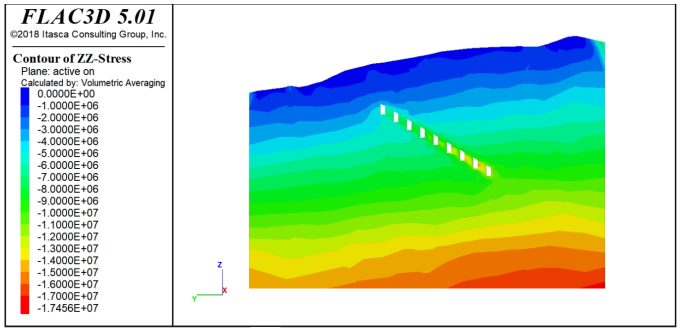

Fig. 16(b). Contour of global stresses (in Pa) after mining.

It is advisable to consider redesigning the pillar within the desired factor of safety limit so that the redistributed load does not lead the state of the pillar to its yielding point where substantial deterioration may occur. Through this study, the modeling results allow us to visualize the stress levels at which the maximum ore could be extracted while maintaining the local stability and safety of the miners. Figure 17 shows the current existing stress levels and the pillar strength results for the different constitutive models.

6. CONCLUSIONS

This paper analyzes the strength and design of a karst-affected pillar in a multi-level room-and-pillar underground limestone mine. Varying results are achieved when the pillar is tested with and without karst cavities. The case study mine has faced many ground failure incidents due to the prevalent karst network in the limestone deposit. As expected, the presence of voids affects pillar strength, and this rationale led the mine management to choose a highly conservative dimension and design for the concerned pillar. However, their decision was based on the experience of geologists and geotechnical engineers working at the site, and not on any numerical study. This study quantifies the effect of voids that led to an attenuation in pillar strength. It is important to assess the pillar numerically for improving pillar and heading design for future operations when encountering karsts. Other important takeaways from this study are:

(i) Ground failure due to karst voids during excavation may occur during stone mining operations. These voids, filled with clay and boulders, can interact with the fracture network and destabilize immediate roof and sidewalls leading to hazardous conditions. These incidents endanger the safety of the miners.

(ii) The pillar model was simulated for two scenarios. The first scenario tested pillar strength by assuming no voids are present in it. The second one simulated the original condition of the pillar with the voids discovered with the help of a GPR survey. This was important to assess the effect of karsts on the pillar strength. Also, two constitutive models were employed to simulate the pillar rock mass: Elastic and Mohr-Coulomb criteria.

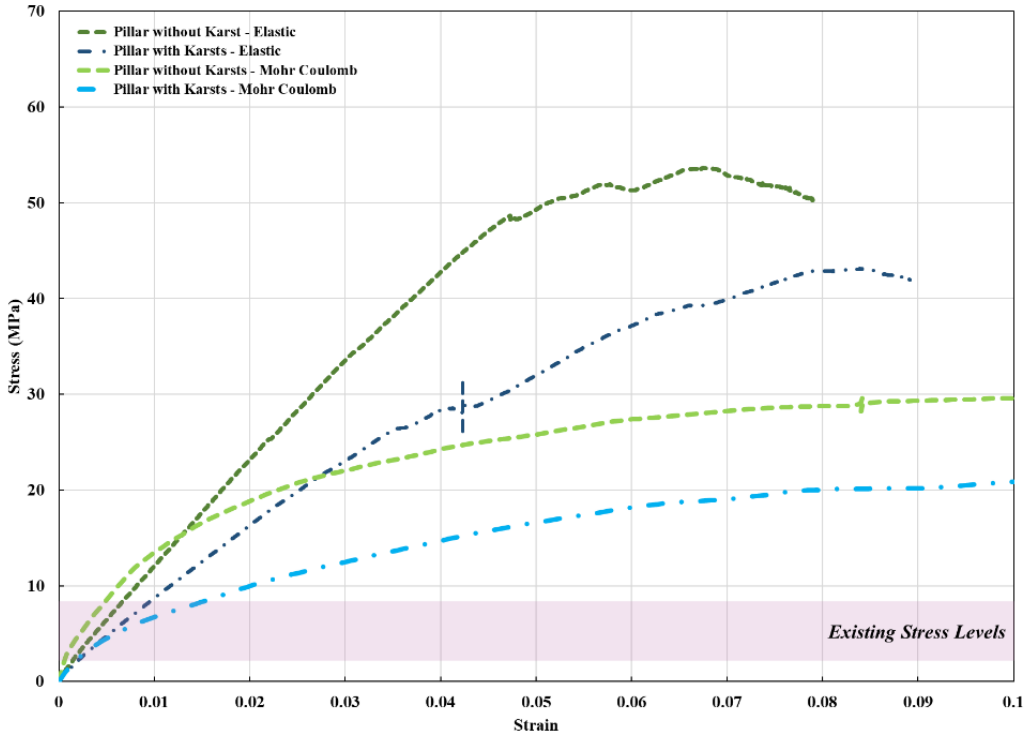

Fig. 17. Pillar strength results for Elastic and Mohr-Coulomb constitutive models.

(iii) The pillar with no karst voids failed at ~54 MPa for the Elastic model and ~30 MPa for the Mohr-Coulomb model. A higher deterioration of the pillar was observed in the former case due to the plastic nature of the Mohr-Coulomb material.

(iv) The pillar with the karst voids yielded and ultimately failed at ~43 MPa for the Elastic model and ~20 MPa for the Mohr-Coulomb model. The models exhibited a reduction in strength due to the presence of karst. For the Elastic criterion, the pillar strength dropped by almost 20% whereas that for the Mohr-Coulomb criterion reduced by 33%.

(v) When the pillar strength is compared to the current redistributed stresses in the mine level, it becomes apparent that the pillar is capable of enduring a higher load. This could be made possible by extracting the stopes around the pillar, thus leading to an increased pillar height. There is further scope for a numerical study for testing the pillar strength in case secondary recovery around the pillar is planned in the future.

This research enables the assessment of pillar deterioration with the increase in stresses and further improvements in design by maintaining a reasonable factor of safety in the pillar. The authors recommend extracting the stopes around the pillar, which were not excavated to leave the pillar with its conservative height. Separate research is being published to suggest appropriate design modifications to the pillar given its strength and existing stress range. Literature is scarce on modeling studies for improving pillar design in underground stone mines with karst issues. Itasca's 3DEC software is effective for distinct-element modeling of limestone deposits and enables one to represent the discontinuities as DFN to simulate the blocky nature of rock mass. This study could also be an important step in assisting research for secondary recovery from the pillars which have been poorly designed.

REFERENCES

1. Andriani, G. F., and M. Parise. (2017). Applying rock mass classifications to carbonate rocks for engineering purposes with a new approach using the rock engineering system. *Journal of Rock Mechanics and Geotechnical Engineering*, pages 364-369.
2. Annan, A., and Davis, J. L. (1976). Impulse radar sounding in permafrost. Radio Science. 383-394.
3. Baggett, J.G. (2019). A Study of Ground Penetrating Radar Methods in an Underground Stone Mine to Improve Ground Control. *Thesis*, Virginia Tech.
4. Bandis, S., Lumsden, A., & Barton, N. (1983). Fundamentals of Rock Joint Deformation. *International Journal of Rock Mechanics, Mining Sciences & Geomechanics*. 249-268.
5. Bishop, R. (2020). Applications of Close-Range Terrestrial 3d Photogrammetry to Improve Safety in Underground Stone Mines. *Thesis*. Virginia Tech.
6. Cacciari, P. P., and M. M. Futai. (2016). Mapping and characterization of rock discontinuities in a tunnel using 3D terrestrial laser scanning. *Bulletin of Engineering Geology and the Environment*. 75(1), 223-237.

7. Davis, J. L, and A. Annan. (1989). Ground-penetrating radar for high-resolution mapping of soil and rock stratigraphy. *Geophysical prospecting*. Res. 37.5: 531-551.
8. Esterhuizen, G. S., D. R. Dolinar and J. L. Ellenberger. (2011). Pillar strength in underground stone mines in the United States. *International Journal of Rock Mechanics and Mining Sciences*. 48(1), 42-50.
9. Esterhuizen, G. S., D. R. Dolinar and J. L. Ellenberger. (2008). Pillar strength and design methodology for stone mines. In *Proc. 27th International Conference on Ground Control in Mining*. Morgantown WV: West Virginia University, pp. 241-253.
10. Esterhuizen, G. S., D. R. Dolinar, J. L. Ellenberger and L.J. Prosser. (2011). Pillar and roof span design guidelines for underground stone mines. *NIOSH Publication*, No. 2011–171.
11. Garside, M. (2022). U.S. crushed stone production 2011-2021. Statista. *https://www.statista.com/*.
12. Gongyu, Li, and Z. Wanfang. (1999). Sinkholes in karst mining areas in China and some methods of prevention. *J. Engineering Geology*. 52.1-2: 45-50.
13. Grasmueck, M. (1996). 3-D ground-penetrating radar applied to fracture imaging in gneiss. *J. Geophysics*. 1050-1064.
14. Iannacchione, A. T. (1999). Pillar design issues for underground stone mines. *NIOSH*.
15. Itasca. (2018). 3DEC Software, Version 5.2. Itasca Consulting Group, Minneapolis, Minnesota, USA.
16. Itasca. (2018). FLAC3D Software, Version 5.01. Itasca Consulting Group, Minneapolis, Minnesota, USA.
17. Kuniansky, E. L., D.J. Weary, and J. E. Kaufmann. (2016). The current status of mapping karst areas and availability of public sinkhole-risk resources in karst terrains of the United States. *J. Hydrogeology*. 613-624.
18. McDowell, R.C. and Schultz, A.P. (1990). Structural and stratigraphic framework of the Giles County area, a part of the Appalachian Basin of Virginia and West Virginia (No. 1839-E).
19. Miyoshi, T., Elmo, D., & Rogers, S. (2018). Influence of data analysis when exploiting DFN model representation in the application of rock mass classification systems. *Journal of Rock Mechanics and Geotechnical Engineering*, 10(6), 1046-1062.
20. Monsalve, J. J., Baggett, J. G., Soni, A., Ripepi, N., & Hazzard, J. (2019). Stability analysis of an underground limestone mine using terrestrial laser scanning with stochastic discrete element modeling. In *Proc. 53rd US Rock Mechanics/Geomechanics Symposium*, New York City, NY. American Rock Mechanics Association.
21. Monsalve, J. J., Pfreundschuh, A., Soni, A., & Ripepi, N. (2021). Automated Discontinuity Extraction Software Versus Manual Virtual Discontinuity Mapping: Performance Evaluation in Rock Mass Characterization and Rockfall Hazard Identification. *Mining, Metallurgy & Exploration*, 38(3), 1383-1394.
22. Mine Safety and Health Administration. (2021). Pillar Collapse Initiative. *https://www.msha.gov/news-media/special-initiatives/2021/10/29/pillar-collapse-initiative.*
23. National Institute for Occupational Safety and Health. (2022). Number of active underground stone mines by year 1983-2020. *https://www.cdc.gov/NIOSH-Mining/MMWC.*
24. Pierce, M. (2017). An introduction to random disk discrete fracture network (DFN) for civil and mining engineering applications. *ARMA e-Newsletter*. 20, 3-8.
25. Soni, A., Monsalve, J. J., Bishop, R., Ripepi, N. & Baggett, J. G. (2022). Estimating Strength of Pillars with Karst Voids in a Room-and-Pillar Limestone Mine. *Mining, Metallurgy & Exploration*. 1-14.